Modelling and field data analysis of subglacial hydrological conditions in West Greenland.

Dow, Christine Fiona

Modelling and field data analysis of subglacial hydrological conditions in West Greenland.

Christine Fiona Dow

Submitted to Swansea University in fulfilment of the requirements for the Degree of Doctor of Philosophy.

Swansea University

2013

Abstract

The rapid drainage of Greenlandic supraglacial lakes injects a substantial volume of water to the bed of the ice sheet, however the impacts of this water pulse on the development of basal hydrological systems are largely unknown. In this thesis, a coupled hydrological model approach is introduced whereby two established models are linked together to better examine short- and long-term (i.e. diurnal vs. seasonal) subglacial impacts of rapid lake drainage. The primary aim of the thesis is to test whether substantial, efficient channels form during or following a lake drainage event, particularly in regions of thick ice.

Modelling is constrained by field data from an inland site on Russell Glacier catchment, with the model also applied to a simple tidewater glacier and a marginal glacier geometry. Basal boundary conditions in the model are examined using reflection seismic techniques, including amplitude-vs.-angle analysis to determine properties of the subglacial substrate in Russell Glacier catchment.

Modelling results indicate subglacial conduits do not generally form during lake drainage events, particularly under thick ice. Instead, lake drainage water is evacuated by a temporary turbulent sheet. Following lake drainage, a distributed drainage system continues to dominate in the inland ice case-study; variable basal topography at this site enhances the highly transient behaviour of this drainage system. Both shallower surface slopes and thicker ice at the inland site contribute to a lack of seasonal conduit growth. Nearer the ice margin, efficient channels develop during the melt-season at a similar rate as recorded at Alpine glaciers, although these channels are transient features and a distributed system continues to contribute to ice dynamics. However, despite increased efficiency, modelled channel size near the margin does not generally exceed $2\,\mathrm{m}^2$. Seismic analysis indicates that subglacial sediment is a feature in various regions of Russell Glacier catchment and could impact hydrological development.

Declaration

This work has not previously been accepted in substance for any degree and is not being concurrently submitted in candidature for any degree.

Signed .... (candidate)

Date 19/3/14

Statement 1

This thesis is the result of my own investigations, except where otherwise stated. Where correction services have been used, the extent and nature of the correction is clearly marked in a footnote(s).

Other sources are acknowledged by footnotes giving explicit references. A bibliography is appended.

Signed ... . (candidate)

Date 19/3/14

Statement 2

I hereby give consent for my thesis, if accepted, to be available for photocopying and for inter-library loan, and for the title and summary to be made available to outside organisations.

Signed . ..... (candidate)

Date 19/3/14

Acknowledgements

I would like to begin by thanking my supervisors, Bernd Kulessa and Ian Rutt, who have provided encouragement and support, along with valuable input, throughout this entire process.

The modelling in this thesis has benefited from the help and insight of various individuals. In particular, thanks go to Victor Tsai for providing me with the water blister model code and assistance in setting up and linking the models. Sam Pimentel provided the flowband hydrological model code, developed by himself and Gwenn Flowers. Thanks also to both for hosting me at Simon Fraser University for several weeks and providing much help with the modelling process. Whilst in Vancouver, I also benefited greatly from conversations with Mauro Werder and Ian Hewitt who were very much responsible for pointing me down the coupled hydrological modelling route. The simple R-channel model in Chapter 4 was entirely born from very helpful conversations at the Karthaus 'Ice Sheets and Glaciers in the Climate System' summer school with Ed Bueler and Felix Ng. The thesis has also been improved by comments from Glenn Jones and Martin OLeary.

The seismic reflection and AVA analyses in this thesis would not have been possible without the help and support from Adam Booth. In addition, data provided by Glenn Jones, Adam Booth, Andy Fitzpatrick, Dirk van As, Sam Doyle, Rickard Petterson and Katrin Lindbäck have all contributed towards applying and testing the models in this thesis. Thanks also go to Alun Hubbard for providing me with several months of amazing field-work experiences in Greenland. Much-appreciated funding for this Ph.D. was provided by a NERC studentship and the Greenland Analogue Project.

Finally, a million thanks go to my family (mum, dad and Anna) and friends for their support and encouragement over the past four years. In particular, Ingrid, Anne, Sue and Alison have been there for me throughout this whole process and made the experience enjoyable and much less frustrating than it could have been. Thankyou to Charlotte for the knitting tutorials and to Ash for laughs over odd websites. Thanks to my office mates who have kept the atmosphere light over the last year with friendly abuse, and the Swansea glaciology group in general who have been integral to the Ph.D. experience. Thanks also to Alistair for coping with me during the write-up year and looking after me during the surfing-induced convalescence. On that note, some advice to those in the final three months of writing up: if you decide going surfing is a good idea, make sure to wear a helmet (even if it does look silly)!

Contents

List of Figures

List of Tables

List of Symbols

α	seismic attenuation
β^*	geometric threshold for water flow
$\beta^\dagger$	thermal threshold for water flow
χ	friction parameter
χ_w	vertical crack friction near overburden
Δa	ice surface gradient
Δb	ice bed gradient
ΔP_{in}	pressure in excess of overburden
Δx	flowband grid-step size
$\dot{b}^c$	channel source term
$\dot{b}^{sh}$	water sheet source term
η	dynamic viscosity of water
γ	pressure dependence of the melting point
λ	numerical compressibility parameter
λ_s	seismic wavelet wavelength
μ	shear modulus
$\nabla\psi$	gradient of hydraulic potential
ν	Poisson's ratio
ϕ	geometric hydraulic potential gradient
$\phi^{sh:c}$	sheet to channel exchange
ψ	hydraulic potential
ψ_0	reference potential
$\Re$	Reynolds number
ρ	material density
ρ_i	density of ice
ρ_w	density of water
τ	shear stress
τ_b	basal drag
ξ	coefficient of proportionality
A	Glen's flow law coefficient
a	ice surface elevation
A_0	lake surface area
A_0	normal incidence source amplitude
a_c	vertical crack half-width

A_m	multiple arrival amplitude
A_p	primary arrival amplitude
B	bulk modulus
b	bed elevation
C_1	constant
C_2	constant
c_p	specific heat capacity of water
C_s	volumetric specific heat of water
C_w	Clausius-Clapeyron gradient
d_c	lateral channel spacing
d_n	no. of channels in the flowband
d_p	primary arrival travel distance
E	Young's modulus
f	Darcy-Weisbach friction factor
f_0	frictional constant
f_s	seismic wavelet frequency
f_w	water pressure coefficient
Fr	first Fresnel zone
g	gravitational acceleration
H	ice thickness
h	basal uplift
h^{sh}	average water sheet thickness
h_c^{sh}	critical water sheet thickness
h_p	primary reflection depth
h_s	ice surface uplift
H_w	height of water in the lake
K	sheet hydraulic conductivity
k	Nikuradse roughness height
K_{IC}	fracture toughness
K_I	stress intensity factor
L	blister radius
l	conduit segment length
L_f	latent heat of fusion
m_i	channel wall melt rate
N	effective pressure
n	Glen's flow law exponent
n'	Manning roughness coefficient
N_x	number of grid-cells overlapped by the blister
P	pressure in the crack
P_w^c	channel water pressure
P_w^{sh}	sheet water pressure
P_i	ice overburden pressure
P_{out}	coupled model outlet pressure
P_{wet}	channel wetted perimeter
P_w	water pressure
Q	channel water flux
Q^c	channel discharge
Q_b^c	channel upstream boundary flux
q^{sh}	sheet discharge

Q_b	flow rate within the blister
Q_G	geothermal heat flux
Q_s	seismic quality factor
R	distance from the blister centre
r	conduit radius
$R(\theta)$	angle-specific reflection coefficient
R_H	hydraulic radius
S	channel cross-sectional area
s	distance along the channel
S_ϵ	initial channel size
t	time
t_{p-j}	time of grid-cell overlap by blister
t_p	coupled hydrological model primary time-step
U	vertically-averaged fluid velocity
u_0	vertical crack opening
u_b	basal sliding velocity
u_s	ice surface horizontal displacement
U_v	water velocity in the vertical crack
v	channel water velocity
V_0	lake volume
V_b	water volume in the blister
V_c	water volume in the vertical crack
V_{end}	stage when all lake water is in the subsurface
V_f	blister:flowband overlap volume
V_{new}	adjusted blister volume
V_{out}	flux from margin of the blister
V_p	P-wave velocity
V_r	blister partial grid-cell overlap volume
V_s	S-wave velocity
W	flowband fixed width
w	homogeneous material crack opening
x	horizontal dimension
$X^{sh:c}$	water exchange coefficient
X_0	horizontal distance from water input
y	dummy variable
Z	acoustic impedance
z	elevation above a reference datum
Z_{thin}	thin layer acoustic impedance
Z_{under}	underlying layer acoustic impedance

List of Acronyms

ASTER Advanced Spaceborne Thermal Emission and Reflection Radiometer.

AVA amplitude-versus-angle.

AWS automatic weather station.

CMP common mid-point.

DEM digital elevation model.

DOY day of year.

ELA equilibrium line altitude.

FP F-Lake planar topography model.

FR F-Lake real topography model.

GEUS Geological Survey of Denmark and Greenland.

GPR ground penetrating radar.

GPS Global Positioning System.

GrIS Greenland Ice Sheet.

K-Z Knott-Zoeppritz.

MG marginal glacier model.

MODIS Moderate-resolution Imaging Spectroradiometer.

NMO normal move-out.

PDD positive degree day.

RGC Russell Glacier catchment.

RMS root mean squared.

SPOT Satellite Pour l'Observation de la Terre.

TG tidewater glacier model.

UTC Coordinated Universal Time.

Chapter 1

Introduction

1.1 Motivation

The Greenland Ice Sheet (GrIS) has the potential to contribute up to 7 m towards sea level rise in a warming world (IPCC, 2007). Additionally, increased influx of fresh water from Greenland could substantially affect the overturning of deep water currents that form in the North Atlantic, thus potentially directly influencing changes in global climate (Alley *et al.*, 2005a). With projections suggesting a temperature rise of ~2-4°C over the next 100 years (IPCC, 2007), it is important to quantify the effect of changing climate on the ice dynamics, and as a result, the mass balance of the GrIS. However, IPCC models currently do not include feedbacks related to the dynamical changes of ice sheet outlet glaciers (Alley *et al.*, 2005a; Shepherd and Wingham, 2007), primarily because there is very little direct information and no consensus on the various variables that affect the velocity of Greenland outlet glaciers. Knowledge of whether subglacial water is an important contributing factor to Greenland ice dynamics is necessary if predictions about the impact of future warming on the GrIS are to be accurate.

Surface meltwater accesses the bed of the GrIS by propagating through fractures in the ice during rapid drainage of surface meltwater lakes (van der Veen, 1998; Boon and Sharp, 2003; Das *et al.*, 2008; Doyle *et al.*, 2013) and through moulins once a surface-to-bed connection has been established (Das *et al.*, 2008; van de Wal *et al.*, 2008; Bartholomew *et al.*, 2012). This water flux can directly impact variations in

ice dynamics by lubricating the subglacial environment (Zwally *et al.*, 2002; van de Wal *et al.*, 2008; Shepherd *et al.*, 2009). Analysis of Moderate-resolution Imaging Spectroradiometer (MODIS) imagery by Sundal *et al.* (2009) indicated that there is substantial variability in surface meltwater and lake development across the GrIS. The concern is that with warming air temperatures, greater volumes of surface meltwater might access the bed and speed up outlet glacier flow (Alley *et al.*, 2005b; Das *et al.*, 2008). Such a draw down of ice could significantly impact the mass balance of the GrIS (Alley *et al.*, 2005a; Bamber *et al.*, 2007).

However, the subglacial hydrological system of the GrIS has recently been compared to that of an Alpine glacier (Bartholomew *et al.*, 2010, 2011b, 2012; Chandler *et al.*, 2013; Cowton *et al.*, 2013). Such a system involves the development of channels during the summer melt-season as a result of increased volumes of water accessing the bed (Nienow *et al.*, 1998). The growth of a channelised system is argued to encourage the coincident shrinkage of a distributed system that persists over the winter months (Schoof, 2010). The seasonal hydrological transition between an inefficient distributed system and an efficient channelised system has a direct impact on ice dynamics as a result of the reduction in basal lubrication (Kamb, 1987). This Alpine-like system has been identified in Greenland from a) dye tracing and proglacial discharge studies indicating increasing channelisation during the melt-season (e.g. Chandler *et al.*, 2013; Cowton *et al.*, 2013), b) Global Positioning System (GPS) records (e.g. Bartholomew *et al.*, 2010, 2011b) and c) remote sensing studies (e.g. Sundal *et al.*, 2011), with the latter two methods identifying velocity transitions between fast and slow flow, argued to be associated with subglacial channelisation. It is interesting to note that many studies of hydrological development have been focussed in areas of the GrIS where the conditions are similar those seen under Alpine glaciers, such as towards the margin where ice is relatively thin and surface slopes are steeper (e.g. Bartholomew *et al.*, 2010; Sundal *et al.*, 2011; Cowton *et al.*, 2013). Little attention has been paid to basal hydrological development in areas of thick and flat inland ice; such conditions are traditionally associated with channel closure rather than growth (Nye, 1976). It is also in such regions that many of the rapidly draining surface lakes are found (Sundal *et al.*, 2009; Selmes *et al.*, 2011; Fitzpatrick *et al.*, 2014).

The rapid drainage of supraglacial lakes has been argued to allow rapid growth of subglacial channels (Sole *et al.*, 2011; Cowton *et al.*, 2013). Ice surface GPS records show uplift within the initial stages of lake drainage, followed by subsidence several hours later (Das *et al.*, 2008; Doyle *et al.*, 2013). These records have been

suggested to indicate rapid removal of the lake water at the ice-bed interface, in turn attributed to the presence of large channels (Das *et al.*, 2008; Hoffman *et al.*, 2011; Pimentel and Flowers, 2011). For example, one of the few modelling studies applied to lake drainage events (Pimentel and Flowers, 2011) required a pre-existing channel of 22 m^2 cross-sectional area in order to stably remove the lake water during drainage. Thus, channels are argued both to grow quickly as a result of rapid drainage (Cowton *et al.*, 2013) and in some cases are suggested to have formed prior to the lake drainage event (Das *et al.*, 2008; Pimentel and Flowers, 2011).

1.2 Aims and objectives

Based on numerical modelling and field data collection, it is the primary aim of this thesis to determine the role of rapid lake drainage in subglacial hydrological development, and advance understanding of the basal drainage system characteristics in different areas of the GrIS.

Using numerical modelling techniques, the specific objectives are to:

- Determine the mode of subglacial water evacuation during rapid supraglacial lake drainage events in West Greenland.
- Examine seasonal subglacial hydrological development once a surface-to-bed connection has been made as a result of lake drainage, allowing diurnally-varying water input into the basal system.
- Establish the impact of lake drainage on basal hydrological development in different glaciological settings, i.e how does channel growth differ between inland ice, a tidewater glacier and a land-terminating marginal glacier?

The specific objectives of the field data collection are to:

- Use in-situ data from a rapid lake drainage event to constrain the numerical model.
- Investigate subglacial conditions that might impact hydrological development, including basal material and topography.

The objectives are achieved by applying a unique approach to numerical modelling where two world-leading and complementary lake drainage models are coupled together. This coupled model approach allows analyses of both short- (diurnal) and long-term (seasonal) hydrological development as a result of rapid lake drainage. The coupled hydrological model is constructed with known inputs from in-situ data collected from a case-study site on Russell Glacier catchment (RGC), a land-terminating region in West Greenland; these in-situ data also provide tests for the model outputs. Uncertainty in the model is established with a large range of sensitivity experiments. The model is then applied to simplified domains representative of different areas of the GrIS (i.e. lake drainage at a tidewater glacier and a near-margin land-terminating glacier) in order to assess the larger scale subglacial hydrological development in Greenland. Subglacial conditions are examined by analysing reflection seismic data in RGC to determine whether the bed is comprised of sediment or bedrock. Also, the basal topographical variation in the vicinity of the case-study lake site is examined to establish the role of overdeepenings and supercooling in drainage development under the ice sheet.

By combining these modelling and geophysical approaches, this thesis gives insight into basal hydrological development characteristics that can be applied not only to the RGC, but to other areas in Greenland and allows improved determination of the impact of subglacial hydrology on ice dynamics.

1.3 Thesis structure

This thesis is separated into ten chapters and is laid out as follows:

Chapter 1: This introductory chapter gives an overview of the thesis topic within the wider scope of Greenlandic glacier research and introduces the aims of the hydrology modelling and geophysical processing efforts in relation to understanding the impacts of Greenland subglacial hydrological development.

Chapter 2 gives an overview of the literature to date that is relevant to this thesis including: theories of subglacial hydrology, ideas of hydrofracture and lake drainage events, rapid floods in glacial settings, approaches to modelling glacial hydrological systems and finally, reports of GrIS dynamics with particular focus on RGC. The aim of this chapter is to put the thesis research into context.

Chapter 3: Here, the case-study research site, F-Lake, is introduced in addition to the data collected in the vicinity of this site. Most of the data in this chapter were collected and processed by collaborators; such data include surface and basal digital elevation models (DEMs), GPS records, passive and reflection seismic data, satellite remote sensing imagery analysis, automatic weather station (AWS) data and surface energy balance modelling. These data are briefly discussed along with analyses completed by the author including lake bathymetry calculations, lake drainage rate, and hydraulic potential and supercooling calculations. In addition, the characteristics of the case-study lake drainage event are discussed.

Chapter 4: In this chapter, a simple R-channel model is introduced based on equations from Nye (1976) and run on a basic domain for thick ice. This model is applied to a) lake drainage events, with sensitivity tests based on the length of time of channel pressurisation as a result of lake drainage, and the effects of channel roughness and hydraulic potential and, b) diurnally-varying water input akin to drainage through a moulin to the ice-bed interface. The aim of the simple model is to test how rapidly channels can grow under thick ice and how long they will persist under different pressure conditions.

Chapter 5 introduces two models that are coupled together to assess subglacial hydrological development in different regions of the GrIS. The first model is a radial water blister model developed by Tsai and Rice (2010) that calculates elastic opening and uplift of the englacial and subglacial systems respectively during a rapid lake drainage event. The second model is a coupled distributed and channelised drainage model developed by Pimentel and Flowers (2011) and applied with a fixed-width flowband. Both of these models have limitations when applied independently to rapid lake drainage events; the approach in this thesis is to link the two models together, which reduces many of the limitations and produces a more accurate environment to test hydrological development. The implementation and equations of each model are discussed along with the method of linking the models together.

Chapter 6: In this chapter the implementation of the coupled hydrological model for addressing the aims of this thesis is discussed. The model is applied to four domains: 1) the case-study lake in a region of thick ice with a simple planar topography; 2) the case-study lake with varied topography determined from surface and basal DEMs; 3) a tidewater glacier located in a region of thick

ice; and 4) a land-terminating glacier close to the margin with thinner ice. The range of parameters used for model sensitivity testing and the approach to data analysis are also discussed.

Chapter 7: The results and sensitivity analysis of the coupled hydrological model are reported in this chapter. First, some simple tests of the water blister model are examined. Second, the results from the baseline coupled hydrological model runs for each modelled geometry are reported. The impact of individual parameters on model outputs are then discussed, followed by addressing and comparing the outputs for the individual model domains. Analysis is primarily focussed on channel growth both during and after rapid lake drainage.

Chapter 8 presents analysis of two seismic reflection lines acquired in different regions of RGC. The first site is located 5 km to the NE of the case-study lake over a subglacial basin. The second site is downstream of the case-study site, ~15 m from the terminus of Russell Glacier. To determine the basal material present at each site a seismic stack is built and amplitude-versus-angle (AVA) analysis performed on the reflection seismic data. Due to complications in data analysis for the second site as a result of noise in the data, a new method for AVA analysis is developed. Finally, the implications of the seismic data analysis at both sites are discussed in relation to application of the coupled hydrological model.

Chapter 9: This chapter brings together the results from chapters 3, 4, 7 and 8 to address the aims outlined in Section 1.2. A detailed examination of the contribution of the results to current knowledge of both hydrological development in Greenland and the related impact on ice dynamics is given. The limitations of the modelling approach introduced in this thesis are also discussed.

Chapter 10 concludes this thesis by summarising the major findings from the numerical modelling and geophysical analysis. Areas of suggested future work are also discussed.

1.4 Published material

Some of the methods and results from Chapter 8 in this thesis are published in Dow *et al.* (2013). The published material includes development of a new AVA analysis method for application to noisy seismic reflection data and the results from applying this method to a site near Russell Glacier terminus. The author has also contributed to a range of other publications associated with the field data collection discussed and utilised in this thesis. These include publications examining passive seismic processing from the case-study site (Jones *et al.*, 2013); GPS data from the lake drainage event (Doyle *et al.*, 2013); and satellite remote sensing analysis of RGC lake drainage patterns (Fitzpatrick *et al.*, 2014).

Chapter 2

Greenland glacial hydrology

2.1 Introduction

This thesis examines basal characteristics of the GrIS and subglacial hydrological development in response to rapid supraglacial lake drainage events. This chapter will put the thesis research into context by discussing the following range of topics: 1) an introduction to glacial hydrology theory including discussions of both inefficient (slow flow) and efficient (fast flow) subglacial drainage systems; 2) a discussion about rapid lake drainage events, observed in both Alpine and Greenlandic glacier settings; 3) approaches to modelling subglacial hydrological systems and, 4) an examination of current theories about Greenland hydrological systems, focussing on research conducted on RGC, where the thesis case-study is located.

2.2 Glacial hydrology

In this section, several types of hydrological systems will be introduced including: 1) distributed, 2) channelised, and 3) sediment-based. Although these drainage networks are presented here as independent entities, it is likely that multiple hydrological systems exist under a glacier (Vivian, 1980), creating a complex set of interactions that are challenging to replicate in numerical models.

2.2.1 *Distributed drainage*

During winter, pressures under glaciers are argued to typically equilibrate near overburden with little temporal or spatial variation due to lack of water input from the surface (Harper *et al.*, 2005). Glacial melt-seasons predominantly begin in late spring as rising temperatures melts surface snow and ice (Röthlisberger and Lang, 1987). Water accesses the glacier bed through moulins (Stenborg, 1973; Hooke, 1989)), crevasses (Weertman, 1973; Boon and Sharp, 2003), or conduits through the ice (Röthlisberger and Lang, 1987; Fountain and Walder, 1998).

Early in the season, the first water to reach the base of the ice tends to intersect a highly undeveloped, low-capacity drainage system (Röthlisberger and Lang, 1987; Nienow *et al.*, 1998). Where ice flows over rock, water is argued to initially flow into cavities in the bedrock where the pressure is lower (Lliboutry, 1964), as shown in Figure 2.1 b. With further water input, small channels are melted between the cavities, allowing slow inefficient flow through a highly anastomosing system (Lliboutry, 1968; Iken and Bindschadler, 1986), as shown in Figure 2.2 a. The high water pressures associated with such distributed systems can, with sufficient water input, overcome the overburden pressure of the ice and lift the glacier off the bed (Bindschadler, 1983; Iken *et al.*, 1983; Iken and Bindschadler, 1986). Such uplift is referred to as hydraulic jacking and, by reducing the frictional contact between the bed and ice, often allows an increase in the ice velocity until an ice-bed reconnection is made (Iken *et al.*, 1983; Röthlisberger and Lang, 1987). This temporary increase in velocity at the beginning of a melt-season is often referred to as a spring event (Röthlisberger and Lang, 1987).

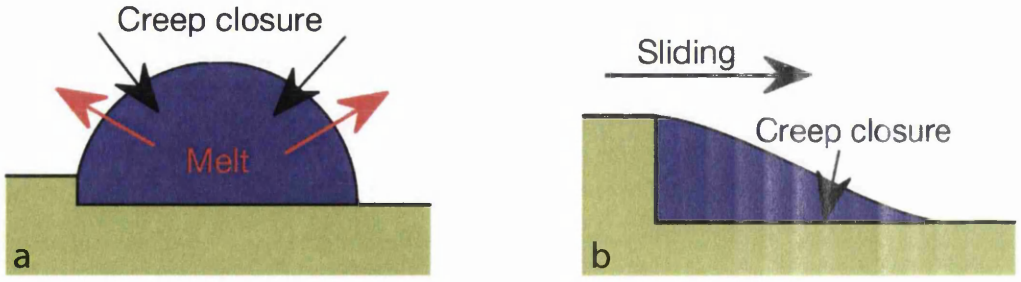

Figure 2.1: *Schematic of ice/water balances for a) channels and b) linked cavity systems. From Schoof (2010).*

Weertman (1972) suggested that a film of water, formed from frictional and geothermal heating, can flow in a thin (~1 mm) layer at the ice-bed interface providing water

fluxes to more efficient drainage regions from isolated areas of the glacier bed. If regions with more efficient drainage become overpressurised due to rapid increases in water volume Weertman (1972) also argued that the excess water would spread out into a film. However, Nye (1973) countered that basal roughness would cause inherent instability in a water film that would favour development of a linked-cavity or channelised system. In addition, Walder (1982) argued that water films would rapidly become unstable due to differences in basal melt rates related to spatial variation in ice thickness.

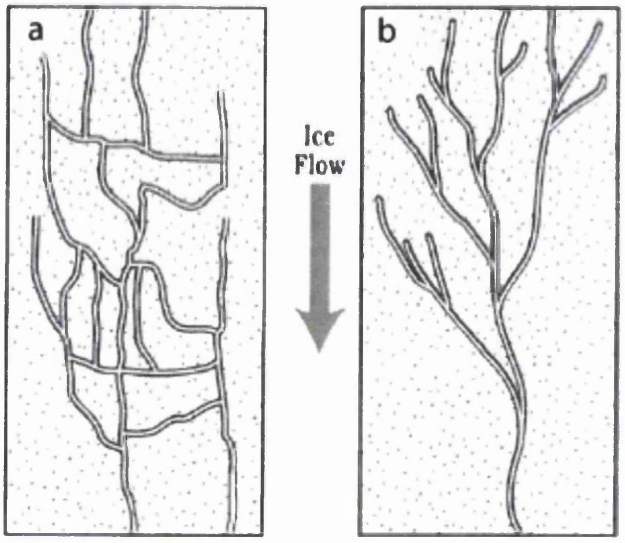

Figure 2.2: *Plan view of a simplified a) distributed linked-cavity drainage system and b) channelised drainage system. From Fountain and Walder (1998).*

2.2.2 *Channelised drainage*

As the melt-season progresses and water input into glacial systems continues, cavity drainage in temperate glaciers often develops into efficient channelised drainage (Nienow *et al.*, 1998). A similar seasonal evolution has been proposed for the outlet glaciers of the GrIS (Bartholomew *et al.*, 2010, 2011b; Joughin *et al.*, 2013). Basal channels that melt up into the ice are called Röthlisberger (R-)channels; the size of these R-channels is controlled by the relationship between viscous dissipation of heat from flowing water that acts to melt the ice walls, and the creep of ice into the channel (Röthlisberger, 1972), as shown in Figure 2.1 a. Conduits are therefore highly dynamic features and are continually changing over the course of a melt-season (Nye, 1973). In valley glacier systems, dye tracing experiments (Schuler *et al.*,

2004) and mathematical modelling (Schuler and Fischer, 2009) have demonstrated that basal R-channels can adjust to changes in water input on the scale of hours to days.

Water pressure will be lower in larger channels than in smaller channels with the same discharge and, as water flows from high to low pressure, larger channels will tend to draw water from smaller channels (Röthlisberger, 1972). In this manner, linked-cavities can develop into an arborescent (i.e. dendritic) network of efficient channels (Shreve, 1972), as shown in Figure 2.2 b. Such discrete channelisation limits the influence of water on ice dynamics as the channels make up a much smaller proportion of the bed than linked-cavities. As such, towards the end of a season, ice velocities tend to decrease because hydraulic jacking is less likely to occur with an efficient channelised drainage system (Paterson, 1994). Because greater volumes of meltwater input are necessary to maintain the pressure within larger channels, these efficient drainage systems begin to shut down towards the end of a melt-season when surface melt reduces in volume (Hoffman *et al.*, 2011). It is during such conditions (and at night when little meltwater is input into the system) that water in channels might flow at atmospheric pressure (Cutler, 1998).

Additional water can be supplied to a glacier throughout the year through groundwater influx and geothermally-driven melt of subglacial ice (Hooke *et al.*, 1985; Paterson, 1994). Such water sources tend to be limited and, as a result, the hydrological drainage systems that develop through the summer melt-season constrict over the winter period when little water reaches the glacier bed from the surface (Röthlisberger and Lang, 1987; Fountain and Walder, 1998).

2.2.3 *Drainage through sediment*

With the presence of sediment at the ice-bed interface, the development of a basal hydrological system differs somewhat from that in a ice-rock system. Water can flow slowly through sediment pores as Darcian flow (Iken and Bindschadler, 1986; Paterson, 1994), although such flow is often restricted in terms of both velocity and capacity (Lliboutry, 1983; Iken and Bindschadler, 1986; Walder and Fowler, 1994). It has been assumed that a sediment base will cause an even distribution of basal water pressure as movement of sediment particles, particularly under high water pressures or during deformation, would fill in cavities and channels that might otherwise cause spatial pressure variability (Iken and Bindschadler, 1986).

However, with increasing volumes of water input to the ice-bed interface during a melt-season, it is not clear how the fluid interacts with basal sediment. Flow through broad, low canals eroded down into the sediment and up into the ice (Walder and Fowler, 1994) and cavities in the sediment (Kamb, 1987) have been proposed as possible efficient sediment-based drainage paths but were contested by Paterson (1994) as being too unstable to persist. Evidence for sediment canals is very limited; King *et al.* (2004) found changes in seismic reflectivity at the bed of Rutford Ice Stream, West Antarctica, and argued that it represented a canal eroded down into till. However, little other evidence has been found. On the other hand, it is likely that fast water flow occurs in areas with sediment; the dissipation of viscous heat during water flux will likely cause areas of concentrated flow even in a sediment-based system (Wadham *et al.*, 1998). Water could potentially flow through sediment in pipes or in a macroporous horizon (Clarke, 1987); pipes are created through fine sediment eluviation and constitute a faster version of Darcian pore-water flow (Clarke, 1987), whereas a macroporous horizon forms when sediment grains are re-aligned by water flow, creating larger pore spaces and thus resulting in greater hydraulic conductivity in the sediment (Clarke, 1987). Establishing what types of hydrological systems exist in areas of soft till is still an area of research that requires further attention.

The velocity of warm-based glaciers flowing on a hard bed is controlled primarily by visco-plastic ice deformation and water-lubricated basal sliding (Paterson, 1994). Sediment-based glaciers can additionally undergo enhanced basal flow through sediment deformation (Clarke, 1987; Iverson *et al.*, 1995). If the yield strength of basal material (determined primarily by the pore-water pressure within the sediment) is lower than the shear stress from overlying ice, the sediment will deform allowing accelerated ice flow (Iverson *et al.*, 1994, 1999; Fischer and Clarke, 2001). Evidence of faulting and folding of sediment in deglaciated regions is indicative of widespread deformation that occurs under ice in areas with a sediment base (Iverson, 2010). However, Piotrowski *et al.* (2004) suggested that the presence of fast water-flow features such as conduits in sediment could have an important role in removing pore water and thus increasing sediment strength, thereby limiting sediment deformation under certain water flow conditions.

2.2.4 *Ice dynamics*

The presence of water at the ice-bed interface impacts ice dynamics primarily in terms of storage capacity and related water pressure. Peaks in ice velocity have been associated with ice uplift; however the maximum velocity tends to correlate most closely with the greatest rate in change of uplift rather than the maximum absolute uplift (Iken *et al.*, 1983). A similar relationship has been seen between the rising limb of surface water influx and ice velocity (Mair *et al.*, 2002), thus closely relating the rate of change of subglacial storage capacity (and therefore the increase of basal water pressure) with ice motion, as opposed to the total water volume within the system (Bartholomaus *et al.*, 2007; Colgan *et al.*, 2011; Bartholomew *et al.*, 2012).

If water input exceeds the existing system capacity, water can be forced out of conduits into a distributed system allowing greater lubrication of the ice-bed interface (Hubbard *et al.*, 1995; Bartholomaus *et al.*, 2007). However, with development of a highly efficient drainage system during the summer melt-season, it has been reported that large influxes of meltwater are necessary to overwhelm the basal system and allow increases in ice surface velocity (Andersen *et al.*, 2011). Schoof (2010) suggests that sudden pulse-like inputs of water causing short but high frequency variations in ice velocity can have more dynamic impact than a steady seasonal increase in water input.

2.3 Rapid lake drainage events

Water input into a subglacial system via moulins generally varies concurrently with surface air temperatures over a melt-season (van As *et al.*, 2012). However, sudden pulses of high pressure water can also be delivered to the ice-bed interface due to rapid lake drainage events. These drainage events take many forms (see Fig. 2.3) but are all generally associated with short-term increases in ice velocity (e.g. Das *et al.*, 2008; Sugiyama *et al.*, 2008; Magnússon *et al.*, 2010; Danielson and Sharp, 2013; Tedesco *et al.*, 2013). On the GrIS and on high Arctic glaciers, lakes can drain rapidly through hydrofracture from the surface to the bed (Weertman, 1973; van der Veen, 1998; Boon and Sharp, 2003; Tedesco *et al.*, 2013), whereas in Alpine glaciers, lakes can be supraglacial or marginal and often drain by breaching an ice dam (Nye, 1976; Walder *et al.*, 2005). In Iceland, rapid lake drainages, or jökulhlaups,

are associated with geothermally-enhanced melt rates allowing growth of subglacial lakes with drainage again usually controlled by an ice dam (Roberts, 2005).

Despite the different mechanisms of drainage, lake outburst events have some features in common, primarily the rapid input of relatively large quantities of water into the subglacial system. Observations from both Icelandic jökulhlaups and Alpine lake outburst events can therefore be utilised to better understand the dynamic impact of GrIS supraglacial lake drainage events. This section will begin by introducing some of the research from Icelandic jökulhlaups and Alpine outburst events, followed by a description of ice-hydrofracture mechanics and rapid supraglacial lake drainage events in Greenland.

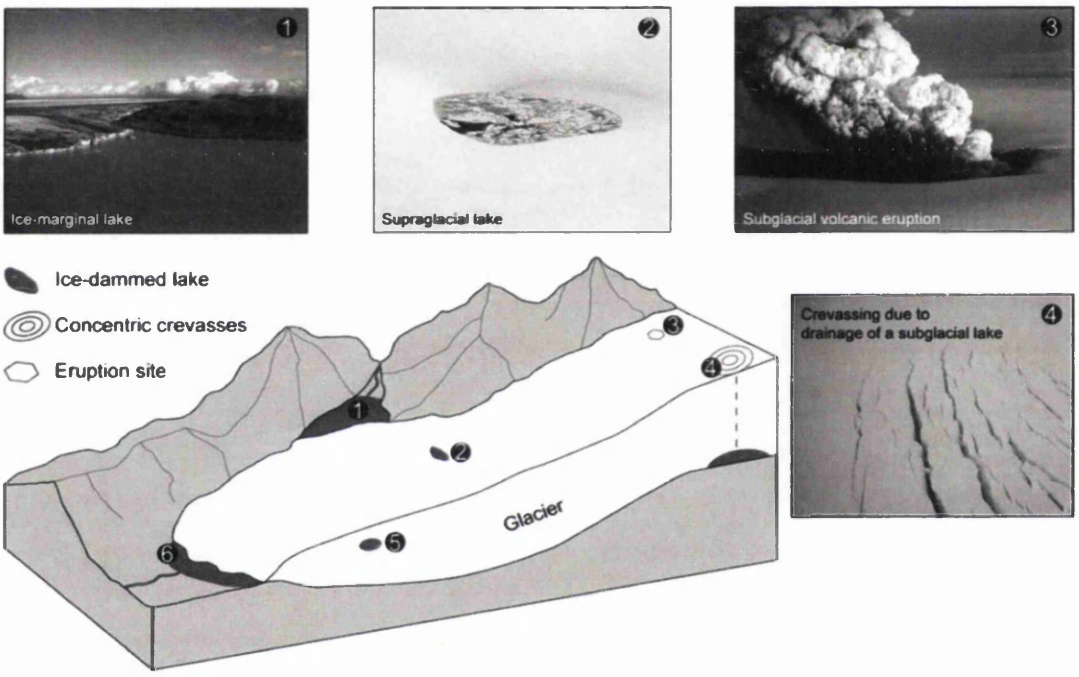

Figure 2.3: *A glacier schematic showing examples of types of lake drainage events. Numbers 5 and 6 refer to release of englacially-stored water and drainage of moraine-dammed lakes, respectively. From Roberts (2005).*

2.3.1 *Jökulhlaups*

Icelandic or valley glacier rapid lake drainage events are often both referred to by the Icelandic term, jökulhlaups, or alternatively as glacial lake outburst floods. Ice-marginal or subglacial lakes are argued to drain when the lake level increases to a height that can float (or hydraulically jack up) an ice dam and allow outflow of the

water into the subglacial system (Nye, 1976; Sturm and Benson, 1985; Walder and Costa, 1996; Walder *et al.*, 2005). It is argued that once the dam is breached, lake water drains through and enlarges an R-channel that runs from the lake to the terminus of the glacier (Nye, 1976; Clarke, 1982; Sturm and Benson, 1985; Walder and Costa, 1996; Ng and Björnsson, 2003). At the cessation of the lake drainage event, the lower pressure in the channel allows rapid closure; these drainage characteristics result in a pro-glacial discharge hydrograph with a gentle rising limb and a sharp falling limb (Nye, 1976; Walder and Costa, 1996), as shown in the 1954 data for Grímsvötn, Vatnajökull in Iceland plotted in Figure 2.4.

As will be discussed in greater detail in Section 2.4.2, jökulhlaups are generally modelled incorporating R-channel growth but with no provision for sheet flow or distributed systems (e.g. Nye, 1976; Spring and Hutter, 1981; Clarke, 1982, 2003; Werder and Funk, 2009); this approach assumes that channels are the predominant means of draining jökulhlaup lake water. For example, Sturm and Benson (1985) calculated the potential energy available for melting a basal conduit during the 1982 jökulhlaup at Triumvirate Glacier, Alaska, and suggested a channel of 18 m radius could persist for 4 km beneath the glacier, between the drainage input point and the terminus. In a similar jökulhlaup in 1984 at the same glacier, a tunnel of 10 m radius at the terminus was observed, implying the calculations of Sturm and Benson (1985) captured the dominant melt characteristics of the drainage event. Tweed and Russell (1999) suggested that volcanically-induced jökulhlaups are associated with enhanced conduit growth because of the excess thermal energy available for melting channel walls. Additionally, Magnússon *et al.* (2010) argued that surface velocity records from Grímsvötn indicated that water was slowly leaking out of the subglacial lake prior to full drainage. This could allow formation of an R-channel before the main drainage event, which would limit the spreading of highly pressurised water into a distributed system during the jökulhlaup (Magnússon *et al.*, 2010).

There is increasing evidence, however, that jökulhlaups can also be associated with pressurised water sheet flow and hydraulic jacking. By comparing moulin water pressures and proglacial discharge of a drainage event from Gornersee located on Gornergletscher, Switzerland, Werder *et al.* (2009) found that half of the lake volume was stored temporarily within the glacier; they suggested that storage was achieved by lateral flux from a subglacial channel. The water from this lake drainage event did not drain directly to the bed but instead flowed over the ice surface into a moulin. The moulin remained pressurised for 1.5 days and maximum subglacial water flux was determined by dye tracing to reach 1.05 $\mathrm{m\,s^{-1}}$ approximately one day

after drainage initiation (Werder and Funk, 2009). This evidence suggests that a sufficiently large channel developed within 24-36 hours to allow water flow through the basal system preventing further lateral flux or overpressurisation. A different drainage event from Gornersee was examined by Sugiyama *et al.* (2007); during this drainage, peak pro-glacial discharge was achieved three days after initial lake drainage and the lake took five days to empty. This drainage event caused ice surface uplift of 0.2 m and temporarily increased ice velocity by 50% over a period of four days. In addition, borehole water pressures increased to levels above overburden throughout the initial three days of lake drainage. In order to explain surface GPS records, Sugiyama *et al.* (2007) calculated that the drainage pathway had to be greater than 300 m in diameter. As result, they argued that the lake drainage caused extensive sheet flow that separated the ice and the bed by hydraulic jacking instead of growing a conduit.

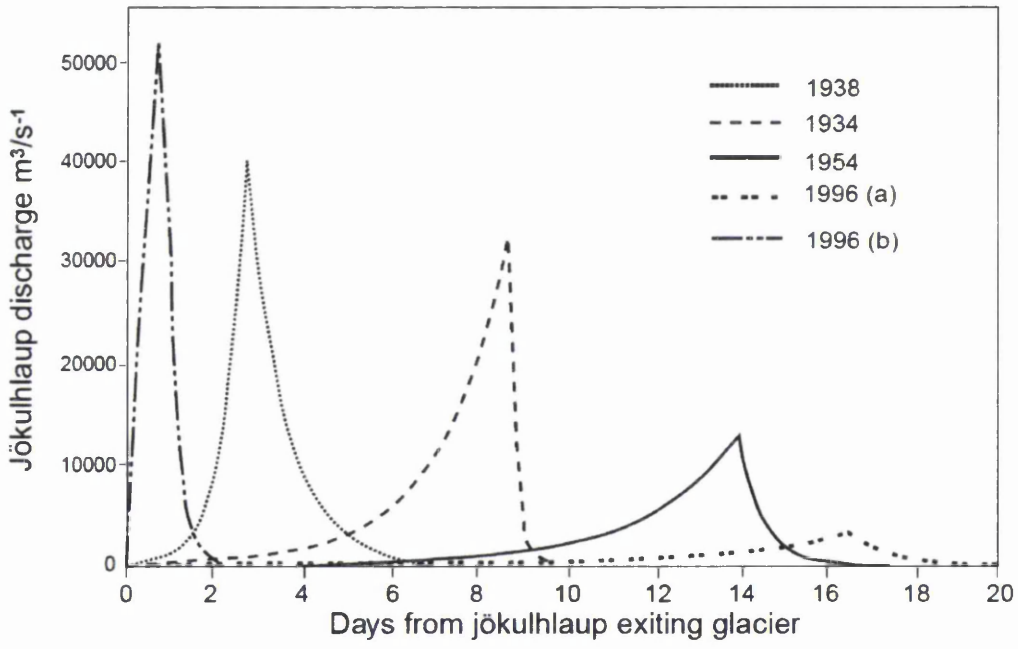

Figure 2.4: *Pro-glacial discharge hydrographs recorded during drainage events from Grímsvötn, Vatnajökull in the period from 1938–1996. From Tweed and Russell (1999).*

Evidence from Icelandic jökulhlaups also suggests that channels are not necessarily the only means of draining lake water. Johannesson (2002) argued that the rising limb of some floods from Grímsvötn lasts more than a week in conjunction with R-channel growth rates (for example, the 1934, 1954 and 1996(a) floods, see Fig. 2.4; Tweed and Russell, 1999). However, there are floods from Grímsvötn that reached

their maximum discharge within the scale of hours rather than days. For example, the 1996(b) Grímsvötn flood reached a maximum discharge of 50000 $m^3 s^{-1}$ within 16 hours of flood initiation (Fig. 2.4; Tweed and Russell, 1999). It is argued by Johannesson (2002) that a conduit would not have grown sufficiently quickly to allow such rapid transition of the water. Instead, it was suggested that a wave of high pressure water travelled through the subglacial system, allowing uplift of the ice from the bed. It was estimated that the width of the flowpath was ~1 km and the sheet thickness was 10 m; the appearance of supraglacial artesian fountains and cracking of 30 m-high ice blocks during the flood implied that the pressure was ~5-10 bars above overburden pressure (Johannesson, 2002). It is not clear however, why some jökulhlaups from Grímsvötn appear to be related only to channel growth and others related to the propagation of a high pressure water sheet.

2.3.2 *Hydraulically-driven ice fracture*

The initiation of rapid supraglacial lake drainage events in Greenland differ significantly from valley glacier jökulhlaups. For surface meltwater to access the bed of the GrIS it must first penetrate ~1 km of cold (where the ice is entirely below the pressure melting point) or polythermal ice (where some of the ice mass is cold and the remainder is temperate, at the pressure melting point); this is achieved by hydrofracture (see Fig 2.5). One of the first discussions regarding the flux of water from the ice surface to the bed through hydrofracture was by Glen (1954). In this paper it was explained that if a crevasse is filled with water, the horizontal stress exerted by the hydrostatic pressure of the water can, with sufficient depth, be greater than vertical and longitudinal stresses and can allow the crevasse to enlarge. This analysis was based on comparison of ice and water stress components rather than calculating fracture mechanisms directly. Glen (1954) suggested that this stress-based mechanism might allow glacier-dammed lake and surface meltwater streams to access the ice-bed interface. Boon and Sharp (2003) confirmed the occurrence of hydrofracture through observations of surface meltwater ponding in crevasses followed by rapid drainage on the polythermal John Evans Glacier on Ellesmere Island in the Canadian High Arctic.

There are several conditions that must be met for fractures to propagate and be maintained through sub-freezing ice. For the crack tip to propagate, the tensile stress must exceed the fracture toughness (van der Veen, 1998). At depths of ap-

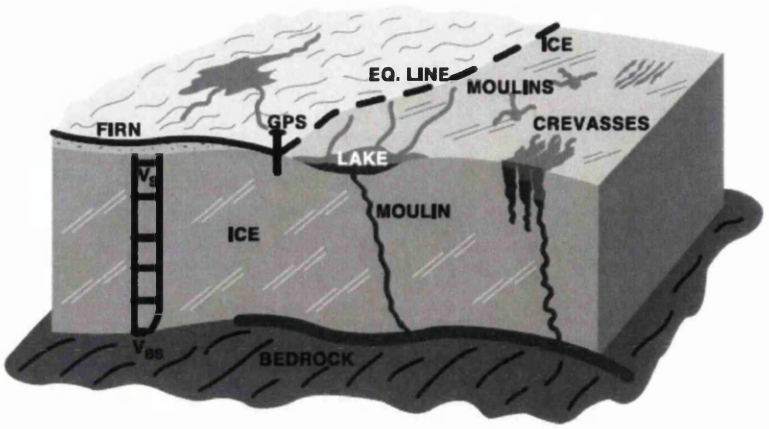

Figure 2.5: *Schematic of some of the glacial hydrological features that occur in Greenland, including supraglacial lake and moulin drainage to the bed. From Zwally* et al. *(2002).*

proximately 30 m (Tsai *et al.*, 2008), dry cracks will close due to the lithostatic stress of the ice (van der Veen, 2007; Krawczynski *et al.*, 2009). However, if the fractures are filled with water, the higher density of the liquid can allow crack tips to propagate to greater depths in the ice (Weertman, 1973; van der Veen, 1998). In cold ice, sufficient turbulent energy must be available to prevent the water freezing within the crack (Alley *et al.*, 2005b). For example, if fractures intersect an undeveloped drainage system, Boon and Sharp (2003) suggested that water might be retarded from flowing out of the fracture at the base, thus allowing refreezing of water within the englacial zone due to limited turbulent heating. Boon and Sharp (2003) also argued that in a polythermal glacier, several unsuccessful fracturing events (i.e. those that do not connect with the bed) are potentially necessary so that the latent heat from refreezing can increase the temperature of the ice; subsequent water draining in the fracture would then be less likely to freeze. For fracture propagation, there must be a sufficient supply of meltwater to maintain the hydraulic head in the fracture and thus the pressure at the fracture tip (Alley *et al.*, 2005b; Krawczynski *et al.*, 2009). Van der Veen (2007) calculated that a filling rate of $\sim$1 m hr^{-1} is necessary to maintain an open crevasse to the bed of a polythermal glacier. With this volume of water flow, van der Veen (2007) argued that freezing of water in the crevasse will not be sufficient to block it.

Calculations by van der Veen (1998) suggest that a tensile stress of >30-80 kPa is necessary for crevassing and fracture propagation. However, surface lakes form in concave areas of the ice surface that correspond to concave bedrock topogra-

phy (Lampkin and Vanderberg, 2011; Sergienko, 2013) As a result, areas with surface lakes are likely to be areas of ice compression, which retards the formation of crevasses (Das *et al.*, 2008). On the other hand, Krawczynski *et al.* (2009) argued that narrower fractures forming in areas of limited tension or minor compression will be able to propagate deeper than wider fractures, as the criteria for maintaining sufficient water height in the crevasse is more likely to be met for fractures of lesser volume. As a result, Krawczynski *et al.* (2009) suggested that surface lakes will actively encourage ice fracturing. Presumably, this is highly dependent on the compressive stresses at the lake site and the other conditions necessary for fracture propagation (Jones *et al.*, in prep.) as there are many lakes that do not drain during the melt-season (see e.g. Box and Ski, 2007; McMillan *et al.*, 2007; Sundal *et al.*, 2009).

2.3.3 *Greenland lake drainage events*

On the GrIS, lakes generally reform annually in the same area due to basal topographic control of undulations in the ice surface (Luthje *et al.*, 2006; Box and Ski, 2007; Lampkin and Vanderberg, 2011). These lakes provide a large volume of water that could maintain the necessary head to allow fracture to the base (Das *et al.*, 2008).

Das *et al.* (2008) recorded the drainage of a lake towards the western margin of the GrIS, where ice is ~980 m thick, in July 2006; from hereafter in this thesis, this event will be referred to as the 'Das lake drainage event'. The lake filled to a maximum volume of 0.044 km^3 after which the surface lowered at a rate of 1.5 cm hr^{-1} for 16 hours. At this time, rapid drainage initiated and persisted for ~1.4 hours until the lake was empty. The average drainage rate was 8700 $m^3 hr^{-1}$ and the maximum lowering rate of the lake surface was 12 m hr^{-1}. Within <1.5 hours of rapid drainage initiation, a GPS station located 0.5 km from the lake recorded a maximum horizontal displacement of ~0.8 m (perpendicular to the average flow direction) and ~1.2 m of ice surface uplift that gradually lowered over the following 24 hours; these data are shown in Figure 2.6. The rapid drainage event was accompanied by significant seismic activity that initiated half an hour before drainage, continued through the event and persisted for ~1 hour following drainage initiation. Das *et al.* (2008) argued their data indicate slow initial drainage. then rapid drainage through ice fracturing, followed by moulin development that allowed continued access of

water to the bed throughout the melt-season. The uplift of the ice recorded by the GPS station suggested the presence of a temporary subglacial lake; however this lake is argued to have rapidly drained within the period of 24 hours (as suggested by GPS station lowering) due to the presence of a pre-existing channelised drainage system (Das *et al.*, 2008).

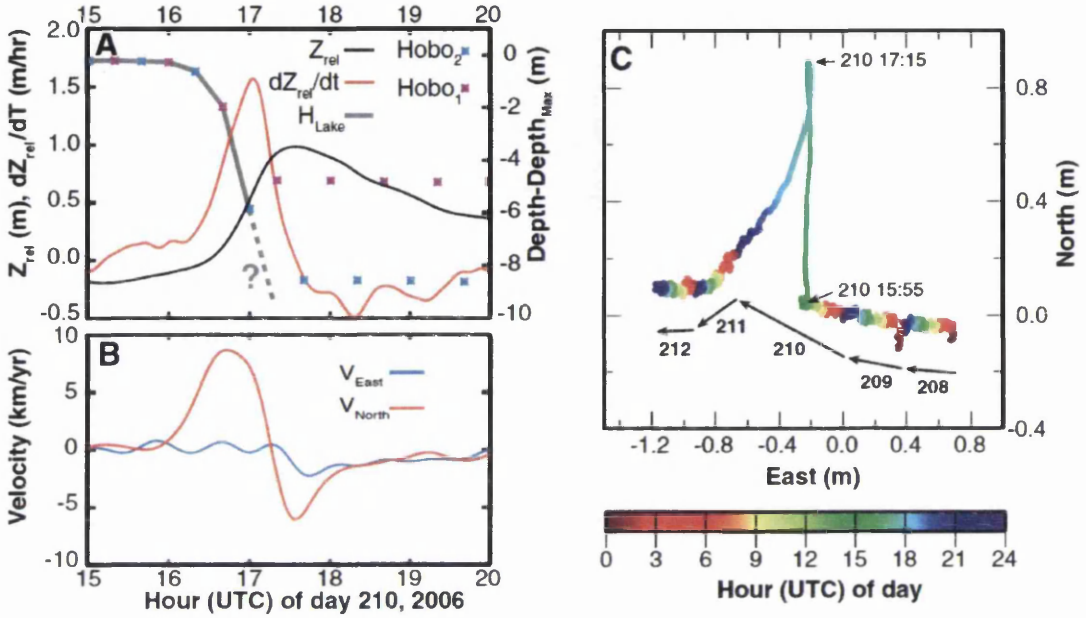

Figure 2.6: *Data from a lake drainage event recorded in West Greenland. a) Lake level (grey curve), relative surface elevation (Z_{rel}, black curve) and rate of surface elevation change (dZ_{rel}/dt, red curve). b) GPS surface velocity records separated into northing (red curve) and easting (blue) components. c) Plan-view of relative GPS motion over five days incorporating the period leading up to, during and following lake drainage. The hour of the day is indicated by the colour-bar. From Das* et al. *(2008).*

Box and Ski (2007) mapped supraglacial lakes on the GrIS using MODIS imagery. They observed rapid (<1 day) drainage of several surface lakes and calculated that the necessary volume of water to pressurise ice fractures or moulins (and thus allow continued englacial drainage) is about 0.1% of the water volume in a typical Greenland surface lake. Analysis of Landsat-7 and Advanced Spaceborne Thermal Emission and Reflection Radiometer (ASTER) imagery in Western Greenland (McMillan *et al.*, 2007) showed that lakes primarily drain towards the end of their seasonal development. Lakes at lower elevations (with more water input due to higher air temperatures) therefore drain earlier than those at higher elevations (McMillan *et al.*, 2007; Sundal *et al.*, 2009; Johansson *et al.*, 2012). However, due to the steeper slopes near the margin, lakes in these regions tend to be smaller than lakes at higher elevations (Sundal *et al.*, 2009; Fitzpatrick *et al.*, 2014).

The regional development of supraglacial lakes on the GrIS appears to be both spatially and temporally variable (Selmes *et al.*, 2011). Analysis of MODIS imagery between 2005–2009 identified 2600 lakes across the ice sheet, 55% of which were located in the SW of Greenland and only 2% in the SE. During this time period, 1313 rapid lake drainage events were identified (constituting 13% of all lake drainage events, with the remainder either draining over the surface or freezing in-situ), 61% of which were in the SW sector of Greenland. The lack of rapid lake drainage events in areas of the GrIS that are subject to the most dynamic thinning, such as the SE, suggests that lake drainage events are not important in these regions although they may influence ice dynamics in the SW (Selmes *et al.*, 2011).

It is not clear whether supraglacial lake drainage events have a substantial impact on ice dynamics (Das *et al.*, 2008; Hoffman *et al.*, 2011; Tedesco *et al.*, 2013). Bartholomew *et al.* (2011b) suggested that lake drainage events will have little impact on ice velocity other than short-term perturbations due to the rapid development of efficient channelised systems that evacuate the water. Hoffman *et al.* (2011) examined lake drainage characteristics near Swiss Camp, located to the north of Jakobshavn Isbrae in West Greenland, using Landsat imagery and ice surface GPS records from the record melt year of 2007. Over the temporal scale of a full melt-season, ice acceleration attributed to the rapid drainage events constituted <5% of the total horizontal ice flux. In most cases, the dynamic impact of lake drainage events constituted an acceleration of ice flux to ~4 times the background (average winter) velocity; however this enhanced flow lasted no longer than a day (Hoffman *et al.*, 2011). Similarly, Bartholomew *et al.* (2012) reported GPS records from a lake drainage event on the RGC that coincided with a 400% increase in horizontal velocity and uplift of 0.3 m (although the plotted records in Bartholomew *et al.* (2012) only show an uplift of 0.2 m at most). Hoffman *et al.* (2011) suggested that the limited period of ice acceleration indicates that subglacial drainage networks in the vicinity of the lake drainage events were channelised at the time of drainage, allowing rapid evacuation of water. Despite this, Hoffman *et al.* (2011) also suggest that the pulses of high pressure water from lake drainage events might be necessary for enhanced basal sliding, particularly once efficient drainage systems have developed. As such, this suggests that not all water during lake drainage can be removed by channels as the water in the efficient system would have little impact on ice dynamics. Tedesco *et al.* (2013) recorded GPS station uplift and horizontal motion for both a fast and a slow-draining supraglacial lake in the Paakitsoq region, West Greenland. The fast-draining lake emptied in 2 hours 10 minutes and caused a ten-fold increase in

ice surface velocity and maximum uplift of 0.1 m. This extreme dynamic response lasted less than 24 hours but, following this, ice velocities were still twice as high as the those recorded prior to the lake drainage. In contrast, the slow-draining lake caused a four-fold, but longer-lasting, increase in ice velocity at the initiation of drainage into a downstream moulin. These differences in drainage characteristics were argued by Tedesco *et al.* (2013) to suggest that the more commonly-found slow draining lakes (Selmes *et al.*, 2011; Liang *et al.*, 2012) allow greater time for basal hydrological adjustment to the water input and therefore cause less of an overall dynamic impact than fast-draining lakes.

2.4 Hydrology modelling

Modelling of glacial hydrological systems has been complementing field-based studies since the 1950s. The limitations of modelling a physically-based system lie in the inability to include the details inherent in the natural world within a computer programme. It is not possible to reliably estimate all the variables that could affect a natural system. However, modelling can provide a grounding in the type of variables that are most important in natural systems and as a result can complement field-based knowledge of glaciological processes. For subglacial hydrological studies in particular, modelling is a convenient tool for estimating system properties that are difficult to physically access and measure.

The development of hydrological models in relation to different glaciological systems will be discussed here. For lake drainage modelling, both a sheet, or water blister, approach (Tsai and Rice, 2010, 2012) and an integrated channelised and distributed system model (Pimentel and Flowers, 2011) have been previously applied. Both of these models will be utilised in this thesis and are discussed in detail in Chapter 5. However, the basis of glacial hydrological modelling approaches will be discussed here in terms of: sheet system and linked-cavity (inefficient) drainage modelling; R-channel (efficient system) modelling; the treatment of jökulhlaups; and models that incorporate coupled efficient and inefficient drainage systems.

2.4.1 *Distributed drainage*

Water sheets

As discussed in Section 2.2.1, water sheets are not considered to be stable features in glacial hydrological systems (Nye, 1973; Walder, 1982). However, Creyts and Schoof (2009) revisited the idea of a thin film of water, originally suggested by Weertman (1972). The film model of Weertman (1972) was criticised after publication as it was argued greater viscous dissipation of heat in areas with a thicker film would soon disperse the water into cavities or conduits rendering the film inherently unstable (Walder, 1982). However, Creyts and Schoof (2009) suggested that clasts can create a bridge between the bed and the ice through the water film, allowing a more even distribution of the ice stresses. With a thickening film, there is less pressure on the clasts and the downward creep motion of the ice can increase; this ice creep increases the water pressure and limits further thickening of the film until the ice stress is supported once more by the basal clasts. The model outputs indicate that stable films can exist in areas with high sliding velocities and low hydraulic gradients, such as found in ice streams. A switch occurs at a threshold of sheet thickness that causes development of an efficient system, controlled by the water pressure, the hydraulic potential gradient and the number and size of basal clasts.

Flowers and Clarke (2000, 2002) modelled a distributed sheet-based system in a 2-D domain and applied it to Trapridge Glacier, Yukon Territory, Canada. They modelled three layers: the ice, a sediment layer at the ice-bed interface and a subglacial aquifer underlying the sediment. The distributed system is modelled as a macroporous 'sheet' composed of water and sediment and therefore represents a distributed porous flow system rather than the water film envisaged by Weertman (1972). In the Flowers and Clarke (2002) macroporous sheet, the effective hydraulic conductivity varies with water volume (or thickness), representing a diffusive transport system where fluid pressure increases with discharge. Flowers *et al.* (2003) also applied the macroporous sheet model to analyse the subglacial hydrological conditions at Vatnajökull ice cap, Iceland.

Stone *et al.* (1997) suggested that in situations of overpressure (where water pressures exceed the ice pressure, commonly referred to as ice overburden pressure), it is possible that there is temporary separation between the ice and the bed, allowing water flow as a film. Such water sheets have been modelled in the form of radial water expansion from a borehole or moulin input point. Iken *et al.* (1996) used a radial

sheet flux model to examine the impact of slug tests on subglacial water pressure variation. Their model allowed water to flow radially from a borehole either into a sediment layer beneath the glacier or into a narrow gap between the glacier sole and bedrock. Comparisons between model outputs and slug tests suggested water flux was turbulent but drained through either channels or linked-cavities as opposed to through sediment pore-flow or as a thin film. Engelhardt and Kamb (1997) used a similar model to establish the growth of a water blister around a borehole breakthrough point at Ice Stream B, West Antarctica, comparing the outputs with recorded water pressure levels. The model assumes laminar flow in a water film that expands radially from the borehole and allows ice uplift due to overpressurisation. The authors acknowledged that turbulent flow is more likely in this context, but suggested that including turbulent flow equations would not alter their results substantially. Engelhardt and Kamb (1997) also suggested that channels or canals are likely to develop as a result of water cutting into basal till during drainage of the borehole, however the model was not developed to accommodate this theory.

Cavities

Iken (1981) modelled the impact of variable water pressure in subglacial cavities on glacier velocity. This model was based on the area of the bed calculated to be above a critical water pressure (below overburden), driven by water inputs into the drainage system, and the effect of this relationship on linked-cavity growth and shrinkage. With linked cavities at the bed, the basal shear stress will vary depending on the basal topography; Iken (1981) argued that in lower pressure areas, such as the lee side of bedrock bumps, changes in basal water pressure will have the greatest impact on ice motion. Walder (1986) developed a cavity drainage model incorporating and expanding on equations introduced by Nye (1953); the growth of cavities is balanced through melting of the basal ice as a result of pressurised water flow, and ice creep when water pressures drop below the ice overburden pressure. The equations developed by Walder (1986) illustrate that water input scales directly with water pressure in cavity systems, whereas water input and pressure varies inversely in channelised systems.

2.4.2 *Channelised drainage*

R-channels

Glacial conduit growth is dependent on the balance between viscous dissipation of heat (in turn primarily dependent on water flux and channel roughness) and creep closure. Röthlisberger (1972) developed a steady-state conduit flow model by examining water flux within circular channels surrounded by ice and taking account of frictional melting and inward creep of the ice into the conduits (Fig. 2.1 a). Röthlisberger (1972) also calculated the pressure gradients within the channels and the relationship between channel water pressure and ice overburden pressure.

Nye (1976) expanded on the Röthlisberger (1972) approach by analysing differential equations for time-dependent non-steady state water flux during the growth of a conduit. These equations for a channel with a semi-circular cross-section are defined in Chapter 4. Nye (1976) applied his model to the 1972 jökulhlaup from Grímsvötn, and demonstrated that the channel growth equations could closely match the proglacial discharge hydrograph during the rising limb of the flood. Through the conduit calculations, Nye (1976) suggested that thermal melting of conduit walls through turbulent water flow could be an important contributor to conduit growth. The Röthlisberger (1972) and Nye (1976) equations form the basis of much of the subsequent hydrological modelling to date.

Lliboutry (1983) adapted the conduit equations further by adding in terms for deformation around subglacial obstacles and also allowing for heat influx from groundwater, which is particularly important during the winter months with little surface water input. The primary conclusion was that water flowing within subglacial conduits should generally be at atmospheric pressure unless flowing within an overdeepening. This hypothesis has not been verified by subsequent modelling or in-situ fieldwork. Shoemaker (1987) returned to Nye's (1976) analysis for cylindrical conduits within an infinite ice medium to examine the impact of pressure and temperature effects on the behaviour of R-channels. Heat transfer between water in the conduit and the surrounding cold ice was included in the calculations, and it was discovered that by allowing for this phenomenon within the model, the pressure gradient was increased. The Shoemaker (1987) model however, was based on steady-state flow. Another adaptation of the classic conduit model was suggested by Hooke *et al.* (1990), who modified calculations of subglacial water pressure and channel closure rates by Röthlisberger and Lang (1987) to suggest that the models better match measured

pressure values if the conduit shape is assumed to be broad and low rather than semi-circular.

More recently, Colgan *et al.* (2011) applied conduit evolution equations to a 1-D flowband model of the tidewater glacier, Sermeq Avannarleq, West Greenland. Although a distributed network was not dealt with in this model, an arborescent network of interdependent conduits was allowed to evolve. Semi-circular conduits were prescribed with the amount of overpressure determining conduit growth. Peak conduit radii in the model reached 2 m with pressures varying near (and for short periods, above) overburden. Calculations also suggested that some of the water in the basal system could be stored in conduits for more than a year before being discharged, due to the configuration of variable basal topography preventing rapid water flux in the subglacial system.

Further south in West Greenland, Ahlstrom *et al.* (2005) modelled the impact of changes in surface water input on subglacial channel development in a region including the RGC. The model was implemented within 10 km of the ice sheet margin using bed and surface DEMs and forced by surface water inputs using a positive degree day (PDD) calculation. Channels were modelled using the broad, low conduit equations of Hooke *et al.* (1990) for a steady-state system. As a result, this model is only likely applicable to a system that has developed near to equilibrium. The model results suggest that the ice viscosity and the channel roughness were more important than the surface water input by several orders of magnitude for driving water pressures within the conduits (Ahlstrom *et al.*, 2005). Unfortunately, both channel roughness and ice viscosity are challenging to constrain in the field and thus it is likely that discharge from surface water inputs (that can be more easily determined using surface energy balance models) will continue to be applied as a major driver in conduit development equations.

Banwell *et al.* (2013) used the EXTRAN Storm Water Management Model (originally applied by Arnold *et al.* (1998) to Haut Glacier d'Arolla, Switzerland; see Section 2.4.4) as a basis for a regional subglacial hydrological model for the Paakitsoq region, West Greenland. In this model cylindrical pipes representing subglacial conduits join at junctions to create an arborescent network. Any water that is above the equivalent water table of the ice sheet surface is treated as surface flood water and removed from the system. Water input to the moulin junctions is calculated from both surface runoff and timing of lake drainage events. The resulting modelled discharge outputs for the entire region match well with the measured pro-glacial

discharge. The model results indicate that the system becomes more efficient during the summer with headward expansion of conduits upstream. However, this is punctuated with short term (diurnal) spikes in water pressure associated with rapid lake drainage events and longer term (day to week) periods of high pressure as a result of surface runoff inputs; these results indicate that the system is rarely in steady state during the summer melt-season (Banwell *et al.*, 2013).

Jökulhlaups

The modelling of jökulhlaups is based on equations from hard-bedded R-channel models; these flood models primarily compare flux rates through conduits with pro-glacial discharge records. Most numerical treatments of jökulhlaups do not include a distributed drainage system; instead all flood water flows through R-channels. Although there are various theories postulated about jökulhlaup initiation, a commonly applied initiation parameter in models is that drainage begins when the hydrostatic pressure at the seal (or boundary) of the subglacial lake is equal to the minimum hydraulic potential in the region damming the lake, although in reality lakes have been observed to drain before this threshold is reached (Roberts, 2005).

The Nye (1976) model for jökulhlaup channel formation has been discussed above and has been used as the basis of many analyses of R-channel growth (e.g. Clarke, 1982; Shoemaker, 1987; Ng and Björnsson, 2003; Schuler and Fischer, 2009; Schoof, 2010; Colgan *et al.*, 2011; Hewitt *et al.*, 2012; Chandler *et al.*, 2013). For example, Clarke (1982) adapted Nye's (1976) model to replicate a 1978 outburst flood event from Hazard Lake at Steele Glacier, Yukon Territory, Canada. Clarke (1982) argued that the thermal energy of the lake water is an important factor for subglacial channel development and that, in contrast, creep closure of the channel has little impact on the outburst flood hydrograph. In the Clarke (1982) model, the roughness variable (using the Gauckler-Manning roughness equation) is adjusted to tune the model to the pro-glacial hydrograph.

An adapted application of R-channel equations to jökulhlaup models was proposed by Spring and Hutter (1981) who developed a simplified Navier-Stokes approximation for conduit development. Spring and Hutter (1981) found that, without knowing the initial conduit geometry and flow path, prediction of discharge hydrographs is not possible. Instead, they calculated the discharge with a straight, circular fixed-geometry conduit in which the water input and output relationship

can be reasonably determined. One significant difference between this model and Nye's (1976) model is that the former applied a Darcy-Weisbach roughness variable (developed to calculate friction along a length of pipe), whereas the latter relied on Gauckler-Manning roughness calculations (originally applied for calculating velocities in open channels). The conclusion of the Spring and Hutter (1981) modelling study was that the temperature of the input lake water is a highly significant variable for determining discharge hydrographs. Clarke (2003) simplified the complex application of the Spring and Hutter (1981, 1982) hydrology equations in order that they can be applied more readily to glacier models, and are not restricted to glacier floods applications. The Clarke (2003) adaptation assumes that the channels flow in a straight line, are either circular or semi-circular and are full of water at all times. Additionally, water cannot flow laterally into a distributed system. Although these assumptions may seem to limit the applicability of this conduit model, the hydrographs calculated from the model match reasonably well with those recorded in the field. From the Clarke (2003) modelling, the growth of the conduits during a subglacial flood appear to be initially slow (with maximum discharge occurring several days rather than hours after flood initiation), and strongly dependent on the water temperature. Unfortunately the latter is hard to measure in the field during a basal flood and so must be estimated for model applications.

Werder and Funk (2009) applied the Clarke (2003) semicircular R-channel jökulhlaup model to a rapid drainage events at Gornersee, Gornergletscher. However, to match the model outputs to the dye tracing discharge records, either the channel flowpath sinuosity or the heat transfer rate had to be increased. Also, if the model was tuned to data for the slower flowing water on drainage day 1, the same model could not match the faster fluxes on day 2; the R-channel model therefore appears to not be applicable to the full jökulhlaup drainage cycle in this case.

Roberts (2005) applied a combination of the Nye (1976) conduit model, the Clarke (1982) adaptations and the Spring and Hutter (1981) approach to model the propagation of jökulhlaups. The resulting model of a single, straight subglacial conduit linking a pressure-coupled reservoir of meltwater directly to the glacier terminus was justified by the rapid frictional melting of conduit walls, with the presence of sediment increasing the erosion rate of the ice walls. Thus, even if channels are not assumed to pre-exist in the vicinity of jökulhlaups, it is assumed that they form rapidly due to the highly elevated water pressure gradient imposed by the lake water reservoir.

A justification for the single channel approach for jökulhlaup modelling as opposed to linked distributed and channelised systems was given by Evatt *et al.* (2006): they suggested that water pressure in the channel will always be lower than overburden and so flooding outwith the conduit is not likely. Roberts (2005) also argued that, because the subglacial lake surface lowers during a jökulhlaup, the water pressure at the lake outlet will not exceed overburden and therefore formation of a turbulent sheet is unlikely. The approach of modelling only a single channel developing from a flood point appears to applicable to some jökulhlaups that involve discharge increasing exponentially over the scale of days to weeks (e.g. Hazard Lake, Yukon (Clarke, 1982); Grímsvötn, Vatnajökull (Nye, 1976); and Triumvirate Glacier, Alaska (Sturm and Benson, 1985)). However, other floods such as the 1996 Grímsvötn jökulhlaup involved discharge increasing on the scale of hours (see Section 2.3.1), with flood water emerging at the terminus, 50 km from the lake input, 10.5 hours after flood initiation; peak discharge occurred 20-35 hours after flood initiation (Flowers *et al.*, 2004). Flowers *et al.* (2004) modelled this rapid discharge jökulhlaup using an adapted approach from the Clarke (2003) model, that accounts for water transport both in a sheet-like subglacial layer (macroporous) and in ice-walled conduits in a 1-D flowband configuration. Hydraulic jacking is incorporated for areas of water overpressure. The model outputs indicate that the flood water initially spreads out in a sheet. Conduits then begin to form near the margin and can grow more quickly than in the traditional jökulhlaup model because of the low-pressure effects at the terminus. In the model runs these conduits reached cross-sectional dimensions of 450–1000 m^2 several kilometres upstream from the terminus. The sheet reached a maximum thickness of 7–10 m and pressures along the flowline were above overburden until conduits became extensive enough to reduce the pressure. For model stability, the sheet hydraulic conductivity had to be greater than 1 $m\,s^{-1}$. However, in this model, water temperature is assumed to be at the pressure melting point, whereas previous models (Spring and Hutter, 1981; Clarke, 1982) had suggested that variability in water temperature, particularly in volcanically-induced floods, was important.

2.4.3 *Drainage through sediment*

With the presence of sediment at the ice-bed interface, many models (e.g. Clarke, 1996; Fischer *et al.*, 2001; Flowers and Clarke, 2002) treat water flux as porous Darcian flow. As porous flow will be slow, it is likely that fast flow mechanisms

also exist in areas with sediment when the water input exceeds the system capacity (Shoemaker, 1986; Walder and Fowler, 1994). However, few models simulate water flow through sediment-based conduits or a fast-flow equivalent.

Alley (1992) introduced a simple steady-state model of a channel within sediment. Till creep into the channel is calculated depending on 1) the yield strength and viscosity of the sediment and 2) the gradient of water pressure between the sediment and the channel. The water in the till pores and the channel are shown to be able to co-exist with pressures near to overburden in the former and lower pressures in the latter. However, because till will creep into the lower pressure channel, Alley (1992) suggested that sediment near the conduit could be thinned or removed over the course of a melt-season thus impacting basal drag and further hydrological development. This theory is supported by evidence from borehole turbidity (Hubbard *et al.*, 1995) and self potential (Kulessa *et al.*, 2003) measurements carried out at Haut Glacier d'Arolla that indicated a depletion of sediment fines near active conduits.

The most commonly cited model of fast-flow in sediment is by Walder and Fowler (1994) who developed a steady-state model of sediment canals that are both eroded into the sediment and up into the ice therefore incorporating ice creep, ice melt, sediment influx and sediment removal (Fig. 2.7). Ice creep and sediment influx is modelled using a coupled equation combining the Nye (1953) formulation for cylindrical closure of a borehole and an empirically-determined till creep formula suggested by Boulton and Hindmarsh (1987). Erosion of the sediment is determined using an empirically-based bedload transport equation, dependent primarily on the balance between the shear stress from the water flow and the grain-size. Ice melt is calculated using the approach of Nye (1976) that is described in Chapter 4. The two-phase flow of water partially within ice and partially within sediment complicates the application of these sediment canal equations and thus they are simulated only in steady state. The model results suggest that canals in subglacial till will be broad and shallow with the canal depth unlikely to exceed 10 cm.

Ng (2000a) made improvements to the Walder and Fowler (1994) canal model by incorporating a downstream spatial dimension, allowing for variation in canal effective pressure and also readdressing the problem of sediment transport. Ng (2000a) reported stable growth of canals up to $\sim$0.4 m. An important feature of the sediment canals is that, contrary to modelled R-channel dynamics, the pressure within the canals increases with discharge. Ng (2000b) added to this canal model by investi-

gating the impact of sediment deformation and sediment stress distributions within the vicinity of the canal. These approaches to fast-flow sediment canal modelling are based on steady-state systems so that temporal evolution of the canals is not taken into account. Developing temporally and spatially varying canals in till is an important area for future research.

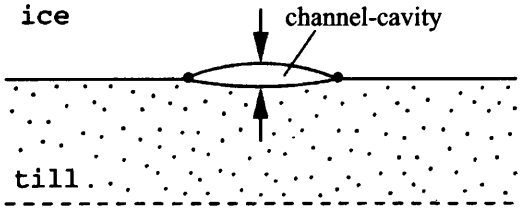

Figure 2.7: *A schematic of a broad-low canal that erodes both down into till and up into the ice. Adapted from Ng (2000b).*

Rempel (2009b) discussed a seepage model in systems where conduits and sediment-based Darcian flow can co-exist. The pressure gradient within the sediment is likely to be greatest near the conduits; however, in areas with no conduits, the water is argued to stabilise near overburden (Rempel, 2009b). On the other hand, borehole studies have shown that basal water pressures can vary substantially over a short spatial scale suggesting that equilibrium at overburden is not always reached in sediment-based systems (e.g. Murray and Clarke, 1995; Dow *et al.*, 2011; Meierbachtol *et al.*, 2013).

2.4.4 *Integrated models*

Field-based investigation into subglacial hydrological systems indicates that competing drainage systems can co-exist under the same glacier, such as a distributed linked-cavity system and an efficient channelised system (Vivian, 1980). For example, as reported in Hubbard *et al.* (1995), borehole evidence from at Haut Glacier d'Arolla suggested that a variable pressure axis drove high pressure water laterally out from channels into a distributed system during the day with the pressure gradient reversing during the night and allowing water flow back into the channels. As a result, in order to replicate basal drainage systems in glacial hydrology models it has become increasingly common to have linked distributed and channelised systems. Such configurations are more computationally demanding but can provide greater insight into the subglacial system, provided that sufficient information is available for reasonable model inputs.

Alley (1996) introduced one of the first linked distributed and channelised models for ice sheet hydrology. This model initiates with water only in channels; pressure changes in the efficient system drive water flow into a film, with the thickness of the latter dependent on the pressure gradient. The thickness of the film in turn changes the basal shear stresses and ice velocity. Arnold *et al.* (1998) applied a coupled distributed and efficient drainage model to Haut Glacier d'Arolla, using the EXTRAN Storm Water Management Model (developed by the U.S. Environmental Protection Agency). The distributed basal system was represented by either small circular conduits or one shallow, wide conduit. The channelised drainage network was represented by one circular conduit; conduit size was determined using the Spring and Hutter (1981) formulae for channel wall melting and closure. Model outputs were compared with discharge hydrographs, borehole water pressure records and dye tracing results. It was found that at the beginning of the melt-season for this Alpine glacier, the meltwater inputs were the primary control on the appearance of discharge hydrographs. Later in the season, the transport capacity of the basal hydrological system was the most important factor for matching model runs and hydrographs.

Similar to the integrated jökulhlaup model presented in Flowers *et al.* (2004), Flowers (2008) modelled a coupled distributed and channelised width-averaged drainage system, but also included exchange with a groundwater aquifer. The distributed system is treated as a macroporous sheet, as described in Flowers and Clarke (2002), and the efficient channels are modelled as semi-circular, following the equations of Spring and Hutter (1982) and Clarke (2003). The transition from a predominantly distributed system under a valley glacier towards an efficient conduit-based system is determined in the model by the critical water sheet thickness (dependent on sediment thickness, porosity and the resulting transmissivity). Pimentel and Flowers (2011) used similar flowband equations as Flowers (2008) to examine lake drainage events in Greenland and subglacial drainage of valley glaciers fed by moulins. In this latter model, dynamic effects such as basal shear stress, longitudinal stress and basal sliding velocity were also modelled, utilising a Coloumb friction sliding law. The flowband equations used in Pimentel and Flowers (2011) are the basis of part of the modelling in this thesis and are described in detail in Chapter 5.

An original approach to a coupled channelised and cavity-based drainage model was introduced by Schoof (2010). These equations involve a single expression for the cross-sectional area of a cavity and channel that indicates when the system switches from one system to the other in response to a critical threshold discharge. The

results from this coupled model suggest that higher melt rates in Greenland will suppress the duration and spatial impact of increased ice velocities due to channelisation. However, the model also captures short-term (< 1 day) accelerations in ice velocity due to rapid increases in water supply, even with the presence of a pre-established channelised system. The short-term ice velocity spikes occur because the hydrological system evolves too slowly (with channels adjusting on a scale of days) to incorporate additional rapid water influx. The short-term ice velocity events can be of a significantly higher magnitude than acceleration due to seasonal changes in water input. As a result, if greater total surface melt volumes reach the bed, the system can channelise more quickly and only short-term rapid increases in basal water input such as from supraglacial lake drainage events or rain storms will significantly perturb the velocity. Understanding the balance between hydrological development and ice acceleration is important for determining the dynamic response of the GrIS to increasing air temperatures and related meltwater input to the ice-bed interface (Schoof, 2010).

The Nye (1976) equations were once again applied by Hewitt (2011) to a steady-state distributed and channelised system. The distributed system was modelled as a porous medium representing cavities or a patchy water sheet depending on the hydraulic conductivity. However, the modelled distributive system is likely too conductive to represent flux through basal sediment. This distributed sheet system is similar to that discussed in Creyts and Schoof (2009), where the thickness of the sheet is determined by ice melting, ice creep and creation of cavities due to sliding over obstacles at the bed. The location of the channels are determined only by their separation width; it is not possible with this approach to track locations of channels or grow arborescent channel networks within the sheet. The model results suggest that channels will form further upstream and be spaced more closely together with a larger hydraulic potential gradient, slower opening of the porous sheet, lower sheet hydraulic conductivity and higher water discharges. Channels are therefore likely to be spaced closer together towards the glacier terminus.

Another subglacial drainage model incorporating both distributed drainage represented by a porous sheet and channelised flow was presented in twin papers by Schoof *et al.* (2012) and Hewitt *et al.* (2012). The distributed sheet involves porous flow but also ice melt and ice creep, akin to linked-cavity models. The conduits are grown using the standard Nye (1976) equations. A 2-D configuration was introduced where conduits meet at nodes and can therefore converge and diverge. However, as these 2-D calculations are computationally intensive, most analysis of the coupled

sheet-conduit model was conducted on a simpler version of the model, configured as a 1-D fixed-width flowband. The model was used primarily to examine subglacial drainage characteristics in situations of underpressure or overpressure. Underpressure was defined as periods when the pressure is atmospheric resulting in air gaps within cavities. Overpressure was defined as periods when the water pressure equals or exceeds the ice overburden pressure and causes ice uplift. However, the model is simplified to deal with water pressure only at or below overburden because elastic ice deformation is not taken into account and the hydraulic jacking that would be caused by overpressured water cannot be realistically incorporated; instead, a hydrofracture model such as that discussed by Tsai and Rice (2010) (which is applied in this thesis and introduced in detail in Chapter 5) would be necessary to replicate elastic uplift. As a result, the Schoof *et al.* (2012) and Hewitt *et al.* (2012) sheet-channel model is more applicable for time scales longer than a few hours when elastic uplift processes are likely to be less important. Hewitt *et al.* (2012) discussed a test where it was envisaged that a moulin or hydrofracture allows rapid access of water to the basal drainage system, as would occur during a supraglacial lake drainage event; their model outputs are shown in Figure 2.8. It was found that the water pressure rapidly reached overburden and this pressurised sheet spread both up and down glacier and was sustained for 12 hours before dropping below overpressure levels. Conduit growth did not initially occur but after several days the channels began to increase in size and cause the overpressure sheet to collapse. The conclusions from the Schoof *et al.* (2012) and Hewitt *et al.* (2012) integrated models were that overpressure situations were most likely with high water fluxes in areas with low ice surface and bed slopes. Underpressure, however, was likely to occur under thin glaciers with steep surface and bed slopes.

Hewitt (2013) combined a plan-form subglacial hydrological model incorporating channelised and distributed drainage (similar to that described in Hewitt *et al.*, 2012) with an ice dynamics model to examine the impact of surface water input on ice velocities near the margin of the GrIS. The model configuration stretches 50 km inland from the margin with a flat bed and 50 moulin input sites. Surface water production is varied in tests to determine the impact of different water inputs on the modelled ice velocity. The model shows upstream expansion of a more efficient drainage system from the margin during the melt-season with gradual growth of conduits pulling water from the nearby distributed system and causing deceleration. Tests with greater volumes of water input showed a strong velocity peak early in the season followed by rapid deceleration as efficient channels develop earlier; these

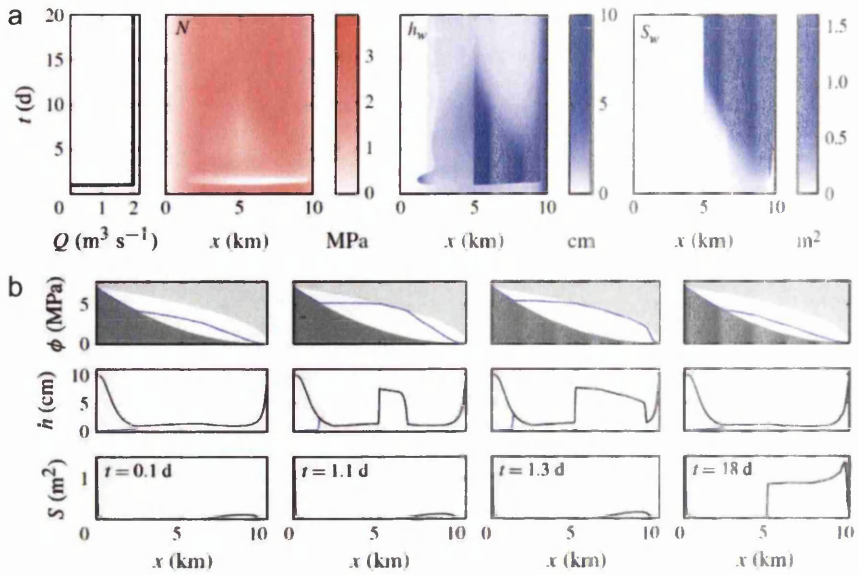

Figure 2.8: *Outputs from a sheet-conduit model when water is suddenly input at time 1d (day), at a rate of $Q = 2 m^3 s^{-1}$, and at a domain distance of $x = 5 km$. a) Distance-time plots of the 10km domain over 20 days. Effective pressure, N, shows overpressure at the time of input; the sheet water thickness, h_w, thickens and spreads both up and downstream; conduit size, S_w, increases after $\sim$ 12 days causing thinning of the water sheet and an increase in effective pressure. b) Time snapshot model profiles of the hydraulic potential, θ, sheet thickness and conduit cross-sectional area before and after the sudden increase in water input. From Hewitt* et al. *(2012).*

two phenomenon tended to cancel each other out so average velocity at the margin was the same for larger and smaller water input volumes. Further from the margin however, greater water volumes allowed larger overall velocity. As a result, for the entire region there was an average positive relationship between water volume input and the ice velocity.

2.5 Greenland Ice Sheet dynamics

This section will discuss the evidence for recent changes in Greenland glacier dynamics and the role of access of water to the glacier bed. In addition, a review of hydrological and dynamic research on RGC, in West Greenland is given to put the thesis case-study data into context.

Land-terminating glaciers in the south-west of Greenland have been subject to relatively little change in terminus position within the last decade (Moon and Joughin,

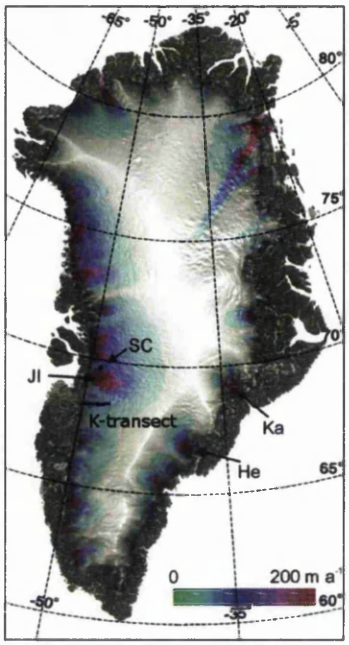

Figure 2.9: *Greenland surface topography and steady-state flow rates. JI (Jakobshavn Isbrae), SC (Swiss Camp), K-transect, Ka (Kangerdlugssuaq) and He (Helheim) are located as marked. Adapted from Bamber* et al. *(2007).*

2008). However, in order to constrain the importance of factors such as water input to the bed of the GrIS on ice-dynamics, these land-terminating glaciers are an ideal region to examine as they are immune to changes in ocean temperature and ice calving rates, the latter of which are highly important for the dynamics of tidewater glaciers (Thomas *et al.*, 2003; Joughin *et al.*, 2008a,b; Chylek *et al.*, 2004; Holland *et al.*, 2008; Hanna *et al.*, 2009). Investigations on land-terminating glaciers are therefore the focus of this section and tidewater glacier dynamics will not be widely discussed here.

2.5.1 *Mechanisms for Greenland glacier dynamic changes*

Zwally *et al.* (2002) presented GPS data collected between 1996-1999 near Swiss Camp, which lies ~35 km from the ice margin on the western side of Greenland (see Fig. 2.9). Zwally *et al.* (2002) argued that there was a direct correlation between ice surface velocity at Swiss Camp and the volume of meltwater on the ice surface. They suggested that surface water was able to access the bed of the ice throughout the melt-season over a large area, causing an increase in ice velocity through basal lubrication. Once meltwater production ceased at the end of the melt-season, the

ice velocity also slowed, again indicating a direct link between ice velocity and basal hydrology (Zwally *et al.*, 2002). Price *et al.* (2008), however, modelled variations in ice velocity around Swiss Camp and found that acceleration ~12 km downglacier, towards the ice sheet margin, could produce the variability in ice surface velocity at Swiss Camp through longitudinal coupling. Therefore, although Price *et al.* (2008) did agree that surface water input into the basal system is important for ice motion, they suggested this occurs primarily near the thinner ice-sheet margin and not in the area of Swiss Camp. GPS data reported by Joughin *et al.* (2008a) indicated that, on the ice sheet near Jakobshavn Isbrae, ice speed increased during the 2006 and 2007 melt-seasons (by ~50%) with short periods of faster flow correlated with the drainage of surface lakes through the ice and moulin development. At the end of the melt-season, ice velocity decreased to the lowest value of the year, then gradually increased over the winter season (Joughin *et al.*, 2008a). There is therefore no consensus on the impact of lake drainage events and access of water to the subglacial system on ice dynamics.

2.5.2 *Russell Glacier catchment dynamics*

Various other studies also indicate that the correlation between surface meltwater production and ice velocity is not as simple as implied by Zwally *et al.* (2002). In particular, since 1999, the RGC located at 67°N on the south-western side of the GrIS has been an area of focussed scientific research, primarily due to its relatively easy access from the nearby hub of Kangerlussuaq. As a result, there has been considerable investigation of hydrological development in this catchment.

Initially, a transect of stakes and weather stations were installed to measure mass balance changes on RGC (known as the K-Transect; see Fig. 2.9) up to an elevation of 1850 m (Greuell and Oerlemans, 2005; van de Wal *et al.*, 2005; van den Broeke *et al.*, 2008). GPS measurements from 2005-2006 along this transect showed an increase in ice speed coincident with initiation of surface melting in May (van de Wal *et al.*, 2008). Variations in ice velocity up to 30% occurred over the time scale of a week, with the most significant velocity fluctuation recorded at a site, called SHR, 13 km from the ice margin. Van de Wal *et al.* (2008) suggested that the variability at the latter site was due to the presence of many moulins in this area draining water to the bed. On seasonal and annual time scales however, the total volume of meltwater input did not seem to directly correlate with ice velocity, perhaps due to

adjustment of the subglacial hydrological system to water input later in the melt-season (van de Wal *et al.*, 2008). Shepherd *et al.* (2009) presented summer 2007 GPS data from K-transect and compared this with MODIS imagery to characterise supraglacial lake formation, depth and drainage, along with a PDD model to calculate average surface melt. They found ice surface velocity varied both seasonally and diurnally, with the most significant fluctuations near the ice margin, which showed a maximum of 110% flow variation in one day. Along the transect, diurnal change included accelerations of 55%, as shown in Figure 2.10, that were often coincident with ice surface uplift of ~1-4 cm. Seasonally, the velocity along the transect was ~52% greater than the winter speed. Shepherd *et al.* (2009) found that ice surface acceleration was greatest after a series of surface lake drainage events, followed by a pronounced deceleration in ice speed several days later.

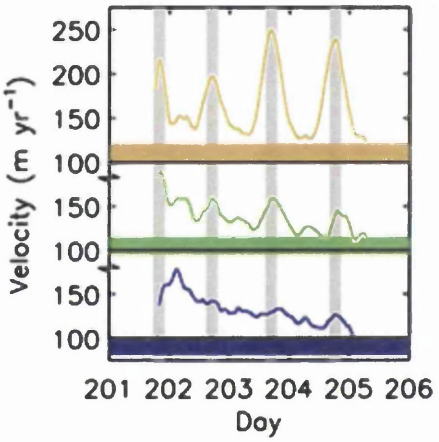

Figure 2.10: *Ice surface velocity along K-transect during summer 2007. The yellow curve is from a site 37 km from the margin, green = 53 km from the margin, blue = 72 km from the margin. The horizontal lines in equivalent colours are from InSAR-derived winter velocities at the same sites. Grey lines indicate the time of peak diurnal velocity. From Shepherd* et al. *(2009).*

Within 35 km of the terminus of Russell Glacier, GPS records have shown increases in velocity up to 220% above the winter average (Bartholomew *et al.*, 2010). Accelerations in ice surface velocity begin near the ice margin and migrate up-glacier during the melt-season; however velocity spikes superimposed on the background signal have been recorded throughout the season, some of which can be attributed to rapid lake drainage events (Bartholomew *et al.*, 2010). Bartholomew *et al.* (2011b) extended the GPS station transect further inland; they recorded spring event velocity peaks up to an elevation of 1482 m above sea level. The spring events at

sites above 1229 m appeared to be initiated by lake drainage events. Variable acceleration patterns up to elevations of 1500 m were also identified by Palmer *et al.* (2011), who analysed synthetic aperture radar interferograms to determine velocity changes across RGC between 1995 and 1996 (see Fig. 3.2). This analysis indicated that the areas of greatest acceleration corresponded to sites of water input to the bed. The pattern of surface speed-up appeared to follow topographic depressions in the ice surface that are argued to be indicative of similar variations in the basal topography, suggesting the flux of lubricating subglacial water through these basal valleys (Palmer *et al.*, 2011; Fitzpatrick *et al.*, 2013).

2.5.3 *Russell Glacier catchment hydrology evolution*

Recent work on the RGC has suggested the subglacial hydrological system evolves in a similar pattern as observed in Alpine glacier systems; an inefficient distributed system develops into an efficient channelised system as the season progresses due to greater volumes of meltwater input into the basal system (Bartholomew *et al.*, 2010, 2011b, 2012; Chandler *et al.*, 2013; Cowton *et al.*, 2013). Bartholomew *et al.* (2012) suggested that moulins on RGC concentrate drainage in discrete input points so that a small number of conduits rapidly form and interact with a pre-existing distributed drainage system. This channelisation of the RGC hydrological system is argued to be indicated by the general ice deceleration during the melt-season (Bartholomew *et al.*, 2010, 2012), progressing from the glacier margin to inland ice areas (Bartholomew *et al.*, 2011b).

Analysis of changes in ice surface velocity in the region of RGC (within 20 km of the margin) suggested that the switch between distributed and channelised drainage occurred when surface runoff increased above a monthly average of 1.4 cm per day (Sundal *et al.*, 2011). These data showed that greater input of meltwater in warmer years allowed a larger maximum rate of ice flow but the development of channels earlier in the melt-season lowered both the average ice flow speed in the summer and the duration of fast ice flow (Sundal *et al.*, 2011). Discharge and electrical conductivity data recorded from a pro-glacial stream at Leverett Glacier (directly adjacent to Russell Glacier) in 2009 also suggested an increase in efficiency and channelisation of the subglacial hydrological system during the melt-season (Bartholomew *et al.*, 2011a). Sole *et al.* (2013) presented GPS station measurements of ice surface uplift and horizontal acceleration from 2009–2012 along a transect that stretches 115 km

inland from the margin on Leverett Glacier and RGC. They found that there was greater average regional acceleration in warmer years. However, the accelerated speed in warmer years was then followed by slower speed in the winter and so the average yearly ice velocity was very similar between warmer and cooler years. The reason given for slower winters following warm summers was the presence of large conduits that continue to modulate distributed drainage during the winter season; these conduits are argued to be larger in years with greater surface melt and therefore have a larger impact on winter dynamics (Sole *et al.*, 2013). However, Fitzpatrick *et al.* (2013) presented ice velocity maps from RGC produced from TerraSAR-X image pairs in 2009 and 2010. They found that, although the melt in the warmer 2010 lasted for 53 days longer than in 2009, after melt had ceased it took ~90 days in both years for ice velocity to return to the winter average of the previous year.

Cowton *et al.* (2013) carried out moulin-based dye tracing experiments on Leverett Glacier, which demonstrated channelisation of the drainage system by late May. However, these dye tracing experiments were limited to a region within 14 km of the glacier terminus, thereby not providing any information about drainage development at higher elevations. Chandler *et al.* (2013) also used tracers input into moulins on Leverett Glacier catchment between 2009–2011 to determine the rate of water flow and the dispersivity through the basal system. Repeat tracer surveys of moulins between 7–41 km from the terminus indicated an increase in water velocity during the season. This result is interpreted as hydrological development from an inefficient drainage system towards an efficient channelised one. However, a tracer input 57 km from the margin returned slowly and indicated channelisation did not occur in this region; the thick ice in this area (~1180 m) and small volumes of supraglacial water produced during the night are suggested to have prevented basal channelisation (Chandler *et al.*, 2013). However, Bartholomew *et al.* (2012) argued the channelisation under inland ice should be possible despite the thick ice because of the presence of large supraglacial conduits that deliver water to moulins. Sole *et al.* (2011) and Cowton *et al.* (2013) also suggested that channelisation of inland areas with thick ice is likely to occur very rapidly as a result of lake drainage events in contrast to slower channel development at lower elevations.

In contrast, Meierbachtol *et al.* (2013) argued channels are less likely to form further inland on RGC. They drilled 23 boreholes along a 34 km transect on RGC between 2010–2012. Water pressure records in these boreholes indicated a mixed channelised (with water pressures varying between 30 and >100% of overburden) and distributed (with water pressures always close to overburden) regime towards

the margin. However, between 17 and 30 km from the margin, no channels were found. Meierbachtol *et al.* (2013) also used a simple channel model to demonstrate that conduit melt rates at the inland sites would be significantly lower compared to the near-margin sites. The evidence from the boreholes and modelling is used to suggest that efficient distributed drainage networks operate in the inland region rather than a network of R-channels.

Bartholomew *et al.* (2011b) noted that diurnal variations in horizontal velocity were visible until mid-August at sites between 617–794 m elevation on the Leverett and Russell catchments, which suggests that the local hydrological system became overpressurised due to meltwater influx. It was suggested that overpressurisation was due to the lack of steady-state in the hydrological system that prevented the channels adjusting sufficiently quickly to changes in water input (Bartholomew *et al.*, 2011b). This implies that the channel networks were not large enough to efficiently remove diurnal water inputs. In addition, if the size of channels is related to the volume of meltwater input and consequently the slowest velocities are associated with regions of the largest channels, it suggests that areas near the margin should have the slowest velocities as they receive proportionally more meltwater than other areas. However, Bartholomew *et al.* (2011b) showed that the increase in summer velocity appeared to be similar at sites near the margin and in regions up to 794 m a.s.l. This implies that the basal system is controlled by the change in input rate rather than the total volume through-flow as also suggested by the modelling of Schoof (2010).

2.5.4 *Russell Glacier catchment lake drainage events*

McMillan *et al.* (2007) identified 150 supraglacial lakes on RGC in 2001 with a total area of 18±1.6 km^2. For the 2003 drainage year, Leeson *et al.* (2013) estimated that 12% of the surface runoff on RGC was stored in supraglacial lakes. An analysis of the seasonal evolution of lakes on RGC by Fitzpatrick *et al.* (2014) between 2002-2012 indicated that on average, 200 lakes form on the ice surface with individual surface areas as large as 8.2 km^2. There is substantial inter-annual variability in lake formation and drainage times, but there is a correlation between earlier lake formation and drainage in higher melt years; lakes also form at greater elevations in higher melt years (Fitzpatrick *et al.*, 2014). Fitzpatrick *et al.* (2014) found that ~28% of lakes on RGC drained rapidly with evidence that clusters of lakes drain

at the same elevation band. From this study there was no correlation between lake volume and the time of rapid drainage, suggesting mechanisms other than the hydraulic head of lake water are necessary for initiating lake drainage events.

Pro-glacial discharge records discussed by Bartholomew *et al.* (2011b) include several pulses of water volume, electrical conductivity and suspended sediment concentration that were suggested to be due to the drainage of several lakes from similar elevation bands on Leverett Glacier catchment. However, Bartholomew *et al.* (2011b) argued that lake drainage events have little impact on ice velocity other than short-term perturbations due to the development of efficient channelised systems that evacuate the water; lake drainage events are therefore suggested to be only important for creating a meltwater route from the surface to the bed.

Investigations of sediment plumes in Kangerlussuaq fjord suggested that, at the height of the melt-season, there was a short lag between increases in surface meltwater and the appearance of sediment in the fjord that implied fast flow times in the glacier system (McGrath *et al.*, 2010). However, drainage of supraglacial lakes that can cause velocity spikes (Bartholomew *et al.*, 2011b) are not seen in the fjord plume dynamics, implying that lake water is hindered from through flow by a distributed basal hydrological system (Chu *et al.*, 2009). Coupling this with the dye tracing evidence from Chandler *et al.* (2013), that demonstrates inland drainage systems (at distances greater than 41 km from the terminus) remain distributed, suggests the assumption that lakes drainage events rapidly form efficient channelised drainage systems is oversimplified.

2.6 Summary

The literature review presented in this chapter has been designed to set the work of this thesis in context. A description of various subglacial hydrological systems has been given and, as one aim of the thesis is to determine whether efficient subglacial channels develop during rapid supraglacial lake drainage events in Greenland, several studies that have examined lake outburst floods from ice-marginal lakes, subglacial lakes and supraglacial lakes have been discussed. A brief (and non-exhaustive) history of subglacial hydrology modelling has also been given to provide context for the models applied within this thesis. Finally, research and analyses of hydrological and dynamic conditions in the RGC in West Greenland, the region where the thesis

case-study lake is located, have been introduced.

Chapter 3

Case-study field site

3.1 Introduction

The primary goal of this thesis is to investigate subglacial hydrological development during rapid supraglacial lake drainage events using mathematical modelling and geophysical techniques. In order to test models of hydrological development, in-situ field data are necessary. However, in areas with thick ice, e.g. inland on the GrIS, the collection of data from the subglacial environment using techniques such as borehole drilling and dye tracing is challenging. As an alternative, data collected on the ice surface using, for example, GPS and seismic techniques can provide useful information that can be compared with model outputs and used to remotely analyse conditions at the ice-bed interface.

This chapter introduces the case-study field site at a rapidly draining supraglacial lake on RGC in West Greenland. A campaign was carried out in summer 2010 to collect data comprising: surface GPS records around the lake, passive seismic records, deep-look radar lines, reflection seismic lines, the lake water lowering rate, weather station data and satellite remote sensing records. These data have primarily been processed by collaborators.

This chapter will first describe the field campaign; the following sections discussing the topographic setting of the case-study region, lake instrumentation and the lake drainage event involve data that were processed and analysed by the author unless otherwise specified. The second part of this chapter describes data provided and processed by collaborators; the author was not involved directly in processing or

analysing these latter datasets.

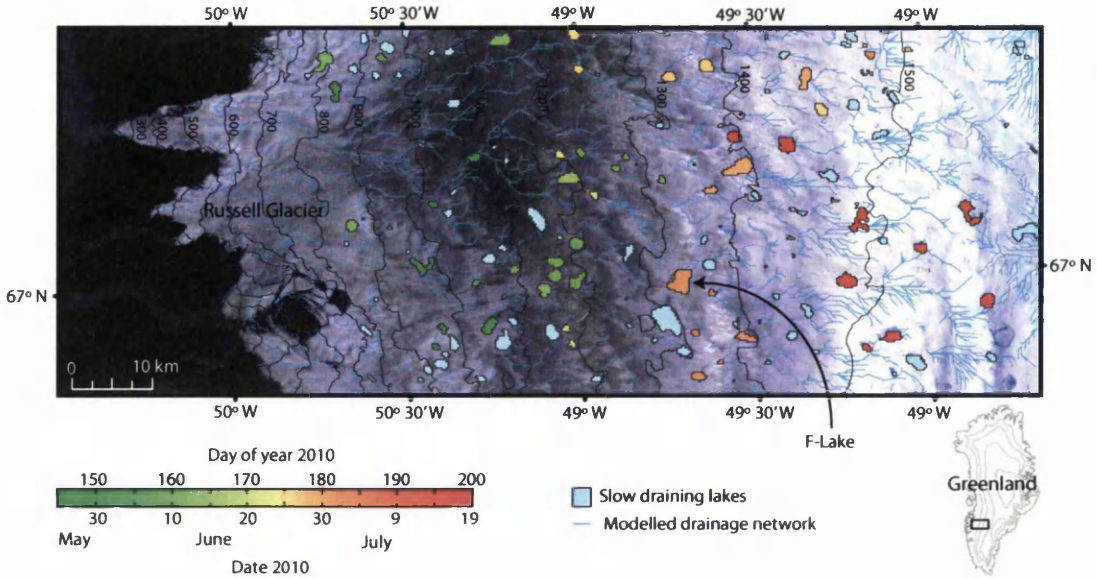

Figure 3.1: *Map of supraglacial lakes in RGC plotted in relation to drainage dates during the 2010 melt-season. Rapidly draining lakes (< 4 days) are colour-coded with the green-red scheme in relation to their drainage date (see key); F-Lake is noted by the arrow. Slow draining lakes (> 4 days) are shown in blue. A model of the supraglacial drainage network is shown by the blue curves. The background is a Landsat image from 18 August 2010. Adapted from Doyle* et al. *(2013).*

3.2 Field campaign

A field campaign was undertaken between June and August 2010 and the collected data used to ascertain inputs and constraints for the mathematical modelling of rapid supraglacial lake drainage events and subsequent basal drainage development. The site was based around a supraglacial lake, named F-Lake, located at 66°0' N and 48°43' W. This lake is situated ~70 km from the ice margin, at an elevation of ~1350 m, within the catchment of Russell Glacier. The location of the lake is shown in Figure 3.1. Ice thickness in the vicinity of F-Lake is approximately 1000 m.

Russell Glacier is a land-terminating glacier with a catchment size of ~6500 km^2 that extends to an elevation of 2000 m (Fitzpatrick *et al.*, 2014). Russell Glacier has been the focus of many remote and in-situ glaciological data collection campaigns over the last decade (e.g. McMillan *et al.*, 2007; van de Wal *et al.*, 2008; Sundal *et al.*, 2009; Bartholomew *et al.*, 2010; Doyle *et al.*, 2013), some of which are summarised in Section 2.5.2. A velocity map of Russell Glacier was produced by Palmer *et al.*

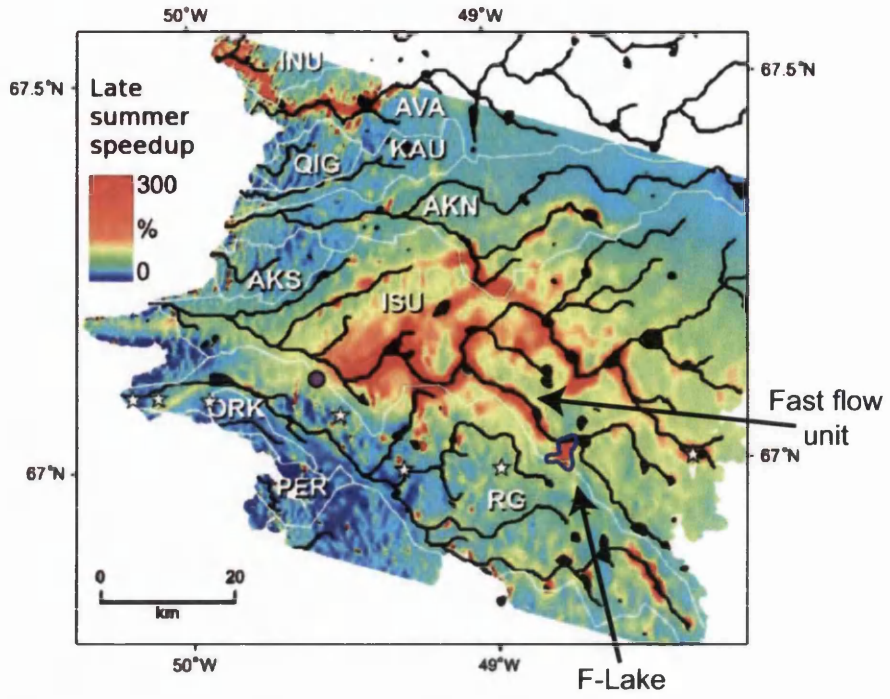

Figure 3.2: *Map of seasonal velocity change between summer 1995 and winter 1996. White lines indicate the supraglacial hydrological catchments; black lines show supraglacial meltwater streams with the sinks also shown in black; and the white stars show the location of the K-Transect (discussed in Section 2.5.2). The outline of F-Lake is shown in blue. Adapted from Palmer* et al. *(2011).*

(2011), and is shown in Figure 3.2, with the outline of F-Lake included. It can be seen that F-Lake lies at the head of a fast flow unit within the catchment. As a result, F-Lake is an ideal case-study for examining subglacial hydrological development as the water input during the lake drainage could have a catchment-wide impact. The data collected at F-Lake in 2010 constitutes the largest instrumentation campaign of a rapidly draining supraglacial lake to date, and thus provides a substantial dataset that is well-suited to test models of rapid lake drainage events.

3.3 Topography

Subglacial and surface DEMs of the region around F-Lake have been produced by collaborators Rickard Petterson and Katrin Lindbäck, Uppsala University. These maps were provided at a resolution of 250 m and were linearly interpolated onto a 50 m grid by the author. Maps of the regional surface and bed topography are shown in Figure 3.3 having been run through a 1-cell rectangular smoothing filter. A sub-

glacial valley runs into the region of F-Lake from the NE and turns at the lake site, continuing toward the NW; this valley coincides with the fast-flow unit indicated in Figure 3.2. The topographic maps are highly valuable for analysing subglacial hydrological development, including assessing hydraulic potential gradients and areas that may be subject to supercooling freeze-on (as discussed in Sections 3.3.1 and 3.3.2).

3.3.1 *Hydraulic potential*

Water flow at the ice-bed interface is estimated by gradients of hydraulic potential (Shreve, 1972). The calculation of hydraulic potential (ψ) requires knowledge of the spatially and temporally variable basal water pressure. Following Shreve (1972),

$$\psi = \psi_0 + P_w + \rho_w g z, \tag{3.1}$$

where P_w (Pa) is the water pressure, g=9.81 m s^{-2} is acceleration due to gravity, ρ_w=1000 kg m^{-3} is the water density, ψ_0 is a reference potential and z (m) the elevation above a reference datum level. However, without direct access to the subglacial environment it is difficult to determine basal water pressures. A common alternative approach (see e.g. Richards *et al.*, 1996; Arnold *et al.*, 1998; Pattyn *et al.*, 2005, 2009) is to assume that basal water pressure is uniformally at ice overburden pressure ($P_i = \rho_i g H$, where H (m) is the ice thickness and ρ_i=920 kg m^{-3} is the density of ice), thus allowing the subglacial hydraulic potential gradients $\nabla\psi$ to be calculated (Shreve, 1972):

$$\nabla\psi = (\rho_w - \rho_i)\, g\Delta b + \rho_i g \Delta a, \tag{3.2}$$

where Δa and Δb are downflow gradients of the ice surface and glacier bed elevations, respectively. Water flows from high to low potential and, at overburden pressure, is driven primarily by the ice surface gradients. Although the assumption of uniform overburden pressure is likely incorrect (Dow *et al.*, in prep.), hydraulic potential maps can be useful for estimating water flow directions. Figure 3.4 shows the overburden hydraulic potential gradients for the F-Lake region prior to lake drainage, calculated using the regional basal and surface DEMs. The hydraulic potential gradients suggest that water that accessed the bed during the rapid F-Lake drainage

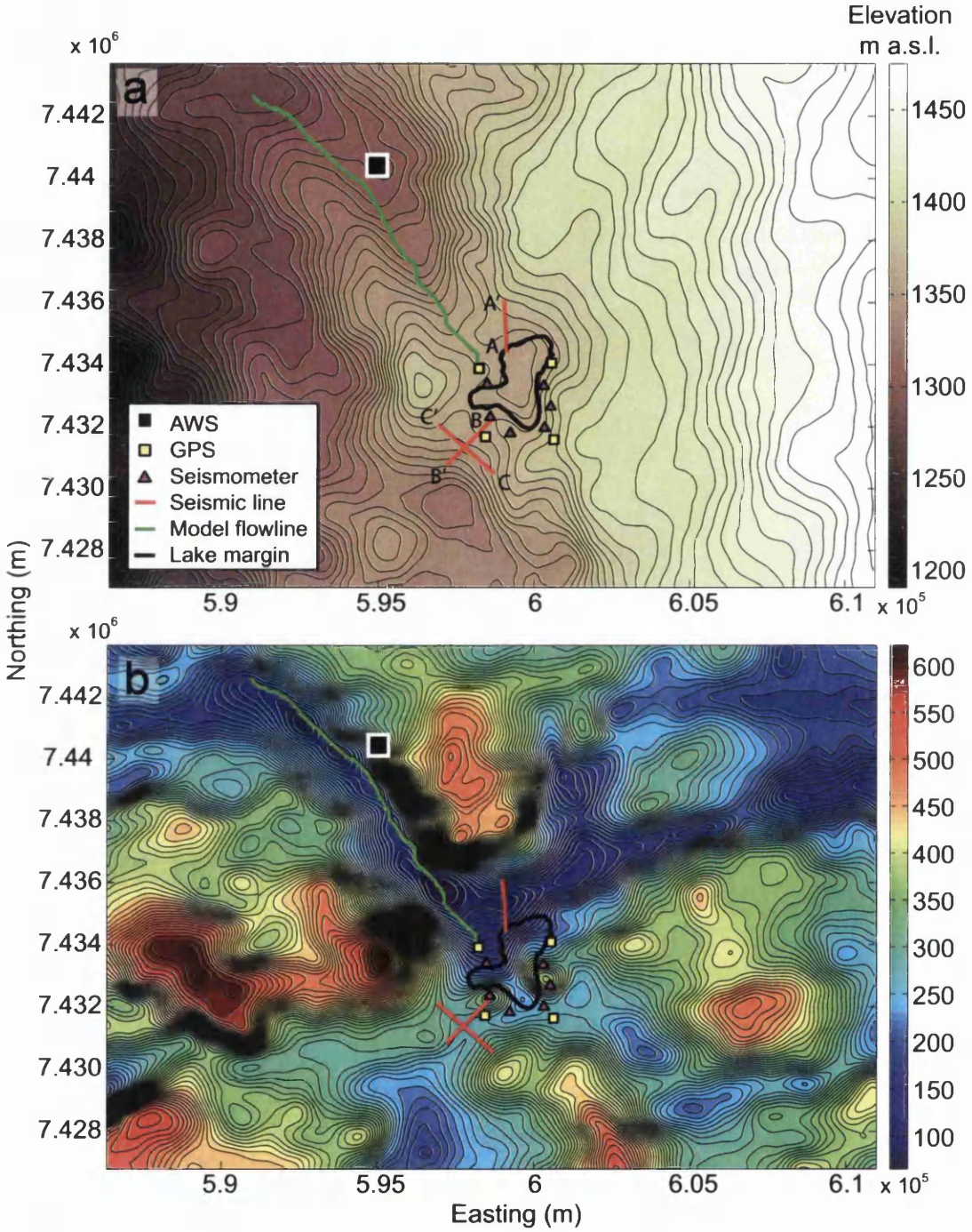

Figure 3.3: *a) Surface and b) basal DEMs of the F-Lake region with elevation contours plotted in grey. The lake extent just prior to drainage is shown by the thick black curve. The location of the model flowline, reflection seismic lines, GPS, weather station and passive seismic stations in relation to F-Lake are noted on the DEMs.*

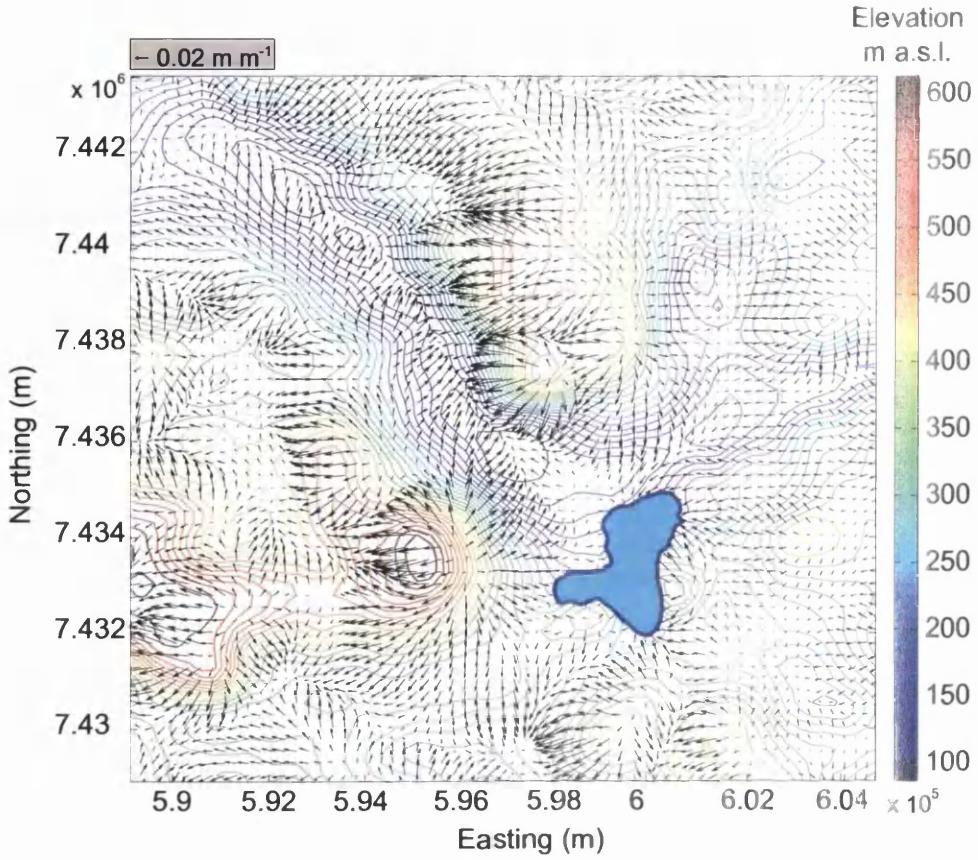

Figure 3.4: *Hydraulic potential gradients at F-Lake assuming the lake is full (therefore giving a flat surface gradient at the height of the estimated lake level in the lake basin) and basal water pressures are everywhere at overburden. Basal elevation contours are plotted in colour. F-Lake is shown in solid blue.*

event would have flowed to the NW through the basal trough, corresponding to the fast-flow region shown in Figure 3.2.

3.3.2 *Supercooling*

As indicated in Figure 3.3 b, the basal topography in the region of F-Lake is not flat, and such undulations might impact the flux of water in the region. Shreve (1972) defined the limit of uphill basal water flow, β^* using calculations of hydraulic potential:

$$\beta^* = -f_w \left(\frac{\rho_i}{\rho_w - \rho_i} \right) \Delta a, \tag{3.3}$$

where f_w=P_w/P_i is a pressure coefficient in the form of a fraction of ice overburden. When basal water pressures are at overburden, an adverse bed slope ~11 times the ice surface slope will effectively block water flow. However, to accurately determine where basal topography might impact water flow, supercooling must be taken into account. When water moves from areas of higher pressure (where the pressure melting point is depressed) to areas of lower pressure (such as areas with thinner ice) it initially flows at levels below the ambient temperature; the water is therefore supercooled. Frazil ice formation takes place as the water equilibrates to the local temperature and, depending on this rate of supercooling freeze-on and the hydrological configuration, can block water flow pathways (Tsang and Hanley, 1985; Cook *et al.*, 2006). Following Alley *et al.* (1998), the slope threshold for supercooled water flow, $\beta^\dagger$, can be calculated with

$$\beta^\dagger = \frac{\rho_i \kappa}{\rho_i \kappa - \rho_w} \Delta a. \tag{3.4}$$

Here $\kappa = 1 + \gamma C_s$ where $C_s = 4.2 \times 10^6 \, \mathrm{J\,m^{-3}\,K^{-1}}$ is the volumetric specific heat of water; $\gamma = -9.8 \times 10^{-8} \, \mathrm{K\,Pa^{-1}}$ is the pressure dependence of the melting point for air-saturated water and $\gamma = -7.4 \times 10^{-8} \, \mathrm{K\,Pa^{-1}}$ for air-free water (the true value of γ will thus likely fall between these two values). If water pressures are at overburden, the supercooling slope threshold is therefore $\beta^\dagger = -1.2\Delta a$ for air-saturated water suggesting that if the adverse basal slope is >1.2 times the surface slope in the opposite direction, supercooling freeze-on will occur at overburden water pressures. Following Eq. 3.4, for water at pressures below overburden, supercooling freeze-on will occur on shallower adverse slopes.

A supercooling analysis is applied to the F-Lake region using the surface and basal DEMs. The water flow paths are analysed in relation to the overburden hydraulic potential vectors (see Fig. 3.4). Figure 3.5 shows the water pressure (as a percentage of overburden) that would be necessary to prevent supercooling freeze-on. As water pressures are unlikely to be greater than 100–120% of overburden during a lake drainage event, areas requiring pressures greater than this are likely to be subject to supercooling freeze-on. The results show that, due to the undulating topography along the trough to the NW of F-Lake, supercooling freeze-on is likely to take place along the flowline.

Unfortunately, subglacial hydrological models are not currently configured to take account of supercooling freeze-on. Although thermal exchange between the water

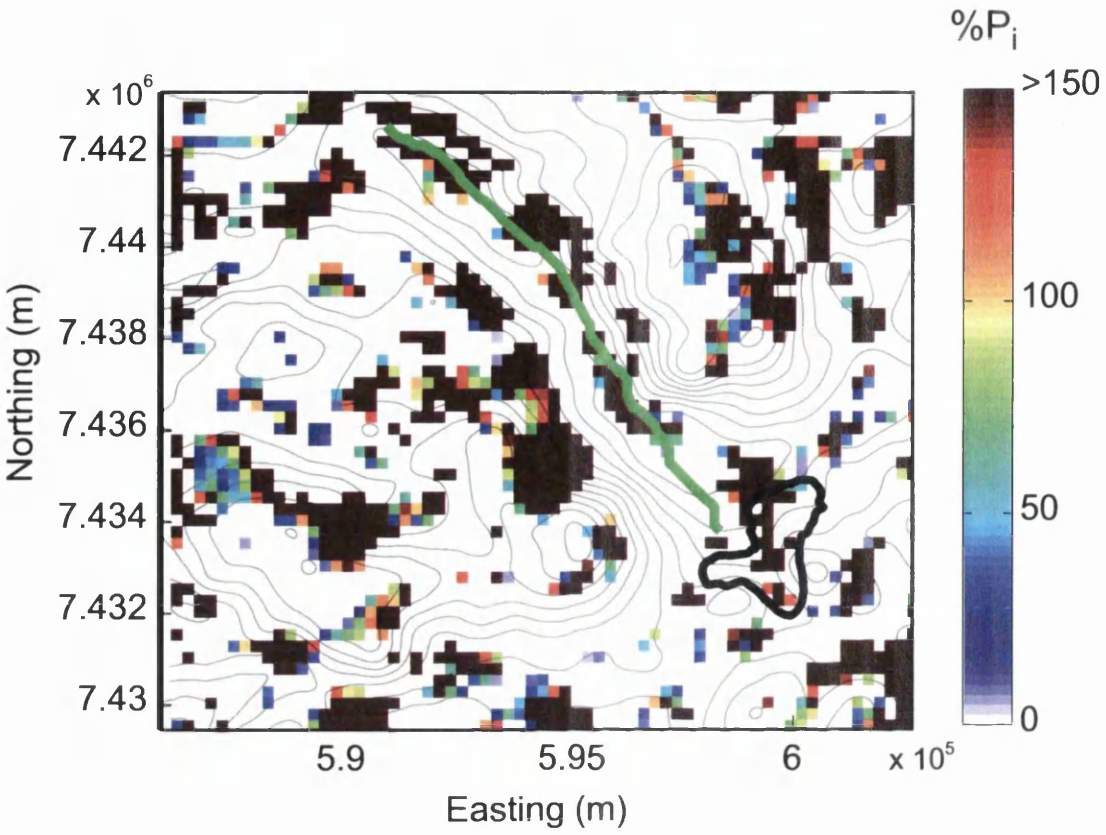

Figure 3.5: *Map of the F-Lake region showing the minimum water pressure necessary for supercooled water to continue flowing up reverse bed slopes without freezing. Basal topography contours are shown in grey. The F-Lake margin is shown by the thick black line and the model flowline by the green line.*

and ice walls in channels is often taken into account, the complexity of variations in pressure melting point and water temperature diffusion is often neglected. It is beyond the scope of the study presented in this thesis to include supercooling processes within the hydrological models, however it is an important area for future research. Despite this, the supercooled map presented here can be used for subglacial hydrology analysis and will be applied when discussing the modelling outputs in Section 9.2.4.

3.3.3 *Model flow-line*

Using the basal topography map and the hydraulic potential gradient calculations, a suitable flow-line can be extracted for modelling purposes. A water input point was chosen based on the outputs from passive seismic analysis of the lake drainage

event (see Section 3.6.2). From this point, the flowline was calculated following the vectors of hydraulic potential gradient for overburden. The line is shown in green in Figure 3.3 and the along-line elevation change of the surface and the bed in Figure 3.6. In the latter figure, the areas in red represent the parts of the line subject to the gravity-driven flow threshold described in Eq. 3.3. The areas in blue represent the slopes that exceed the supercooling threshold described in Eq. 3.4. Both the red and blue regions show the slope barriers for water flow at overburden pressure. These are not absolute barriers as supercooling freeze-on reduces the hydraulic conductivity of the drainage system but might not fully prevent water flow over the slopes. In addition, if water flows at temperatures above the pressure melting point due to geothermal heating within a sediment pack for example, the supercooling analysis will not apply (Dow *et al.*, in prep.).

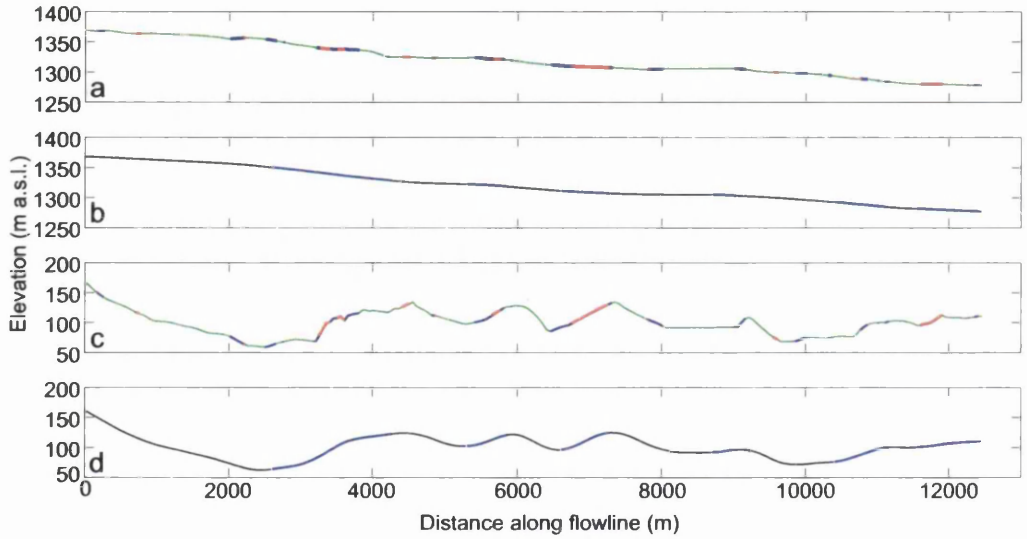

Figure 3.6: *Elevation changes along the flowline shown in Fig. 3.3. The red areas show where the slopes exceed the hydraulic potential flow threshold at overburden and would thus not allow downstream water flow. The blue areas show the reverse slopes where supercooling freeze-on would occur on the flowline. a) Surface elevation change along the flowline. b) Smoothed surface elevation flowline to apply in the hydrological model. c) Basal elevation change along the flowline. d) Smoothed basal elevation flowline to apply in the hydrological model.*

If the areas on the flowline do block water flow it is an important consideration for hydrological development and is discussed in more detail in Section 9.2.3. However, for the purposes of modelling, the flowline is smoothed so that water flow is not affected by gravity-driven blockage, which could cause instability in a model. Smoothing is achieved by running a linear least-squares regression filter. The smoothed flowlines that will be applied in the hydrological modelling (described in Chapter 5) are

plotted in Figure 3.6 b and d.

3.4 Instrumentation

In this section, the instrumentation and data recorded during the rapid drainage of F-Lake is discussed. Unless otherwise specified, the data collection and processing were carried out by the author.

3.4.1 *Pressure Transducers*

Two pressure transducers (Solinst Model 3001 Levelogger Junior) were installed in F-Lake on June 26th (day of year (DOY) 177), at 23.37 Coordinated Universal Time (UTC), five days prior to lake drainage, with a sample rate of two minutes (pers. comm. S. Doyle, Aberystwyth University). Pressure Transducer 1 (P1) was installed towards the deepest region of the lake and Pressure Transducer (P2) was installed towards the margin of the lake (see Fig. 3.7). The transducers recorded pressurehead, which is equivalent of the height of water overlying the sensor. Both pressure transducers were recovered and the data processed to remove air pressure and elevation factors. The data output from P1 is shown in Figure 3.8.

3.4.2 *Bathymetry*

Following the F-Lake drainage event, six GPS transects were collected by walking over the lake bed with a Leica SR520 receiver that recorded a point at one-second intervals. These data were later processed against a static off-ice receiver by S. Doyle, Aberystwyth University. The maximum lake extent was extrapolated from: 1) a composite of Landsat images from 16th June 2010 (before lake drainage) and 2nd July (post-drainage, when the former lake extent could be picked out due to differences in surface colouration) and 2) the combination of recorded lake water height from the pressure transducers and the elevation of the lake bed where the transducers were installed (recorded by a hand-held GPS unit when transducers were recovered following lake drainage). The resulting estimated lake boundary corresponded with a maximum lake surface height of 1363 m a.s.l, a lake depth of 9.93 m and a surface area of 3.8 km^2.

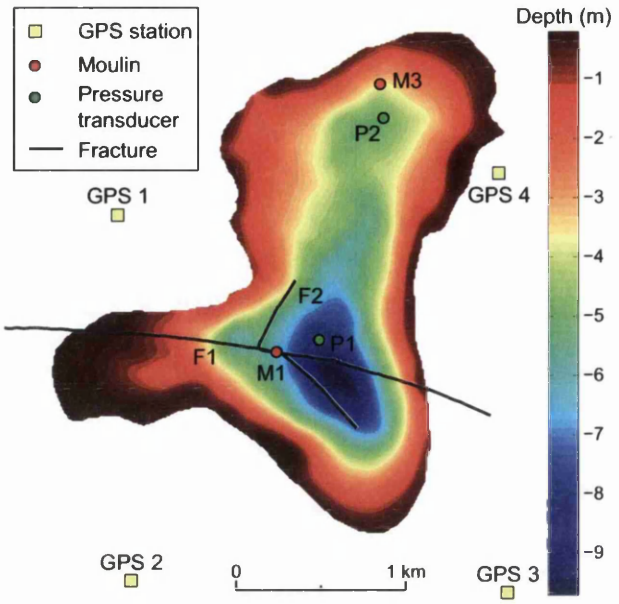

Figure 3.7: *Bathymetric map of F-Lake. The red points are moulins; the green points are the location of pressure transducers installed prior to lake drainage; the black lines are major fractures mapped on the lake bed post-drainage; and the yellow squares are the locations of the GPS units. The bathymetry is plotted using a 5-cell rectangular smoothing filter.*

The estimated lake boundary was combined with the GPS transect data and interpolated onto a 10×10 m grid using the kriging function in Surfer (Golden Software). Uncertainty in this approach arises from extrapolation of the Landsat-based lake margin location (± 15 m resolution), uncertainty in the location and elevation of the pressure transducers on the lake bed (± 0.7 m), and GPS surveying errors (± 0.01 m). Incorporating these errors gives a maximum lake volume of $11{,}050{,}000 \pm 8400\,\mathrm{m}^3$ (Fig. 3.7).

3.5 F-Lake rapid drainage event

3.5.1 *Drainage characteristics*

In 2010, F-Lake drained at 01.05 UTC on June 30th, (DOY 181). The pressure records show that the lake was losing volume from the time of pressure transducer installation, with a drop of 1.33 m over 74 hours (an average of $1.8\,\mathrm{cm\,hr^{-1}}$; see Fig. 3.8). It is not clear whether this volume loss is due to water input into the

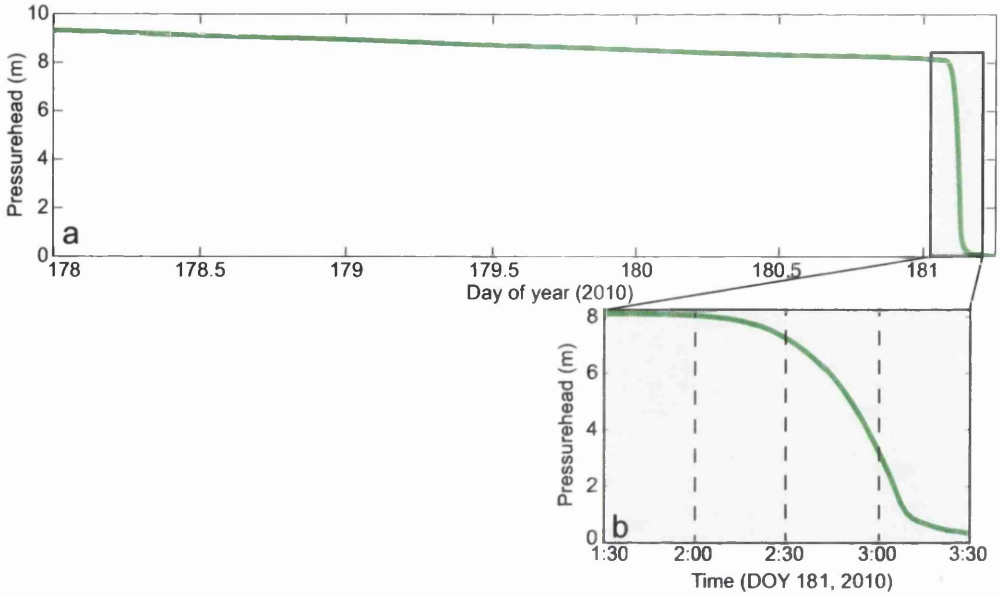

Figure 3.8: *Records from P1 (see Fig. 3.7 for location). a) The full pressurehead record from the time of installation until the cessation of lake drainage. b) The pressurehead record during the rapid lake drainage event.*

subsurface prior to lake drainage or due to an imbalance in supraglacial in-flow and out-flow, although passive seismic records discussed below would suggest the latter. In addition, a large river observed flowing out of the southern margin of the lake during a pre-drainage helicopter survey suggests much of the lake volume loss was supraglacial.

Just prior to lake drainage, the volume of F-Lake was 7,137,700 m^3. At 01.40 UTC on June 30th (DOY 181), the lake level began to rapidly drop, reaching a maximum lowering rate of 0.6 $m\,s^{-1}$ at 03.05 UTC. The lake drained in ~1 hour, 45 minutes. The lake drainage rate was calculated using the pressure transducer data and the surface bathymetry DEM. The maximum drainage rate was $3190 \pm 130\,m^3\,s^{-1}$ at 2:47 am UTC (Fig. 3.9), with the uncertainty in the volumetric drainage rate arising from the bathymetric gridding and the pressure transducer uncertainty. Further details of the rapid lake drainage event can be found in Doyle *et al.* (2013).

3.5.2 *Fracture mapping*

Following the lake drainage event, several fracture mapping expeditions were conducted to establish surface stress and fracture trends in the vicinity of the lake. The main feature was a crevasse that ran generally west to east across the lake (labelled

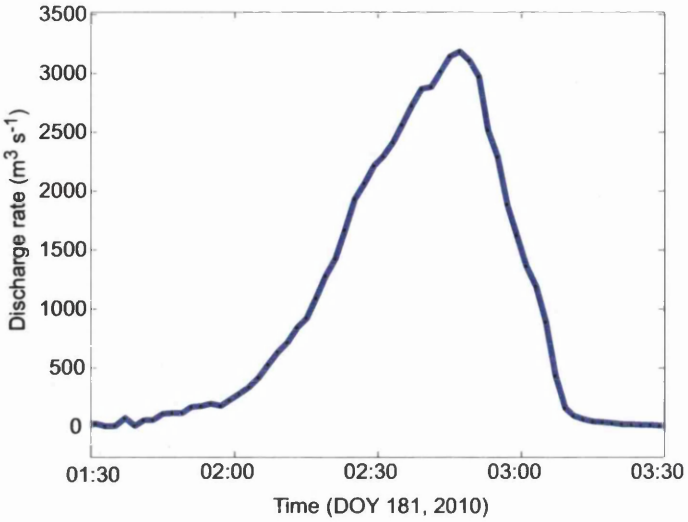

Figure 3.9: *Drainage rate calculated for F-Lake during the rapid drainage event using the bathymetry calculations and the lake lowering record.*

'F1' in Fig. 3.7). This crevasse was visible prior to lake drainage as shown in Figure 3.10 a. A major fracture cut across F1 perpendicularly, running approximately south to north (labelled 'F2' in Fig. 3.7) and is highlighted by the passive seismic analysis as an active region during hydrofracture associated with the lake drainage event (see Section 3.6.2).

In the centre of F1, toward the middle of the lake, there was a large moulin (labelled 'M1' in Fig. 3.7) with a surface area of ~12 x 10 m (see Fig. 3.10 b) and no water flow from the surface. Exploration of this moulin by the field team identified that it was an open shaft until a depth of ~40 m, where ice collapse prevented further exploration. Several other moulins (some active) were noted along the major crevasse, although it is not known whether multiple moulins drained through the crevasse towards the bed or whether they amalgamated at depth. At the northern end of F-Lake, three moulins were found post-drainage (labelled 'M3' in Fig. 3.7); these features were within the lake perimeter prior to drainage. It is not clear if these moulin features were present before lake drainage or if they only connected to an active drainage system following the rapid lake drainage event.

During these fracture mapping expeditions it was noted on the 2nd July (DOY 183) that there was a small lake reforming in the deepest part of the basin in the region of F1. This area had been free of water immediately following lake drainage. By July 3rd (DOY 184) this small lake had drained. This is discussed further in Section 9.2.6.

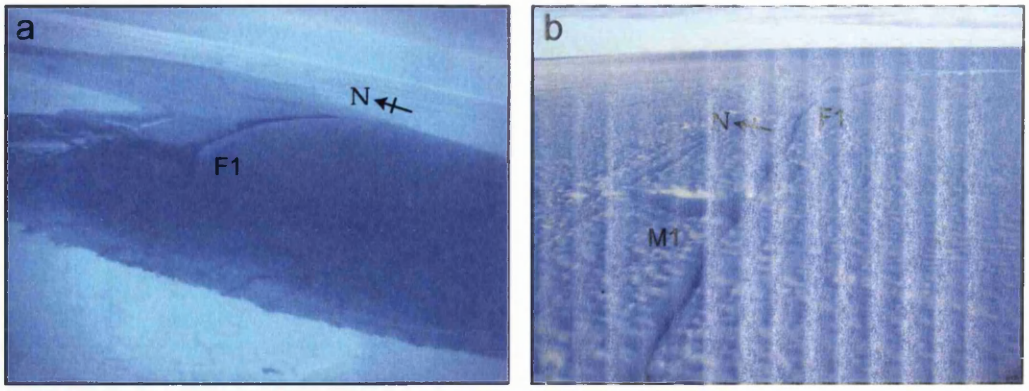

Figure 3.10: *Photos of crevasse F1 and moulin M1 taken during helicopter surveys. a) Taken 15 days prior to lake drainage on the 15th June, 2010. b) Taken 9 days after lake drainage on the 9th July, 2010.*

3.6 Collaborator data

Data collected and analysed by collaborators are introduced here in order to determine suitable model inputs and so that the lake drainage event can be analysed in context with the full suite of available data. Unless otherwise specified, all data collection and processing was performed by collaborators.

3.6.1 *GPS*

Four Trimble R7 and Leica SR520 GPS receivers were installed at F-Lake in 2010 in a strain diamond configuration by S. Doyle, Aberystwyth University (see Figs. 3.7 and 3.3). The GPS results and analysis in relation to the drainage event are reported in detail by Doyle *et al.* (2013). Horizontal and vertical motion records were sampled at 10-second intervals and processed against an off-ice base station. Data were filtered, constraining errors to <0.02 m in the horizontal domain and <0.05 m in the vertical domain.

The horizontal and vertical GPS outputs during the lake drainage event are plotted in Figure 3.11. These data are compared with model outputs and used to constrain appropriate model parameters. It can be seen from the GPS 1 record (red) in Figure 3.11 a, that the greatest surface uplift occurred to the NW of F-Lake, suggesting that water primarily flowed along the basal trough consistent with the hydraulic potential gradient analysis (see Fig. 3.4).

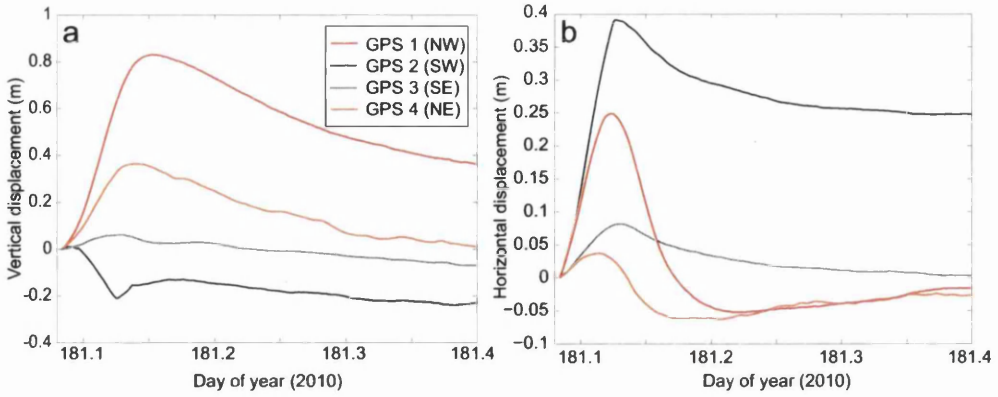

Figure 3.11: *GPS outputs from the strain diamond plotted in Figs. 3.7 and 3.3. a) Relative ice surface vertical displacement during the lake drainage event. b) Relative horizontal ice displacement during the lake drainage event.*

3.6.2 *Passive seismic data*

Six GS-11-D geophones were installed around F-Lake prior to lake drainage to record passive seismic waves generated by the drainage event (see Fig. 3.3). The passive seismic data and results are discussed in detail in Doyle *et al.* (2013); Jones *et al.* (2013), and Jones *et al.* (in prep.). Some of the results from the passive seismic analysis are shown in Figure 3.12 and constitute the first imaging record of hydrofracture in ice, processed by G. Jones, Swansea University. The passive seismic data suggest that there was no fracturing in the lake prior to drainage and therefore the drop in pre-drainage lake level was due to supraglacial out-flow. The data also indicate that several hydrofractures were generated during drainage, at the intersection of F1 and F2 and laterally along the plane of F1, the pre-existing fracture. The lake water appeared to reach the bed following the direction of flow suggested by the hydraulic potential analysis and the GPS uplift results, i.e. to the NW along the basal trough (pers. comm., G. Jones, Swansea University).

3.6.3 *Reflection seismic data*

Three reflection seismic lines were run in the vicinity of F-Lake to gain information about basal interface properties. The data were processed by A. Booth, Swansea University (now at Imperial College London), to construct seismic stacked sections. AVA analysis was then performed to determine the characteristics of the substrate. Information on reflection seismic processing procedures and AVA analysis is given

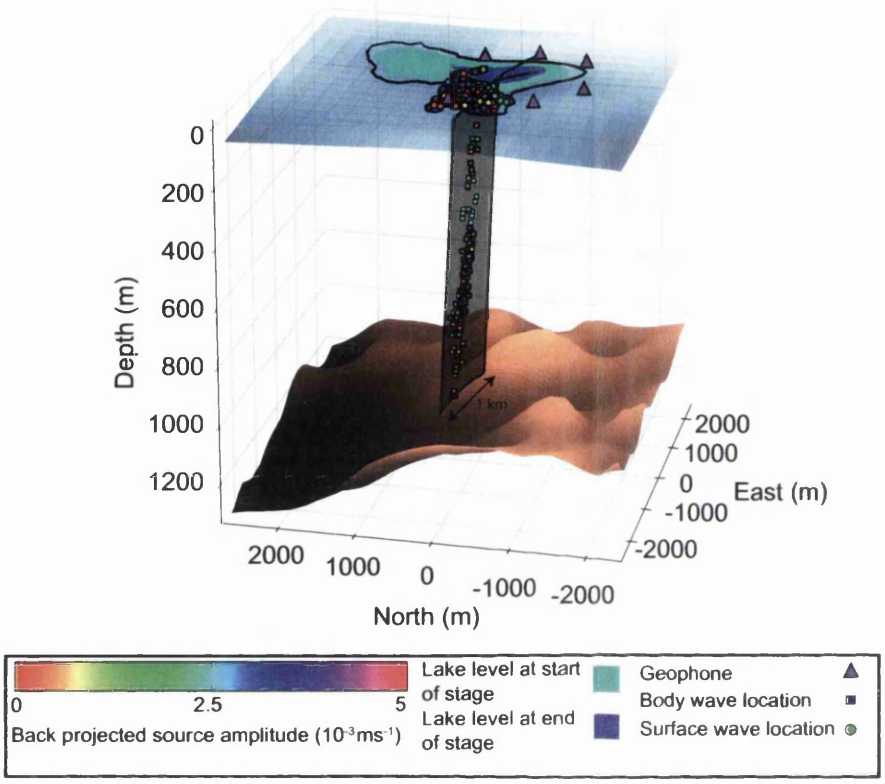

Figure 3.12: *3-D snapshot (between 02:20–03:00 UTC) of surface (circles) and body (squares) waves recorded during the F-Lake drainage. The events define a fracture plane laterally along F1 with a width of ~1 km. Figure adapted from Jones et al. (in prep.).*

in Chapter 8. The processing of the F-Lake seismic lines was complicated by the discovery of substrate layers thinner than the nominal seismic vertical resolution. A thorough discussion of the processing and analysis of the thin layer data from the F-Lake seismic lines is given in Booth *et al.* (2012).

The F-Lake seismic reflection results aid in determining the necessary substrate to apply in the hydrological model. The locations of the seismic lines in relation to F-Lake are shown in Figure 3.3 and the results plotted in Figure 3.13. The perpendicular lines to the SW of F-Lake intersect a basin that includes deformable sediment, underlain by lithified sediment (lines B-B′ and C-C′ in Fig. 3.13). However, the line that intersects the flowpath from the lake drainage event (line A-A′ in Fig. 3.13) indicates the presence of lithified till with no indication of soft, porous

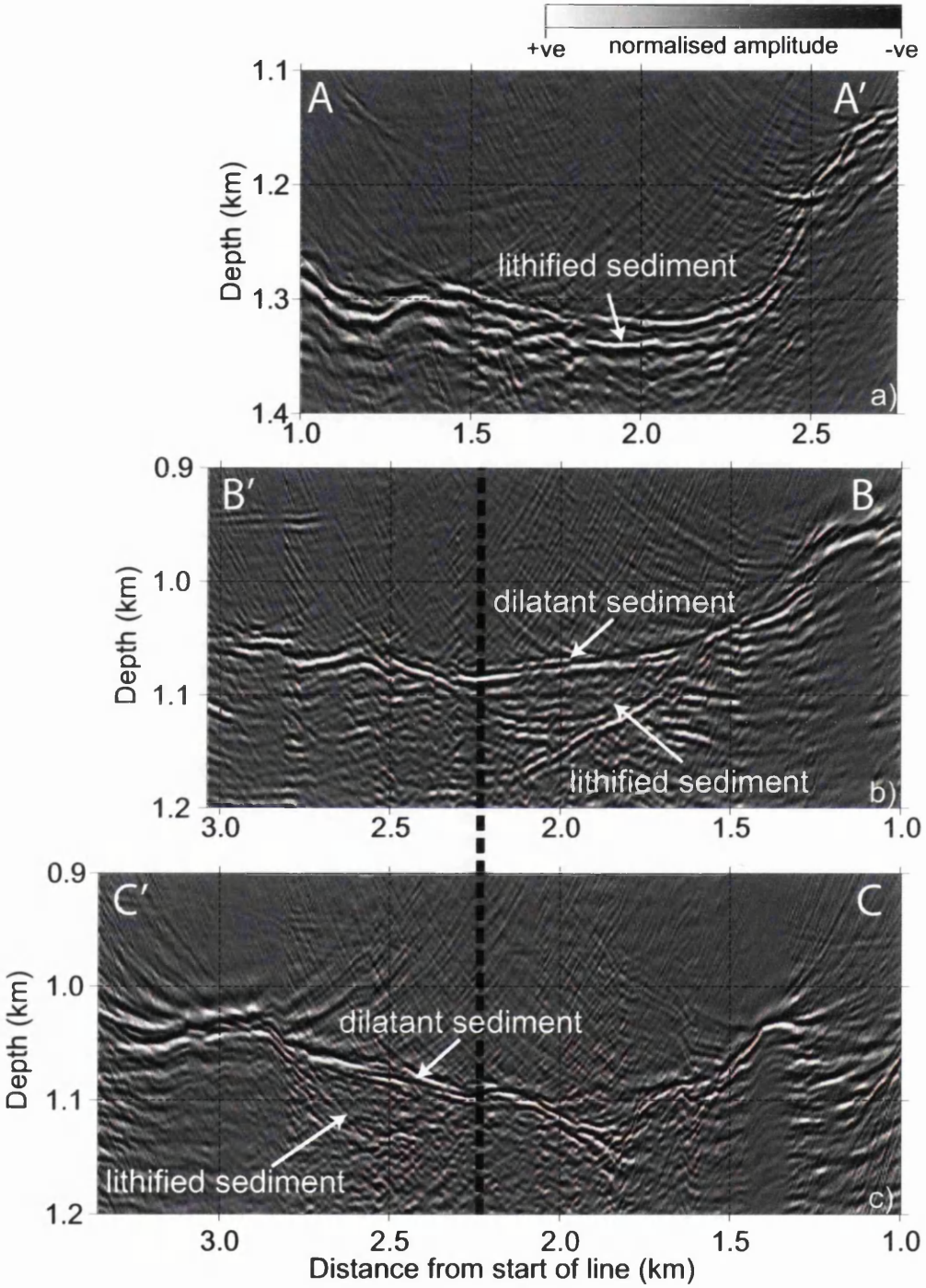

Figure 3.13: *Seismic stacked sections with locations indicated in Fig. 3.3 and the basal sediment conditions as indicated by AVA analysis. a) Seismic stacked section of the area to the NW of F-Lake with lithified sediment at the base. b) and c) Perpendicular stacked sections over a basin to the south of F-Lake with a thin layer of dilatant sediment overlying lithified till. The black dashed line indicates where the seismic lines intersect. Figure provided by A. Booth, Imperial College London.*

sediment. These results suggest that in the vicinity of the lake most of the substrate can be treated like a hard-bedded system as lithified sediment is unlikely to involve substantial pore-water flow on a short (diurnal) timescale. Therefore, modelling semi-circular hard-bedded R-channels is likely applicable to this rapid drainage event. If softer sediment is present within the F-Lake drainage path, processes might occur (such as the erosion of fast-flow sediment canals) that cannot be taken into account with the modelling presented in this thesis.

3.6.4 *Weather station data*

An AWS called KAN-M was installed ~8.5 km from F-Lake in 2008 by the Geological Survey of Denmark and Greenland (GEUS); the location of KAN-M is noted in Figure 3.3. For the purposes of the modelling presented in this thesis, the pertinent information from the AWS records is the air temperature and the predicted runoff from the site. van As *et al.* (2012) presents the method for calculating the runoff and the model was adapted by D. Van As, GEUS, to provide hourly runoff records applicable for F-Lake. The air temperature records and modelled runoff are plotted in Figure 3.14. The catchment melt rate is calculated from this information and applied to the hydrological modelling; these data are presented in Section 5.4.5.

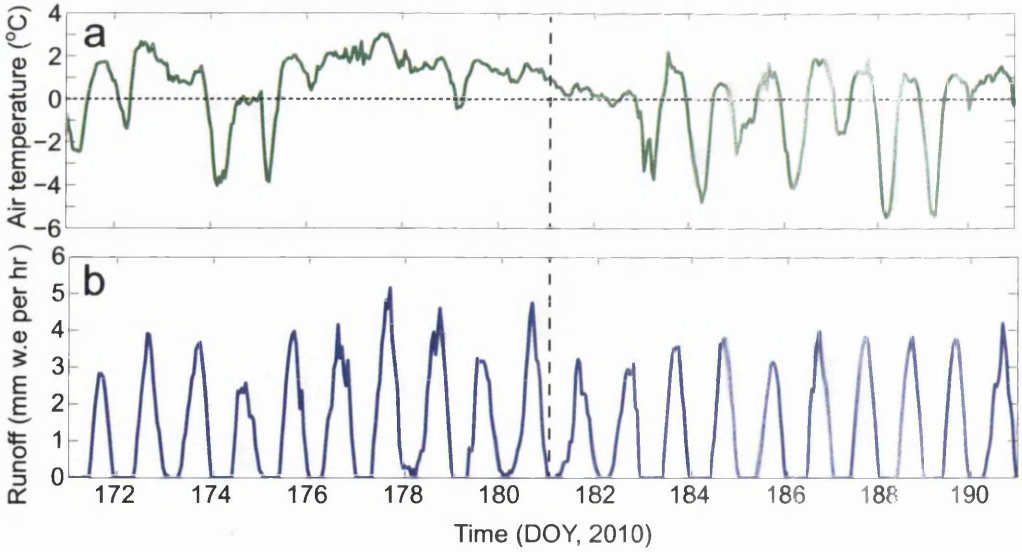

Figure 3.14: *a) Air temperature data recorded during the 10 days preceding and following lake drainage; 0° is denoted by the short dashed line. b) Modelled vertical runoff in mm water equivalent per hour at the AWS site for 10 days preceding and following lake drainage. The vertical dashed line shows the time of rapid lake drainage initiation.*

Table 3.1: *F-Lake rapid drainage dates from analysis of MODIS imagery.*

Year	Date	Day of year
2002	17/07-19/07	198-200
2003	25/06–26/06	176-177
2004	17/07-18/07	198-199
2005	27/07-30/07	208-211
2006	23/07-25/07	204-206
2007	29/06-02/07	180-183
2008	14/07	195
2009	20/07-22/07	201-203
2010	30/06	181
2011	n/a	n/a
2012	18/06-19/06	170-171

3.6.5 *Remote sensing*

Satellite remote sensing analysis of RGC puts the F-Lake drainage event in context and illustrates that F-Lake has consistently rapidly drained over the last decade (pers. comm. A. Fitzpatrick, Aberystwyth University). Table 3.1 gives the dates of lake drainage, determined by analysis of MODIS imagery, with the date uncertainty due to cloud cover preventing collection of surface images. In 2011, the year following the instrumented lake drainage event, F-Lake did not form and appeared to drain directly into a moulin. However, in 2012, the lake formed and drained in the middle of June, earlier than in previously examined years.

Figure 3.1 shows the timing of lake drainage events in RGC during the 2010 melt-season. It can be seen that F-Lake drained within the same period as a band of five lakes in the near vicinity. However, due to cloud cover for three days around the time of F-Lake drainage it is not clear whether these other draining lakes had a dynamic impact on the drainage of F-Lake. For more information on regional lake drainage characteristics on RGC see Fitzpatrick *et al.* (2014).

3.7 Summary

The hydraulic potential analysis, supercooling analysis, lake bathymetry map and lake drainage rate calculations introduced in this chapter were all processed by

the author. The case-study area DEMs and data from GPS units, passive seismic stations, reflection seismic lines, the weather station and satellite remote sensing analysis reported in this chapter were all processed by collaborators.

The records of the F-Lake drainage event and the supplementary data provide an excellent basis for modelling the lake drainage event and analysing the impact of the rapid drainage on local hydrological development. In particular, for modelling purposes, the lake lowering rate and lake bathymetry map, can be combined to give an accurate drainage rate that can be compared with model outputs. The GPS data presented in Doyle *et al.* (2013) give horizontal and vertical displacements during the lake drainage event, which will be a primary method for testing the outputs of the modelling effort presented in this thesis. The basal and surface topography records provided by colleagues from the University of Uppsala are highly valuable for determining a suitable model flowline and examining the hydraulic potential gradients. Reflection seismic work presented in Booth *et al.* (2012) provides information about the substrate in the location of the lake. Calculation by D. van As of the local melt rate near F-Lake allows modelling of seasonal hydrological development following lake drainage by providing estimates of water input to the bed. Finally, satellite remote sensing analysis discussed in Fitzpatrick *et al.* (2014), puts the drainage event into the catchment-wide context. These records will be used as inputs and constraints for the case-study model in addition to allowing a more complete hydrological analysis of the F-Lake drainage event.

Due to the availability of this extensive data set collected during a rapid supraglacial lake drainage event, F-Lake is an ideal case-study to apply to hydrological development modelling. The substantial data collection and analysis of RGC dynamics over the last decade (e.g. McMillan *et al.*, 2007; van de Wal *et al.*, 2008; Sundal *et al.*, 2009; Bartholomew *et al.*, 2010; Doyle *et al.*, 2013) also allows analysis of the F-Lake drainage event in a wider hydrological context. By using F-Lake as a case-study, contributions can be made to understanding of hydrological processes under areas of thick ice in RGC specifically, and the dynamics of ice sheets in general.

Chapter 4

Simple subglacial channel model

4.1 Introduction

Efficient drainage networks consisting of arborescent systems of R-channels have been postulated to develop under Greenland outlet glaciers during the summer melt-season, akin to those beneath Alpine glaciers (Shepherd *et al.*, 2009; Bartholomew *et al.*, 2010, 2012; Cowton *et al.*, 2013). In particular, large ($>20\,\mathrm{m}^2$ cross-sectional area) R-channels have been argued to pre-exist in areas of rapid lake drainage (Pimentel and Flowers, 2011) in order to efficiently evacuate the large volumes of water that reach the bed (Das *et al.*, 2008; Hoffman *et al.*, 2011; Pimentel and Flowers, 2011). However, a significant difference between Alpine glaciers and ice sheets is the ice thickness, which directly affects the creep closure rate of conduits. It is not yet clear from direct measurement or modelling how rapidly R-channels grow and under what conditions they can be maintained under thick ice.

This chapter presents a simple 1-D numerical model of conduit growth under thick ice. Simple models can be highly valuable for determining important variables in system development (Oerlemans, 2008). Whilst a more in-depth model including representations of both conduits and a distributed drainage system is necessary to replicate complex hydrological interactions (see Chapter 5), it is a useful exercise to independently test which variables have the greatest impact on the growth of R-channels. The equations to define R-channel growth were developed by Röthlisberger (1972) for a steady-state system and adapted by Nye (1976) to apply to spatially and temporally varying hydrological networks. These R-channel equations have

since been applied to many models of subglacial hydrological development (e.g. Lliboutry, 1983; Spring and Hutter, 1982; Clarke, 1996, 2003; Pimentel and Flowers, 2011; Hewitt *et al.*, 2012) as discussed in Section 2.4.2. However, despite the prolific application of the R-channel equations, an analysis of how fast R-channels can grow in overpressured situations under thick ice (such as during rapid supraglacial lake drainage events) has yet to be made. In addition, it is not clear how rapidly channels under thick ice would close once water pressure drops below overburden or how they react to diurnally changing water input.

The model described in this chapter utilises the original specifications of the Nye (1976) equations; the novel aspect of this approach is to apply these equations in a region with thick ice, as found in the case-study site, and investigate the important variables for channel growth under an ice sheet. In total, 11 tests are run with the simple model in order to address the following specific aims:

1. Determine the impact of overpressure during a lake drainage event on R-channel growth (using data from the case-study field site described in Chapter 3). Tests include investigating the impact of overpressure duration and channel length scale (tests 1–3); channel roughness (test 4); surface and bed slopes (test 5); and initial channel cross-sectional area (test 6) for conduit growth.
2. Investigate the rate of channel closure at pressures below overburden in a region of thick ice (test 7).
3. Examine the effects of varying diurnal pressures (such as would be found in a moulin-driven hydrological system; Iken and Bindschadler, 1986) on conduit growth under thick ice (tests 8–11).

In this chapter, the Nye (1976) R-channel equations will be detailed, followed by a description of how the model is applied for these test cases. The results from the 11 tests are then presented and a discussion given about the implications of the model outputs.

4.2 R-channel equations

Nye (1976) defined a system of equations to describe R-channel growth based on the competition between ice melting from viscous dissipation of heat within the

channel, and closure of the conduit due to the weight of the overlying ice, whilst conserving mass and momentum. For modelling the development of R-channels, the Nye equations will here be restated for clarity (and comparability with equations in Section 5.3) in terms of the channel cross-sectional area S (m^2), and the effective pressure, $N = P_i - P_w$ (Pa), where P_w (Pa) is the water pressure and $P_i = \rho_i g(a-b)$ is the ice overburden pressure with g ($\mathrm{m\,s^{-2}}$) the acceleration due to gravity, ρ_i ($\mathrm{kg\,m^{-3}}$) the density of ice, and a (m) and b (m) the elevations of the ice surface and ice bed respectively. The temporal evolution of S is

$$\frac{\partial S}{\partial t} = \frac{m_i}{\rho_i} - \frac{2A}{n^n} S N^n, \tag{4.1}$$

where m_i ($\mathrm{m\,s^{-1}}$) is the melt rate of the channel walls. The second term on the right-hand-side is related to the creep closure of ice where A ($\mathrm{s^{-1}\,Pa^{-3}}$) and n in Glen's flow law represent the ice softness. The melting condition through frictional heat generation is given by

$$m_i L_f = Q \left(\frac{\partial \psi}{\partial s} \right), \tag{4.2}$$

where L_f ($\mathrm{J\,kg^{-1}}$) is the latent heat of fusion, Q ($\mathrm{m^3\,s^{-1}}$) is the flux of water through the channel, ψ (Pa) is the hydraulic potential and s (m) is the distance along the channel. The effects of geothermal heating and water produced by frictional heating from sliding are ignored because they are likely insignificant in comparison to the viscous dissipation of heat generated from the potential gradient (Alley *et al.*, 2003). Following Shreve (1972), the hydraulic potential is $\psi = \rho_w g b + P_w$, where ρ_w ($\mathrm{kg\,m^{-3}}$) is the density of water. The along-flow gradient of hydraulic potential is given by

$$\frac{\partial \psi}{\partial s} = \left[\rho_w g \frac{\partial b}{\partial s} + \rho_i g \left(\frac{\partial a}{\partial s} - \frac{\partial b}{\partial s} \right) \right] - \frac{\partial N}{\partial s}. \tag{4.3}$$

The terms in the square brackets represents the geometric portion of the hydraulic potential gradient and is hereafter denoted as ϕ. Q is related to S by

$$Q = Sv, \tag{4.4}$$

where v ($\mathrm{m\,s^{-1}}$) is the velocity along the channel. Using the Gauckler-Manning-

Strickler formula for flow,

$$v = \frac{R_H^{2/3}}{n'} \left(\frac{1}{\rho_w g}\right)^{1/2} - \frac{\partial \psi}{\partial s} \left|\frac{\partial \psi}{\partial s}\right|^{-1/2} = \frac{Q}{S}, \tag{4.5}$$

with n' ($\mathrm{s\,m^{-3}}$), the Manning roughness coefficient typically varying between $0.01\,\mathrm{s\,m^{-3}}$ for a smooth channel and $0.1\,\mathrm{s\,m^{-3}}$ for a rough channel wall (Cuffey and Paterson, 2010). The hydraulic radius for a semi-circular conduit, R_H, is

$$R_H = \frac{\pi\sqrt{(2S/\pi)}}{(2\pi + 4)}. \tag{4.6}$$

Rearranging Eq. 4.5 for Q gives

$$Q = \left(\frac{SR_H^{2/3}}{n'\sqrt{\rho_w g}}\right) - \frac{\partial \psi}{\partial s} \left|\frac{\partial \psi}{\partial s}\right|^{-1/2}. \tag{4.7}$$

By substituting Eq. 4.7 into Eq. 4.2 and rearranging for m_i, the resulting expression can be in turn substituted into Eq. 4.1 to gain an expression in relation to S:

$$\frac{\partial S}{\partial t} = \left(\frac{SR_H^{2/3}}{n' L_f \rho_i \sqrt{\rho_w g}}\right) \left(-\frac{\partial \psi}{\partial s} \left|\frac{\partial \psi}{\partial s}\right|^{-1/2}\right) - \frac{2A}{n^n} S N^n. \tag{4.8}$$

4.3 Model geometry

The Nye (1976) equations are the basis for the simple model described here; a schematic of the model geometry is shown in Figure 4.1, model constants are given in Table 4.1, and test parameters for each model run are shown in Table 4.2. The basal and surface topography are assumed to be on a plane for all model runs with bed, Δb, and surface, Δa, angles of 0.2 and 0.35 degrees, respectively (aside from test 5 when the angles are varied). The ice thickness is defined as 1200 m at the water input point, assumed to be at the beginning of the spatial domain. The slope and thickness parameters are average values of those found at the case-study site discussed in Chapter 3. The end of the model domain is determined by considering a length, l, representing a segment of a conduit. The ice thickness at the end of the model domain is dependent on the values of l, Δa and Δb. Using these variables,

the geometric component of the hydraulic potential, ϕ, can be defined as

$$\phi = \rho_w g \Delta b + \rho_i g \left(\Delta a - \Delta b \right). \tag{4.9}$$

The model is applied assuming a constant drop in effective pressure over the conduit length segment, l (m), and as a result, $\partial N / \partial s$ can be replaced with $(N_2 - N_1)/l$. These approximations can be used to simplify Eq. 4.8) to a time-dependent ordinary differential equation:

$$\frac{dS}{dt} = \left(\frac{S R_H^{2/3}}{n' L_f \rho_i \sqrt{\rho_w g}} \right) \left[-\phi + \left(\frac{N_2 - N_1}{l} \right) \left| \phi + \left(\frac{N_2 - N_1}{l} \right) \right|^{-1/2} \right] - \frac{2A}{n^n} S N^n. \tag{4.10}$$

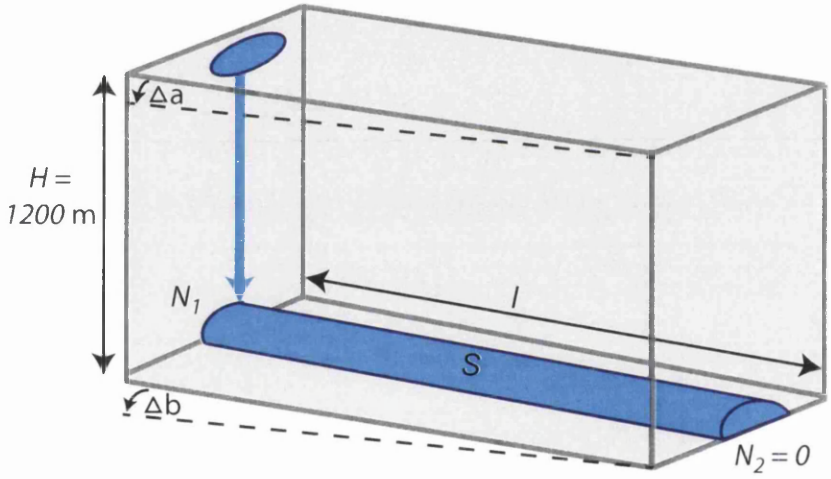

Figure 4.1: *Schematic of the simple R-channel model, applied for a lake drainage overpressure scenario.*

In all model tests, Eq. 4.10 is applied with an initial condition of $dS/dt = 0$; the initial size of S is defined for each individual model run (see Table 4.2). The boundary condition at the domain outlet is assumed to be zero effective pressure ($N_2 = 0$) for all lake drainage tests (aside from test 7 where $N_2 > 0$); this therefore represents a scenario where the outlet P_w is equal to ice overburden pressure. N_1 is either $P_w > P_i$ or $P_w = P_i$ depending on the model test (values of N_1 for each of the tests are detailed in Table 4.2). All tests are run with a time-step of two minutes so that the short-term behaviour of R-channel growth can be estimated.

Table 4.1: *Simple R-channel model constants.*

Symbol	Description	Value	Units
A	Glen's flow law coefficient	1.6×10^{-24}	$s^{-1}\,Pa^{-3}$
n	Glen's flow law exponent	3	dimensionless
ρ_w	Density of water	1000	$kg\,m^{-3}$
ρ_i	Density of ice	917	$kg\,m^{-3}$
g	Acceleration due to gravity	9.81	$m\,s^{-2}$
L_f	Latent heat of fusion	3.35×10^5	$J\,kg^{-1}$
H	Ice thickness	1200	m

4.4 Model tests

4.4.1 *Supraglacial lake drainage (tests 1–3)*

The simple model is first used to examine R-channel growth during rapid lake drainage events in regions of thick ice. Model input data are supplied from measurements of lake surface lowering during the case-study rapid drainage event (see Section 3.5). The measured lake lowering rate is shown by the black curve in Figure 4.2 a and determines the level of overpressure in the model (i.e. $N_1 < 0$). Tests 1–3 examine R-channel growth during the recorded lake drainage event but also in scenarios where the overpressure during lake drainage is extended by 2, 5 and 10 times the original duration (the blue, green and red curves respectively in Fig. 4.2 a). The aim of changing the overpressure duration is to determine whether there are lake drainage events that might have a greater impact on subglacial R-channel growth than those with duration similar to that recorded at F-Lake; lake drainage events of significantly shorter duration than F-Lake have not been reported in the literature and so the measured lake lowering rate is taken as a minimum in these experiments. Tests 1–3 have the same model parameters apart from l, which is varied in each run (see Table 4.2).

Test 1: overpressure duration

Test 1 examines the effect of different overpressure durations on R-channel growth with a length scale of l=500 m. Initial conditions of S must be prescribed and for test 1, a cross-sectional area of 0.01 m^2 is used to represent channels growing from

Table 4.2: *Simple R-Channel model input parameters (tests 1–11).*

Parameter	*Units*	*Pressure duration*	*Pressure l scale*	*Pressure l scale*	n'	ϕ	*Drainage time*	*Channel persistence*	*Moulin pressure*	*Moulin pressure*	*Moulin pressure*	*Moulin pressure*
Test no.		1	2	3	4	5	6	7	8	9	10	11
Drainage	-	lake	lake	lake	lake	lake	lake	n/a	moulin	moulin	moulin	moulin
l	m	500	200	varied	200	500	200,500, 1000	500	200,500	200,500	200,500	200,500
n'		0.05	0.05	0.05	varied	0.05	0.05	0.05	0.05	0.05	0.05	0.05
Δb	deg.	0.2	0.2	0.2	0.2	varied	0.2	0.2	0.2	0.2	0.2	0.2
Δa	deg.	0.35	0.35	0.35	0.35	varied	0.35	0.35	0.35	0.35	0.35	0.35
Initial S	m^2	0.01	0.01	0.01	0.01	0.01	varied	varied	varied	varied	varied	varied
N_1	Pa	<0	<0	<0	<0	<0	<0	0	varied	varied	varied	varied
N_2	Pa	0	0	0	0	0	0	>0	0	0	0	0

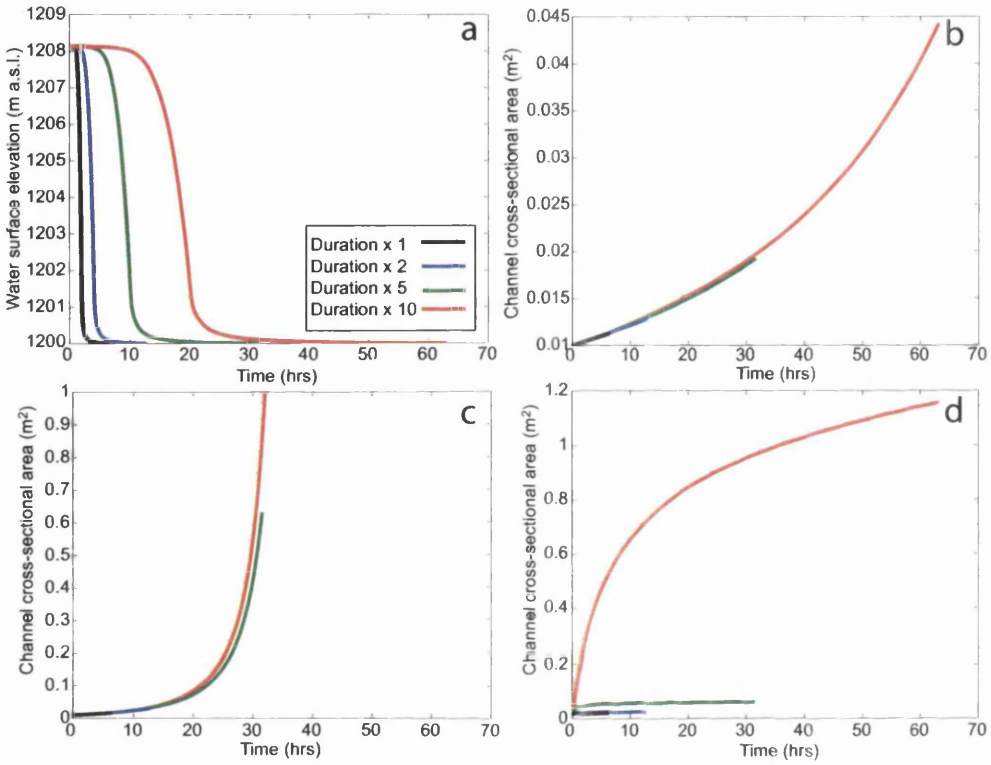

Figure 4.2: *Inputs and outputs from the simple R-channel model testing the impact of change in overpressure duration and pressure length scale on channel growth. a) Change in water height during a lake drainage event with the time of overpressure extended in duration. The outputs from the measured drainage duration are shown by the black curves; two times the measured duration by the blue curves; five times the measured duration by the green curves and 10 times the measured duration by the red curves. b) Test 1 - channel cross-sectional area change at a static length of 500 m for the times of lake drainage duration shown in a). c) Test 2 - channel cross-sectional area change at a static length of 200 m. d) Test 3 - channel cross-sectional area change for a linearly-increasing channel length between 5 and 5000 m, with the temporal change in channel length scale dependent on the duration of lake drainage. Note that ordinates in b)–d) have different scales.*

an inefficient system. Other model parameters for test 1 are shown in Table 4.2.

As the overpressure duration is lengthened (with results shown in Fig. 4.2 b), there is little R-channel growth. Even with an overpressured duration of >60 hours (10 times the length of the recorded lake drainage at F-Lake), R-channel cross-sectional area grows by only $\sim$0.04 m^2. R-channel growth in test 1 is limited by the long length scale that prevents a strong hydraulic gradient.

Tests 2 and 3: radius of overpressure impact

Tests 2 and 3 examine the effect of l, which acts as a proxy for the radius of influence of overpressure. In the situation of lake drainage, this could be envisaged as the radius of a pressurised film of water expanding radially outwards (see e.g. Tsai and Rice, 2010). These tests examine how much channel growth would be possible over that overpressure radius.

In test 2, l is shortened from 500 m to 200 m. Other than the length scale, all model parameters in test 2 are the same as for test 1 (see Table 4.2). Figure 4.2 c illustrates that the shorter length over which the water pressure drops has a substantial effect on the growth of R-channels. Over shorter distances, the pressure gradient is higher and there is therefore greater potential energy for melting channel walls. During the recorded duration of lake drainage (the black curve), R-channel cross-sectional area only grows by a few cm^2. However, if the basal system over a length scale of 200 m is overpressured for >30 hours, the channels can grow very large and, at $\sim$33 hours becomes unstable; in this situation, the Nye (1976) equations can no longer be used for determining channel growth. However, it is unlikely that a channel could be overpressurised for such a long duration over this length scale as water would spread into a distributed system in order to stabilise the pressure within this time period (Hewitt *et al.*, 2012); as a result, the instability seen in the R-channel growth in Figure 4.2 c is not problematic for model output interpretation if care is taken.

From tests 1 and 2 it can be determined that both the duration of overpressure and the length scale of the pressure change are important factors for channel growth. However, the length scale of pressure change at the bed will not be static during the lake drainage event due to the expansion of the radius of overpressured water as the drainage proceeds, possibly due to hydraulic jacking (e.g. Tsai and Rice, 2010). For test 3, the length of overpressured channel is therefore changed on a linear scale from 5 to 5000 m over the period of drainage (which depends on the applied lake

drainage duration). The temporally changing length scale is based roughly on the temporal expansion of an overpressured water blister radius calculated for the Das *et al.* (2008) drainage by Tsai and Rice (2010).

Figure 4.2 d shows the outputs of test 3; it can be seen that, with the temporal increase in pressure length scale, and an initial channel size of 0.01 m^2, there is negligible R-channel growth if the overpressured scenario is extended by 5 times the original duration. However, for the long (~60 hour) drainage duration, there is substantial channel growth.

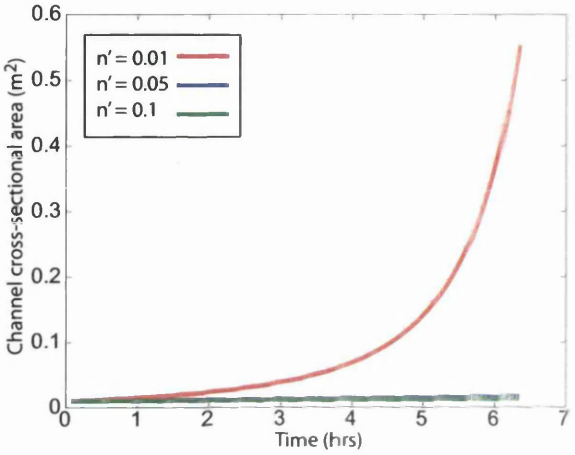

Figure 4.3: *Manning roughness (test 4) - R-channel growth rates with different Manning roughness parameters. A roughness parameter $n' = 0.01$ (red curve) indicates a smooth channel wall with $n' = 0.1$ (green curve) emulating a rough boulder-strewn channel. These experiments are based on a static channel length of 200 m and the measured lake drainage duration.*

4.4.2 *Test 4: Manning roughness*

The Manning roughness parameter, n', is related to the frictional resistance within an R-channel. A channel with a rough wall will slow the water flux and therefore reduce the melt on the channel walls. Test 4 is run for a length scale of 200 m with the observed F-Lake drainage rate and an initial channel size of 0.01 m^2 to determine the impact of changing n'. Model parameters are listed in Table 4.2. Values for n' in an R-channel are thought generally to be less than 0.1 (Cuffey and Paterson, 2010) and therefore R-channel growth is tested for n'= 0.01, 0.05 and 0.1 (the red, blue and green curves respectively in Fig. 4.3). The results indicate that smooth channels (n'=0.01) will grow significantly faster than rough channels. It is often not possible to determine the roughness of a subglacial channel without independent evidence of

basal conditions (such as bedrock vs. sediment) and, as a result, all of our remaining tests are run with a median roughness of $n' = 0.05$. It is likely that sediment is present at the ice-bed interface (see Chapter 8 and Booth *et al.*, 2012; Dow *et al.*, 2013) and therefore it is probable that the channel base will not be fully smooth; as a result $n' = 0.01$ would be an unrealistically low value for Manning roughness. However, if the channel walls are very smooth, the channel growth rates analysed here are likely an underestimate.

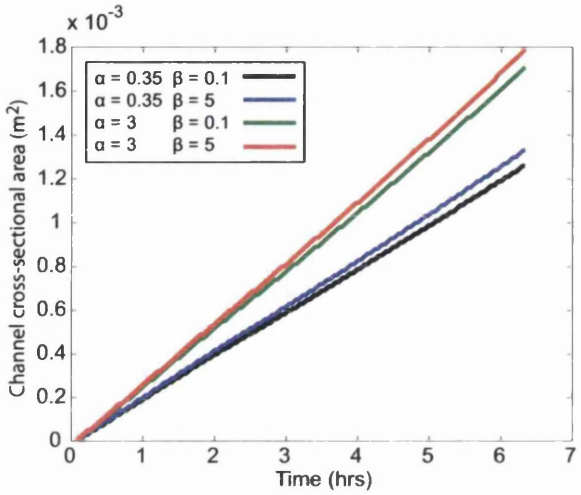

Figure 4.4: *Gravitational hydraulic potential (test 5) - a plot of R-channel growth with different surface (Δa) and basal (Δb) slope angles. Test 5 is run with $S = 0.01\ m^2$, $l = 500\ m$ and the measured lake drainage duration.*

4.4.3 *Test 5: geometric hydraulic potential*

The values of surface and basal slope used in the tests are averages for the region of the case-study lake. However, variable surface and basal topography might have a significant effect on the geometric hydraulic potential and therefore on the growth or closure of the R-channels. In test 5 (shown in Fig. 4.4), four different topographical scenarios are tested: a shallow (0.35°) surface and bed (0.1°) slope (black); a shallow surface slope and a steep (5°) bed slope (blue); a steep (3°) surface slope and a shallow bed (green); and a steep surface and basal slope (red). Test 5 is run with an initial channel size of $S = 0.01\ \mathrm{m}^2$, a length scale of $l = 500\ \mathrm{m}$ and the measured lake drainage duration (see Table 4.2 for other parameter values).

The model run with both shallow surface and basal slopes produces the least R-

channel growth due to a shallow geometric hydraulic potential gradient. However, having a significantly steeper basal slope (of 5 degrees) but retaining a shallow surface slope (blue curve) does not significantly increase the R-channel growth rate. For example, with a steeper surface slope, R-channel growth is greater but within the period of F-Lake overpressure, the increase in geometric hydraulic potential only causes additional channel growth of $\sim 7 \times 10^{-5}\,\mathrm{m}^2$.

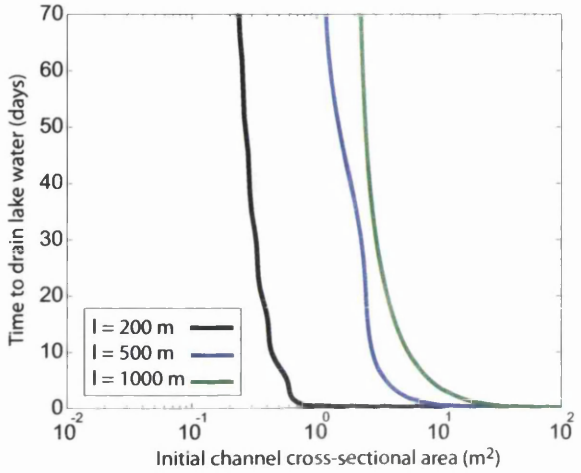

Figure 4.5: *Drainage time (test 6) - Plot showing the time to drain the volume of water in the lake given different initial cross-sectional channel areas. Outputs are given for static length scales of 200 m (black curve), 500 m (blue curve) and 1000 m (green curve).*

4.4.4 *Test 6: lake drainage time*

For tests 1–4, the initial channel size was set as $0.01\,\mathrm{m}^2$ in order to replicate a system with essentially no pre-existing channels. However, it is clear that, due to the limited area available for melting on the hydraulic radius, small channels grow slowly over a period of hours, even with a strong pressure gradient. For test 6, an experiment is conducted for channels of different fixed lengths to determine the time it would take to drain all the water in the F-Lake site (a volume of $7.1 \times 10^6\,\mathrm{m}^3$) given different initial channel dimensions. The overpressured conditions are prescribed from the drainage rate of the study lake; following this initial drainage period, a linear decrease in pressure towards overburden over a time-scale of three hours is calculated (to emulate water level lowering within the moulin). After this period, water pressure is set at overburden and R-channel growth is driven only by the geometric hydraulic potential gradient. Test 6 is run for three length scales of 200 m (black curve), 500 m (blue curve) and 1000 m (green curve).

Figure 4.5 shows the results from test 6 and illustrates that a large channel (>20 m^2) is necessary to drain water in less than 1 day for a length scale of 1000 m. For a shorter length scale of 500 m, a channel of >7.3 m^2 is necessary to drain lake water in less than a day. At a length scale of 200 m of overpressure, the initial channel would need to be >0.7 m^2 to drain the lake water in less than a day. For channels with initial cross-section of <1 m^2 and length scale of >500 m it would take more than 70 days to drain all of the water from the lake drainage event. For length scales of 200 m, a channel of initial cross-section <0.25 m^2 would need more than 70 days to drain all of the lake water.

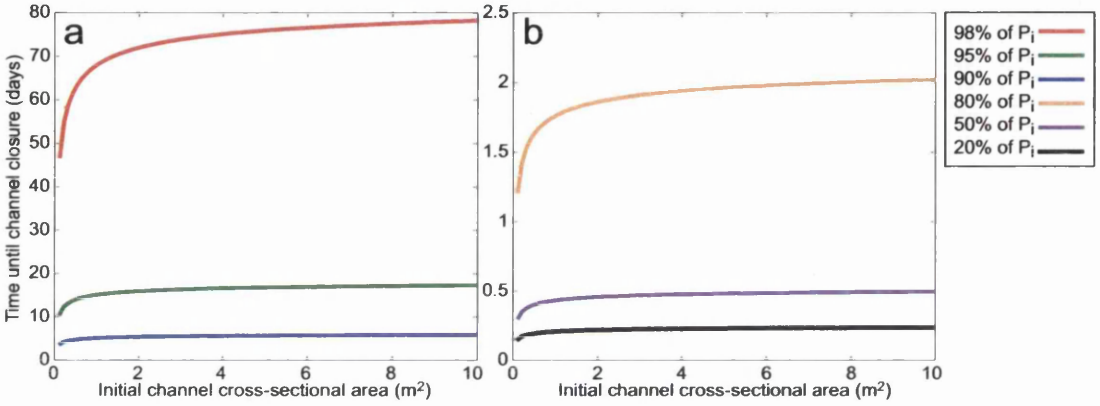

Figure 4.6: *Channel persistence (test 7) - Plot of the time taken for channels of varying initial cross-sectional area to close, given a drop in pressure from overburden to a) 98% (red), 95% (green) and 90% (blue) of overburden; and b) 80% (orange), 50% (pink) and 20% (black) of overburden over a length scale of 500 m.*

4.4.5 *Test 7: channel persistence*

Pimentel and Flowers (2011) argued that, to remove the lake water from the Das lake drainage event, a channel with a >22 m^2 cross-sectional area must have pre-existed in the vicinity of the lake. The results from the simple model presented here concur in that, if R-channels are the only mechanism to remove lake water, they would have to have a large initial size to drain the water within several days. To determine if pre-existing channels are likely in areas of rapid lake drainage, the duration of persistence of an R-channel under kilometre-thick ice is therefore of interest. For test 7, channel closure rate is examined with the upstream pressure as overburden ($N_1 = 0$) and the downstream pressure less than overburden ($N_2 > 0$). If there is no effective pressure difference over the length of the channel (i.e. if both N_1 and N_2 are equal to zero), the geometric hydraulic potential will still drive water flow if the

channels are full of water. However, by allowing an underpressured gradient, closure of the conduit is possible while still allowing for some melting by water flux. Several scenarios are postulated to determine the closure time for channels that begin with cross-sectional areas between 0.1–10 m^2. Closure rates are tested for pressures of 20, 50, 80, 90, 95 and 98% of overburden (see Fig. 4.6). Due to the geometric hydraulic gradient, the channel will never fully close if filled with water, so instead the critical closure time is determined (shown in the y-axis of Fig. 4.6), defined as the time when the channel cross-sectional area becomes $<0.01\,m^2$.

The results show that, as pressures become close to overburden (at 98%, the red curve in Fig. 4.6), it takes more than 46 days to close even the smallest tested channel and 80 days for a channel of $10\,m^2$. At 95% of overburden, channels can close at a faster rate although it still takes more than ten days to close a channel of $0.1\,m^2$. Once pressure at the outlet drops to 90% of overburden, channels can close within 3.5–6 days. At lower pressures, such as 50% and 20% of overburden at the outlet, channels close within a matter of hours (between 7 and 12 hours, and between 3 and 6 hours, respectively, for the full range of channel sizes). Therefore, if pressures remained close to overburden, R-channels could persist for a substantial period of time.

4.4.6 *Tests 8–11: Moulin overpressure*

The growth of R-channels is now tested for a scenario with time-varying flux, such as often associated with a moulin, which will be the hydrological link from surface to bed once a lake has drained, assuming that surface water is not elsewhere directed. At the study lake, surface water was observed to drain into the fracture following drainage and therefore emulates a moulin-based drainage system (see Section 3.5). There are no records of pressure changes in the moulin following lake drainage and therefore four pressure scenarios are postulated (tests 8–11 with test parameters shown in Table 4.2 and sinusoidally varying pressure conditions plotted relative to the ice overburden pressure in Fig. 4.7 a). The first pressure scenario (blue) represents a situation where water flows into an already pressurised basal system, causing diurnal fluctuations of overpressure. The remaining pressure scenarios represent an increasingly efficient drainage system that allows pressure to drop below overburden (to a minimum of 40% P_i). Change in channel cross-sectional area is shown in Figure 4.7 b–e for initial channel sizes of 0.01. 0.1, 1 and 10 m^2. The solid curves show the

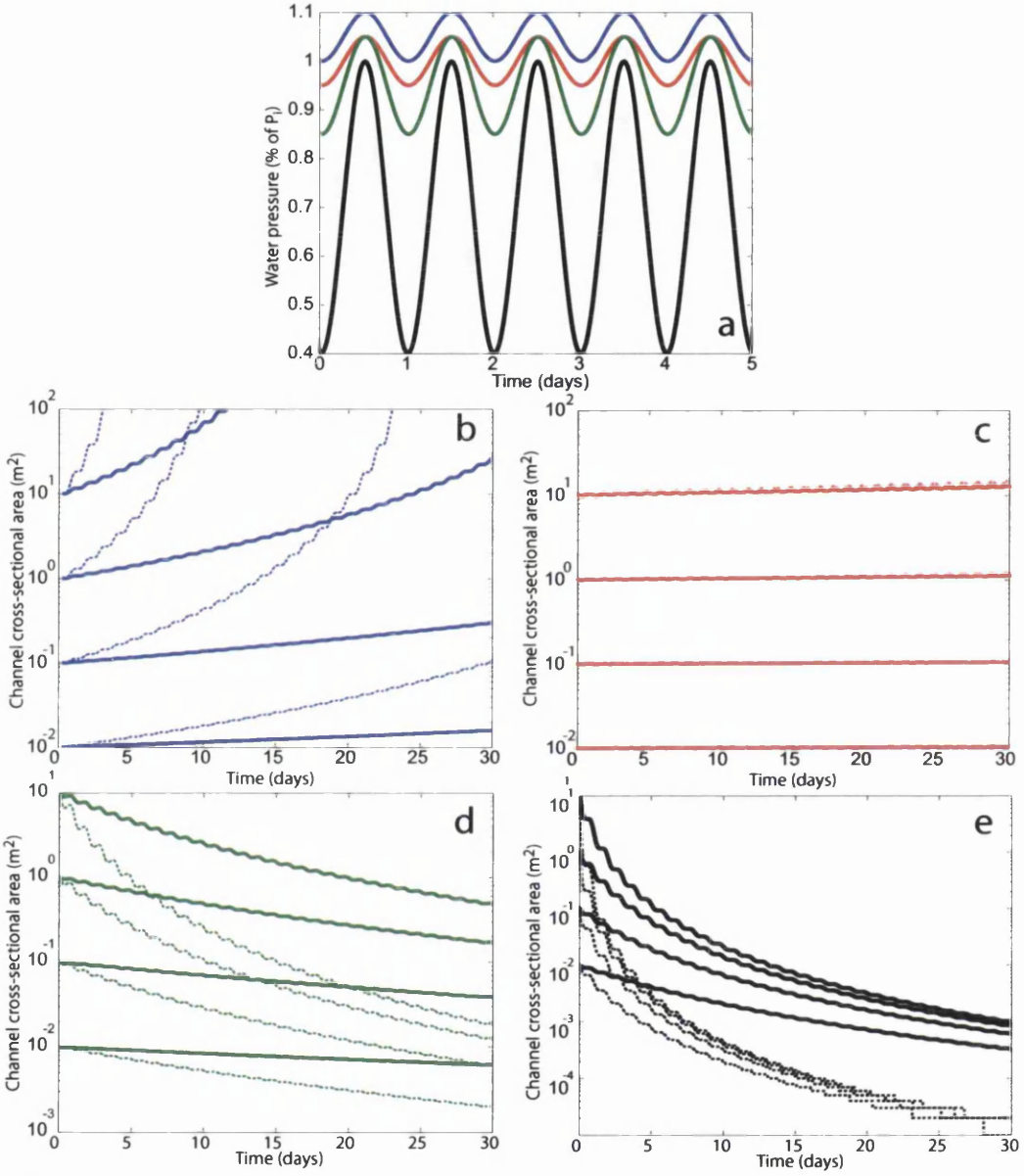

Figure 4.7: *Outputs from an R-channel model driven by simulated moulin water pressure. a) Diurnally-varying water pressure (as a percentage of overburden). b)–e) Tests 8–11: Channel cross-sectional area change over the period of 30 days for different initial channel cross-sectional areas ranging between 0.01–10 m^2. Solid lines indicate changes over a static length scale of 500 m; dashed lines show changes for a length scale of 200 m. Note that ordinates in b)–e) have different scales.*

change in channel size for a length scale of 500 m and the dashed curves for a length scale of 200 m. All tests are run for a period of 30 days.

The results (shown in Fig. 4.7 b–e) show that, even if water pressures are above overburden for part of the day, pressures below overburden during the remainder of the day prevent channel opening and mostly act to reduce the size of the channel. With pressures varying above overburden over the period of 30 days (Fig. 4.7 b), a channel with an initial cross-sectional area of $1\,m^2$ can grow to $10\,m^2$ with a pressure gradient length of 500 m, and over shorter distances will grow unstably. With pressures varying between overburden and 40% of overburden, channels under thick ice will reduce from $1\,m^2$ to $<0.1\,m^2$ within 30 days. The closure rate for channels under thick ice is sufficiently rapid that substantial channel growth or persistence is only seen with pressures consistently above overburden pressure.

4.5 Discussion

4.5.1 *Variable relationships*

The results from the tests of R-channel growth using the simple model can elucidate some important relationships between variables that affect the development of subglacial drainage systems. Although a simple model does not capture the complexity of the subglacial hydrological environment, if appropriately constructed it can provide useful information on the sensitivity of the system. A particularly important variable for channel growth according to test 3 is the Manning's roughness coefficient. With smoother walls, a channel will grow significantly more rapidly than a channel with a rougher wall (Fig. 4.3). Unfortunately, it is very difficult to predict the roughness of a channel unless glacial speleological (Gulley and Benn, 2007; Gulley *et al.*, 2009) or dye tracing (Gulley *et al.*, 2012) approaches are taken; furthermore these studies indicate that roughness can vary widely during a melt-season.

From tests 1 and 2 where the duration of the lake drainage event was altered, it is clear that a longer period of overpressure allows greater channel growth. However, with a small initial channel at the ice-bed interface (i.e. an initial condition of S $= 0.01\,m^2$), even a long duration of overpressurisation, such as over a period of 30 hours, is not sufficient to rapidly grow channels. Given that much glacial hydrological research has explored the development of R-channels from highly pressurised

distributed systems over the course of a melt-season for both Alpine glaciers and the GrIS (e.g. Röthlisberger and Lang, 1987; Fountain and Walder, 1998; Nienow *et al.*, 1998; Bartholomew *et al.*, 2012), the conclusion from these tests that a period of several days is necessary to grow R-channels is not surprising. This suggestion that R-channels cannot form within a period of hours agrees with the conduit growth rate suggested both by jökulhlaup observations (Tweed and Russell, 1999; Björnsson, 2003) and jökulhlaup models (Clarke, 2003; Flowers *et al.*, 2004), where a minimum of 12 hours is necessary to grow channels sufficiently large to evacuate the flood water. In the context of an entire melt-season, 12 hours is indeed a short period of time, but it does suggest that the time frame of lake drainage events (often < 3 hours of overpressure; Das *et al.*, 2008; Doyle *et al.*, 2013) is too short to allow substantial channel growth.

4.5.2 *Applicability to lake drainage analysis*

Greenland lake drainage research to date has assumed that a large channel is necessary to evacuate the substantial volumes of water that drain from supraglacial lakes to the bed (Das *et al.*, 2008; Hoffman *et al.*, 2011; Pimentel and Flowers, 2011; Cowton *et al.*, 2013). The tests of the R-channel equations suggest that conduits are unlikely to grow rapidly within the short duration of a lake drainage event. Das *et al.* (2008), Pimentel and Flowers (2011) and Hoffman *et al.* (2011) instead argue that a pre-existing channel is likely present for efficient evacuation of lake drainage water. In test 6, it was estimated how long it would take for an R-channel alone (discounting any flow through an accompanying water sheet) to remove all the water in the study lake (Fig. 4.5). This is a simplified analysis in that it involves a static R-channel length and an average change in cross-sectional area, although in reality these will vary both temporally and spatially. However, this analysis suggests that a large channel $>20\,\mathrm{m}^2$ is necessary to evacuate lake drainage water within the period of 1 day. There are therefore three likely scenarios for the evacuation of water during lake drainage events: a) large ($>20\,\mathrm{m}^2$) subglacial channels have been formed in the vicinity of the lake prior to drainage, b) water is evacuated from the vicinity of the drainage lake by a sheet and some limited channel growth, or c) the water from the lake drainage event does not evacuate rapidly (in the period of a few hours) and instead, more gradually over a period of days, disperses in a distributed drainage system. Although scenario a) is possible, it is perhaps unlikely because

lakes tend to drain in bands of increasing elevation so those downstream will drain prior to those upstream (Liang *et al.*, 2012; Howat *et al.*, 2013). As test 7 illustrates, under kilometre-thick ice where lakes often form in Greenland, R-channels will rapidly (within several days) close after the cessation of overpressurised conditions if pressures drop to <90% of overburden. If pressures at the outlet are <90% of overburden, channels can close within hours. However, if pressures remain >98% of overburden, channels of cross-sectional area $>1\,m^2$ can exist for more than 70 days (Fig. 4.6). Therefore, to have a large channel in the vicinity of a lake drainage event, it must have formed recently and been sustained with high pressure (>98% of overburden) to have persisted. However, as seen for the tests that have a small initial channel size (Fig. 4.2), it would require sustained high pressure to grow the upstream channel in the first place. As a result, to grow a pre-existing channel would require: 1) the presence of a moulin feeding the basal system over several days/weeks upstream of the lake drainage event to create a large channel, 2) sustained high pressure to maintain the channel size until the lake drainage event, and 3) subglacial hydraulic gradients that would drive basal water from the upstream moulin to the site of the lake drainage event. It is not clear that these conditions would be met in many situations at high elevations on the GrIS, although analyses of moulin and lake drainage location and timing along with hydraulic potential calculations would be necessary to test this. It would require a lot of water from upstream to maintain a large ($>20\,m^2$) channel at levels near overburden and a subglacial catchment analysis would be necessary to test whether this is possible under areas of thick ice. The model presented here cannot be used to ascertain which postulated scenario is the most likely for lake drainage events in Greenland because of the assumptions involved in the analysis; instead an approach using a coupled radial sheet drainage model and distributed/channelised model will be used to test these hypotheses (see Chapter 5).

4.5.3 *Moulin overpressure*

The test case of an overpressurised moulin is possibly only applicable at the beginning of a melt-season prior to basal drainage development or immediately following lake drainage events. However, records of uplift in the vicinity of moulin water inputs (Shepherd *et al.*, 2009; Bartholomew *et al.*, 2012) suggest that basal pressures commonly reach levels of overburden and likely become overpressurised. The sensitivity test results show that, even if water pressures in the moulin are above

overburden for part of the day, pressures below overburden during the remainder of the day prevent channel opening and mostly act to reduce the size of the channel. However, these moulin overpressure tests are unlikely to be realistic closer to the ice margin where channel pressures can become atmospheric near the terminus, thus creating a much steeper pressure gradient. Surface slopes inland on the GrIS are much shallower than those towards the margin and therefore have less impact for driving geometric potential flow. The ice thickness at higher elevations acts to rapidly close channels when water pressures are less than overburden so that rapid and sustained growth is not possible.

4.5.4 *Model limitations*

A significant assumption in the model is that uniform growth of the channel occurs over the domain, although in reality the growth of the channel will vary in both space and time due to the variation in water discharge input into the conduit at the beginning of the domain. With the short time-step used in the analysis, the model outputs will therefore only give an estimate of R-channel behaviour. However, the simple model can be used to test which variables are important for R-channel growth under thick ice and the general time-scales of channel dynamic variation.

Another assumption made in this analysis is that only one channel is forming during a lake drainage event. However, with turbulent water flow at the bed and a non-uniform basal roughness it is plausible that multiple channels will form during initial drainage and will only later form an arborescent network. If multiple channels form, the analysis of timing for water evacuation in these tests will not be accurate. In addition, lateral flow into and out of a channel from the surrounding region is not configured in the model. With pressures above overburden, hydraulic jacking will occur and water would be able to flow out in a sheet. As a result, a more detailed modelling venture is necessary to determine such conditions, like that described in Chapter 5. The R-channel equations used in the simple model assume that heat transfer between the water and the channel walls is instantaneous. However, Clarke (2003) suggests that the frictional heating of the water must be taken into account and that the Nye (1976) approach likely overestimates the cross-sectional area of R-channels. On the other hand, recent treatments of R-channel formation (Schoof, 2010; Hewitt *et al.*, 2012) have reverted to the Nye (1976) equations assuming instantaneous heat transfer in the channels and so the simple model presented here is

approached in a similar way.

Despite these limitations, the simple model approach can estimate whether channels can grow sufficiently large during a lake drainage event to independently evacuate lake drainage water within the range of hours to days. The model tests have elucidated that channel growth occurs much more slowly than the time frame of a lake drainage event and also that under thick ice with shallow surface slopes (where many of the rapidly draining lakes exist in Greenland) the possibility of pre-existing channels is unlikely (see Fig. 4.6), contrary to that expressed in various analyses of lake drainage events (Das *et al.*, 2008; Hoffman *et al.*, 2011; Pimentel and Flowers, 2011). Lack of persistence of large channels under thick ice (unless pressures are maintained consistently close to overburden) would also suggest the argument that Greenland emulates an Alpine-type hydrological system (Shepherd *et al.*, 2009; Bartholomew *et al.*, 2010, 2012) is not applicable inland where many lakes and moulins are observed to drain to the bed. Further analysis is necessary to determine the relationships between ice dynamics and basal hydrological systems under thick inland ice in Greenland; in this thesis this will be achieved by applying a coupled hydrological model at the ice-bed interface that allows turbulent sheet flow, channel development and flux through a distributed system (see Chapter 5).

4.6 Summary

This simple model indicates that the most important variables influencing R-channel growth are the duration (and persistence) of overpressure; the Manning roughness coefficient; and the length scale over which pressure change occurs. For a supraglacial lake drainage event, the model suggests that the duration of overpressure is insufficient to allow substantial channel growth, unless a large channel is already present within the vicinity of the lake drainage. However, under thick ice with shallow slopes, it is unlikely that a pre-existing channel would persist for more than several days. For moulin drainage, channel growth does not appear to be substantial unless the system is overpressured for the majority of the time, likely due to the thickness of the ice causing rapid channel closure. It is therefore plausible that subglacial hydrological systems at the higher elevations of the GrIS do not behave in a similar manner to the dendritic development of Alpine glacier hydrological systems.

This simple model suggests that an approach where only R-channel development

is examined for supraglacial lake drainage events is not sufficient to determine the subglacial hydrological conditions during rapid drainage. Instead, an approach is needed where radial flux from the input point is allowed, along with both distributed and channelised drainage; the following chapters (5–7) describe such an approach.

Chapter 5

Coupled hydrological model methods

5.1 Introduction

Investigation of the development of subglacial hydrological systems during rapid supraglacial lake drainage events in RGC must primarily be achieved by numerical modelling due to difficulty of basal instrumentation in areas of thick ice. The sudden input of substantial volumes of water to the bed of the ice sheet creates an interesting but challenging set of conditions to model. Although a complex, coupled 3-D model would be useful to apply to hydrological development during rapid lake drainage events, it would not necessarily output better results than a 1-D model due to unknown parameters in the subglacial hydrological system. As a result, in this thesis, the approach is to use two linked 2-D models that have been individually extrapolated from 1-D numerical configurations. This chapter will introduce the methodology behind the two models and the process by which they are linked.

Chapter 4 discussed the application of a simple numerical model to rapid lake drainage events and overpressured systems. In this current chapter, a more complex approach is utilised to determine the hydrological development using two established, but very different, models that have previously been applied to rapid lake drainage events by their developers. The first model from Tsai and Rice (2010), that is hereafter referred to as the 'water blister' model, uses elastic mechanics equations to determine englacial expansion of a connecting crack from the surface

to the bed, hydraulic jacking at the bed, and the subglacial radial spreading of a turbulent blister of water. The water blister model involves no temporal forcing so that blister growth drives the drop in lake level rather than the converse. The second model from Pimentel and Flowers (2011) is a 1-D flowband model comprising coupled distributed and channelised drainage systems. The novel approach taken in this thesis is to link the blister and flowband models together so that the growth of the water blister feeds into a developing down-stream hydrological network. By using this approach, the aim is to determine whether efficient channels are likely to develop during rapid lake drainage events in Greenland, and if not, establish the characteristics of a distributed system during and after lake drainage.

This chapter will introduce the equations from the water blister model and the flowband model. It will also include a discussion of how these models were applied by the developers to a lake drainage event described by Das *et al.* (2008) and a description of the limitations of each model. Following this, the method of linking the two models together will be described.

5.2 Water blister model

The water blister model is introduced in this section along with some assumptions behind the modelling process. The numerical implementation of the blister model is then detailed and the primary equations used for analysis of the model outputs highlighted. Following this, the previous application of this model and the limitations of this type of model approach are discussed.

The water blister model (Tsai and Rice, 2010, 2012) represents a turbulent sheet of water that flows between the ice and the substrate in a 'crack' along a flat bed. In glaciological terms this 'crack' represents hydraulic jacking of the ice and the related flux of water through the gap at the ice-bed interface (see Fig. 5.1). The extent of hydraulic jacking is established though elastic ice mechanics: in this case, the balance between subglacial pressure force and resistive elastic forces in the overlying ice. Elastic mechanics are also applied to determine the flux through the englacial fracture that is formed during initial lake drainage (see van der Veen, 2007). The blister model does not calculate a vertical hydrofracturing criteria (such as that discussed by van der Veen, 2007) that would allow initial flux of lake water into the ice subsurface, but instead assumes a surface-to-bed englacial crack already exists

and that water has reached the bed prior to model initiation. By including a pre-existing englacial fracture in the blister model, it allows the modulation of flow due to frictional resistance of the vertical crack walls to be taken into account (Fig. 5.1).

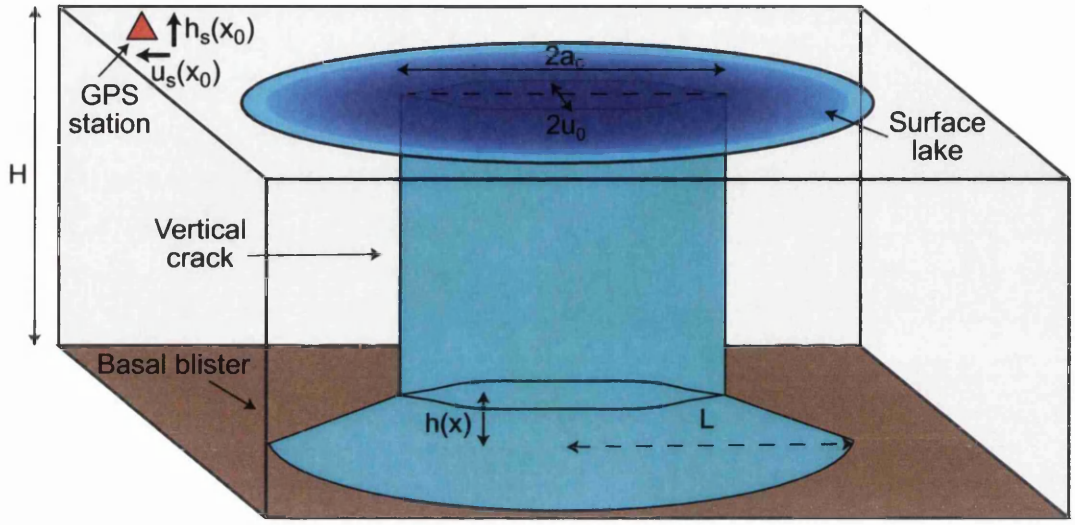

Figure 5.1: *Schematic of the blister model including illustrations of key variables for the vertical crack, basal blister and surface displacement.*

Tsai and Rice (2010) presented three variations of the blister model for examining the growth of a turbulent basal water blister under a draining supraglacial lake. The first model is a uniform representation of plane-strain crack expansion that allows water flux along one dimension (x) with a total length, $2L$, and spatially- and temporally-varying uplift, $h(x)$. The second model is a radial generalisation of the plane-strain model that represents a fully circular blister flowing from a water input point; there is no preferential flow direction within the blister and conditions are assumed to be identical in all directions. The third model is similar to the second model but uses a clamped elastic plate in order to more realistically represent the expansion of the water blister when the radius is greater than the ice thickness. In the three models, the vertical crack expands horizontally relative to the growth of the blister and has a total length of $2a_c$. A spatially variable opening rate of the vertical crack is calculated perpendicular to the crack plane (u_0). Using the englacial opening calculation of u_0 and the basal uplift calculation of $h(x)$, the vertical (h_s) and horizontal (u_s) motion of a GPS station at a prescribed distance (X_0) from the water input point can be estimated for the duration of the drainage event. Other calculations in the water blister model include the frictional resistance in the vertical crack and the lake lowering rate as a result of volume loss to the englacial and subglacial cracks.

The openings created by englacial and basal water fluxes are described by Tsai and Rice (2010) as 'cracks' because they are calculated using fracture mechanics equations. The fracture toughness of ice, K_{IC}, is defined by a stress intensity factor, K_I, and the Young's modulus, E (with the latter defining the stiffness of an elastic material); these factors determine how much shear stress is necessary on the walls of the crack to cause further fracturing along a pre-existing flaw. As the water blister crack equations are adapted for an ice-bed interface, it is assumed that the margin of the blister is not frozen to the bed and therefore the fracture toughness is zero. Using this approach, the fracture equations can be used to describe the vertical stress exerted by turbulent water on the overlying ice that causes elastic uplift, whilst removing the need for physical fracturing at the boundary of the water blister. The uplift of the ice allows expansion of the gap between the ice and the bed and thus water can flow to greater radii along the bed.

There are various important assumptions of the water blister model that should be taken into account when analysing the outputs:

- The bed is assumed to be flat, based on the premise that the hydraulic potential gradient driven by the overpressured water in the vertical crack is likely greater than a gravitational hydraulic potential gradient.
- Water flows as a turbulent medium. The Reynolds number (that is associated with the level of turbulence) is calculated during blister propagation to determine that this assumption is appropriate.
- Water does not flow out of the domain. This assumption suggests that the water blister will continue to expand radially as long as overpressure exists within the vertical crack. In reality, it is likely that water is preferentially directed down-stream and that hydrological development and/or pre-existing hydrological systems remove some of the blister water.
- Water does not flow into a basal sediment layer but remains as a film or sheet between the substrate and the ice.
- Melting in either the englacial or basal crack is assumed to be minimal in relation to elastic expansion and is therefore not taken into account.
- The ice responds elastically to water injection. The latter is a reasonable approximation for stresses propagating on a short-time scale, such as that seen

during initial stages of a lake drainage event (Tsai and Rice, 2010). However, after several hours, the Maxwell relaxation time is reached and the ice begins to deform viscously, limiting the applicability of this model.

- The fracture energy is not taken into account. However, Tsai and Rice (2010) suggest that the energy loss over the pressure gradient is sufficiently significant that the fracture energy can be ignored.
- The pressure gradient is large enough that acceleration terms in the Navier-stokes equations can be ignored.
- The region where the vertical crack exists is not subject to compressional or extensional longitudinal stresses during the period of lake drainage.
- It is assumed that the ice is impermeable and no englacial conduits or subglacial fractures are present to modulate the flux of water from the lake.
- No water is present at the ice-bed interface prior to drainage of the lake.

5.2.1 *Model implementation*

The water blister model code with equations detailed in this section was written and supplied by V. C. Tsai, California Institute of Technology. Adaptation of the model for this thesis by the author is discussed in Section 5.4.

Fundamental crack equations

Fracture is envisaged to occur through an infinite elastic medium as a result of flux of turbulent water that causes plane-strain cracking (see Fig. 5.2). Plane-strain occurs in thick bodies and assumes that relative to the plane, normal strain and perpendicular shear strain are zero. With plane-strain, a crack will deform elastically followed by brittle fracture at the crack margin. However, as the fracture toughness is treated as zero in the equations described here because the ice is assumed to not be frozen to the bed, only elastic deformation is accounted for.

The fracture calculations are adapted for bimaterial case of ice overlying bedrock (or stiff till) by assuming a constant ratio between the calculated full homogeneous crack height (w) and the bimaterial subglacial crack height (h) of $h = \xi w$, where ξ is a constant coefficient of proportionality:

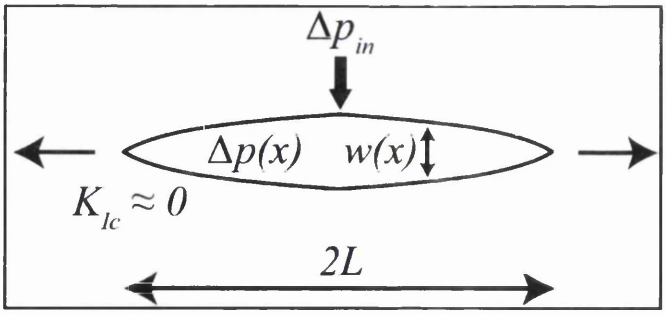

Figure 5.2: *Cross-section of a crack in an infinite homogeneous ice medium, opened by stress on the walls due to turbulent water flow. $K_{IC} = 0$ is the fracture toughness at the crack margin; this is 0 because the margin of the crack at the ice-bed interface is assumed to be unfrozen and therefore boundary fracturing is not necessary. L is the crack radius; $w(x)$ is the crack opening (w) as a function of distance from the crack centre (x); ΔP_{in} is the excess pressure necessary to open the crack; and $\Delta P(x)$ is the change in pressure as a function of distance from the crack centre.*

$$\xi \approx \frac{1 + (E'_{ice}/E'_{bed})}{2} \approx 0.55, \tag{5.1}$$

where $E' = E/(1-\nu^2)$, with ν the Poisson's ratio; the latter relates to the amount of stretching or compression of the ice due to the crack growth. As ice can be uplifted whereas the bed is assumed incompressible, the crack expands only upward from the bed and therefore the bimaterial subglacial crack height is almost half of the homogeneous crack height; the full mathematical justification for this choice of ξ is given in Appendix A of Tsai and Rice (2010).

The turbulent flow condition through the bimaterial crack is calculated from the Gauckler-Manning-Strickler model that allows approximation of the shear stress, τ, on channel walls due to turbulent water flow:

$$2\tau = \frac{f}{4}\rho_w U^2 = -h\frac{\partial P}{\partial x}, \tag{5.2}$$

where ρ_w is the water density, U is the vertically-averaged fluid velocity, and $\partial P/\partial x$ is the pressure gradient with x the horizontal distance along the crack. The Darcy-Weisbach friction factor, f is calculated with

$$f = \frac{8gn'^2}{R_H^{1/3}} = f_0\left(\frac{k}{h}\right)^{1/3}, \tag{5.3}$$

with g the acceleration due to gravity, n' Manning's roughness parameter, $R_H = h/2$ the hydraulic radius, k the Nikuradse channel roughness height and f_0 a frictional constant. Eq. 5.2 can then be rearranged for $\partial P/\partial x$:

$$-\frac{\partial P}{\partial x} = \frac{f_0}{4}\rho_w U^2 \frac{k^{1/3}}{h^{4/3}}. \tag{5.4}$$

Returning to the elliptical crack opening, the relationship between $w(x,t)$ and $P(x,t)$ is determined from elasticity theory:

$$\Delta P(x,t) = P(x,t) - P_i = \frac{E'_{ice}}{4\pi}\int_{-L}^{L} \frac{\partial w(y,t)}{\partial y}\frac{dy}{x-y}, \tag{5.5}$$

where t is the time, y is a dummy variable and L is the radius of the basal blister. Ice overburden pressure is P_i, and $P(x,t)$ is the water pressure (which will be above overburden as the lake is draining). Finally, to link $w(x,t)$ and $U(x,t)$, a mass conservation equation is applied:

$$\frac{\partial(wU)}{\partial x} + \frac{\partial w}{\partial t} = 0. \tag{5.6}$$

Self-similar analysis

Tsai and Rice (2010) use these equations as a basis to determine a steady-state blister model and then find exact solutions for the temporally and spatially varying blister model using non-dimensionalised self-similar analysis; these processes will not be described here, but for more information see Tsai and Rice (2010), section 2.5. Within the steady-state analysis, Tsai and Rice (2010) state that for the basal blister, $\Delta P(x,t) = P - P_i = 0$ in order to approximate a fracture mechanic state under static loading. As a result, the pressure driving the blister expansion will be the ice overburden pressure. Although this is not a realistic scenario, as the lake will create an overpressured system, the water input at overburden pressure will still cause basal uplift and blister propagation. The second assumption made within the steady-state analysis is that the elastic medium is infinite, whereas the free surface at the top of the ice will impact the model results when the blister radius exceeds a length equal to the ice thickness. The self-similar analysis by Tsai and Rice (2010) and the steady-state solution are used to determine the basal uplift, blister volume

and flux for a 2-D plane-strain case. Within this analysis, two constants (C_1 and C_2) are introduced to be applied to average uplift and blister radius equations, respectively; for values of these constants and other applied parameters see Table 5.1.

Vertical crack

The crack connecting the ice surface to the bed is modelled by Tsai and Rice (2010) as a plane-stress crack, which assumes that relative to the plane, normal stress and perpendicular shear stresses are zero. A plane-stress crack is used (instead of the plane-strain crack applied to the ice-bed interface) because the englacial ice is treated as a thin body with the ice as a free surface. The ice within the vicinity of the crack is assumed to be homogeneous and not subject to longitudinal stresses; incorporating such stresses into this model would require significantly more numerical analysis and computational power.

The horizontal length of the englacial crack is defined as $2a_c$ and the opening as $2u_0$ (see Fig. 5.1). High basal shear stresses out-with the radius of the basal blister would act to close the vertical crack and so suggests that $a_c < L$ (with L being the length of the blister radius, see Fig. 5.1). The vertical crack is opened horizontally ($2u_0$) by overpressure averaged by depth ($\Delta P_{avg} = \Delta P/2$); therefore the approximation is made that the crack opens at the same rate with depth, whereas in reality it is likely that both the pressure and the vertical crack width will vary between the ice surface and the bed. This average opening width of the vertical crack is given by

$$2\bar{u} = \frac{\pi \Delta P_{avg} a_c}{2E}. \tag{5.7}$$

This equation for vertical crack opening allows calculation of a flux rate into the basal blister, volume stored in the englacial system, and horizontal displacement during lake drainage.

3-D approximation

The equations described for blister growth using the self-similar analysis are only applicable to a 2-D plane-strain scenario. By assuming an identical radial geometry and homogeneous material, Tsai and Rice (2010) extrapolate the blister equations

to a 3-D penny-shaped basal crack. Assuming that $L < H$, where H is the ice thickness, the 3-D basal opening is described by

$$w^{3D}(R) = \frac{8\Delta PL}{\pi E'_{ice}}\sqrt{1-(R/L)^2}, \tag{5.8}$$

where R is the distance from the centre of the blister. The 2-D total blister length of $2L$ is therefore replaced by a blister area of πL^2. The 3-D blister is calculated with clamped edges so the average basal opening of the bimaterial blister is then

$$\bar{h}^{3D} = \xi w^{3D} = \frac{\xi}{\pi L^2}\int_0^L 2\pi R\bar{w}^{3D}(R)\,dR = \frac{16\xi\Delta PL}{3\pi E'_{ice}}. \tag{5.9}$$

Tsai and Rice (2010) then adapt the 3-D model for a blister of radius $L > H$, although they note that the free surface constitutes a complex boundary condition that is not fully represented with the simplifications that they present. The approach to deal with $L > H$ is to apply an elastic beam equation and radially extrapolate to represent an elastic plate. The average basal opening when applying an elastic plate with clamped edges and uniform loading is

$$\bar{h}^{P} = \frac{1}{16}\frac{\Delta PL}{E'_{ice}}\frac{L^3}{H^3}, \tag{5.10}$$

In order to apply the elastic plate to the average opening of a water blister, Tsai and Rice (2010) sum the equation for blister opening in ice where $L < H$ (Eq. 5.9) and for ice where $L > H$ (Eq. 5.10) thereby giving

$$\bar{h}^{S} = \frac{16\xi\Delta PL}{3\pi E'_{ice}}\left[1+\frac{3\pi}{256\xi}\frac{L^3}{H^3}\right]. \tag{5.11}$$

Vertical flux friction

One important consideration in the blister model is the modulation of englacial flow due to frictional resistance in the vertical crack. Frictional resistance will reduce the velocity of water that intersects the basal crack relative to the velocity of water that enters the vertical crack from the lake. In order to determine the effect of englacial friction, the loss in average water pressure as a result of vertical crack roughness is

calculated using the Manning-Strickler equation for turbulent flow shown in Eq. 5.4. In this equation, h (the basal uplift height) is replaced by $2\bar{u}$ (the width of the englacial crack opening, as expressed in Eq. 5.7), so that

$$(1-\chi)\Delta P = \frac{\frac{f_0}{4}\rho U_v^2 k^{1/3} H}{(\frac{\pi a_c \chi \Delta P}{2E})^{4/3}}, \tag{5.12}$$

where U_v is the vertical crack velocity and χ is a friction parameter. In the applied blister equations (see Section 5.2.2), ΔP is replaced by $\chi\Delta P$ where $0 \leq \chi \leq 1$. In order to maintain mass conservation, the total volume in the model is capped at the initial lake volume. Once the lake has emptied, the calculation of χ changes to determine friction in an emptying vertical crack. Thus, for a lake in the process of emptying, χ is

$$\chi = \frac{(\frac{a_c}{L})^{10/3}(\frac{L}{H})}{0.033(1+\frac{3\pi}{256\xi}\frac{L^3}{H^3})^{10/3} + (\frac{a_c}{L})^{10/3}(\frac{L}{H})}, \tag{5.13}$$

whereas once water is emptying from the vertical crack alone, χ_w is

$$\chi_w = \frac{EV_0}{\pi\Delta P L^3} \frac{L/H}{\frac{16\xi C_1(1-\nu^2)}{3\pi}(\frac{L}{H})(1+\frac{3\pi}{256\xi}\frac{L^3}{H^3}) + (\frac{a_c}{L})^2}, \tag{5.14}$$

where V_0 is the lake volume.

5.2.2 *Applied blister equations*

As it would be beneficial to determine the impacts of lake drainage on the hydrological system several kilometres downstream of the water input point, the blister model incorporating $L > H$ is applied in this thesis so that blister expansion can be determined beyond a radius equal to the ice thickness. The main equations are highlighted here; for clarity, the nomenclature below will be kept primarily the same as in Tsai and Rice (2010). These equations cannot be solved analytically and are therefore solved numerically in Matlab using the explicit Runge-Kutta `ode45` solver for differential equations. The time evolution of the blister length, L, is given by

$$\frac{\partial L}{\partial t} = C_2 \sqrt{\frac{\chi \Delta P}{\rho_w}} \left(\frac{\bar{h}^S}{L}\right)^{2/3} \left(\frac{L}{k}\right)^{1/6}. \tag{5.15}$$

The volume in the water blister, V_b, is calculated with

$$V_b = C_1 \pi L^2 \bar{h}^S. \tag{5.16}$$

The flow rate within the blister, Q_b, is calculated with

$$Q_b = \frac{dV_b}{dL} \left[C_2 \sqrt{\frac{\chi \Delta P}{\rho_w}} \left(\frac{\bar{h}^S}{L}\right)^{2/3} \left(\frac{L}{k}\right)^{1/6} \right]. \tag{5.17}$$

The volume in the vertical englacial crack, V_c, is given by

$$V_c = \frac{2\pi \chi \Delta P_{avg} a_c^2 H_w}{E}, \tag{5.18}$$

where H_w is the height of the water in the lake or vertical crack. The horizontal displacement is related to the elastic opening of the vertical crack, rather than due to melting from frictional heat generated by water flow, which has been ignored. Horizontal displacement due to flux in the vertical crack is calculated with

$$u_s(X_0) = \frac{2\chi \Delta P_{avg} a_c}{E} \left[\sqrt{1 + (X_0/a_c)^2} - \frac{X_0}{a_c} + \frac{1+\nu}{2} \frac{X_0}{a_c} \left(1 - \frac{X_0/a_c}{\sqrt{1 + (X_0/a_c)^2}} \right) \right], \tag{5.19}$$

where X_0 is the location on the ice surface where the displacement is calculated. The ice surface uplift, h_s, is given by

$$h_s(X_0) \approx \frac{H^3 \bar{h}^S}{\xi \pi^2 L^3} \int_{-1}^{1} \frac{\hat{w}(\hat{x})\, d\hat{x}}{[((\frac{x}{L}) - (\frac{X_0}{L}))^2 + (\frac{H}{L}^2)]^2}, \tag{5.20}$$

where variables with hats represent non-dimensionalised versions of the respective unhatted parameters. The change in the lake level is calculated using either a paraboloid lake geometry, or measured lake geometry (with the latter being an adaptation of the blister model by the author); the volume is then adjusted for mass loss to the englacial crack and basal water blister. Following lake drainage, the change of water height in the englacial crack is given by

$$H_w = \frac{H\rho_i}{\rho_w} + \frac{\rho_w - \rho_i}{\rho_w}\chi_w, \tag{5.21}$$

where χ_w is the friction in the englacial system as the water height approaches overburden. The Reynolds number, $\Re$, is calculated as

$$\Re = \frac{\rho_w Q_b}{\eta}\frac{\partial L}{\partial t}, \tag{5.22}$$

where η is the dynamic viscosity of water. In order for these equations to be applicable, $\Re$ should be $> 10^5$, suggesting turbulent water flux.

5.2.3 *Previous application*

Tsai and Rice (2010) applied their models to the Das lake drainage event, with the latter described in Section 2.3.3. Data from the Das drainage event used by Tsai and Rice (2010) as model inputs included the lake area, lake estimated volume and the ice thickness at the lake drainage site. The water blister model outputs were compared with records from a GPS station located ~1.7 km from the lake water input and the results are shown in Figure 5.3. Tsai and Rice (2010) found their blister models did not match the Das lake observations perfectly, with the recorded drainage rate occurring slower than that predicted by the water blister models. The recorded horizontal and vertical displacements were greater at the Das lake site than those predicted in any of the Tsai and Rice models. Tsai and Rice (2010) suggested that treatment of ice as elastic rather than visco-elastic might be an important factor in the mismatch between modelled output and the observations. However they suggested that the modelled and observed values agreed sufficiently closely that the blister model can be used as a valid approach for replicating subglacial conditions during lake drainage events.

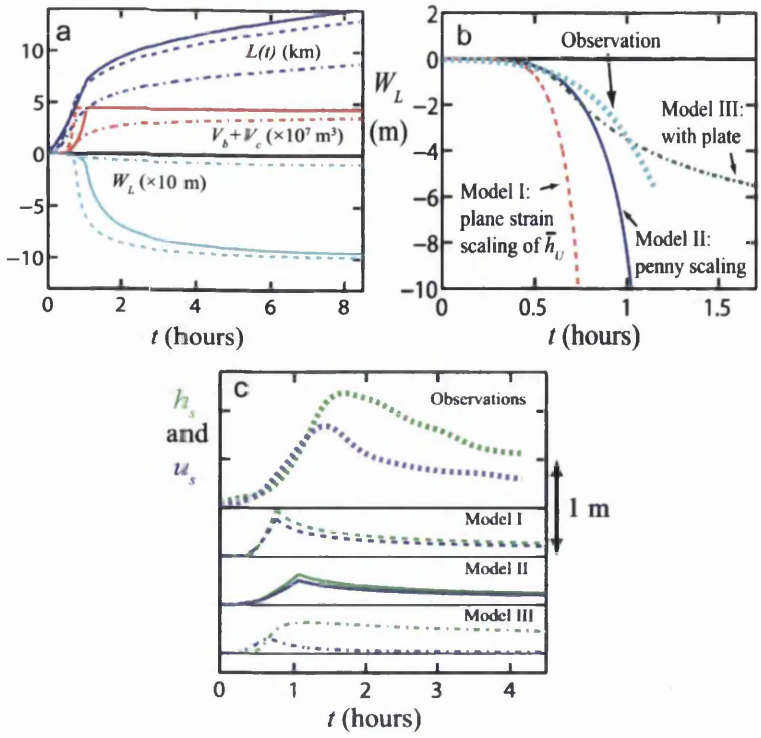

Figure 5.3: *Outputs from three Tsai and Rice models applied to the Das lake drainage event. Model I outputs refer to the steady-state approximation and are shown by the dashed lines; Model II is the 3-D model for $L < H$ and is shown by the solid lines; and Model III is the 3-D model for $L > H$ and is shown by the dashed-dotted lines. a) Basal blister length ($L(t)$, blue curves), total volume ($V_b + V_c$, red curves) and water height (referred to as W_L byTsai and Rice (2010), cyan curves). b) The lake level height (W_L) compared to lake level observations discussed by Das* et al. *(2008). c) Vertical (h_s, green) and horizontal (u_s, blue) ice surface displacements compared to observations from Das lake (thick dotted curves). Adapted from Tsai and Rice (2010).*

5.2.4 *Limitations*

The Tsai and Rice (2010) models are a novel way to approach rapid drainage events; however, they are not without limitations. For the purpose of establishing subglacial hydrological characteristics and resulting ice dynamics during and after lake drainage, the water blister model can only contribute to establishing conditions within a short (several hour-long) time period. If allowed to run for longer time periods the modelled radius of the water blister continues to expand considerably further than would be expected in a subglacial system. The assumption is that no topography exists at the bed of the ice and therefore the blister can continue to expand essentially indefinitely, although becoming thinner and thinner over time once

the lake drainage has ceased. For example, the blister radius modelled for the Das lake drainage reached ~15 km before the model run ceased (see Fig. 5.3 a), which is almost halfway to the ice margin from the location of the lake (68.72°N, 49.50°W). Recent availability of NASA Operation IceBridge radar data collected from airborne surveys over Western Greenland (Bamber *et al.*, 2013) has given greater insight into the characteristics of the subglacial topography of the GrIS. Both the IceBridge data and the deep-look radar from the case-study F-Lake in RGC (see Section 3.3) indicate that basal topography is highly variable and it is very unlikely that a water blister could flow both uniformally and radially for more than several kilometres. In addition, in many places in Greenland, gravitational hydraulic potential gradients will drive water flow in a preferential direction. As a result, application of a uniform water blister is only realistic for the initial stages of water input into the basal system.

There is also no provision for either a pre-existing drainage system or the siphoning of water from the blister downstream that might contribute to development of subglacial hydrological systems. However, in the region of the case site study area and in other inland areas of the GrIS, the surface slopes are gentle (~-0.35 °) and therefore provide little driving force for downstream water flux (with surface slopes significantly more influential for geometric hydraulic potential gradients than basal topography). It is therefore possible that the initial blister dynamics override the existing drainage system and hydraulic potential gradients, and it is only once the water overpressure approaches overburden that local potential gradients influence the water flux.

Tsai and Rice (2010) noted various drawbacks of the blister models. Model 3 (applied in this study) is based on self-similar analysis for $L < H$ and an infinite elastic medium; therefore the outputs for $L > H$ might be unrealistic as the free surface at the top of the ice will impact the pressure approximation when the blister radius exceeds a length equal to the ice thickness. Although the free surface might cause problems for analysing uplift rates at radii of $L > H$ because the 2-D solution to uplift is an upper bound, if X_0 is within (or at least near) a horizontal distance less or equal to H, the calculated uplift rate should be realistic. However, because the models use an extrapolated 2-D estimation of surface displacement converted to 3-D to gain volumes of a radial blister, the results are likely not fully applicable to reality. Also, no melting and freezing is taken into account, although Tsai and Rice (2010) calculate that the average melt rate due to turbulent heating would be ~1 mm hr^{-1} and therefore can be discounted.

The horizontal growth rate of the englacial crack radius, a_c, in relation to the basal blister radius, L, is a limitation within the model as it suggests that a_c could be as large as L at all times during the drainage event. It is assumed that outside the blister radius the basal shear stress will rapidly close a_c; however, given that basal blister radii of up to 15 km were calculated for the Das lake drainage, it is unreasonable to suggest that an equivalent horizontal crack of 24–30 km was also formed (assuming $0.8 < a_c < 1$) from the centre of the lake.

In the self-similar analysis of Tsai and Rice (2010) it becomes apparent that the pressure at the fracture tip is significantly below overburden in order to balance the overpressure at the input point within the basal crack. Although this is necessary within the mathematical formulation, it is not envisaged to accurately represent the conditions at the margin of the water blister in reality, as the presence of a pre-existing drainage network out-with the blister radius would likely be at or near overburden and therefore underpressure at a blister margin would rapidly be re-pressurised. However, this formulation is not believed to strongly impact the analysis in this thesis and it is assumed for model linking purposes that the pressure at the margin of the blister is at overburden.

5.2.5 *Blister model summary*

The blister model uses equations developed by Tsai and Rice (2010) to determine growth of a radial turbulent water sheet between the ice and the substrate during a lake drainage event. Limitations of the model include difficulty in applying equations to blister radii greater than the ice thickness (due to the presence of a free surface), the assumption that no water pre-exists at the ice-bed interface, and the problem of variable basal topography. Another important limitation is the inability of the model to allow downstream subglacial hydrological development (such as channel formation) that might modulate the growth of the blister. However, Tsai and Rice (2010) applied their model to the Das lake drainage and found model outputs and observations agreed within an order of magnitude; this suggests that the blister model is a useful tool for analysing basal hydrological development during a rapid overpressurised lake drainage event.

5.3 Flowband model

The flowband model is introduced in this section. The model implementation is detailed, including the pertinent equations. This is followed by a discussion of treatment of boundary conditions. The previous application of this model by Pimentel and Flowers (2011) and the limitations of the flowband model are then discussed.

The Pimentel and Flowers (2011) flowband model is a coupled hydrological model incorporating distributed and efficient water flow components. The flowband model is based on hydrological equations discussed by Clarke (2003), in turn adapted from the Spring and Hutter (1982) approach. Both Spring and Hutter (1982) and Clarke (2003) use the Nye (1976) equations introduced in Section 4.2, to analyse glacial lake outburst hydrographs whilst also taking account of frictional heating of the water. These equations have since been incorporated into a coupled fast and slow drainage configuration by Flowers *et al.* (2004) and Flowers (2008) and are the basis for the flowband model discussed here. For more information about coupled hydrological models see Section 2.4.4.

The flowband model is based on a 1-D flowline configuration extrapolated to 2-D with a fixed width throughout the entire domain. The distributed system consists of a water sheet with thickness averaged across the width of the flowband but spatially variable downstream, and a fixed hydraulic conductivity. As such, it represents a simplified version of a linked-cavity system or a sediment-based drainage system. The efficient system is based on the standard conduit equations for a semi-circular channel overlying a hard bed discussed by Clarke (2003). The semi-circular conduit grows by viscous dissipation of heat that melts the surrounding ice, offset by creep driven by the weight of the overlying ice.

5.3.1 *Model implementation*

The flowband model code and the equations detailed in this section were supplied by S. Pimentel, Simon Fraser University. Adaptation of the model for this thesis by the author is discussed in Section 5.4. The flowband model has a fixed finite-difference domain geometry with downstream temporal evolution but static lateral conditions. The model is discretised with staggered grid nodes in order that scalar variables are calculated within each grid-cell but vectors are calculated across the cells (see e.g. Flowers and Clarke, 2002). Two water flow components are included and coupled in

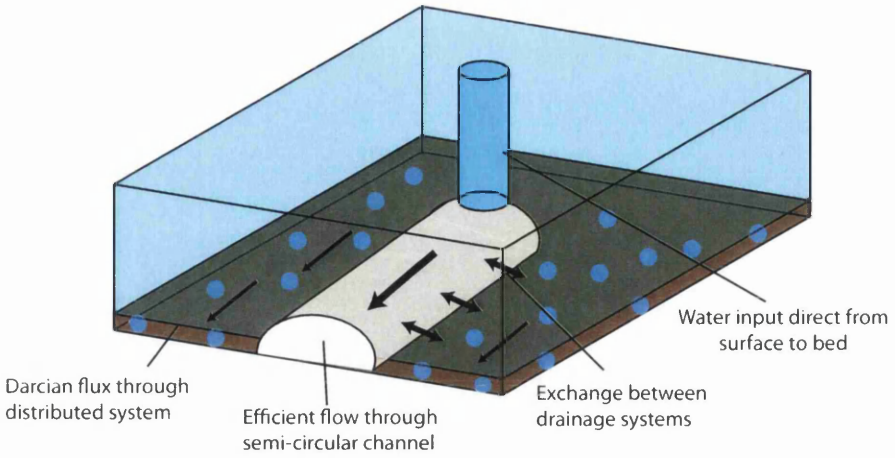

Figure 5.4: *Schematic of the flowband model showing a linked inefficient (in this case, sediment-based) system and channelised system.*

the flowband model: 1) a distributed sheet of water and 2) temporally and spatially evolving conduits (see Fig. 5.4 for a schematic of the flowband configuration). The conservation of mass in the water sheet is given by

$$\frac{\partial h^{sh}}{\partial t} + \frac{\partial q^{sh}}{\partial x} = \frac{Q_G + u_b \tau_b}{\rho_i L_f} + \dot{b}^{sh}, \tag{5.23}$$

where h^{sh} is the thickness of the water sheet, q^{sh} is the vertically integrated water flux through the sheet, Q_G is the geothermal heat flux, L_f is the latent heat of fusion, u_b is the basal sliding velocity, τ_b is the basal drag, $\dot{b}^{sh}$ is the source term for the sheet (directly from surface melt and ignoring englacial transport), x is distance in the downflow direction and t is time. Flux through the flowband model is described by the Darcian flow equation

$$q^{sh} = -\frac{K h^{sh}}{\rho_w g} \frac{\partial \psi}{\partial x}, \tag{5.24}$$

where K is the hydraulic conductivity, g is the gravitational acceleration and ρ_w is the density of water. The value of K determines whether the distributed system acts more akin to a sediment interface with flux through pores (lower hydraulic conductivity) or more like a linked cavity system (higher hydraulic conductivity). The gradient of hydraulic potential ($\partial \psi / \partial x$) is calculated in the same manner as described in Section 4.2:

$$\frac{\partial \psi}{\partial x} = \Delta P_w + \rho_w g \Delta b, \tag{5.25}$$

where b is the bed elevation and P_w is the water pressure. The sheet water pressure calculation is based on an empirical formula developed originally for Trapridge Glacier (see Flowers and Clarke, 2002):

$$P_w^{sh} = P_i \left(\frac{h^{sh}}{h_c^{sh}} \right)^{7/2}, \tag{5.26}$$

where h_c^{sh} is the critical water sheet thickness. The critical water sheet thickness is a width-averaged water thickness that either represents water within cavities or water in a porous medium across the flowband dependent on the prescribed hydraulic conductivity; when the critical sheet thickness is reached, the water pressure, P_w^{sh}, is equal to the ice overburden, $P_i = \rho_i g H$, where ρ_i is the density of ice and H is the ice thickness.

Conduits are described in a similar way to those in Section 4.2, although here, thermal exchange between the water and the ice walls is incorporated into the equations. Discharge through a semi-circular R-channel is described by

$$Q^c = -\left(\frac{8}{P_{wet} \rho_w f} \right) S^{3/2} \left(\frac{\partial \psi}{\partial x} \right)^{1/2}, \tag{5.27}$$

where S is the cross-sectional area of the conduit, $P_{wet} = (\pi + 2)r$ is the wetted perimeter (with r the conduit radius), $f = (8gn'^2)/R_H^{1/3}$ is the Darcy-Weisbach friction factor with n' representing the Manning roughness parameter and $R_H = \pi r/(2\pi + 4)$ is the hydraulic radius for a semi-circle. Although it uses different notation, Eq. 5.27 is the same as Eq. 4.7 in Chapter 4. The development of the conduit cross-sectional area, S, is described by

$$\frac{\partial S}{\partial t} = -\frac{Q^c}{\rho_i L_f} \left(\frac{\partial \psi}{\partial x} - c_p \rho_w C_w \frac{\partial P_w^c}{\partial x} \right) - 2AS \left(\frac{P_i - P_w^c}{n} \right)^n, \tag{5.28}$$

where c_p is the specific heat capacity of water, C_w is the Clausius-Clapeyron gradient, A and n are parameters in Glen's flow law, and P_w^c is the water pressure in the conduit. The conduit pressure is determined by

$$\frac{\partial P_w^c}{\partial t} = -\frac{1}{\lambda S}\left[\frac{\partial S}{\partial t} + \frac{\partial Q^c}{\partial x} + \frac{Q^c}{\rho_w L_f}\left(\frac{\partial \psi}{\partial x} - c_p \rho_w C_w \frac{\partial P_w^c}{\partial x}\right) - d_c\left(\dot{b}^c - \phi^{sh:c}\right)\right], \quad (5.29)$$

where λ is an artificial parameter to overcome model stiffness (see Clarke, 2003), d_c is the lateral conduit spacing within the domain, $\dot{b}^c$ is the water source term to the conduit and $\phi^{sh:c}$ is the exchange between the conduit and the sheet given by

$$\phi^{sh:c} = X^{sh:c}\frac{K h^{sh:c}}{\rho_w g d_c^2}(P_w^{sh} - P_w^c), \quad (5.30)$$

where $X^{sh:c}$ is an exchange coefficient and $h^{sh:c}$ is the water sheet thickness determined from Eq. 5.26, with the pressure in the latter equation determined by the maximum pressure for that node in either the conduit or the sheet. The final partial differential equation is for the temporal change in water sheet height given by

$$\frac{\partial h^{sh}}{\partial t} = -\frac{\partial q^{sh}}{\partial x} + \frac{Q_G}{\rho_i L_f} + \dot{b}^{sh} - \phi^{sh:c}. \quad (5.31)$$

The basal sliding u_b and basal drag τ_b that were included in Eq. 5.23 have been ignored in Eq. 5.31 as these terms are not calculated within this model; it is therefore assumed that the effect of these ice dynamic parameters are negligible in comparison to viscous dissipation of heat from the water.

5.3.2 *Boundary conditions*

The flowband boundary conditions depend on the application of the model. The upstream boundary conditions consist of a prescribed background flux into the conduit system and a calculated background flux into the sheet ($Q_G/\rho_i L_f$, in Eq. 5.31). There is also a source term to the conduit ($\dot{b}^c$) and/or the sheet ($\dot{b}^{sh}$) that was used by Pimentel and Flowers (2011) to input the lake drainage water into the model. If the flowband domain ends at either the ice margin or in tidewater, the outlet boundary pressure condition for P_w^{sh} and P_w^c can be defined as atmospheric or as the ocean water pressure, respectively. The conduit cross-sectional area is defined as a zero-gradient at the boundary. The outlet boundary condition for the sheet water thickness is given by

$$h^{sh} = h_c^{sh} \left(\frac{P_w^{sh}}{P_i} \right)^{2/7} . \tag{5.32}$$

Eq. 5.32 is determined by rearranging Eq. 5.26 for sheet thickness, h^{sh}. This condition means that the outlet sheet thickness should approximately equal the critical sheet thickness, h_c^{sh} that is envisaged to exist when basal pressures are at overburden. Such a configuration is applicable for model runs with a domain ending within the ice that could be expected to have an overburden pressure boundary condition. However, if the boundary is atmospheric or less than overburden, this water sheet thickness boundary condition might be unrealistic, although necessary for model stability.

5.3.3 *Previous application*

In common with the Tsai and Rice (2010) model, Pimentel and Flowers (2011) applied the flowband model to the Das lake drainage (described in Section 2.3.3). They used records from the Das lake drainage as inputs in the flowband model including: a) a sinusoidal drainage rate estimated from the surface area of the lake and the lowering rate of the water level recorded during drainage, and b) the ice thickness at the lake input point. As the basal topography was not known in the region, Pimentel and Flowers (2011) estimated a profile with ice thickness decreasing from 1200 to 500 m over a distance of 50 km and terminating in the ocean; this topography involved a horizontal bed and a parabolic surface slope (see Fig. 2b, Pimentel and Flowers, 2011). They input the water where the ice is 980 m thick in accordance with the ice thickness at the Das lake site. Pimentel and Flowers (2011) tested the flux boundary condition at the upstream end of the domain at levels of $Q_b^c = 0$, 10 and $100\,\mathrm{m^3\,s^{-1}}$ to recreate conditions with no pre-developed conduits and increasingly developed subglacial hydrological networks respectively.

The choice of parameters in the flowband model affects, for example, the transition between efficient and inefficient drainage. Parameter choices for application of the model in this thesis are discussed in greater detail in Section 6.4. However, it should be noted that the subglacial sheet transmissivity, in other words the capacity of the inefficient system, is a product of both the hydraulic conductivity, K and the sheet thickness, h^{sh}. The approach of Pimentel and Flowers (2011) was to maintain the hydraulic conductivity as a static value of $0.1\,\mathrm{m\,s^{-1}}$ and instead change the critical

thickness of the sheet, h_c^{sh}, for different model tests. For example, in an Alpine situation, h_c^{sh}, was set as 0.15 m but for the Greenland lake drainage tests it was set as 5 m. The latter value was deemed necessary to compensate for the high pressures that were output during the tests.

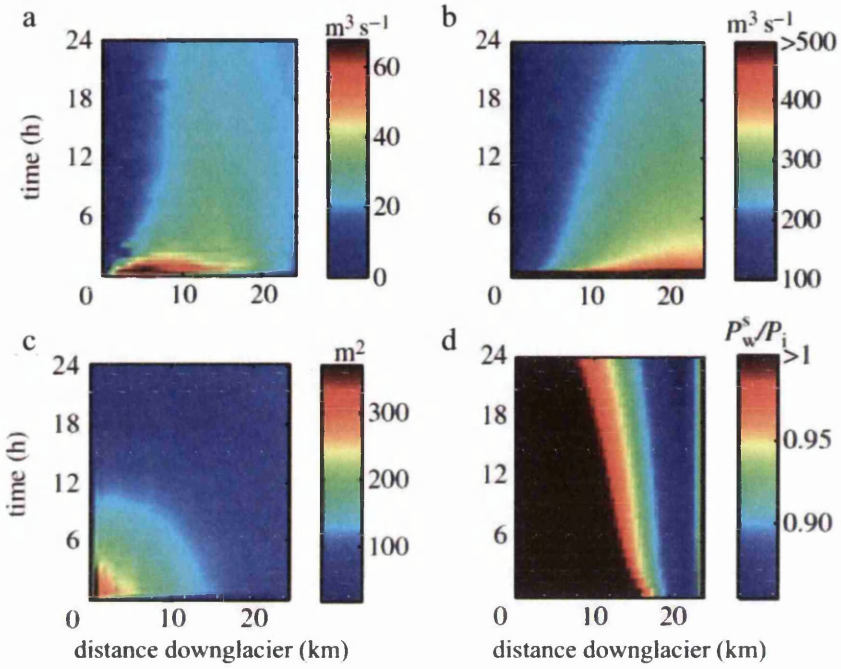

Figure 5.5: *Outputs from application of the flowband model to the Das lake drainage event, assuming a pre-existing channel of 22 m²: a) subglacial sheet discharge, b) conduit discharge, c) conduit cross-sectional area and d) subglacial water pressure as a percentage of overburden. From Pimentel and Flowers (2011).*

The results from the application of the flowband model by Pimentel and Flowers (2011) to the Das lake drainage are shown in Figure 5.5. When they applied the flowband model with only a distributed system the water pressure spiked up to 8 × overburden and took up to 9 days to settle below flotation. Including a small vestigial channel in the steady-state spin-up runs (of 10^{-3} m^2) still produced pressures above overburden with a long settling time. Noting that the Das lake drainage appeared, from surface GPS records, to have a dynamic impact for less than one day, Pimentel and Flowers (2011) agreed with Das *et al.* (2008) that a pre-existing drainage system was likely to have been in place. The best match to the Das data was achieved when Pimentel and Flowers (2011) introduced a background flux of 100 m^3 s^{-1} into the spin-up runs, growing a pre-existing steady-state channel of 22 m^2. The results shown in Figure 5.5 were output using this large background flux scenario. As shown in Figure 5.5 c, during lake drainage the pre-existing channel grew to >300 m^2 cross-

sectional area. Despite this, approximately 8 km of the upstream end of the domain remained above flotation level 24 hours after the lake drainage event (Fig. 5.5 d). During the first hour of lake drainage, the flux through the conduit was. to some unstated extent, greater than, $500\,m^3\,s^{-1}$ (Fig. 5.5 b).

5.3.4 *Limitations*

The flowband model involves several assumptions that are important to note when applying the model to a rapid lake drainage event:

- No lateral flow is possible outside the fixed-width domain of the flowband. Any flux into the system from a moulin or connecting englacial crack is forced downstream and not allowed to flow laterally or radially.
- Hydrological processes are integrated across the fixed width so that it is assumed that topography, hydraulic potential, hydraulic conductivity and the related water flux and pressure within the sheet do not vary across the flowband.
- Water is input directly from the ice surface to the bed. There is no modulation from englacial flow, either frictionally or elastically. A lake drainage event has very high discharge rates from the base of the lake into the ice subsurface; in the flowband model this discharge is all forced into the subglacial domain without accounting for englacial modulation of the water flux.
- It is assumed that hydraulic conductivity in the distributed system is uniform.
- An exchange parameter was developed by Flowers *et al.* (2004) for flux between conduits and a distributed water sheet in order to analyse Icelandic jökulhlaups; this parameter was applied to the Pimentel and Flowers (2011) model. A lake drainage event is similar in character to a jökulhlaup and therefore the exchange parameter is likely applicable. However, a lack of in-situ data precludes testing the applicability of the exchange parameter.
- An empirical water sheet pressure parameter was developed by Flowers (2000) and published in Flowers and Clarke (2002) for application of a distributed flux model to Trapridge Glacier, Yukon Territory, Canada. It is not clear that this empirical pressure value is applicable to anywhere other than Trapridge

Glacier, particularly since the GrIS is very different in character. However, few alternatives have been suggested and limited in-situ datasets are available to test the parameters. As a result, the empirical value continues to be used although it is adapted by the author for overpressured situations as described in Section 5.4.4.

- Supercooling-induced freezing on reverse bedrock slopes is not taken into account within the flowband model and therefore lowering of the hydraulic conductivity of either the sheet or the channels as a result of uphill flow is not taken into account (see Section 3.3.2). However, supercooling freeze-on is not currently incorporated into any kilometre-scale hydrology models and is therefore an area for future research, although not possible within the scope of this thesis.

- The flowband model is configured for semi-circular channels melted up into the ice and assumed to overlie a bedrock boundary. It is likely that sediment underlies the GrIS (Booth *et al.*, 2012; Dow *et al.*, 2013) and therefore incorporating sediment canals would be advantageous. However the equations for canals have not been adapted for non-steady state application and is again an area for future research.

5.3.5 *Flowband summary*

The flowband model presented by Pimentel and Flowers (2011) combines channelised and distributed drainage configurations in a fixed-width domain. Pimentel and Flowers (2011) applied this flowband model to the Das lake drainage event. They found that a pre-existing channel of $22\,m^2$ (developed from a background boundary flux of $100\,m^3\,s^{-1}$) along with an aerially-averaged sheet thickness of 5 m were necessary in the model to recreate realistic pressures in the flowband. It is not clear that these model conditions are applicable to the GrIS. The limitations of the flowband model include input of the lake drainage water directly to the bed as a flux condition with no englacial modulation, and also a lack of radial and lateral flow (all water is directed downstream from the input point). It is likely that these limitations of the model caused the excessive pressures reported by Pimentel and Flowers (2011) during the simulated lake drainage event rather than the results being indicative of conditions in the subglacial hydrological system. As a result, the flowband model cannot be applied alone for analysing lake drainage events. However, the coupled

efficient and inefficient drainage model is highly applicable for assessing downstream development of basal drainage systems once a surface-to-bed connection has been made following a lake drainage event.

5.4 Model linkage

Two different modelling approaches that replicate subglacial hydrological development during rapid lake drainage events have been introduced in this chapter. As noted in Sections 5.2.4 and 5.3.4, both models have limitations. To summarise, the water blister model is limited because 1) there is no possibility for drainage development that might remove water downstream from the blister and reduce the rate of growth, 2) it is assumed that no water pre-exists at the ice-bed interface and 3) the free surface likely makes model outputs unrealistic at radii greater than the ice thickness. The flowband model is limited because 1) the lake drainage rate is used as a water flux boundary condition and is therefore a driver of flow in the model rather than the inverse where the drainage rate is controlled by the conditions at the bed; thus no englacial modulation of flow is taken into account and 2) no radial or lateral flux is allowed within the model and therefore all of the water from a lake drainage event is forced downstream.

The approach in this thesis is to overcome the greatest limitations of the water blister model and the flowband model by coupling them together. As discussed in detail in this section, the drainage of the lake causes growth of a radial water blister that simultaneously drives the hydrological development in the flowband (Fig. 5.6). As a result, the modulation by englacial flow through the fracture and radial flux are both accounted for. Once all the water has drained from the lake, the characteristics of the blister are used as initial conditions in the flowband so that longer-term seasonal development as a results of diurnal water inputs to the bed can be determined.

5.4.1 *Model implementation*

Four model geometries with a grid-step of 100 m are constructed for this thesis. Details of these domains and the choice of grid-step are given in Section 6.3.1. The constants used in the coupled hydrological model are shown in Table 5.1. For each model run there are four sequential stages that are described in greater detail below

Table 5.1: *Coupled hydrological model constants.*

Symbol	Description	Value	Units
C_1	Uplift scaling factor	0.592	dimensionless
C_2	Velocity scaling factor	3.571	dimensionless
c_p	Specific heat capacity of water	4.22×10^{3}	J kg^{-1} K^{-1}
C_w	Clausius-Clapeyron gradient	9.8×10^{-8}	K Pa^{-1}
f_0	Darcy-Weisbach friction parameter	0.143	s $m^{-1/3}$
g	Acceleration due to gravity	9.81	m s^{-2}
L_f	Latent heat of fusion	3.35×10^{5}	J kg^{-1}
n	Glen's flow law exponent	3	dimensionless
Q_G	Geothermal heat flux	0.07	W m^{-2}
$X^{s:c}$	sheet-conduit coupling coefficient	0.1	dimensionless
γ	Numerical compressibility parameter	10^{-9}	Pa^{-1}
η	Dynamic viscosity of water	1.78×10^{-3}	Pa s^{-1}
ν	Poisson's ratio	0.3	dimensionless
ρ_w	Density of water	1000	kg m^{-3}
ρ_i	Density of ice	920	kg m^{-3}
ξ	Ratio of h to w	0.55	dimensionless

but can be summarised as:

Stage 1. The flowband model is run to steady state to represent a pre-existing distributed system at equilibrium. Final outputs from the spin-up steady-state system are used as initial conditions for the flowband in stage 2.

Stage 2. The water blister model is run and linked to the flowband model so that the blister a) incorporates flowband water that it overlaps and b) loses water from the blister boundary that is removed by flux through the flowband. This linked configuration is continued until the lake is empty, so that water is entirely within the englacial and subglacial system.

Stage 3. The characteristics of the blister at the final time-step in stage 2 are treated as initial conditions in the flowband so that, in the area of the flowband domain where the blister has overlapped, the pressure and water thickness is determined by the blister water reservoir. With these initial conditions, the flowband model is run for either a) 40 hours (i.e. the maximum time of overpressure suggested by surface GPS records) or b) when pressures at the water input point in the flowband domain reach overburden.

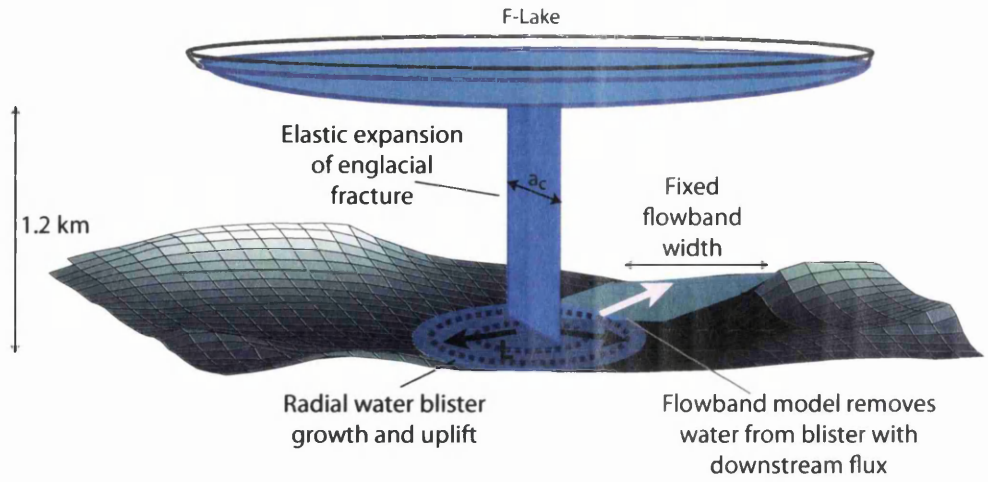

Figure 5.6: *Schematic of the linking process between the blister model and the flowband model using the case-study F-Lake basal topography as an example.*

Stage 4. After the water pressure from the lake drainage event has dissipated, the flowband model is run with surface water inputs for 30 days to examine the longer-term subglacial hydrological development.

These models are run with a series of sensitivity tests that are described in Section 6.4, with the aim to a) determine whether substantial efficient channels can form during rapid lake drainage events in Greenland and b) examine the likely seasonal hydrological development following the surface-to-bed connection made as a result of the lake drainage. Details of each model process are given below.

5.4.2 *Steady-state system (stage 1)*

The steady-state flowband model uses the equations described in Section 5.3.1 to determine an equilibrium pressure state and water sheet thickness for a stable system prior to lake drainage. The spin-up model is run with a background flux of $\geq 0.001\,\mathrm{m^3\,s^{-1}}$ because, with no flux, the model becomes unstable; in some model runs greater background fluxes were necessary for model stability and are detailed in Table A.1. The spin-up model is run for between 20 and 130 days (with the time for each spin-up model run also noted in Table A.1, italicised in brackets); the system is determined to be at equilibrium when temporal convergence of the water sheet pressure, conduit water pressure and water sheet thickness occurs. Convergence is deemed satisfactory with a temporal water sheet pressure variation of $\leq 1\times10^{-4}\,\mathrm{Pa}$.

The final model domain values for water sheet thickness, sheet pressure, conduit pressure and conduit cross-sectional area are saved.

The spin-up model is run for every sensitivity test so that altered parameters such as sheet hydraulic conductivity and sheet thickness are taken into account. The Matlab implicit `ode15s` solver, used for stiff partial differential equations, is here set with a relative tolerance of 1×10^{-6} and an absolute tolerance of 1×10^{-8}. The spin-up time-step is five minutes (see Fig. 5.7) and the steady-state model is run on a downstream mesh grid of 100 m. The sensitivity of the model time-step and grid-step are discussed in Section 6.3.

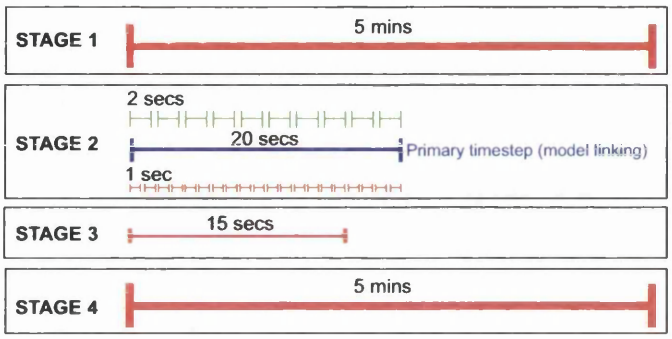

Figure 5.7: *Diagram of the time-steps used in the four stages of modelling. Red lines indicate the flowband model time-steps, the green lines illustrate the blister model time-steps, and the blue line shows the primary time-step when the blister and flowband models are linked.*

5.4.3 *Lake drainage (stage 2)*

For each linked model run, the water blister is allowed to expand to a threshold radius value equal to the size of one grid-step in the flowband model (i.e. 100 m), prior to linkage. Once this threshold is reached the blister model is linked to the flowband model. This linkage means that for every primary blister time-step, the flowband evolution is also calculated and a flux relationship between the two is determined.

Time-steps

A schematic of the blister and flowband time-steps is shown in Figure 5.7. The blister model is run at an internal time-step of two seconds. The partial differential

equations are solved with the explicit Runge-Kutta Matlab `ode45` solver with relative and absolute tolerances of 1×10^{-4}. Linkage between the blister and flowband models occurs every twenty seconds (referred to hereafter as the primary time-step). The linked flowband internal time-step is one second. These time-step choices are discussed as part of the sensitivity tests in Section 6.3.2. The flowband model is run with the same Matlab `ode15s` solver and tolerance as described for the spin-up model runs.

Model overlap

The flowband domain initially begins at the location where the vertical fracture from the lake reaches the bed. However, as the blister model grows, it 'overlaps' the flowband model domain. In order to conserve mass, the water in the part of the flowband domain that is overlapped by the blister is incorporated into the blister and therefore removed from the flowband. A schematic of the linking process and the model overlap is shown in Figure 5.8. The length of overlap between the two models is established by rounding the blister radius value to the nearest grid-step (i.e. 100 m). The volume of water in those overlapped grid-cells, V_f, is relative to the size of the blister radius, L, until the latter equals or exceeds the size of the flowband fixed width, W, so that,

$$V_f = \begin{cases} 2L\,\Delta x\,d_n \sum_{i=1}^{N_x} \left(h_i^{sh} + S_i\right) + V_r, & \text{if } 2L < W \\ W\,\Delta x\,d_n \sum_{i=1}^{N_x} \left(h_i^{sh} + S_i\right) + V_r, & \text{if } 2L > W, \end{cases} \tag{5.33}$$

where Δx is the size of one grid-step, d_n is the number of channels within the fixed width, N_x is the number of grid-cells overlapped by the blister, h^{sh} is the average water sheet thickness, S is the channel cross-sectional area and V_r is any volume overlapped as a result of blister growth over grid-cells from previous time-steps, as shown in Figure 5.9. V_r is defined as

$$V_r = \begin{cases} (W - 2L)\,\Delta x \sum_{i=1}^{N_x} h^{sh}_{(i,t_{p-j})}, & \text{if } 2L < W \\ 0, & \text{if } 2L > W, \end{cases} \tag{5.34}$$

where t_{p-j} is the primary time-step at which grid-cell i was originally overlapped.

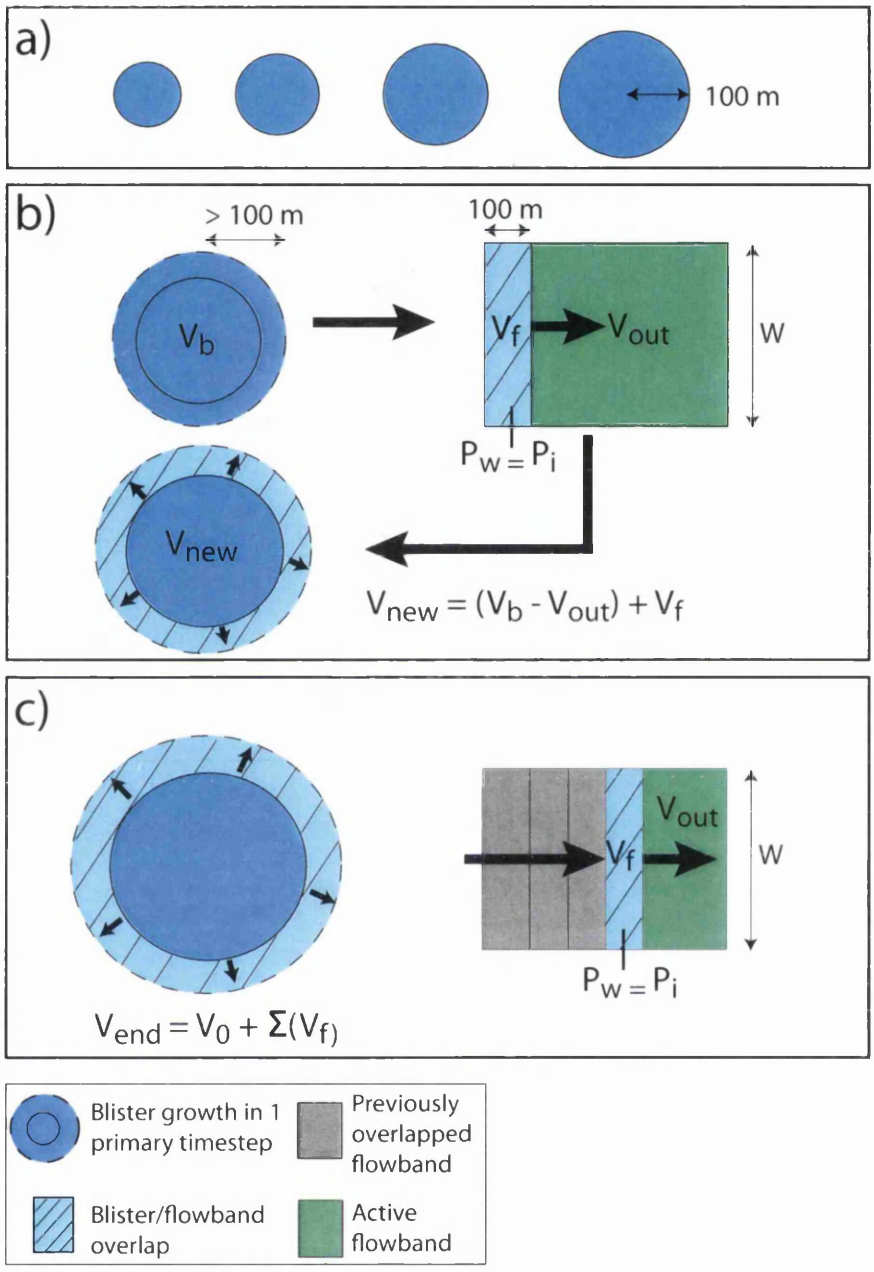

Figure 5.8: *Flow diagram of the linking process between the blister model and the flowband model. a) The blister grows in volume (V_b) until it reaches a threshold point equal to one flowband grid-step, in this case 100 m. b) The blister begins to overlap the flowband model, incorporating the water in the flowband domain (V_f); flux is removed from the boundary of the models (V_{out}), where the water pressure is equal to the ice overburden. The blister size is readjusted accordingly within the same time-step (V_{new}). c) The blister continues to grow, overlapping the flowband domain; growth ends when all of the lake water is either in the englacial crack or at the bed (V_{end}). W indicates the fixed flowband width.*

Because the blister is radial whereas the flowband has a rectangular geometry, the calculated overlap volume will be an overestimate of the downstream blister flux. However, the blister is expanding radially and is therefore also overlapping areas with pre-existing drainage upstream of the water input, which is here assumed to have a similar configuration to that downstream. Therefore, approximating the radial overlap within a rectangular shape necessary for interaction with the fixed-width flowband is a reasonable simplification. Although water is not likely in reality to expand equally in all directions it is beyond the scope of this study to address a scenario with a non-uniform expanding blister.

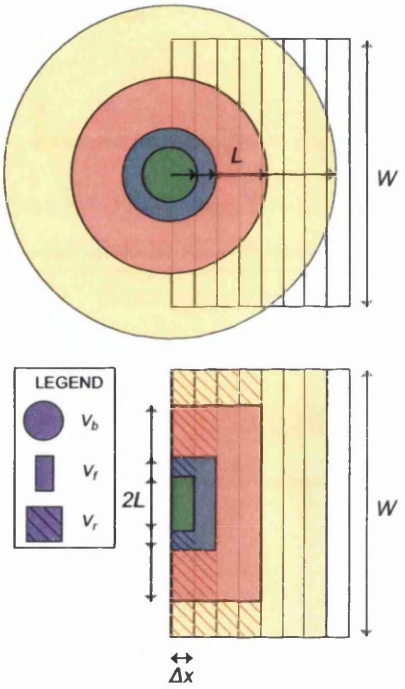

Figure 5.9: *Schematic of the volumes applied at different stages during the stage 2 modelling process. Each colour represents one primary time-step. The upper diagram shows the growth of the blister in relation to the flowband. The lower diagram shows the resulting approximation of the blister overlap into the fixed width domain of the flowband.*

The second impact of the overlap of the blister into the flowband domain is that for each primary time-step, the overlapped grid-cells are removed from the flowband domain. As a result, as the blister grows, the flowband domain shrinks (see grey cells in Fig. 5.8 c). This is a reasonable approximation as it is likely that the growth of the blister will overwhelm any pre-existing drainage system, particularly when dealing with a hard-bed drainage configuration. With the presence of sediment, the situation would be more complex and vertical fluxes into and out of the sediment

from the blister on the sediment surface would have to be calculated; including such a process within the modelling is beyond the scope of this study. It is also possible that, with the presence of large channels, water could be directed out of the water blister in a direction dictated by the lower hydraulic potential within the conduits. However, as the water blister model is currently configured in a static radial framework it is not possible to incorporate differential flow within the blister itself. As a result, any pre-existing channels that have developed where the blister overlaps the flowband are assumed to become overwhelmed by the blister water.

Flowband boundary conditions

The upstream boundary pressure condition for the stage 2 model in both the sheet and the conduit is defined as the ice overburden pressure. As discussed in the limitations of the blister model (Section 5.2.4), the blister pressure at the tip is calculated to be below overburden (to balance the overpressure at the water inlet); this would drive water from the flowband into the blister rather than the converse. However, as a pre-existing pressurised drainage system is present in the flowband it is assumed that the blister boundary pressure is instead at overburden.

For each primary time-step, the upstream flux boundary condition for both the conduit and the sheet at the new starting grid-cell are defined to be the flux at that grid-cell in the previous primary time-step (e.g. $Q_b^c(x, t_p) = Q^c(x, t_{p-1})$ for the conduit boundary flux). This approach allows the previous configuration of the hydrological system to continue to drive downstream development at the time of blister overlap rather than stipulating a static flux boundary condition.

Blister readjustment

Within each primary time-step, the length of the blister is adjusted to incorporate 1) the volume of water in the flowband that the blister overlaps, V_f, and 2) the flux removed from the blister by the flowband model as a result of downstream hydrological development, V_{out}. The former is described in Eq. 5.33 and the latter is

$$V_{out} = \begin{cases} t_p \, \Delta x \, L \, d_n \, (q_2^{sh} + Q_2^c) & \text{if } L(t_p) < W \\ t_p \, \Delta x \, W \, d_n \, (q_2^{sh} + Q_2^c) & \text{if } L(t_p) \geq W, \end{cases} \tag{5.35}$$

where t_p is the primary time-step, q_2^{sh} is the sheet flux out of grid-cell 2, and Q_2^c is the channel flux out of grid-cell 2. Within one primary time-step, the volume change within the blister is therefore $V_{new} = V_f - V_{out}$.

Because the blister model is based on elastic mechanics, the volume and length of a blister will always be the same for a certain rate of ice uplift in one region. As a result, by knowing the adjusted volume of the blister, the corresponding radius can be calculated within the same primary time-step. Once the new blister radius is established, the blister model can be used to calculate the corresponding characteristics of the blister domain including water level and volume in the lake or englacial crack, frictional resistance in the englacial crack, blister tip velocity, blister flux, Reynolds number for the blister flux, basal separation and surface displacement (both vertical and horizontal). Concurrently, the flowband model calculates conduit flux, cross-sectional area, hydraulic potential and water pressure; water sheet flux, water thickness, hydraulic potential and water pressure; and the exchange rate between the conduit and the water sheet.

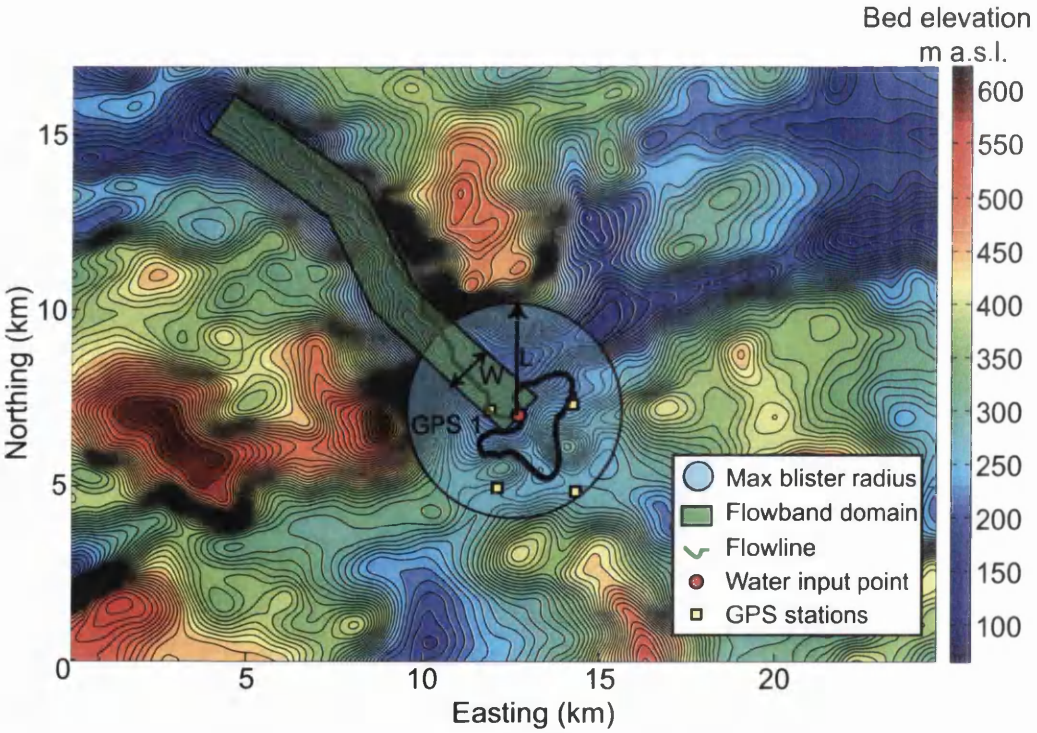

Figure 5.10: *Basal DEM of the region surrounding the case-study lake. The maximum radial extent of the blister model is indicated in blue and the fixed width of the flowband model shown in green. The flowline on which the flowband topography is based is shown by the green line. The lake water input point is indicated by the red dot.*

Cease linkage

One of the limitations of the water blister model is that it will continue to radially expand up to radii of 15-20 km before reaching equilibrium. As illustrated by the basal topography from the case-study lake site in Figure 5.10, the subglacial topography is not flat for a radius of 15 km around the lake water input point; indeed, extensive flat topography is unlikely to occur anywhere under the GrIS. As a result, it would be unrealistic to allow the blister to expand to radii much larger than allowed by the topography. The linked model is therefore stopped at the point when all lake water is either within the englacial fracture or in the subglacial system (in the blister or the flowband domain). This is a reasonable assumption because a) the flowband model is not capable of interacting directly with draining lake water and thus the blister model must be used to determine hydrological development during the period of lake drainage and b) the radius of the blister at the point where all water has drained from the lake is, in most sensitivity runs, ~3 km (see Tables C.1–C.4) which, as shown in Figure 5.10, is approximately the region surrounding the water input point where a blister could be expected to expand. This maximum blister region is defined by steep basal topography that causes very strong geometric hydraulic potential gradients, as shown in Figure 3.4, that would prevent further up-glacier blister flux. Before the blister reaches this topographic threshold at ~3 km radius, the assumption of a flat basal topography is reasonable.

At the point when all water has drained from the lake into the subsurface, various parameters are calculated from the blister model and used as inputs in the stage 3 model. These data are 1) the thickness of the blister calculated at 100 m intervals between the water input point and the margin of the blister, and 2) the water pressure at the input point which will be a function of the ice thickness when the lake water has fully drained so that $P_w = \rho_w g H$. In addition, the final calculations of water pressure, conduit cross-sectional area and water thickness from the remaining domain of the linked flowband model are saved for stage 3 model inputs.

5.4.4 *Short-term hydrological development (stage 3)*

The third stage of modelling uses the calculated blister as a water reservoir within the flowband model; the blister water is therefore added back into the flowband. As a result, the overpressure that still remains due to water in the connecting englacial

crack is used to drive flowband development. The stage 3 flowband domain is reinstated to its original length (necessary because, in stage 2, the flowband domain shrinks due to blister overlap).

Water thickness

The initial condition for flowband sheet water thickness (h^{sh}) is calculated from a) the blister water thickness over a distance equivalent to that overlapped in stage 2 and b) the water height from the remainder of the domain in the stage 2 flowband. The blister thickness approaches zero towards the radial margin; however, it is assumed that the edge of the blister represents overburden pressure due to the presence of a pre-existing drainage system. In the flowband, that overburden pressure is represented by the critical water thickness. As a result, the blister water thickness is adjusted so it approaches the critical water thickness at the radius margin as opposed to zero water thickness. The water height is then smoothed along the domain with a 30-point lowess (locally weighted scatterplot smoothing) filter in order to remove artificial jumps that might impact the hydraulic potential calculations in the flowband.

Channel cross-sectional area

The stage 3 initial channel size within the blister reservoir is assumed to be the same cross-sectional area as the channel at the blister radial margin (as no other channel size information is available from the flowband model); the remainder of the initial condition channel size is determined from the stage 2 flowband output.

Water pressure

Stage 3 of the flowband modelling is the first circumstance where the flowband water pressure will likely be above overburden due to the remaining water blister reservoir. The equation for sheet water height empirically calculated by Flowers and Clarke (2002) for Trapridge Glacier and used in the Pimentel and Flowers (2011) model is

$$P_w^{sh} = P_i \left(\frac{h^{sh}}{h_c^{sh}} \right)^{7/2} . \tag{5.36}$$

From the GPS measurements at the case-study site (see Section 3.6.1) and from the blister model it becomes apparent that subglacial water can temporarily exist at a thickness of tens of centimetres at the ice-bed interface, coincident with water pressures above overburden. Using Eq. 5.36 to examine this relationship between pressure and water thickness produces the following results: if the blister water thickness is 0.3 m and the critical water thickness (for water at overburden) is 0.15 m, the water pressure would be $11 \times P_i$. Given a maximum uplift of ~0.8 m at the case-study lake site, if this directly translates to water thickness at the bed, the pressure according to Eq. 5.36 would be $350 \times P_i$. Even if the critical water thickness is 0.5 m, a sheet thickness of 0.8 m would cause an excess of $5 \times P_i$. As a result, Eq. 5.36 appears to not be applicable for relating water thickness and pressure at times when water pressures are above overburden. In the flowband model, this equation is therefore replaced with one configured for the lake drainage scenario where

$$P_w^{sh} = P_i \left(\frac{h^{sh}}{h_c^{sh}} \right)^{1/13}, \text{ if } h^{sh} > h_c^{sh} \tag{5.37}$$

This equation is estimated using the relationship between the calculated blister water thickness at the input point and the known pressure when the water is at the ice surface (assuming a fully-vertical englacial crack). Using this equation, if the blister water thickness is 0.3 m and the critical water thickness (for water at overburden) is 0.15 m, the pressure would be $1.05 \times P_i$; and for a blister thickness of 0.8 m, P_w^{sh} $= 1.14 \times P_i$. Eq. 5.37 is applied only when $h^{sh} >, h_c^{sh}$; when $h^{sh} \leq h_c^{sh}$, Eq. 5.36 is instead applied. Although it is difficult to test the validity of Eq. 5.37, the pressures produced agree broadly with surface variability in the GPS uplift records at the case site (as demonstrated in Fig. 9.2) and the outputs are significantly more reasonable than those produced when applying Eq. 5.36 in situations of overpressure.

Model application

Following the time when the blister calculations cease and when all the lake water is within the subsurface, the flowband is allowed to adjust to the water reservoir without further manual adjustment. This is a simplification in that the blister water that radially expanded upstream and outside of the flowband fixed width is not explicitly forced into the flowband model. However, without being able to include lateral fluxes into the flowband or estimate the background flux from the

upstream blister water, this simplification is necessary. It is also likely that surface water inputs reach the bed through the englacial crack in the base of the lake: however it is assumed at this stage that no additional water is added to the blister reservoir in order that the impact of the lake drainage on hydrology development can be independently examined.

The time-step of the stage 3 flowband is 15 seconds. Calculations were performed using the Matlab `ode15s` solver with a relative tolerance of 1×10^{-6} and an absolute tolerance of 1×10^{-8}. The reservoir flowband model is run either for a) 40 hours following initial lake drainage, which is a fixed time criteria based on the maximum time that the GPS uplift at the case-study lake could be attributed to overpressured lake water; following this point diurnal variations are clear, associated with surface water input (which are incorporated in stage 4), or b) when the pressure at the flowband water inlet reaches overburden pressure, suggesting that the blister reservoir has diminished and that surface water inputs will now be important.

The pertinent final outputs that are saved for input into the stage 4 flowband model are the water pressure, the channel cross-sectional area and the water sheet thickness over the domain.

5.4.5 *Seasonal hydrological development (stage 4)*

The final stage of modelling is to determine the impact of diurnally-varying water inputs to the bed through the newly-opened moulin in the lake bed. The stage 4 flowband model is therefore run over a period of 30 days, with initial conditions determined from the outputs of the stage 3 flowband model. A surface water input is used as a boundary flux for the water sheet and it is therefore assumed that there is no modulation in water flow between the ice surface and the bed, following the approach of Pimentel and Flowers (2011) for application of the flowband model to valley glaciers.

Surface water input

The surface water input is determined from the melt calculations for the case-study lake described in Section 3.6.4. Although an approach similar to that described by Banwell *et al.* (2012), where surface flux and routing are modelled, would be

desirable to gain accurate input rates to the lake subsurface, it is beyond the scope of this thesis. Instead, the approach here is to use the 1-D model of melt rate, calculated for a site ~8.5 km from the case-study lake, and extrapolate it to the entire catchment.

The catchment size for the case-study lake is calculated using the watershed algorithm in ArcGIS applied to a Landsat elevationally-corrected image from August 18, 2010. This calculation gives a catchment size of ~14 km^2. Applying this catchment size to the runoff data provided by D. van As (GEUS) produces the time series of surface water input shown in Figure 5.11, which is then used as the diurnal water input into the lake.

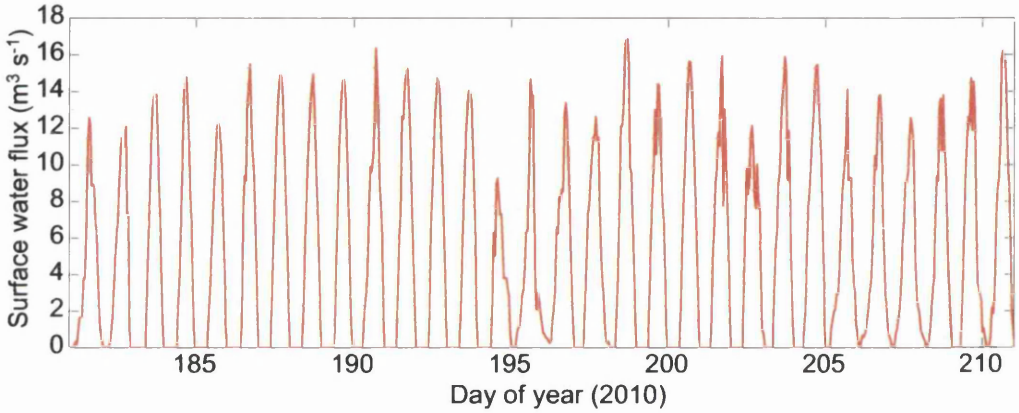

Figure 5.11: *Plot of surface water input into the subglacial system via the lake moulin. Water input is calculated by extrapolating modelled surface runoff over the lake catchment.*

The actual volume input into the lake moulin would involve flux delays over the catchment, different flux times through surface snow and in supraglacial rivers, and also differences in melt rate with increasing elevation. Therefore the surface water input rates are likely maximum values for the lake drainage site.

Model application

For each model run, surface melt input is initiated relative to the time since lake drainage (which differs depending on the stage 2 blister expansion time and the stage 3 flowband run time). The time-step for the stage 4 modelling is increased to be the same as the stage 1 spin-up model at five minute intervals. The same Matlab

`ode15s` configuration is used as described for the spin-up model.

5.4.6 *Coupled model advantages*

By applying the coupled model (stages 1–4), some of the limitations of the individual application of the water blister and flowband model are overcome. A pre-existing steady-state drainage system is calculated in model stage 1 so that the blister expands over water rather than dry bedrock; this scenario is more applicable to the warm-based areas of the GrIS, where water will exist at the ice-bed interface. In addition, by linking the blister and flowband model, downstream hydrological development as a result of lake drainage is allowed to occur and remove water from the blister.

The blister is only allowed to expand in stage 2 until all of the lake water is within the subsurface; this is more topographically realistic than allowing the blister to expand to a radius of >10 km, over which the bed is unlikely to be flat. The secondary advantage of limiting the growth of the blister during lake drainage is that the equations for uplift and blister growth beyond radii equal to the ice thickness are less applicable (see Section 5.2.4) and, although radii expand to two or three times the ice thickness in stage 2, it is preferable to model outputs with a 15 km radius blister. Also, as the horizontal extent of a_c is linked to the growth of the blister, it is more realistic to have a horizontal englacial crack of total length ~5 km rather than 24 km (as would occur with a blister radius of 15 km).

By using the blister model to determine the frictional modulation of water flowing through the englacial system and the uplift associated with the overpressure from turbulent water, the lake water is no longer forced into the flowband model, causing unrealistic pressures. As a result, more realistic inputs to the flowband model can be used. For example, a critical water thickness of 0.15 m as opposed to 5 m (as applied by Pimentel and Flowers, 2011) can be used with realistic model outputs. The adaptation of the sheet pressure equation for situations with overpressure conditions (see Section 5.4.4) also helps with stability in the flowband model.

The coupled model is therefore an improved approach for establishing conditions during and following lake drainage events.

5.4.7 *Coupled model limitations*

The coupled model approach is not without limitations. The remaining limitations of the water blister and flowband model, described in Sections 5.2.4 and 5.3.4 respectively, still exist. There are also additional limitations introduced by the method of model coupling.

The method of overlapping the radial blister model with the rectangular flowband model in stage 2 is not exact. Although it is argued that upstream pre-existing water will also be overlapped by blister expansion, the precise basal volume cannot be estimated without difficulty, and the resulting overlap volume is an estimate. This however, is an improvement on the Tsai and Rice (2010) blister expansion scenario where no water existed at the ice-bed interface prior to lake drainage.

Similar dimensional problems exist when running the stage 3 flowband model with the blister reservoir. Ideally, the entire blister would be able to be incorporated into the flowband. However this is not possible because a) the fixed width of the flowband is determined to be 1500 m by the topography of the subglacial valley downstream of the case-study lake site (see Fig. 5.10) and it would be more unrealistic to expand the flowband width domain than to ignore the blister water outside the flowband; and b) including the blister reservoir upstream of the water input point in the flowband model would create reverse hydraulic potential gradients in the flowband model, which due to the lack of lateral flux, creates instabilities in the model; the domain boundary must therefore always be at the site of the water inlet. The inability to include the entire blister reservoir within the flowband model is a potentially important limitation but would require a more complex 2-D or 3-D model with variable width and lateral flux, both of which are not possible in the current configuration.

Preferential flow is not possible within the blister and any channels that are overlapped by the blister in stage 2 are assumed to be overwhelmed by the blister water and therefore do not drive further preferential water flux. The latter is likely the case for small channels but may not be applicable for pre-existing large channels, for example those with a cross-sectional area of $10\,m^2$.

However, as long as these limitations are taken into account, the coupled hydrological model can give useful insight into basal hydrological development during and following lake drainage events.

5.5 Summary

This chapter has introduced two approaches to lake drainage modelling, a radial turbulent-flux blister model and a fixed-width coupled hydrological flowband model. Some limitations of the blister model are that downstream hydrological development is not possible with a radial configuration and that expansion of the water blister is assumed to occur over a dry bed. The flowband model is limited because using a lake drainage rate as a direct flux into the basal domain causes excessive water pressures and unrealistic flux rates, partially due to the lack of lateral or radial flux possible in the fixed-width geometry. As a result, the chosen approach is to link the two models together, which bypasses significant limitations associated with the individual models and provides a novel method for replicating basal hydrological development during a lake drainage event. The advantages of this approach outweighs additional limitations caused by the method of model coupling. In addition to using the linked blister and flowband configuration to determine hydrological development during lake drainage, the flowband model is utilised to assess hydrological development following lake drainage with the vertical fracture allowing access of diurnally-varying surface meltwater to the ice-bed interface.

Chapter 6

Coupled hydrological model implementation

6.1 Introduction

The implementation of the coupled hydrological model to address the thesis aims is described in this chapter. The model is applied to four model geometries representing different areas of the GrIS that are described below. For each geometry a series of sensitivity tests are run for different parameter values; the choice of baseline parameters around which the sensitivity tests are run along with the range of variables tested are described here.

6.2 Coupled hydrological model geometries

Four model geometries are used to test the hydrological development in different areas of the GrIS using the coupled hydrological model (Fig. 6.1). For the F-Lake case-study, two model geometries are constructed: one with simple planar topography and the second with more realistic geometry extracted from surface and basal DEMs. A tidewater glacier and a marginal glacier (i.e. a glacier within several tens of kilometres of the ice sheet margin) scenario are also tested using idealised model geometries.

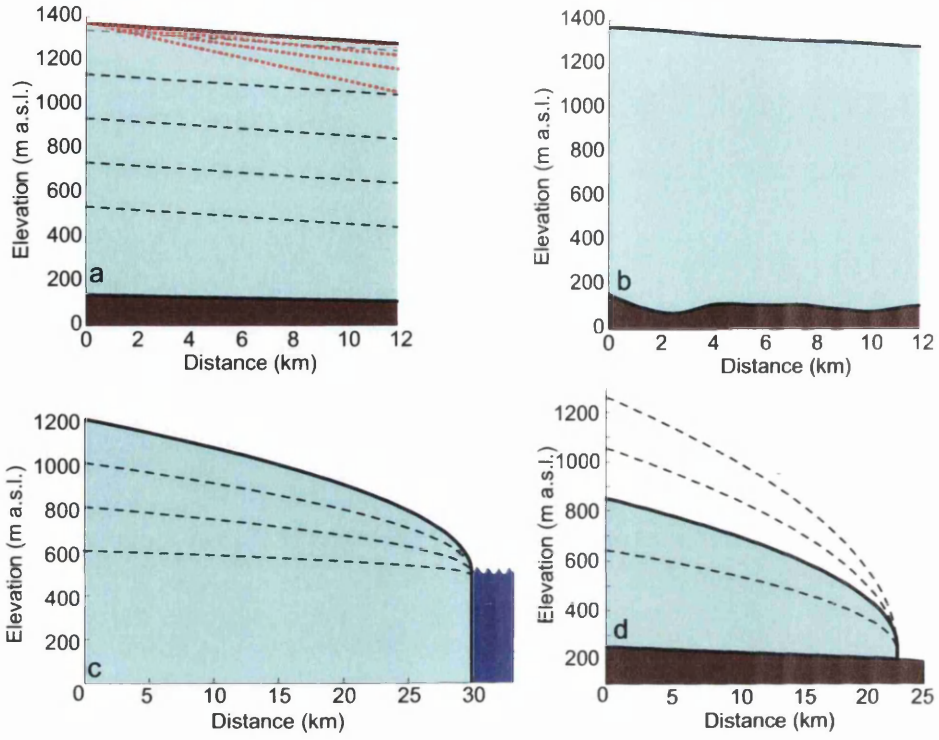

Figure 6.1: *Schematic of the coupled hydrological model geometries. Standard topography is shown by the thick black lines and thickness variations are shown by the black dashed lines. a) Model geometry 1 represents the F-Lake case-study site with a simple planar topography. Surface slope variations in the sensitivity tests are shown by the red dotted lines. b) Model geometry 2 is based on topography extracted from F-Lake surface and bed DEMs. c) Model geometry 3 represents a tidewater glacier with no basal slope. d) Model geometry 4 represents a land-terminating marginal glacier.*

6.2.1 *Geometry 1: F-Lake planar topography (FP)*

Model geometry 1 (Fig. 6.1 a) is a simple planar configuration with constant surface and bed slopes that extend for 12 km downstream from the water input point. The model length of 12 km is due to the extent of available basal topography for the case-study site. To avoid boundary effects, the spatial domain is arbitrarily extended by a further 12 km, but the outputs are only examined up to the edge of the 12 km model rather than the extended spatial domain. The surface and bed heights at the inlet and outlet boundaries of the model are estimated from the F-Lake DEMs (see Section 3.3); these values produce the model geometry shown in Figure 6.1 a with a surface slope of 0.45° and a basal slope of 0.14°. The ice thickness at the upper boundary is 1232 m and at the lower boundary at 12 km distance is 1168 m. This planar geometry is applied to the F-Lake case-study in order to analyse hydrological development without the presence of reverse bedrock slopes, which complicate interpretation.

Table 6.1: *GPS unit positions relative to the F-Lake subglacial water input point.*

	GPS 1	GPS 2	GPS 3	GPS 4
Distance from input (m)	1000	1650	2300	1800
Direction from input	NW	SW	SE	NE

Through initial testing, it was determined that one of the most important variables for channel growth and hydrological system development was the basal pressure outlet boundary condition. Therefore, in order to best examine variability in conditions at the ice-bed interface as a result of lake drainage, all sensitivity parameters for model geometry 1 are tested with three outlet pressure values: 1) ice overburden (P_i), 2) 50% of overburden and 3) 0, representing atmospheric conditions (or partially full channels, noting that in geometry 1 this does not represent the ice sheet margin).

Because of the substantial data collection during the 2010 field campaign at F-Lake (see Chapter 3), some of the coupled model inputs can be well constrained. The width of the flowband for all baseline model runs is fixed at 1500 m as this is the average width of the valley running downstream from the water input point towards the NW (as shown in Fig. 5.10) and agrees generally with the width of flow suggested by overburden hydraulic potential gradients (see Fig. 3.4).

Some adjustments are made to the Tsai and Rice (2010) water blister model when applied to the F-Lake drainage event. Because there is an accurate lake bathymetry map (see Section 3.4.2) rather than assuming a static cubic lake shape, it is possible to get a more exact lowering rate of the modelled water height by adjusting for lake volume rate of change; this is an improvement on the application of the model to the Das lake drainage event (Tsai and Rice, 2010). Other known inputs to the water blister model include the ice thickness at the water input point and the X_0 positions of the four GPS units relative to the water input point (see Table 6.1). The pre-drainage lake volume and area values of 7.14×10^6 m^3 and 2.58×10^6 m^2, respectively were determined through bathymetry calculations (see Section 3.4.2). The impact of the remaining unknown parameters on drainage development are explored in a series of sensitivity experiments, described in Section 6.4.

6.2.2 *Geometry 2: F-Lake real topography (FR)*

Model geometry 2 (Fig. 6.1 b) is a smoothed version of the surface and basal topographic conditions recorded at the F-Lake case-study site. The flowline that geometry 2 is based on is shown in Figure 3.3, with the smoothed surface and bed shown in Figure 3.6 b and d. As discussed in Section 3.3.1, the reverse bedrock slopes along the flowline are sufficiently steep that they would prevent much of the downstream water flux in the coupled hydrological model. The implications of these reverse slopes are discussed in Section 9.2.3, however, for modelling purposes, the flowline is smoothed to remove these effects. The ice thickness at the upper boundary is 1215 m and 1165 m at the lower boundary (Fig. 6.1 b). Again, the model ends at $\sim$ 12 km distance but is artificially extended by 12 km to remove boundary pressure effects; the extended portion of the spatial domain follows a constant basal slope of 0.07° and a constant surface slope of 0.22°, having an ice thickness of $\sim$1133 m at its downstream (24 km) boundary. The outputs from the model geometry 2 are only analysed in the initial 12 km.

In geometry 2, the more realistic topography for the F-Lake region, the outlet pressure conditions are overburden, 80% of overburden and 50% of overburden. The reason that the F-Lake geometry 2 model is not tested for atmospheric outlet pressure conditions is due to the presence of a substantial overdeepening at $\sim$12 km distance along the flowband (see Fig. 3.3) that through supercooling freeze-on and reverse hydraulic gradients would require high pressures for water flow (see Section 9.2.4); as a result, lower pressures ($<0.5\,P_i$) would be unlikely to occur in this region.

6.2.3 *Geometry 3: Tidewater glacier (TG)*

The third model geometry is constructed to represent a tidewater glacier (Fig. 6.1 c). This geometry is generally based on the configuration used by Pimentel and Flowers (2011) for application to the Das lake drainage event and is applied here to a) compare the coupled hydrological model outputs with those produced by Pimentel and Flowers (2011), and b) estimate the difference in hydrological development when comparing land-terminating and tidewater glaciers, particularly since the latter are argued to be the primary contributors to mass loss in Greenland (Thomas *et al.*, 2003; Rignot and Kanagaratnam, 2006; Bamber *et al.*, 2007; Howat *et al.*, 2007). The configuration of model geometry 3 involves no basal slope and a parabolically-

increasing surface profile. The upstream ice thickness is 1200 m and the water-terminating boundary is 500 m thick (Fig. 6.1 c). Pimentel and Flowers (2011) used a model length of 50 km; here, the same surface slope and ice thickness values are applied to a 30 km spatial domain. The reason for the difference in model length is due to the necessary grid-step of 100 m for the coupled model approach (see Section 6.3.1); this can be compared with the 500 m grid-step used by Pimentel and Flowers (2011). A 50 km model length would require too much computational power to apply a series of sensitivity tests with the coupled hydrological model for analysis of hydrological development.

Two downstream pressure boundary conditions are tested for the geometry 3 sensitivity experiments. The first assumes that the outlet is at overburden pressure (i.e. a floating glacier margin); this scenario would involve a water thickness of 447 m if the ocean water density is assumed to be 1030 kg m^{-3}. This application is simplified in that tidal effects and the stress impacts of a floating glacier margin are not taken into account; these aspects are beyond the scope of this study. The second pressure boundary condition is for a water thickness of 300 m which gives an outlet pressure of $0.67\,P_i$; this latter configuration assumes that the ice margin is grounded.

6.2.4 *Geometry 4: Marginal glacier (MG)*

The marginal glacier model (Fig. 6.1 d) is constructed to analyse lake drainage events in the land-terminating RGC in a region closer to the margin than the F-Lake case-study. This model geometry begins 23 km from the ice margin with an upper boundary ice thickness of 600 m (Fig. 6.1 d). The surface profile parabolically increases from the upper boundary to the margin, where the ice thickness is 50 m. The basal slope along the spatial domain is constant at 0.12°. As the ice is land-terminating, the outlet pressure is assumed to be atmospheric and is therefore set to 0.

Because geometry 4 involves much thinner ice than the other three modelled geometries, the stage 2 linking process differs somewhat from the standard approach described in Section 5.4. In the other three modelled geometries, the linking process ceases when all the water from the lake is at the bed or in the englacial system. However, because of the thin ice, the growth of the blister is much more rapid for geometry 4 (due to less overburden resistance to basal uplift) but there is insufficient pressure to maintain the englacial fracture, which begins to close. The approach to

Table 6.2: *Baseline coupled hydrological model parameters.*

Symbol	Description	Value	Units
E	Young's modulus	6.2	GPa
K	Sheet hydraulic conductivity	0.5	m s^{-1}
h_c^{sh}	Critical sheet thickness	0.15	m
S_ϵ	Initial conduit size	0.1	m^2
Q_G	Geothermal heat flux	70	mW m^{-2}
A	Creep parameter	1.6×10^{-24}	Pa s^{-1}
n'	Manning roughness coefficient	0.032	s m^{-3}
k	Nikuradse roughness height	0.01	m
V_0	Lake volume	7.1×10^6	m^3
A_0	Lake surface area	2.6×10^6	m^2
X_0	Sensor distance	1000	m

the latter problems by Tsai and Rice (2010) was to impose a fixed frictional value to force the englacial fracture open once it drops below a closure threshold. Although this solution was applicable for the Tsai and Rice (2010) approach, it does not work when linking the blister with the flowband model because the overlap water volume artificially allows unrealistic uplift and increasing englacial crack volume once the latter should have closed. As a result, instead of allowing the blister to grow until all of the lake water is in the subsurface, the linkage is ceased when the englacial crack closure threshold is reached.

6.3 General sensitivity tests

The approach to sensitivity testing of the coupled blister and flowband model is to choose a baseline set of parameters and vary these one by one to establish the impact of individual variables on the model outputs. An approach such as latin hypercube sampling, where a set of parameters are adjusted within a range of values at random, was considered; however, in order to establish which parameters are important for hydrological development, an approach where the parameters are varied from an estimated baseline seems more appropriate. The coupled hydrological model constants are given in Table 5.1. The parameter baseline estimates are primarily the same for all of the modelled geometries; these values are shown in Table 6.2. Several model inputs differ depending on the modelled geometry and are shown in Table

Table 6.3: *Geometry-specific coupled hydrological model parameters.*

Symbol	Description	Geometry 1	Geometry 2	Geometry 3	Geometry 4
W	Sheet fixed width (m)	1500	1500	1000	1000
H	Inlet ice thickness (m)	1232	1215	1200	600
d_c	Conduit spacing (m)	1500	1500	1000	1000

6.3. In total, 288 full sensitivity tests have been run with the range of parameters shown in Table 6.4. The results from these experiments are presented in Chapter 7.

6.3.1 *Grid-step*

Prior to running model experiments, general operational sensitivity tests were performed for the fully coupled model configuration. These include both time-step and grid-step tests for each of the four stages of modelling (see Section 5.4). Grid-step size was tested for the finite-difference flowband model only, as the water blister model does not operate on a confined grid. As model grid spacing approaches zero, model outputs are expected to converge. However, a finer grid also requires significantly longer computational time. These tests are designed to identify a suitable grid-step size that allows efficient computation but also does not produce errors as a result of a coarser mesh.

As stages 1–4 of the coupled hydrological model run on the same flowband grid-step, one set of sensitivity runs was completed for the chosen grid-step sizes and the outputs compared. The chosen variable for comparing model convergence is the conduit cross-sectional area, as it is this parameter that is primarily being tested with the coupled hydrological model. The following flowband domain grid-steps were tested: 20 m, 50 m, 100 m and 200 m. The 20 m test was unsuccessful as the computational time was in excess of 48 hours. For the remainder of the tests, the difference in maximum conduit size for both stage 2 and stage 3 was $<4\times10^{-4}$ %. For stage 4, the larger grid-step allowed greater channel growth although maximum conduit size differed by <0.2 % between grid tests. Blister growth is better represented on a smaller flowband grid-step; however the 50 m grid-step involved substantial computational time. As a result, a grid-step of 100 m was chosen for faster computational time whilst still allowing more accurate linkage between the blister and flowband model.

6.3.2 *Time-step*

The choice of time-step in the coupled hydrological model is a balance between achieving model convergence whilst also allowing efficient computation time. As shown in Figure 5.7, the time-steps for each stage of the modelling process differ considerably and are therefore tested independently. In the first stage of modelling, a time-step of five minutes was chosen, following Pimentel and Flowers (2011). The choice of flowband time-step does not appear to impact the spin-up model outputs.

For the stage 2 model, the blister model was integrated at two-second time-steps with secondary calculations made every twenty seconds. This can be compared with the implementation of the blister model by Tsai and Rice (2010), where the integration was one second and secondary calculations took place every ten seconds. Linkage between the blister and the flowband is, in this configuration, the same time-step as the secondary blister calculations (and due to the linkage process is referred to in Chapter 5 as the primary time-step). The following linking time-steps were tested: 10 seconds, 20 seconds, 60 seconds and 120 seconds. The latter two values caused instability and output divergence in the water blister model. However, time intervals of 10 seconds and 20 seconds produced the same stable outputs. As a result, the stage 2 linkage time-step of 20 seconds with blister integration over two seconds were used to allow faster processing speeds. When linking the blister with the flowband model, it was found the latter needed a shorter integration time relative to the blister for stability in the hydrological system. The flowband time-step was therefore set as one second, as shorter time-steps than this involved excessive computational time.

In stage 3, the flowband model was tested with time-steps of 5, 15, 30, 60 and 300 seconds. The maximum conduit size for all of these tests differed less than 6×10^{-7} %. As a result, the time-step does not appear to impact the stage 3 model outputs. The calculation time for a time-step of five seconds was too great for effective use of the coupled hydrological model. However at time-steps of $\geq$15 seconds, the calculation time was reasonable; as a result, the time-step of 15 seconds was chosen for the stage 3 model.

The stage 4 flowband model was tested with the following time-steps: 1, 5, 10, 20 and 60 minutes. Similar to stage 3, maximum conduit size differed less than 4×10^{-7} % between runs. Only the one-minute time-step caused excessive computational time. Following Pimentel and Flowers (2011), a time-step of five minutes was therefore chosen for stage 4.

6.3.3 *Filter optimisation technique*

Within the water blister model, different model set-ups are possible based on the initial conditions of the blister radius, L, and the ratio between L and the horizontal extent of the connecting vertical crack, a_c. The blister model was therefore tested with initial crack radii of 10, 20 and 50 m (as without an initial crack, the fracture equations could not be applied). Within each of these initial blister conditions, a_c/L was varied at 0.85, 0.95 and 1. For a_c/L <0.85, the model outputs are sufficiently incomparable to the case-study surface data that they were not further tested.

If these nine L and a_c/L blister sensitivity tests were included in every parameter sensitivity test it would result in a total of 2592 full model outputs. The time required to run all these tests is beyond the scope of this study. As an alternative, a filter optimisation technique was applied to the model geometry 1 (F-Lake planar topography) sensitivity runs, with an outlet pressure value of P_i. For these optimisation tests, the stage 1 spin-up model was run followed by the stage 2 linked model for a maximum of one model hour to obtain the blister model outputs. In total, the nine L and a_c/L blister sensitivity tests were then run for the 30 sensitivity parameters shown in Table 6.4 (excluding lake volume because these blister model outputs could not be compared with recorded surface data). The outputs from the blister model were compared with the data from the case-study site, including the lake lowering rate and the GPS station uplift and horizontal motion records. The lake lowering rate was used as the primary control for determining the most appropriate internal parameter choice of initial L and a_c/L, as the GPS records might be contaminated with uplift due to ice block fracturing rather than uplift only as a result of water blister expansion. In order to compare the blister model lake level outputs (H_w) with the recorded F-Lake lowering level, a trapezoidal integration method was applied to both. The three (of nine) model H_w outputs that most closely matched the area under the curve of the F-Lake water level were weighted as the primary parameters. Because in these tests, the integrated water level value was often the same or at least similar for three of the nine tests, a secondary filter optimisation technique was necessary. Therefore, of these three parameters, the best combination of L and a_c/L for the tested sensitivity parameter was chosen by comparing the blister model horizontal displacement outputs with the horizontal motion records from GPS 1. The primary parameter that had the closest temporal match for 0.1 m of horizontal motion when compared to the GPS 1 record was chosen as the final blister model initial condition.

Table 6.4: *Coupled hydrological model range of sensitivity test parameters.*

E (GPa)	A (Pa s^{-1})	Q_G (W m^{-2})	n' (s m^{-3})	k (m)	K (m s^{-1})	h_c^{sh} (m)	S_ϵ (m^2)	W (m)	V_0 (m^3)
3	9.3×10^{-25}	0.7	0.01	0.01	0.1	0.05	0.1	500	0.01×10^7
6.2	3.5×10^{-25}	0.85	0.032	0.05	0.5	0.15	1	1000	0.1×10^7
8.84	1.6×10^{-24}		0.07	0.1	1	0.3	10	2000	1×10^7
	2.4×10^{-24}		0.1			0.4		1500	3.8×10^7
								(1,2 only)	
								3000	
								(3,4 only)	

It was found that, for the majority of these optimisation tests, an initial blister radius of 50 m was appropriate. However, for a Young's modulus value of 3 GPa, the initial blister size of 10 m was a better match; for E=8.84 GPa the blister size of 20 m was most appropriate. Also, with a critical water thickness >0.15 m, L=20 m was the closest match to the surface data. In all model runs, a_c/L=0.85 was the most appropriate match. In the following sensitivity tests, a_c/L is constantly set at 0.85 but the initial L length is varied depending on the optimisation results described above. Some of the sensitivity tests could not be directly compared with the lake drainage records at the case-study lake, such as varying the lake volume and the ice thickness. For these tests it is assumed that the initial condition of L is 50 m. Model geometries 3 and 4 do not have surface data to compare with the model outputs for filter optimisation and therefore the same L and a_c/L values are applied to these systems as for model geometries 1 and 2. It is recognised that, by not testing the sensitivity of all of the parameters or by applying these constants to scenarios other than the case-study lake drainage might be misleading. However, without data to test the outputs for all of the sensitivity tests, the assumption of a_c/L=85% and L = 50 m seems reasonable.

6.4 Parameter sensitivity tests

The choice of parameter ranges that are applied to the four model geometries are described in this section with the values also given in Table 6.4. The configuration of these sensitivity tests is that each variable is adjusted from the baseline parameters given in Table 6.2 to determine the independent effect of that variable on the hydrological development.

6.4.1 *Young's modulus (E)*

The value of Young's modulus in the model will primarily affect the growth of the water blister as elastic beam uplift is not included within the flowband model. Young's modulus is suggested to vary between 0.9 GPa as recorded from tidal flexure data on ice shelves (Vaughan, 1995), and 9.3 GPa as found from lab-based experiments of visco-elastic response to tidal flexure (Reeh *et al.*, 2003). The values used in the present sensitivity tests include: 3 GPa, based on the value used by Pimentel and Flowers (2011) for application of the flowband model to the Das lake drainage; 6.2 GPa as used by Tsai and Rice (2012) when applying the water blister model to the Das lake drainage (based on laboratory experiments for ice at -5°C); and 8.84 GPa, which is the value of Young's modulus calculated from seismic reflection experiments from the F-Lake region. The latter was calculated using the following equation from Sheriff and Geldart (1983):

$$E = \rho_i V_s^2 \frac{(3(V_p^2) - 4(V_s^2))}{V_p^2 - V_s^2}, \tag{6.1}$$

where V_p is the P-wave velocity and V_s is the S-wave velocity (see Chapter 8 for further information on seismic velocities). Following analysis by Booth *et al.* (2012) of seismic lines in the F-Lake region, a range of V_p values of 3760–3840 m s^{-1} and V_s values of 1858–1938 m s^{-1} are applied to Eq. 6.1. This produces a maximum E of 9.2 GPa, a minimum E of 8.5 GPa and a median E of 8.84 GPa. It is the latter that has been chosen as a representative upper E for the coupled model application. However, because of the presence of fractures in the ice caused by the drainage of the lake, it is possible that this elastic modulus is too high to apply to the F-Lake drainage, as Eq. 6.1 is based on assumptions of homogeneous and isotropic ice. As a result, the value of 6.2 GPa is chosen as the baseline parameter; this is also justified by the good match between the 6.2 GPa value and the recorded surface data as shown in Figure 7.4.

6.4.2 *Creep parameter (A)*

As the temperature and fabric profile of the ice at F-Lake is not known, the creep parameter constant, A, in Glen's flow law is also not well constrained. As a result, the following values of A are tested: 3.5×10^{-25} s^{-1} Pa^{-3} that corresponds with

an ice temperature of -10° C; $9.3\times10^{-25}\,s^{-1}\,Pa^{-3}$ for an ice temperature of -5° C; $1.6\times10^{-24}\,s^{-1}\,Pa^{-3}$ for an ice temperature of -2° C; and $2.4\times10^{-24}\,s^{-1}\,Pa^{-3}$ for an ice temperature of 0° C. These values are taken from Cuffey and Paterson (2010). Following Pimentel and Flowers (2011), the value of $1.6\times10^{-24}\,s^{-1}\,Pa^{-3}$ is chosen as the baseline parameter.

6.4.3 *Geothermal heat flux (Q_G)*

The geothermal heat flux is a parameter that impacts the volume of water melted in the distributed sheet in the flowband. The range of geothermal heat flux for Russell Glacier has been calculated using geological interpretation and thermal crust models by Maule *et al.* (2009). They found that geothermal heat was likely between an average of 70 and 85 $mW\,m^{-2}$ for RGC and therefore these are the two values used in the sensitivity analysis. Following Pimentel and Flowers (2011), the value of 70 $mW\,m^{-2}$ is chosen as the baseline parameter.

6.4.4 *Manning roughness (n')*

The Manning roughness coefficient impacts the rate of flux through conduits and can vary between 10^{-2} and $10^{-1}\,s\,m^{-3}$ (Cuffey and Paterson, 2010). The values of Manning roughness tested here are 0.01, 0.032, 0.07 and $0.1\,s\,m^{-3}$. The value of $0.032\,s\,m^{-3}$ is used because this is the value applied by Pimentel and Flowers (2011) when modelling the Das lake drainage event, and is therefore also used here as the baseline parameter. This value of Manning roughness was originally advocated by Clarke (2003) for application to jökulhlaup modelling; Clarke (2003) argued that the Manning roughness of $0.09\,s\,m^{-3}$ originally applied by Nye (1976) for jökulhlaup modelling was too high a value for channel wall roughness.

6.4.5 *Nikuradse roughness height (k)*

The Nikuradse roughness height parameter is related to the Manning roughness parameter in the current model configuration by $n' = 0.038\,k^{(1/6)}$ (see Tsai and Rice, 2010, Eq. 5). Here, k represents the roughness at the ice-bed interface during water blister expansion as opposed to the walls of a channel. As a result, it is treated

separately from the Manning roughness experiments and will impact only the rate of growth of the water blister.

The Nikuradse roughness height represents grain roughness and is varied in these tests at 0.01 m, 0.05 m and 0.1 m. Tsai and Rice (2010) suggested a maximum range of $0.005< k <0.2$ m although they argue that the limited dependence of blister growth on k means that a value of 0.01 m is acceptable. As a result, the full range has not been tested here and 0.01 m is used as the baseline parameter.

6.4.6 *Flowband hydraulic conductivity (K)*

The hydraulic conductivity of the water sheet determines whether the model configuration represents a primarily sediment-based system or consists of linked-cavities (or a combination of both). Lower hydraulic conductivity would imply Darcian pore-flow through sediment and higher hydraulic conductivity, a linked cavity system. The sheet hydraulic conductivity is varied in these tests at values of 0.1, 0.5 and $1\,\mathrm{m\,s^{-1}}$. A higher hydraulic conductivity implies faster flux through the water sheet and therefore lower water pressures and less exchange between the sheet and the conduit. The median value of $0.5\,\mathrm{m\,s^{-1}}$ has been chosen as the baseline hydraulic conductivity parameter to represent a linked-cavity drainage system.

6.4.7 *Critical flowband sheet thickness (h_c^{sh})*

Another feature determining the hydraulic conductivity of the water sheet is the critical sheet thickness, representing the averaged distributed system water thickness at overburden pressure. Pimentel and Flowers (2011) applied a sheet thickness of 0.15 m for Alpine glaciers and 5 m for the GrIS, presumably to stabilise the flowband model for lake drainage events. However, it is hard to envisage an areally-averaged sheet of 5 m stably underlying the GrIS (unless there was a very low hydraulic conductivity applied for flux through a thick layer of till), particularly since the basal sheet thickness during the F-Lake drainage would have been a maximum of $\sim$1.2 m according to GPS measurements (see Sections 3.6.1 and 7.2.2). Initially, critical water thickness values of 0.05 m, 0.15 m, 0.5 m, 0.7,m and 1 m were tested. However, it was found that with a critical sheet thickness $\geq$0.5 m, the system became unstable as the blister was dispersed almost immediately. As the GPS station uplift data indicate that the blister remained for at least several hours following the lake

drainage (see Fig. 9.2), the range of critical water thickness values tested was changed to 0.05 m, 0.15 m, 0.3 m and 0.4 m. These water thickness values also seem more applicable to a distributed system, such as a linked-cavity network, than water sheets >0.5 m. The value of 0.15 m was chosen as the baseline parameter because of a good match between the blister model outputs and the F-Lake surface data when running the coupled hydrological model with this value.

6.4.8 *Initial channel condition (S_c)*

The initial channel size is a particularly interesting parameter to test with the lake drainage model as it has been suggested that a pre-existing channel is necessary to drain the supraglacial lake water within the scale of hours to days (Das *et al.*, 2008; Hoffman *et al.*, 2011; Pimentel and Flowers, 2011). Channels are therefore tested by establishing a steady-state system with initial conduit sizes of 0.1 m^2, representing the size of a cavity in an essentially distributed system; 1 m^2, suggesting that water drainage from upstream had created a hydrological system prior to lake drainage; and 10 m^2, implying long-sustained, large volumes of water from upstream of the lake site prior to lake drainage. Although model runs were attempted for a larger channel cross-sectional area (22 m^2, following the approach of Pimentel and Flowers, 2011), these systems were not stable and a reasonable steady state could not be produced. Following establishing a steady-state system for model configurations with these initial channel sizes, the conduits in model stages 2–4 can either grow or shrink to a minimum value of 0.1 m^2, depending on the hydrological development of the system. The baseline value of 0.1 m^2 is applied in the sensitivity tests in order to primarily examine drainage evolution for an initially distributed system.

6.4.9 *Flowband width (W)*

The fixed width of the flowband is based on the assumption that water from the lake drainage is flowing through a subglacial valley. For the case-study site, the basal topography is known and a valley of ~1500 m width is clear for ~12 km downstream of the lake site (see Fig. 5.10); this value is therefore used as the baseline value for the F-Lake case-study geometries 1 and 2. To test the impact of the fixed width on hydrological development, geometry 1 is also run with fixed widths of 500 m, 1000 m, 1500 m and 2000 m. Geometry 2 represents the most realistic case for the

case-study site and therefore the width value is not tested. For the tidewater and marginal glacier models (geometries 3 and 4), because they are not based on precise locations, a larger range of fixed widths are tested with 500 m, 1000 m, 2000 m and 3000 m; a baseline width of 1000 m is applied to these geometries. A narrower flowband will become pressurised more quickly than a wider flowband and encourage greater conduit growth.

6.4.10 *Lake volume (V_0)*

Although the lake volume for the case-study lake is well constrained, there is a large variability of lake sizes across RGC and the GrIS (Selmes *et al.*, 2011; Fitzpatrick *et al.*, 2014). Model geometries 1, 3 and 4 are tested for four lake sizes; geometry 2 is only tested with the known volume for the case-study site (i.e. the baseline lake volume and area values of 0.7×10^7m^3 and 0.03×10^7m^2, respectively). These additional lake volume and lake area tests are related to average lake depth by $H_w = 2(V_0/A_0)$ giving lake volumes and depth tests of: 1) 0.01×10^7m^3 with a lake surface area of 0.01×10^7m^2 and an average lake depth of 2 m; 2) 0.1×10^7m^3 with a lake surface area of 0.05×10^7m^2 and H_w=4 m; 3) 1×10^7m^3 with a lake surface area of 0.33×10^7m^2 and H_w=6 m; and 4) 3.8×10^7m^3 with a lake surface area of 0.54×10^7m^2 and H_w=14 m. The latter lake volume value is based on the largest lake observed by Fitzpatrick *et al.* (2014) in RGC. For the largest lake volume a similar problem with the linked model as seen for the marginal glacier model was encountered (see Section 6.2.4); the lake volume could not be dissipated before the englacial crack was shut. As a result, the linked model is artificially stopped at the point when the englacial frictional value reaches a critical closure threshold. The baseline lake volume and area for the tidewater glacier and marginal glacier models are those calculated for F-Lake (i.e. 0.7×10^7m^3 and 0.03×10^7m^2) and are used so that the model outputs from the four geometries can be better compared.

6.4.11 *Surface slope (Δa)*

As model geometry 1 has a planar configuration, the impact of changing the surface slope on hydrological development can be tested. Four constant surface slopes of 0.5°, 0.7°, 1° and 1.5° are tested for the three F-Lake planar model outlet pressure conditions. These slopes are plotted as red dotted lines in Figure 6.1 a. The range

of slopes was chosen as it encompasses the average minimum and maximum slopes found on a RGC surface profile between 4–70 km from the terminus (see Fig. 9.9).

6.4.12 *Ice thickness (H)*

In order to determine the impact of ice overburden on hydrological development, model geometries 1, 3 and 4 are tested with a range of ice thickness values. For the F-Lake planar topography model, the surface and basal slopes are maintained and the upstream boundary ice thickness is varied at 1200 m, 1000 m, 800 m, 600,m and 400 m. Because the surface slope in model geometries 3 and 4 varies parabolically towards the glacier terminus, changing the ice thickness at the upstream boundary also changes the surface slope; thinner ice will result in shallower surface slopes. The relationship between ice thickness and surface slope for geometries 1, 3 and 4 can be seen in Figure 6.1 a, c and d, where the tested profiles are plotted as dashed lines. For the tidewater glacier, ice thickness is tested only at 1200 m, 1000 m, 800 m and 600 m as the outlet ice thickness is 500 m. In the marginal glacier, ice thickness is varied at 200 m intervals between 1200 m and 200 m.

The same linkage problem described for the marginal glacier (see Section 6.2.4) and the lake volume (see Section 6.4.10) tests was encountered with many of the ice thickness tests. As a result, the linkage was stopped prior to all the lake water draining into the subsurface when the englacial fracture reached a closure threshold.

6.4.13 *Runoff*

All of the stage 4 sensitivity experiments are run with diurnal water input estimated from a surface melt model for the F-Lake catchment (see Section 5.4.5). In total, 30 days of surface runoff are input into the coupled hydrological model for the sensitivity tests. However, in order to determine the impact of the full seasonal water input once lake drainage has occurred, the baseline models (including outlet pressure variations) are also run with 90 days of surface water input until September 30th, 2010. The full air temperature record and modelled surface water input are shown in Figure 6.2. It was not possible to run all of the sensitivity experiments with the longer record due to the long computational time for such calculations.

As flux through surface snow, rotten surface ice and channels is not accounted for

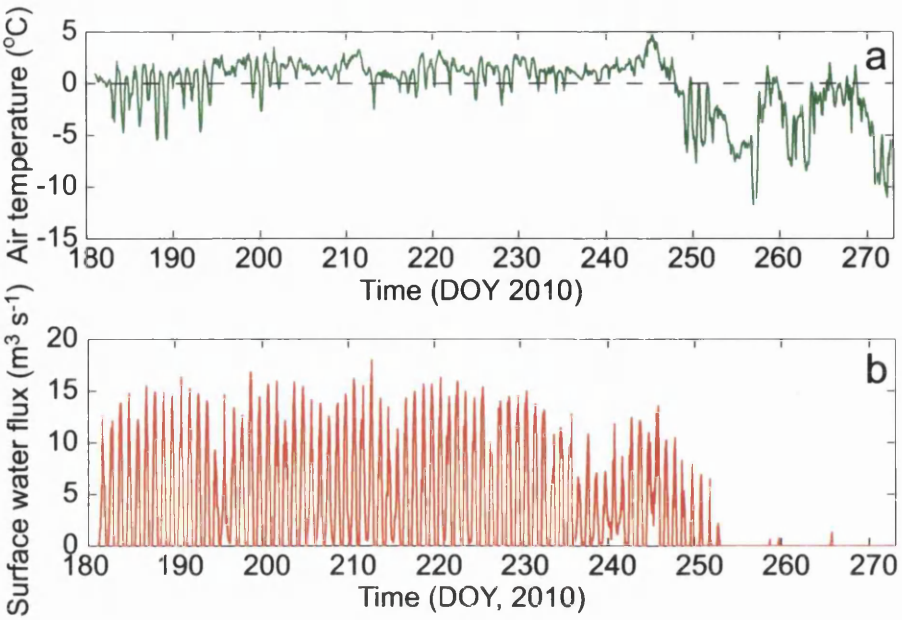

Figure 6.2: *a) Air temperature records for the F-Lake region with 0°C marked by the grey dashed line. b) Modelled F-Lake surface water input for the full 2010 melt-season following lake drainage.*

within the surface water estimate, it is likely that the absolute values of runoff input into the coupled hydrological model are an overestimate. As a result, the baseline models are also tested with half of the calculated catchment runoff to determine the impact of the volume of diurnal water input on hydrological development.

6.5 Analysis approach

The model outputs are divided into four categories in relation to different stages of the modelling process. These four stages are described in Section 5.4. Because of the model linkage and multi-stage processing, many outputs are produced. It is not possible to describe and analyse every output for each model stage and therefore the results are limited to analysis of the parameters most indicative of output variability. The primary output to analyse for each model geometry is the growth of the channel cross-sectional area. However, other outputs are analysed in relation to their model stage and are described below with the results reported in Chapter 7. In addition, examples of the graphed outputs from the baseline F-Lake planar model with outlet pressure at overburden are plotted in Appendix B; this is to demonstrate typical model responses that cannot be individually graphed for each sensitivity test due to

the volume of data.

Steady state system (stage 1): This model stage is run to achieve a steady-state in the flowband prior to linking the models. Depending on the model geometry and parameter values, the necessary background flux and time to achieve steady state varied between model runs. These spin-up inputs are detailed in Table A.1.

Lake drainage (stage 2): In this stage, the blister model and flowband model are linked together; as the lake drains the basal blister grows overlaps the flowband domain both incorporating flowband water and allowing downstream flux of blister water. Although many blister variables are output from these model runs, the most important for the current analysis is the blister size, so that the extent of radial flux relative to basal topography can be discussed. Examples of typical outputs for stage 2 blister growth plotted with the case-study surface data sets are shown in Figure B.1. Examples of the concurrent flowband hydrological development are shown in Figure B.2. This latter type of figure is used extensively for display of the flowband model outputs: the x-axis shows the hydrological system along the domain from upstream to downstream; the y-axis shows the hydrological development over time (with later time displayed higher up the y-axis). The grey portion in Figure B.2 shows the overlap of the water blister into the flowband domain over time. The variation in colour on the remainder of the figure shows the evolution of the plotted parameter.

Short-term hydrological development (stage 3): During stage 3 of the model runs, the flowband is used to assess the speed of blister dispersion downstream and its impact on hydrological development. In order to assess whether lake drainage events cause significant channel growth, the change in channel cross-sectional area is measured 10 hours after lake drainage begins. This growth is measured relative to the initial channel cross-sectional area which, in most cases unless otherwise specified, is $0.1\,\mathrm{m}^2$. An additional variable of interest in this stage is the time taken for the model input region to reach overburden pressure, suggesting that the pressurised blister water has dispersed. For several model runs, the maximum time allowed for dispersion (40 hours) prior to continuing on to stage 4 is reached. Figure B.3 shows plots of key variables for stage 3 including the water pressure in the sheet, the sheet thickness and the conduit growth.

Seasonal hydrological development (stage 4): In the final stage, the flowband model develops as a result of diurnal water input from the surface. There are various

outputs analysed in this stage including the maximum conduit size during the model run, and the time and distance along the domain at which this maximum conduit size occurs. These variables are used to assess whether the model has equilibrated to the diurnal water inputs; if equilibrated, maximum conduit size would likely occur prior to the last model time-step. The maximum conduit distance gives an indication as to the important controls on channel growth such as surface slope, input water volume, output water pressure etc. Similar to the stage 3 analysis, the channel growth is measured 30 days after lake drainage initiates; the distance where this maximum growth occurs is also recorded. Figure B.4 shows key outputs from a baseline stage 4 model run for geometry 1.

6.6 Summary

In this chapter the implementation of the coupled hydrological model for analysing development of subglacial hydrological systems in Greenland has been discussed. Four model geometries constructed to represent different regions of the GrIS have been introduced including the case-study model geometry with both a simplified planar set-up and a more realistic topography based on surface and basal DEMs. In addition a simplified tidewater glacier and a marginal glacier geometry have been described. Several general sensitivity experiments that are necessary prior to full model implementation have been discussed, including the grid- and time-step tests. The range of parameters tested in the sensitivity experiments have been introduced with the results from these tests given in the following chapter. Finally, this chapter included a summary of how the results are analysed in the following chapter.

Chapter 7

Coupled hydrological model results

7.1 Introduction

This thesis introduces a coupled modelling approach to lake drainage analysis that allows estimations of both subglacial radial turbulent water flux and the development of a downstream distributed and channelised subglacial hydrological network. In this chapter, a series of experiments are presented to test the sensitivity of the coupled model and to determine the most important variables for drainage development. As the basal conditions are largely unknown, exploring a range of parameter options is necessary so that the most realistic outputs for lake drainage can be determined.

The three aims of this chapter are to a) determine whether efficient subglacial channels develop during rapid supraglacial lake drainage events, b) examine basal hydrological development at the inland case-study lake drainage site both during and following the lake drainage event once a surface-to-bed connection has been made, and c) establish the impact of lake drainage on basal hydrological development in different glaciological settings such as tidewater glaciers or land-terminating glaciers located close to the ice margin.

To achieve these aims, the chapter begins by examining a simple application of the blister model with the case-study lake drainage data. This is followed by analysis of the baseline coupled hydrological model runs, separated into different stages of the modelling process (see Section 6.5). The baseline results are reported for each

model geometry: 1) the F-Lake planar topography model; 2) the F-Lake real topography model; 3) the tidewater glacier model; and 4) the marginal glacier model (for descriptions of these model geometries see Section 6.2). Following these primary results, the sensitivity test outputs from the coupled hydrological model are examined. This analysis begins by looking at the general impact of the individual parameters on drainage development. The specific range of results from the different model geometries are then discussed. Several additional tests examining the impact of some general characteristics of the model geometries, such as ice thickness and surface slope and the volume of surface runoff input into the model, are examined. This chapter ends by summarising the most important parameters and the impact of the geometries on drainage development.

7.2 Simple blister tests

Prior to running the full coupled hydrological model, incorporating both the blister and flowband models, it is useful to compare blister model outputs with the in-situ field data for the F-Lake case-study site. For a given set of input parameters (such as Young's modulus and ice thickness) the blister model fixes a relationship between the volume, the uplift and the blister radius. This configuration can be used to predict what volume and blister radius would be expected with the uplift rate seen from the surface GPS data. Similarly, the recorded lake level record can be used to predict basal volume and blister radius as a result of loss of lake water volume.

7.2.1 *Subglacial water volume test*

Initially, a simple test was conducted to determine the likely water volume necessary to uplift the ice surface by 0.83 m as seen at GPS 1 (NW) at the F-Lake site (see Fig. 3.11). From the hydraulic potential maps it can be seen that the maximum radial extent of a blister is likely ~2.5 km (see Figs. 3.4 and 5.10). The surface expression of ice uplift will not be as great as basal uplift due to longitudinal coupling preventing a one-to-one hydraulic jacking ratio. Using the simple 1-D version of the blister model (see Section 5.2) it is determined that an uplift of 0.83 m on the surface corresponds to an average of 1.2 m of uplift at the bed if the GPS unit is at a distance of 1000 m from the water input source at the surface.

First, assuming the subglacial water blister takes the shape of a cone, the volume of a cone with a basal radius of 2.5 km and a height of 0.9 m is $\sim 6.2 \times 10^6$ m^3. At the time of maximum uplift of GPS 1, the lake water level in the centre of the basin was $\sim$0.4 m, which is when the water volume in the subsurface was $\sim 7 \times 10^6$ m^3 (see Fig. 3.8). Some water would have been present in the connecting fracture (F2, see Fig. 3.7), which is estimated through passive seismic analysis to have been a maximum of $\sim$1 km in length (see Fig. 3.12). Assuming a crack volume of 1×10^6 m^3 (the difference between the cone volume and full lake volume) and an ice thickness of 1200 m, the average englacial crack width would be 0.7 m. The maximum transient separation between GPS 1 (NW) and 3 (SE) (which lie on a perpendicular transect to F2) is $\sim$0.35 m, as reported in Doyle *et al.* (2013); this separation likely represents the crack width at the surface. Although the simple calculations suggest a larger average crack width than measured at the surface, the general agreement between the figures suggest that applying a radial blister is a reasonable approximation for replicating basal hydrological conditions during a lake drainage event.

7.2.2 *Data-driven blister test*

The applicability of the blister model is tested here with the available F-Lake case-study in-situ data. The parameters used in these tests can be seen in Table 6.2, with an ice thickness of $H = 1232$ m. First, the blister model is run for radii of 1–5000 m increasing at 1 m intervals. At each interval, the crack and basal volume, average basal uplift and surface uplift for a site 1 km from the input (to compare with the F-Lake GPS 1 records) are calculated. Figure 7.1 a shows the basal (solid curve) and surface (dashed curve) uplift that would occur at the 1 km site for specific blister radii.

The blister model is then forced by the recorded lake drainage rate; for each increment of measured cumulative volume in the subsurface, the equivalent blister radius, basal uplift and surface uplift are extracted from the test described above. Figure 7.1 b shows the basal (solid curve) and surface (dashed curve) uplift predicted by the lake drainage rate (blue), along with measured uplift from GPS 1 (red) and GPS 4 (orange). As can be seen from Figure 7.1, the modelled uplift predicted from the lake drainage data matches remarkably well with the measured uplift at the GPS 4 site.

A similar process is used to force the blister model with the GPS 1 and GPS 4 uplift

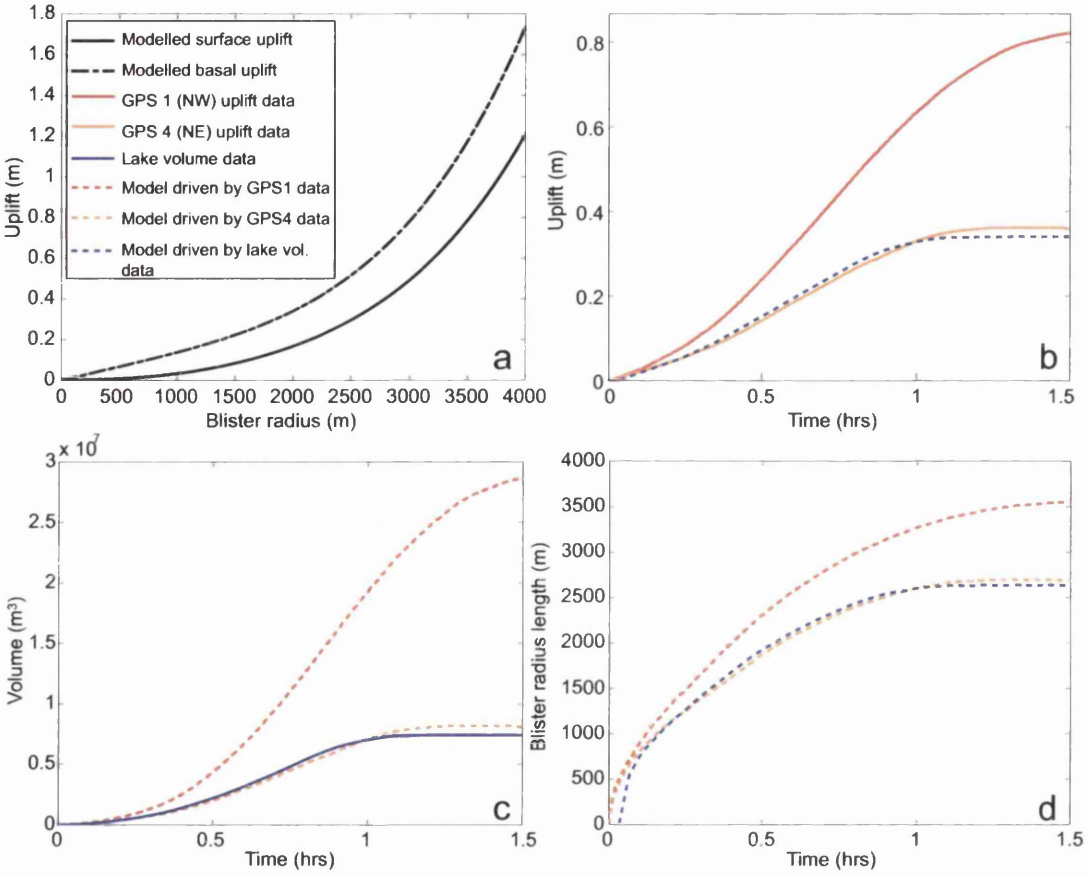

Figure 7.1: *Outputs from simple tests of the blister model performance. a) The equivalent F-Lake basal (dot-dashed curve) and surface (solid curve) uplift at the GPS 1 site for particular blister radii. b) Surface uplift records from the GPS 1 (solid red curve) and GPS 4 (solid orange curve) data sets and the uplift predicted by the blister model when forced by the lake drainage rate (dashed blue curves). c) Blister volume measured from the lake drainage rate (solid blue curve) with basal volumes predicted from the blister model when forced by the GPS 1 (dashed red curve) and GPS 4 (dashed orange curve) data sets. d) The blister radius that would occur when the model is forced by the GPS 1 (dashed red curve), GPS 4 (dashed orange curve) and lake drainage (dashed blue curve) data sets.*

data. For each uplift data point, an equivalent blister radius, blister volume and crack volume are extracted. The blister volume predicted by the GPS records is shown in Figure 7.1 c along with the subusrface volume estimated from measured lake record. As expected from the results shown in Figure 7.1 b, the GPS 4 predicted volume matches very closely to the measured volume.

Finally, the growth in the blister radii predicted by the GPS and lake drainage records are shown in Figure 7.1 d. The maximum radius predicted by the lake drainage record is 2631 m and by GPS 4 is 2691 m (i.e.$\sim 2 \times H$); the maximum radius of blister predicted from the F-Lake hydraulic potential gradients is 2500 m. The basal topography does not control the blister growth driven by the lake drainage rate in the model and therefore the close correspondence with the maximum blister size is coincidental. However, it does demonstrate that for radii up to $\sim$2500 m, the blister model is performing appropriately for the F-Lake region.

This exercise demonstrates that the blister model is appropriate for application to the F-Lake drainage event. The greater uplift from GPS 1 compared to GPS 4 will be discussed in Section 9.2.6. However, the very close match between the predicted and measured records from the lake drainage rate and GPS 4 indicate that a water blister is an important element of the lake drainage event and that the Tsai and Rice (2010) model is applicable for modelling such an event. Secondly, the exercise indicates that the blister parameters shown in Table 6.2 are appropriate as baseline parameters to test the coupled hydrological model sensitivity.

7.3 Baseline results

In this section, the results are given from the full coupled hydrological model run with the baseline parameters. These baseline parameters are shown in Table 6.2 and represent a likely scenario for conditions at the ice-bed interface (as discussed in Section 6.5). The results are divided into the different model stages (see Section 6.5). To recap, Stage 1 is the spin-up model and is not discussed here. In Stage 2, the blister and flowband are linked; Stage 2 lasts only until all the water from the lake is in the subsurface. Stage 3 examines short-term hydrological development in the flowband model within 40 hours of lake drainage; the pressurised blister water in the flowband is dispersed through the domain. Stage 4 of the model is the development of a seasonal system in the flowband driven by diurnal surface water inputs once a

surface-to-bed connection has been made by the lake drainage event

The baseline results for the four model geometries (see Section 6.2) are plotted in Figure 7.2. These results are also given in Tables C.1–C.4, highlighted in bold italics. Distance-time plots from some of the primary variables output in the stage 4 model for the four model geometry baseline runs are shown in Figure 7.3.

7.3.1 *Lake drainage (stage 2)*

The blister radius is smallest for the F-Lake planar model (geometry 1), with the three outlet pressure tests producing blisters of <2900 m (see Fig. 7.2 a), all within $\sim$ 30 minutes of drainage initiation (Fig. 7.2 b). Slightly slower blister growth due to the geometry of the tidewater glacier (geometry 3) allows a greater blister radius, of up to $\sim$2950 m. Blister extent is largest for the marginal glacier (geometry 4), with a radius of 3014 m after 46 minutes of lake drainage; thinner ice at the marginal glacier allows easier (and greater) blister expansion because of the lower ice overburden pressure.

7.3.2 *Short-term hydrological development (stage 3)*

The blister dispersal times for the four model geometries are plotted in Figure 7.2 d. For both the F-Lake model geometries (1 and 2), the runs with outlet pressure at overburden do not allow blister dispersion within stage 3 of the modelling. However, dispersion occurs in <40 hours for model runs with the outlet pressure $< 0.8P_i$. The tidewater glacier blister disperses between 35 and 40 hours. However, the marginal glacier blister is dispersed much more quickly in $\sim$9 hours. The quicker blister dispersion in the marginal glacier is due to a combination of both a low outlet pressure that creates a strong pressure gradient in the basal system and the lower ice uplift in stage 2 of the modelling creating a thinner blister; ice uplift is smaller in the marginal glacier model due to the ice thickness, which allows easier blister expansion without the same rate of hydraulic jacking found in model geometries 1–3 that have thicker ice.

The channel growth in the marginal glacier model over 10 hours of drainage is greater than in the other model geometries (the marginal channel grows by 0.13 m^2 over 10 hours, see Fig. 7.2 c). This is likely due to the strong pressure gradient

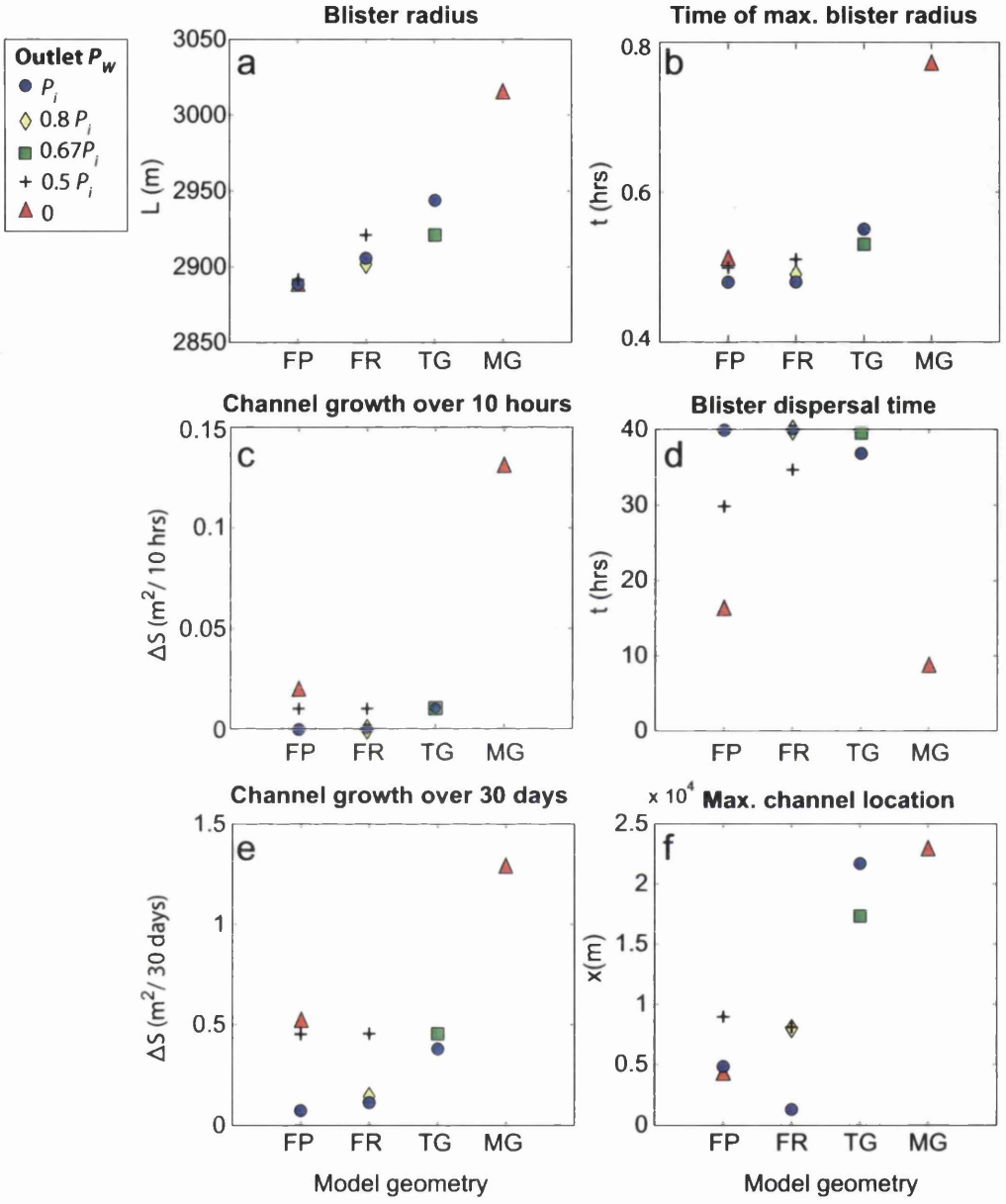

Figure 7.2: *Baseline outputs for the F-Lake planar (FP), the F-Lake real topography (FR), the tidewater glacier (TG) and the marginal glacier (MG) models. The plotted variables are the primary indicators of hydrological development during and after the modelled lake drainage events (see Section 6.5). Outputs for different model outlet pressures are indicated by the coloured markers.*

created by the atmospheric outlet. However the F-Lake planar run with an outlet at atmospheric pressure produces a much smaller channel that grows 0.02 m^2 over 10 hours. Therefore the thinner ice and steeper surface gradient in the marginal glacier model geometry compared to the F-lake site must also have a strong influence on channel growth. The channel growth in the remaining model geometries (1–3) are all insignificant at <0.02 m^2 growth over 10 hours of overpressurised conditions.

7.3.3 *Seasonal hydrological development (stage 4)*

Over 30 days of drainage, the pattern seen for short-term (stage 3) conduit growth is maintained (Fig. 7.2 e). The marginal glacier model produces the greatest conduit growth of 1.3 m^2 over the 30 days following lake drainage. The remaining model geometries have much less growth (of <0.6 m^2) over the same period. The pattern in channel growth is likely due to the difference in ice thickness and surface slope in the model geometries. For the F-Lake planar model (geometry 1), having an outlet pressure at atmospheric pressure does not cause much greater growth than an outlet pressure at 0.5 P_i (i.e. there is only 0.06 m^2 greater growth over 30 days for the atmospheric outlet system). For both the F-Lake case-study model geometries, with pressures at $\geq 0.8 P_i$, conduit growth is small at <0.14 m^2 over 30 days. Conduit growth in the tidewater glacier is greater than at F-Lake for similar outlet pressures, with 0.38 m^2 of growth over 30 days for a floating margin at overburden. This greater growth than the inland ice site is likely due to the steeper surface profile in the tidewater glacier. It therefore appears that conduit growth in the F-Lake models is hampered primarily by the lack of surface slope in comparison to the tidewater glacier and secondarily by the thicker ice in comparison to the marginal glacier.

The locations of the maximum channels grown in the different model geometry runs are shown in Figure 7.2 f; channel development over the 30 days following lake drainage can also be seen in Figure 7.3. The F-Lake models have the largest channels towards the beginning of the spatial domain (Fig. 7.3 b and e), whereas both the tidewater and marginal glaciers have greatest channel growth near to the ice margin (Fig. 7.3 h and k). In the models with steepening surface slopes towards the glacier terminus (geometries 3–4), the increase in hydraulic potential gradient with steeper surface slopes drives greater channel growth. However, in the inland ice cases (geometries 1–2), channel growth is driven primarily by the pressure gradient imposed by the water input at the model upper boundary. The location of the

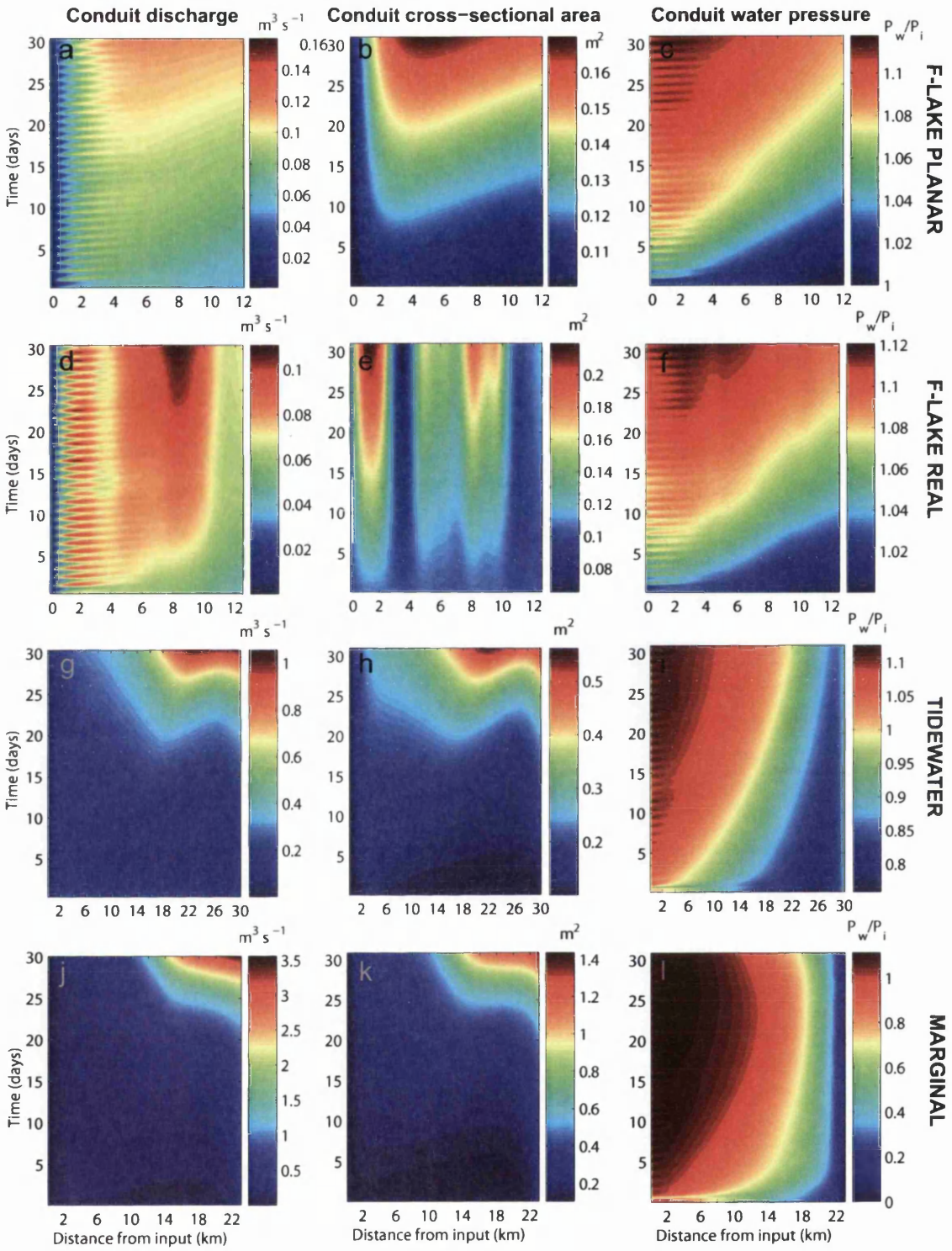

Figure 7.3: *Distance-time plots from stage 4 baseline model runs including conduit discharge, cross-sectional are and water pressure. a)–c) F-Lake planar (geometry 1) outputs for $P_{out} = P_i$; d)–f) F-Lake real (geometry 2) outputs for $P_{out} = P_i$; g)–i) Tidewater glacier (geometry 3) outputs for $P_{out} = P_i$ (i.e. a floating margin); j)–l) Marginal glacier (geometry 4) outputs for $P_{out} = 0$.*

largest channel in the F-Lake real topography model differs from the F-Lake planar model because of the highly variable basal topography preventing conduit growth on reverse slopes (Fig. 7.3 e).

7.4 Parameter sensitivity tests

In this section, the sensitivity test outputs from the coupled hydrological model are presented. The choice of parameter ranges that are applied to the four model geometries are described in Section 6.2. Each variable is tested against the baseline parameter values (see Table 6.2) by running the full four-stage suite of models, producing a large volume of outputs. The variability of parameters produces similar relative outputs (although with different magnitudes) for the four model geometries; the impact of the parameters on drainage development is therefore discussed here independent of model geometry. The conduit growth over the short- (10 hour) and long- (30 day) term are the most important variables for addressing the aims outlined in Section 7.1 and are therefore plotted in Figures 7.5 and 7.6 for the F-Lake planar topography model; Figures 7.8 and 7.9 for the F-Lake real topography model; Figures 7.10 and 7.11 for the tidewater glacier model; and Figures 7.13 and 7.14 for the marginal glacier model. The remainder of the model results discussed in this section can be found in Tables C.1–C.4.

7.4.1 *Young's modulus (E)*

Lake drainage (stage 2): An E value of 3 GPa causes the blister uplift, horizontal separation and lake drainage to occur much more rapidly than seen in the GPS or lake drainage records. This can be seen in Figures 7.4 b, c and d which show outputs for the baseline F-Lake planar model with an outlet pressure at overburden. In essence, the modelled ice is very elastic and can allow blister growth at a rapid rate. In comparison, an E value of 6.2 GPa produces uplift and horizontal displacement which match the measured values closely in terms of timing and gradient. With E=8.8 GPa there is a delay in the modelled ice uplift and horizontal separation due to slow initial blister growth (as a result of the stiff ice).

Short-term hydrological development (stage 3): Conduit growth over 10 hours varies by $<0.01\,m^2$ as a result of E value (see Figs. 7.5 b, 7.8 b, 7.10 b and

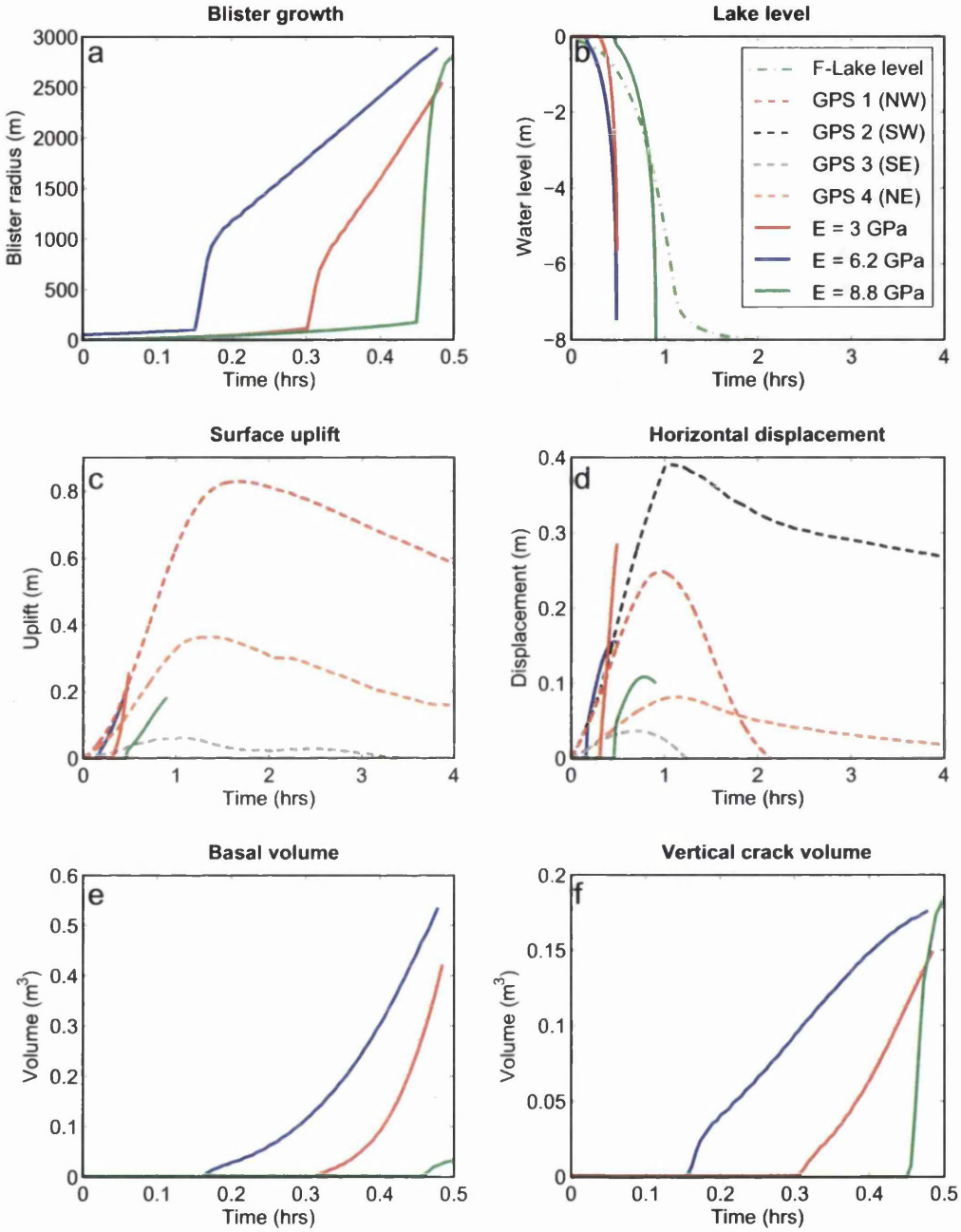

Figure 7.4: *Blister model outputs for the baseline F-Lake planar geometry with an outlet pressure at overburden. The model is run for Young's modulus values of 3 GPa (red curves), 6.2 GPa (blue curves) and 8.8 Gpa (green curves). Recorded F-Lake water level is shown by the green dashed curve. Surface GPS records are shown by the dashed red (GPS 1), black (GPS 2), grey (GPS 3) and orange curves (GPS 4).*

7.13 b) However, due to the difference in blister radius at the end of stage 2, a higher E value causes slower dispersion of the pressurised blister.

Seasonal hydrological development (stage 4): Variability in conduit growth over 30 days of drainage is $<0.08\,m^2$ as a result of the choice of E value, because this parameter impacts only the stage 2 blister growth (see Figs. 7.6 b, 7.9 b, 7.11 b and 7.14 b).

7.4.2 *Creep parameter (A)*

The creep parameter was initially tested for the F-Lake planar geometry with outlet water pressure at overburden. It was found that there was no significant difference in the outputs due to changing the creep parameter. As a result, this parameter was not tested in the remaining three model geometries.

7.4.3 *Geothermal heat flux (Q_G)*

Geothermal heat flux was initially tested for the F-Lake planar geometry with P_{out}=P_i. There was no significant difference in the outputs for any of the model stages as a result of changing the geothermal heat flux. Therefore the geothermal parameter was not tested for the remainder of the model geometries.

7.4.4 *Manning roughness (n')*

Lake drainage (stage 2): As n' only affects the rate of water flow through conduits, this parameter has little impact on the blister growth.

Short-term hydrological development (stage 3): During the development of the flowband hydrological system, the roughness parameter begins to impact the growth of conduits. Within the initial 10 hours of drainage, lower n' values cause growth of larger channels due to the smoother walls that allow higher fluxes of water, which in turn cause greater melt (see Figs. 7.5 d, 7.8 d, 7.10 d and 7.13 d). The pressurised blister is also dispersed faster in a system with a lower n' due to the higher water flux through the channels.

Seasonal hydrological development (stage 4): It is with the longer diurnal

meltwater inputs that the impact of n' is more apparent (see Figs. 7.6 d, 7.9 d, 7.11 d and 7.14 d). Lower n' values (smoother channel walls) allow significantly more channel growth than higher values (rougher channel walls). For the smoothest channel walls ($n' = 0.01\,\mathrm{s\,m^{-3}}$) the conduit cross-sectional area after 30 days is, in some cases, smaller than the maximum channel size (see Tables C.1–C.4), which occurs earlier in the model run. This latter result suggests that the system has fully equilibrated to the water flux from the lake drainage and the following surface water input so that variability in channel cross-sectional area closely echoes changes in surface air temperature and related melt. The faster water flux through the system due to the smoother channel walls therefore appears to encourage hydrological equilibration.

7.4.5 *Nikuradse roughness height (k)*

Lake drainage (stage 2): A lower k value (a smoother ice-bed interface for blister flow) allows the blister to reach its maximum extent more rapidly than a higher k. However, the maximum blister radius and uplift varies little as a result of k.

Short-term hydrological development (stage 3): There is little impact of k on the blister dispersion, with less than two hours difference in full dispersion time within model geometry runs. There is also $<0.01\,\mathrm{m^2}$ difference between the growth of conduits over 10 hours as a result of k within each model geometry (see Figs. 7.5 e, 7.8 e, 7.10 e and 7.13 e).

Seasonal hydrological development (stage 4): Conduit growth over 30 days differs by $<0.01\,\mathrm{m^2}$ as a result of varying k (see Figs. 7.6 e, 7.9 e, 7.11 e and 7.14 e).

7.4.6 *Flowband hydraulic conductivity (K)*

Lake drainage (stage 2): A lower K allows faster blister growth as less water is removed from the blister by the flowband during growth. However, maximum blister size and uplift is not consistently associated with a particular K value; this suggests that the model geometries and outlet pressure conditions have more impact on the blister size and uplift than the hydraulic conductivity of the distributed system.

Short-term hydrological development (stage 3): A higher K allows faster blister dispersion, and channel growth over 10 hours is less for higher K systems than those with lower K (see Figs. 7.5 a, 7.8 a, 7.10 a and 7.13 a). Because a distributed

system with higher K allows more water through-flow it therefore becomes less pressurised than systems with lower K; a lower pressure distributed system would not encourage as much exchange with the conduit system and therefore discourage conduit growth.

Seasonal hydrological development (stage 4): The smallest channel growth over 30 days is found with the highest K systems. However, as can be seen from Figs. 7.6 a, 7.9 a, 7.11 a and 7.14 a, the greatest conduit growth over 30 days is not always associated with the smallest K value. This result suggests that in some tests, the pressure gradient imposed by the model outlet pressure might drive substantial volumes of water through the system. The conduits are then not sufficiently pressurised to allow higher melt rates; this is despite greater exchange between a pressurised distributed system and the conduit due to the smaller hydraulic conductivity of the sheet.

7.4.7 *Critical flowband sheet thickness (h_c^{sh})*

Lake drainage (stage 2): Maximum blister size or the time for full lake drainage is not consistently associated with thicker or thinner flowband water sheets. As a result, the model geometries and outlet pressure conditions appear to have more impact on the drainage development than the sheet thickness during the initial stages of lake drainage.

Short-term hydrological development (stage 3): For higher h_c^{sh} values, the blister is dispersed more quickly. In the case of h_c^{sh}= 0.4 m, dispersion in all cases occurs in <4 hours. In most tests, channel growth over 10 hours is greatest for the smallest water sheet thickness, h_c^{sh}= 0.05; however, in a couple of scenarios the greatest growth is for h_c^{sh}= 0.15 (see Figs. 7.5 c, 7.8 c, 7.10 c and 7.13 c).

Seasonal hydrological development (stage 4): Again, in most cases, the largest channels are seen in the thinnest sheet (see Figs. 7.6 c, 7.9 c, 7.11 c and 7.14 c). This is due to the higher pressures in a thinner sheet that results in higher water flux into the relatively lower pressure conduit.

7.4.8 *Initial channel condition (S_ϵ)*

Lake drainage (stage 2): There is no discernible pattern of change as a result of S_ϵ size during the blister growth.

Short-term hydrological development (stage 3): In general, larger initial S_ϵ allows faster blister dispersion. Over the 10 hours following lake drainage, the systems with S_ϵ=1 m^2 see the greatest channel growth (see Figs. 7.5 h, 7.8 f, 7.10 h and 7.13 h). For S_ϵ =10 m^2, most of the model runs see channel shrinkage rather than growth. Although larger channels have more surface area available for melting, with channels of 10 m^2 there appears to not be sufficient water in the conduits to maintain pressure against creep closure.

Seasonal hydrological development (stage 4): Larger S_ϵ causes larger maximum channel cross-sectional areas (see Tables C.1–C.4). However, for S_ϵ=10 m^2, this maximum conduit occurs at the beginning of stage 4 in all model runs, after which the channel size rapidly shrinks due to insufficient water flow maintain pressure in the channels. For a conduit of S_ϵ=1 m^2 however, growth over 30 days is greater than that for S_ϵ=0.1 m^2 because of the larger cross-sectional area available for melting; therefore few model outputs show shrinkage for S_ϵ=1 m^2 (see Figs. 7.6 h, 7.9 f, 7.11 h and 7.14 h).

7.4.9 *Flowband width (W)*

Lake drainage (stage 2): The overlap volume incorporated by the blister as it expands into the flowband domain is greater for wider flowbands. Therefore a wider fixed flowband allows faster blister growth.

Short-term hydrological development (stage 3): The time for blister dispersion is related closely to the size of the blister radius in stage 2 and there is no pattern in dispersion rate with W. The W parameter impacts channel growth over 10 hours by <0.01 m^2 within model geometry runs (see Figs. 7.5 f, 7.10 f and 7.13 f).

Seasonal hydrological development (stage 4): Narrower flowband widths allow substantially more conduit growth than wider flowbands (see Figs. 7.6 f, 7.11 f and 7.14 f); this result is due to the lower capacity for water input into a narrower flowband, which causes higher water pressure and therefore greater exchange with the relatively lower pressure conduit.

7.4.10 *Lake Volume (V_0)*

Lake drainage (stage 2): The lake volume directly affects the rate and amount of uplift possible during lake drainage. Smaller lake volumes allow little uplift and produce a much smaller size of blister than larger lake volumes.

Short-term hydrological development (stage 3): For smaller lake volumes, the blister dissipates very rapidly due to both the thinner layer of blister water and also the reduced blister extent. Channel growth over 10 hours is not always greatest for the largest lake volume (see Figs. 7.5 g, 7.10 g and 7.13 g). For some of the model runs, because the smaller lake volumes dissipates the blister very quickly (in less than an hour for all model geometries) the conduit growth over 10 hours is also as a result of stage 4 diurnal water input rather than just the lake drainage water. Therefore the apparently larger conduit growth over the short-term for smaller lake volumes is an artefact of the modelling approach and therefore is not included in the final analysis (Section 7.7).

Seasonal hydrological development (stage 4): The maximum conduit size is greater for larger lake volumes due to a more highly pressurised hydrological system imposed by the lake overpressure and the volume of water input to the bed (see Figs. 7.6 g, 7.11 g and 7.14 g).

7.5 Model geometry sensitivity tests

In this section, the model-specific results from the sensitivity tests are reported, beginning with the F-Lake case-study models (geometries 1 and 2, reported in Sections 7.5.1 and 7.5.2, respectively), which have the most well-constrained inputs and geometric data. The tidewater glacier and marginal glacier models (with results reported in Sections 7.5.3 and 7.5.4, respectively) are simplified geometries and have been constructed in order to tests the impact on ice geometry on hydrological development (see Section 6.2).

It is the difference in channel growth following lake drainage in the short- and long-term that is of most interest when comparing the outputs from the modelled geometries. As a result, in this section, only the stage 3 and stage 4 modelled outputs are discussed. The maximum channel growth over 10 hours and 30 days following drainage is given for each model geometry in Table 7.1, along with the

Table 7.1: *Coupled hydrological model maximum channel growth and associated parameters for all sensitivity tests applied to the four modelled geometries.*

		10 hours		30 days	
Model geometry	$\frac{P_w}{P_i}$	Max. growth (m^2)	Parameter	Max. growth (m^2)	Parameter
1 (FP)	1	0.01	S_ϵ=1 m^2	0.96	S_ϵ=1 m^2
	0.5	0.04	$n' = 0.01\,s\,m^{-3}$	0.76	$V_0 = 3.8 \times 10^7 m^3$
	0	0.14	S_ϵ=1 m^2	1.50	W = 500 m
2 (FR)	1	0.05	S_ϵ=1 m^2	1.01	S_ϵ=1 m^2
	0.8	0.02	S_ϵ=1 m^2	1.30	S_ϵ=1 m^2
	0.5	0.03	$n' = 0.01\,s\,m^{-3}$	1.55	$n' = 0.01\,s\,m^{-3}$
3 (TG)	1	0.13	S_ϵ=1 m^2	1.92	$n' = 0.01\,s\,m^{-3}$
	0.67	0.05	S_ϵ=1 m^2	1.51	h_c^{sh} =0.05 m
4 (MG)	0	22.18	S_ϵ=10 m^2	3.44	W = 500 m

parameters that caused the larger growth.

7.5.1 *F-Lake planar topography (geometry 1) results*

The geometry 1 model is used to examine the case-specific F-Lake drainage with well-constrained model inputs, but also the more general case of inland ice lake drainage events. As a result, the impact of different flowband widths and lake volumes are also tested in the F-Lake planar model; these results can then be compared with similar sensitivity tests for the tidewater glacier and marginal glacier models.

Short-term hydrological development (stage 3)

Over 10 hours of drainage, the largest channel growth occurs in the system with atmospheric pressure at the outlet, as shown in Figure 7.5 and Table 7.1; the parameter that produced the largest growth within this system is S_ϵ=1 m^2 (which allows 0.14 m^2 of growth over the 10 hour period, Fig. 7.5 h). The remainder of the parameters for the P_{out}=0 system allow channel growth of $\leq$0.07 m^2 over 10 hours. With P_{out}=0.5P_i, the greatest channel growth occurs in the system with smooth channel walls (i.e. a Manning roughness value of n'=0.01 $s\,m^{-3}$), which produces growth of 0.04 m^2 over 10 hours (Fig. 7.5 d). The remainder of the parameters in this system allow growth of $\leq$0.02 m^2 over 10 hours. With P_{out}=P_i, all channel growth over the 10 hour period is limited to $\leq$0.01 m^2.

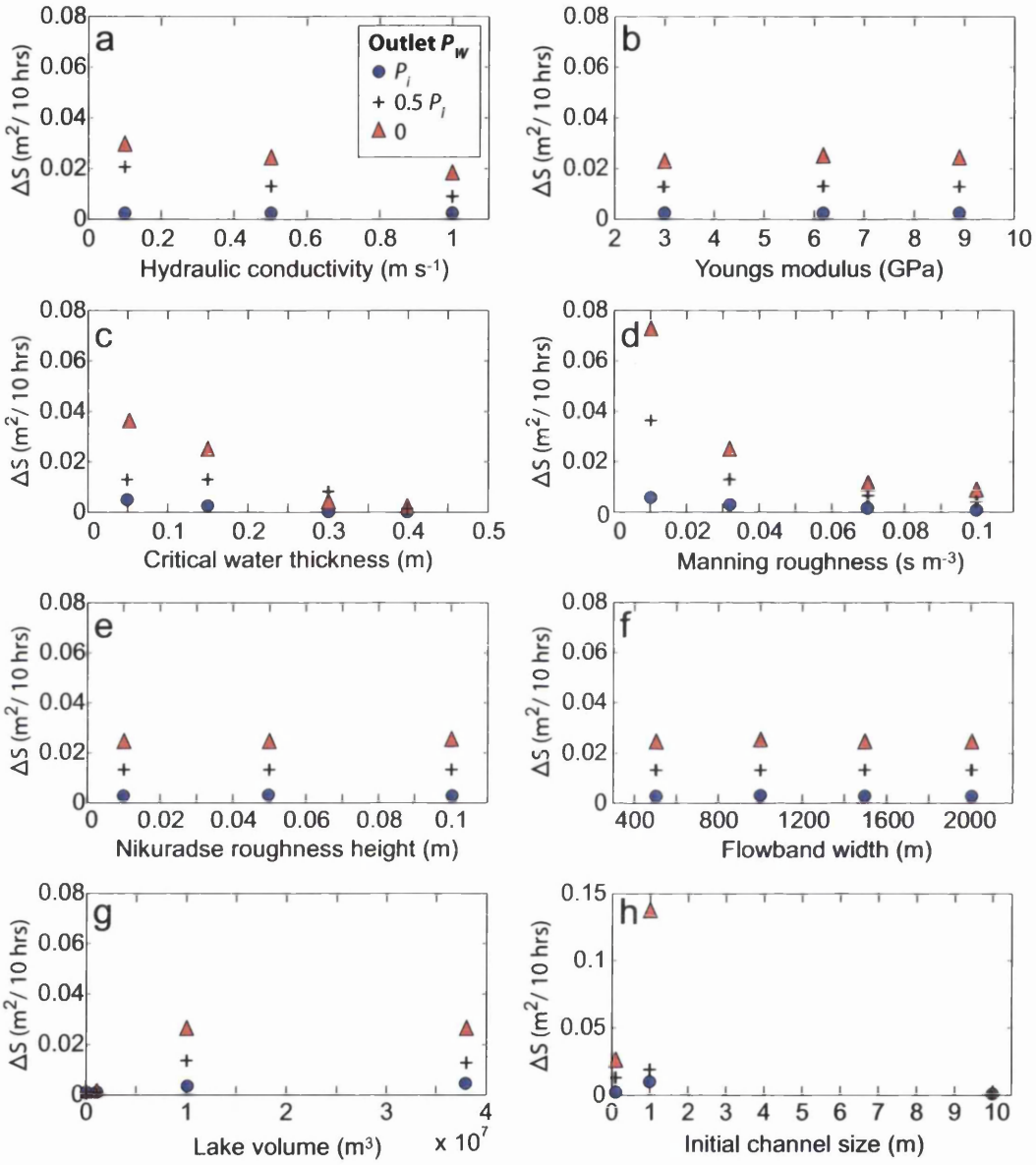

Figure 7.5: *Growth in channel cross-sectional area over the 10 hours following lake drainage initiation for the F-Lake planar model. Outputs for system outlet water pressures of P_i, $0.5\,P_i$ and 0 are plotted as blue circles, black crosses and red triangles, respectively. Each plot represents channel growth when varying one parameter from baseline values.*

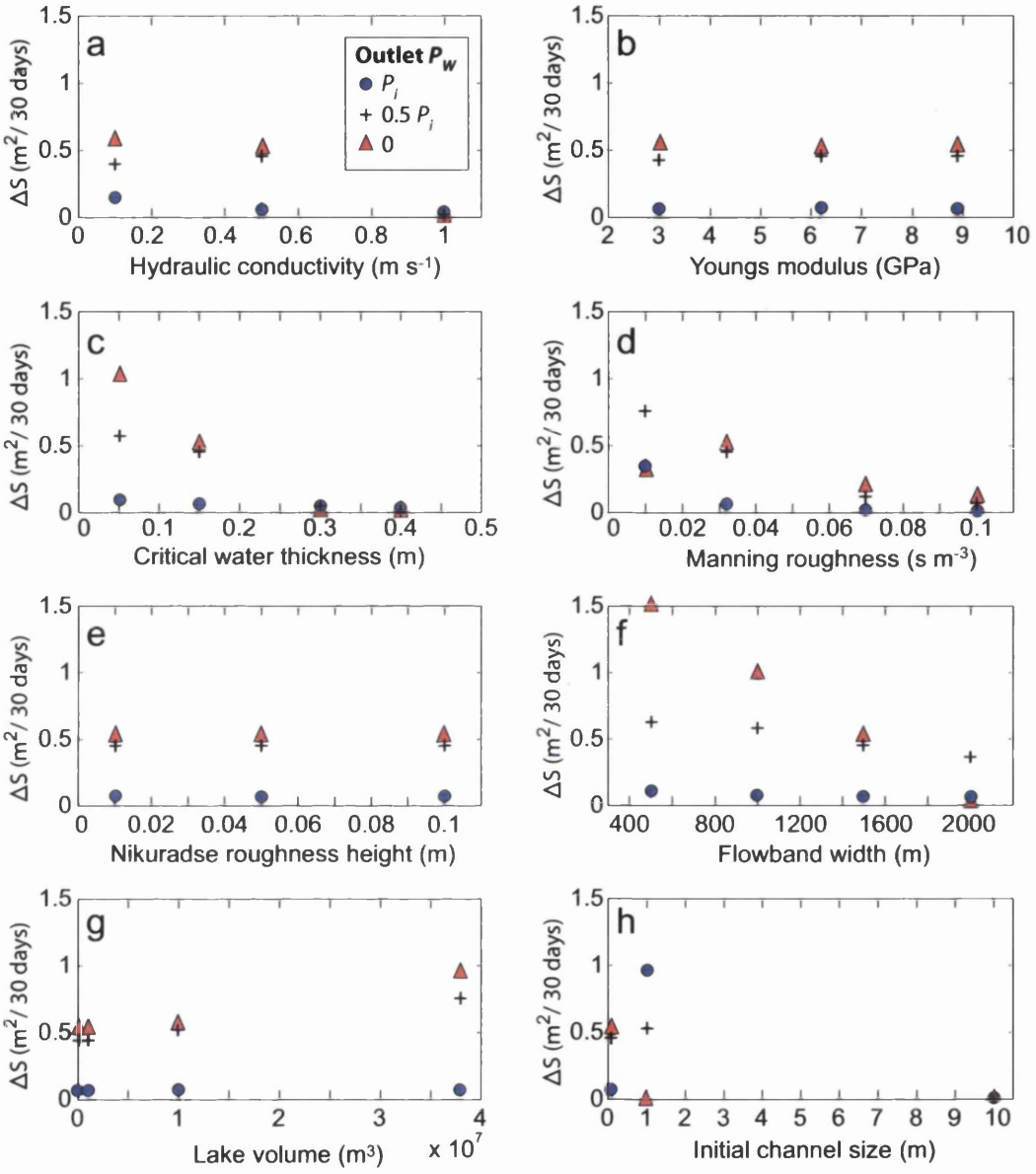

Figure 7.6: *Growth in channel cross-sectional area over the 30 days following lake drainage initiation for the F-Lake planar geometry, driven by surface water inputs. Outputs for $P_{out} = P_i$, $0.5P_i$ and 0 are plotted as blue circles, black crosses and red triangles, respectively. Each plot represents channel growth when varying one parameter from baseline values.*

Seasonal hydrological development (stage 4)

With an outlet pressure at overburden, the maximum channel growth of $0.36\,m^2$ over 30 days is produced with a Manning roughness of n'=$0.01\,s\,m^{-3}$ (discounting the S_ϵ tests, see Fig. 7.6 d). However, an initial channel size of S_ϵ=$1\,m^2$ allows channel growth of $0.96\,m^2$ over 30 days (see Table 7.1 and Fig. 7.6 h); an initial channel size of $10\,m^2$ shrinks throughout the model run. With P_{out}=$0.5\,P_i$, the lowest n' again produces the largest channel growth (including S_ϵ) of $0.76\,m^2$ over 30 days (Fig. 7.6 d). For P_{out}=0, the largest channel growth of $1.50\,m^2$ over 30 days is produced with a flowband width of W=500 m (Fig. 7.6 f).

The only systems that have fully equilibrated to the water input (and therefore have the maximum channel size prior to the end of the stage 4 model run) have an atmospheric outlet pressure (aside from the experiment for n'=$0.01\,s\,m^{-3}$ with P_{out}=$0.5\,P_i$). An example of a semi-equilibrated system is shown in Figure 7.7 for P_{out}=$0.5\,P_i$ and h_c^{sh} $\geq$0.4 m. This system produces the largest channel growth at the end of stage 4, but the channel cross-sectional area and channel water pressure can be seen to vary closely with the water input rate (see Fig. 5.11). The parameters that allow full equilibration when P_{out}=0 are: K=$1\,m\,s^{-1}$, h_c^{sh} $\geq$0.3 m, n'=$0.01\,s\,m^{-3}$ and W=2000 m. These are all systems that allow greater or faster water flux through the sheet and the channel, which coupled with the strong pressure gradient imposed by the atmospheric outlet reduces overpressurisation in the system, necessary for equilibration.

Interpretation

The system with an atmospheric outlet allows greater channel growth for both short- and long-term drainage because of the greater pressure gradient imposed between the model upper and lower boundaries. For the systems with higher pressures at the model outlet (i.e. $\geq$$0.5\,P_i$), the parameters that most directly impact the conduit characteristics such as roughness and the initial size are most important for channel growth over both the lake drainage and seasonal time-scales. However, for a low pressure outlet that imposes a strong pressure gradient, it is conditions that cause increased pressurisation in the distributed system such as flowband width and critical sheet thickness that allow the greatest channel growth over the longer term. This, along with shrinkage of channels $\geq$$1\,m^2$ in the low pressure outlet system, suggests that the pressure gradient driving the flux through the channels is sufficiently

large that parameters allowing greater conduit flux do not have much impact on overall conduit growth because faster water flux reduces channel pressure allowing shrinkage.

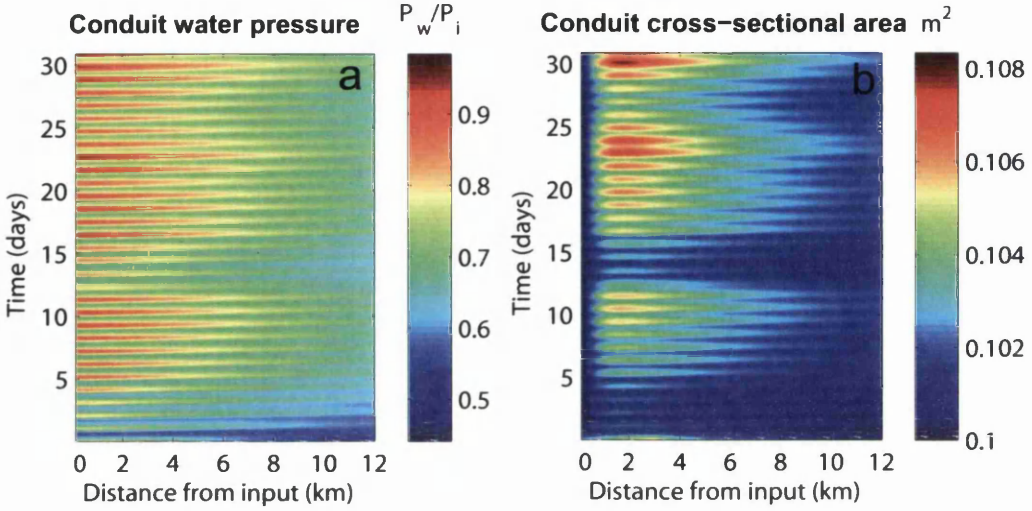

Figure 7.7: *Distance-time plots of a) conduit water pressure and b) conduit cross-sectional area for the F-Lake planar model with an outlet pressure of 0.5 P_i and a critical water thickness of 0.4 m. Variability in conduit growth illustrates semi-equilibration of the system to surface water inputs.*

7.5.2 *F-Lake real topography (geometry 2) results*

Model geometry 2 is based on the surface and basal DEMs for the F-Lake region and therefore is likely to produce more realistic outputs for determining hydrological development in this area. The range of sensitivity experiments for model geometry 2 are the same as performed for model geometry 1, aside from flowband width and lake volume as these are well-constrained for the field site. The outlet pressure condition also differs in geometry 2 as it is unlikely that water pressures would drop below 0.5 P_i ~50 km from the ice margin (see Section 6.2.2); P_{out} is therefore applied at P_i, 0.8 P_i and 0.5 P_i.

Short-term hydrological development (stage 3)

For $P_{out} \geq 0.8\,P_i$, channel growth is $<0.01\,m^2$ over 10 hours for all tests apart from $S_\epsilon \geq 1\,m^2$ (see Fig. 7.8). For $P_{out}=P_i$, a $10\,m^2$ initial channel allows growth of $0.33\,m^2$ over 10 hours and $S_\epsilon=1\,m^2$ allows channel growth of $0.05\,m^2$ over 10 hours (Fig. 7.8 f).

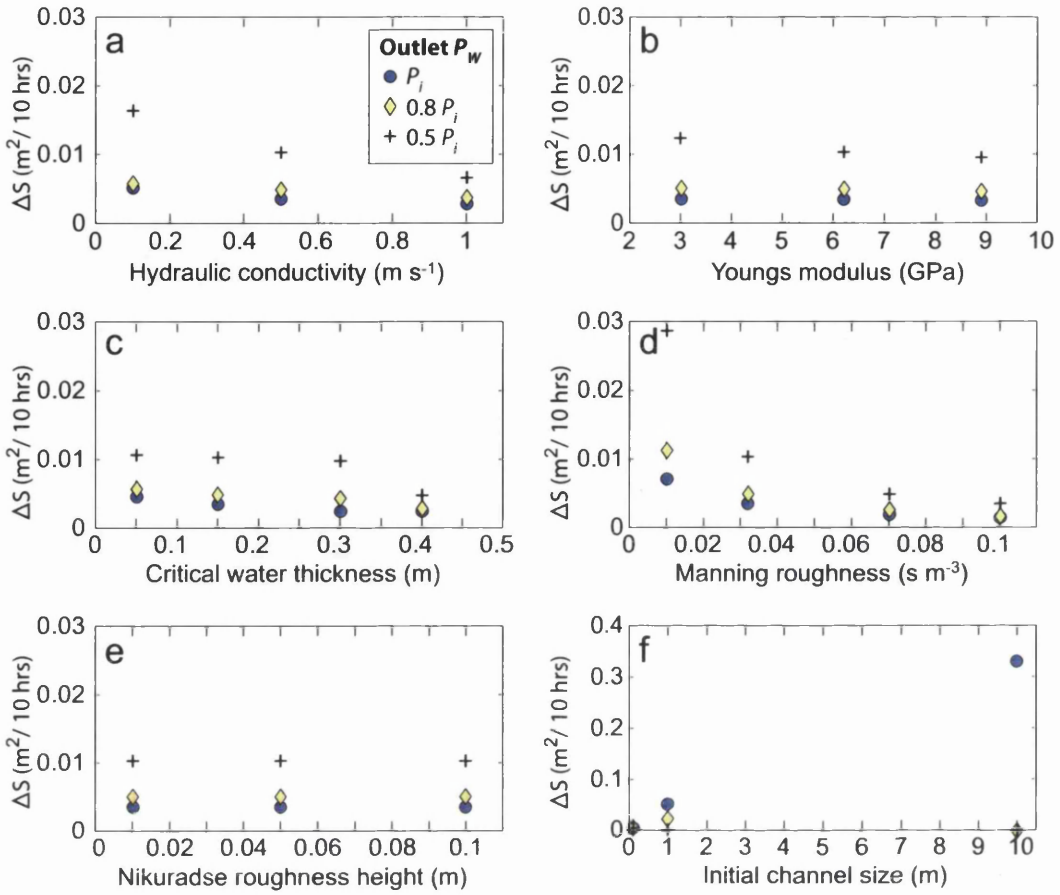

Figure 7.8: *Growth in channel cross-sectional area over the 10 hours following lake drainage initiation for the F-Lake real topography model. Outputs for system outlet water pressures of P_i, $0.8\,P_i$ and $0.5\,P_i$ are plotted as blue circles, yellow diamonds and black crosses, respectively. Each plot represents channel growth when varying one parameter from baseline values.*

With P_{out}=0.8 P_i, the S_ϵ=10 m^2 channel shrinks by 1.95 m^2 over the 10 hour period, but the S_ϵ=1 m^2 channel grows by 0.03 m^2 over the same time. For P_{out}=0.5 P_i, the initial channels $S_\epsilon \geq$1 m^2 shrink; maximum growth is instead seen for a Manning roughness value of n'=0.01 s m^{-3} that allows 0.03 m^2 growth over 10 hours (Fig. 7.8 d; Table 7.1).

Seasonal hydrological development (stage 4)

For the systems with $P_{out} \geq 0.8\,P_i$, the largest channel growth over 30 days is produced with an initial channel size of S_ϵ=1 m^2 (with growth of 1.3 m^2 over 30 days; see Table 7.1 and Fig. 7.9 f). Following this, a Manning value of n'=0.01 s m^{-3} is the

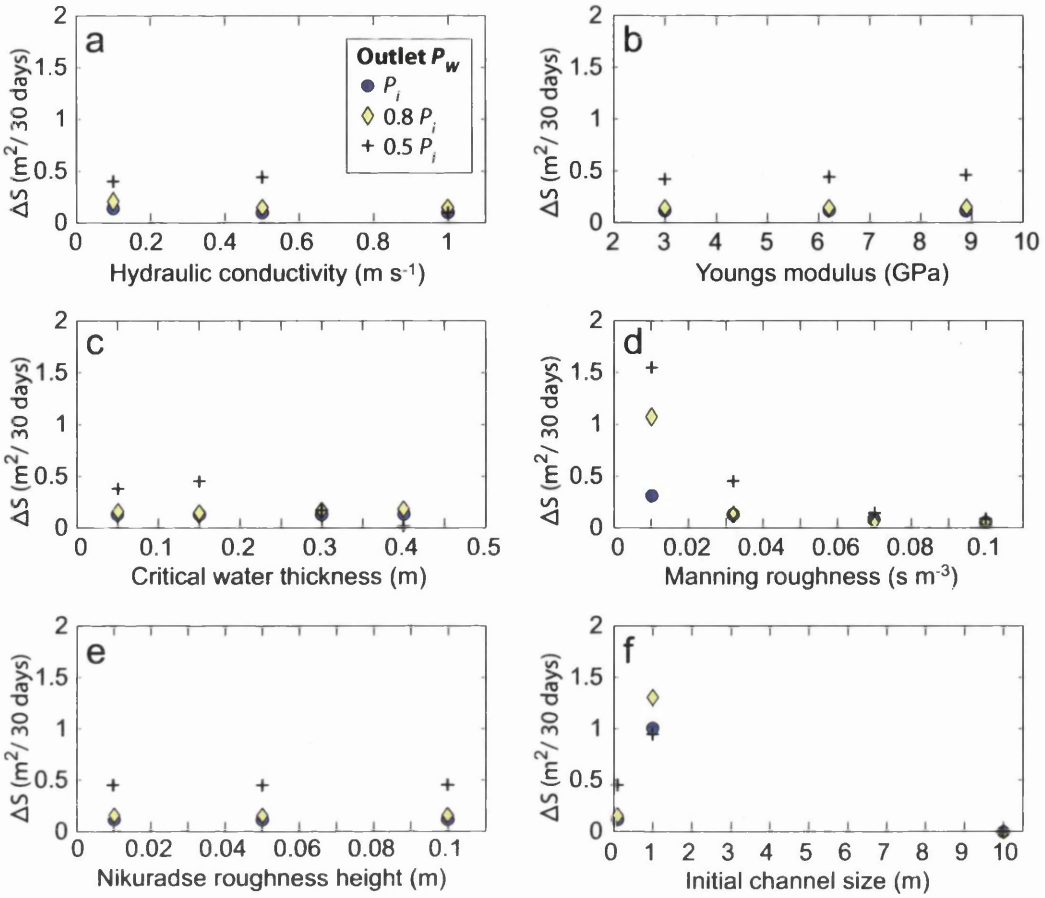

Figure 7.9: *Growth in channel cross-sectional area over the 30 days following lake drainage and driven by surface water inputs for the F-Lake real topography model. Outputs for P_{out}=P_i, 0.8P_i and 0.5P_i are plotted as blue circles, yellow diamonds and black crosses, respectively. Each plot represents channel growth when varying one parameter from baseline values.*

most influential parameter for channel growth (Fig. 7.9 d). With P_{out}=0.5 P_i, this low roughness value allows more growth than a larger initial channel size of S_ϵ=1 m^2 (with 1.55 m^2 and 0.95 m^2 growth over 30 days, respectively). With a initial channel of S_ϵ=10 m^2, all systems have channel shrinkage over the 30 day period.

Interpretation

Compared to the F-Lake planar results (see Section 7.5.1), all the model geometry 2 results show greatest channel growth for the systems that allow greater flux through the channels, i.e. larger initial channel sizes and low channel roughness. The system outlet pressure in the F-Lake real topography model is always $\geq$0.5 P_i and therefore

flux is not driven as quickly through channels by the pressure gradient as in the F-Lake planar model with an atmospheric outlet. Despite this, initial channels of $10\,m^2$ are too large to remained pressurised and therefore do not grow during the longer-term seasonal period in the F-Lake real topography model.

7.5.3 *Tidewater glacier results (geometry 3)*

The range of parameters tested for the tidewater glacier model are the same as for the F-Lake planar model (geometry 1). However, as explained in Section 6.4.9, because of the fictional tidewater glacier geometry, a larger range of flowband widths are tested. Because the tidewater model is based on a simplified geometry rather than a specific region of the GrIS there are some baseline inputs such as the lake volume and the seasonal water runoff that are applied from the F-Lake case-study. Although this might not be the most realistic scenario for the tidewater glacier, it allows comparison between the outputs from all of the model geometries.

Short-term hydrological development (stage 3)

With an outlet at overburden (i.e. a floating tongue), the maximum conduit growth of $0.15\,m^2$ over 10 hours is for the system with S_ϵ=$10\,m^2$ (Fig. 7.10 h). For the systems with S_ϵ=0.1 m^2, the most important parameter for channel growth is a low hydraulic conductivity of K=$0.01\,m\,s^{-1}$, allowing growth of $0.05\,m^2$ over 10 hours (Fig. 7.10 a). For an outlet pressure of $0.67\,P_i$, growth is smaller than for the higher outlet pressure system (maximum growth is $0.08\,m^2$ over 10 hours for a lake volume of $0.01\times10^7\,m^3$; Fig. 7.10 g). The system with an initial channel size of $10\,m^2$ shrunk by $0.95\,m^2$ over the 10 hours following lake drainage for the system with $P_{out} = 0.67\,P_i$.

Seasonal hydrological development (stage 4)

The largest channel growth in the $P_{out} = P_i$ system is for a smooth channel with n'=$0.01\,s\,m^{-3}$, allowing growth of $1.92\,m^2$ over 30 days (Fig. 7.11 d). However, for the $0.67\,P_i$ system, greatest conduit growth is from a thin critical sheet thickness of h_c^{sh} =0.05 m, producing channel growth of $1.51\,m^2$ over 30 days (Fig. 7.11 c).

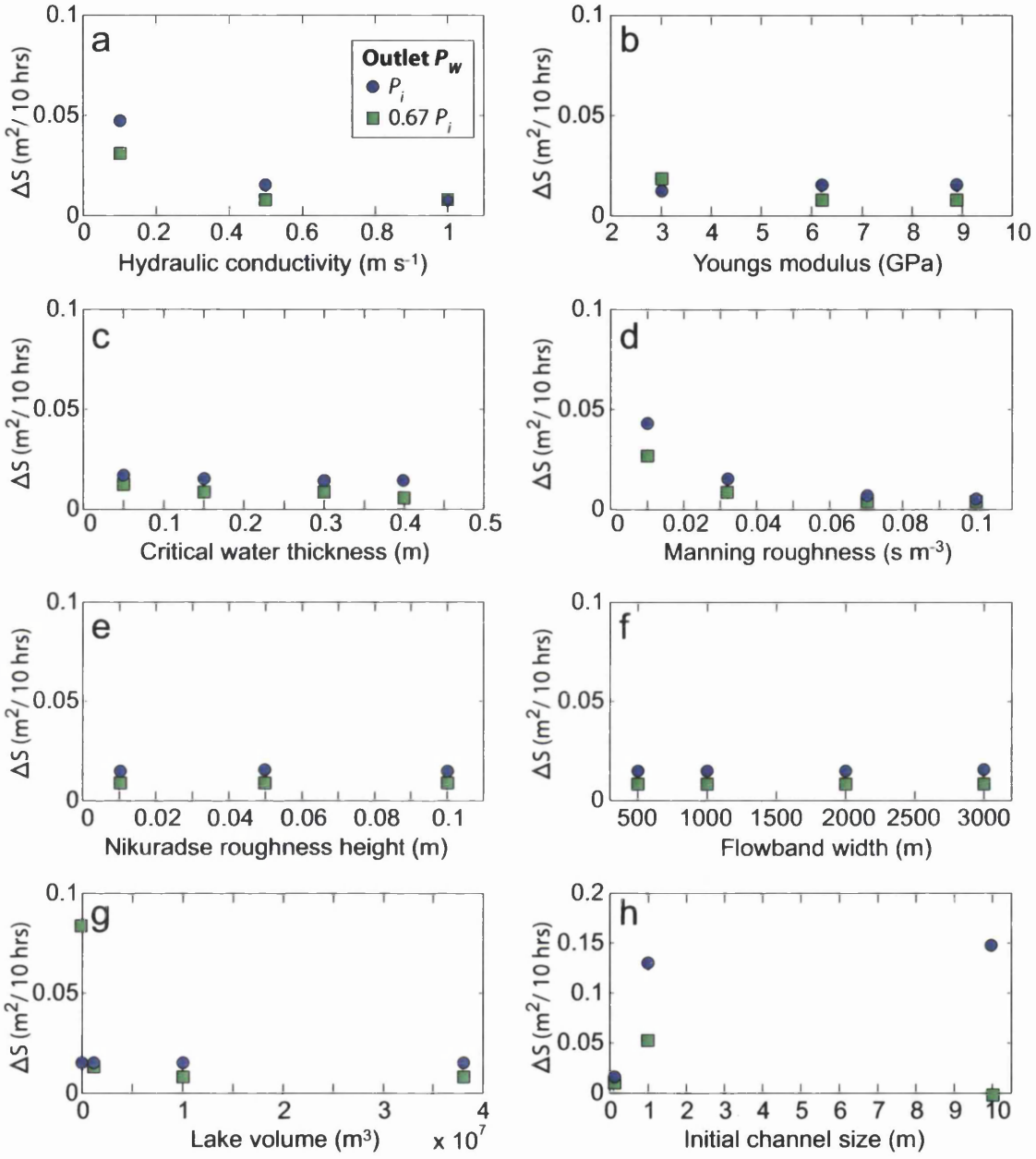

Figure 7.10: *Growth in channel cross-sectional area over the 10 hours following lake drainage initiation for the tidewater glacier model. Outputs for outlet boundary water pressures of P_i and $0.67P_i$ are plotted as blue circles and green squares, respectively. Each plot represents channel growth when varying one parameter from baseline values.*

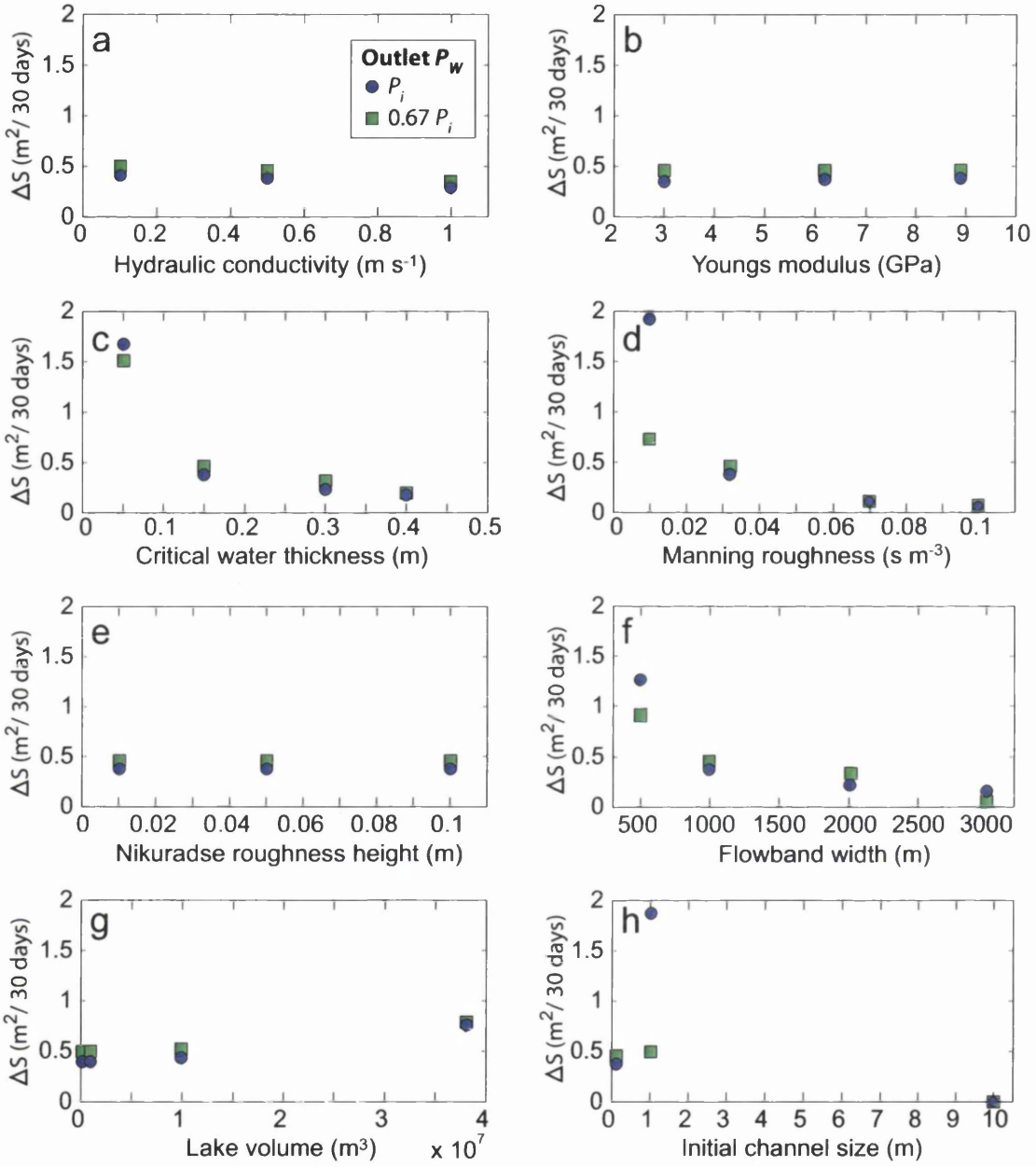

Figure 7.11: *Growth in channel cross-sectional area over the 30 days following lake drainage initiation for the tidewater glacier model, driven by surface water inputs. Outputs for $P_{out} = P_i$ and $0.67P_i$ are plotted as blue circles and green squares, respectively. Each plot represents channel growth when varying one parameter from baseline values.*

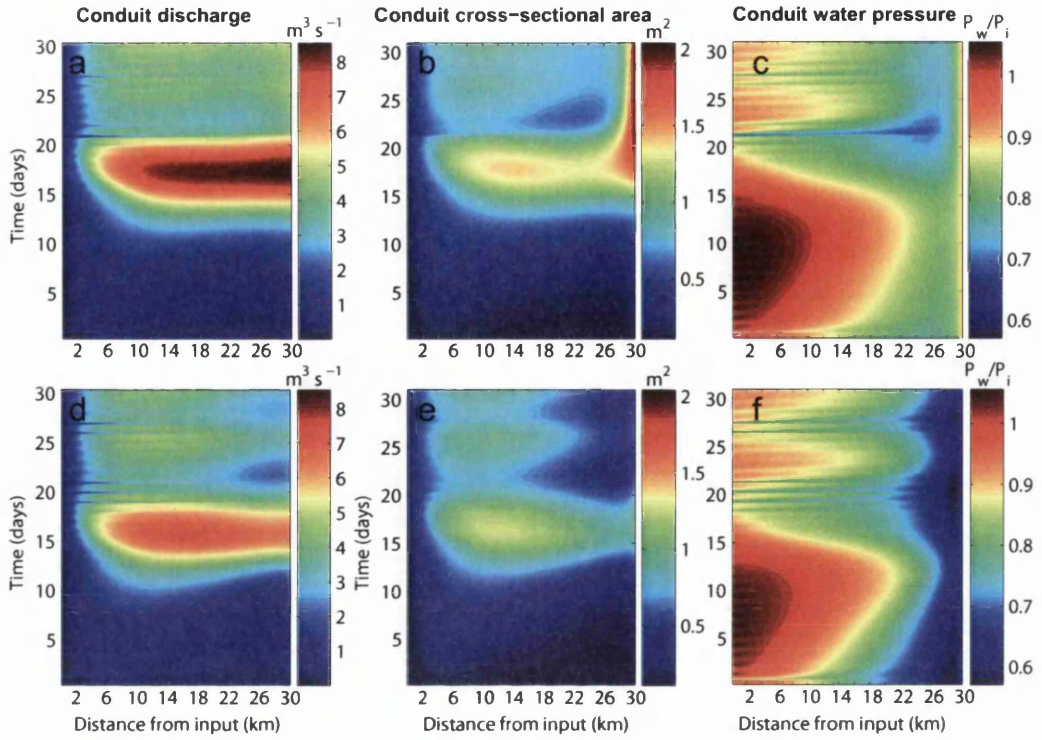

Figure 7.12: *Distance-time plots for the tidewater glacier model with a Manning roughness value of 0.01 s m^{-3} including conduit discharge, conduit cross-sectional area and conduit water pressure for a)–c) a floating outlet pressure of P_i, and d)–f) a grounded outlet pressure of 0.67P_i . With the smoother channel walls (i.e. a low Manning roughness) the system equilibrates to water input so that maximum channel growth occurs ~ 17 days after lake drainage.*

Interpretation

The larger conduit growth for the system with the higher pressure outlet is likely due to the combination of pressure gradient and the steeper surface slope in the tidewater glacier model geometry. A system with P_{out}=0.67 P_i creates a pressure gradient sufficiently steep that larger channels (i.e. 10 m^2) cannot remain pressurised to prevent closure. The greatest channel growth for this lower pressure outlet system over the seasonal time-scale is therefore as a result of conditions creating higher pressures in the distributed system such as low critical sheet thickness (a higher pressure distributed sheet will allow channels to remain pressurised because of greater sheet-to-conduit exchange rates). For the system with $P_{out} = P_i$, over the seasonal time-scale the lower roughness in the channels allows greater melting because, with the smaller pressure gradient across the model domain, channels can remain pressurised more easily and require less exchange with the distributed system to allow higher rates of melting. This can be seen in Figure 7.12, which shows plots of the

model outputs for the tidewater $P_{out} = P_i$ system in a–c and for P_{out}=0.67 P_i in d–f, both run with a Manning roughness value of n'=0.01 s m^{-3}. These systems both equilibrate to the water input, but the $P_{out} = P_i$ system remains pressurised for longer (see Fig. 7.12 c and f) and therefore allows greater channel growth.

7.5.4 *Marginal glacier results (geometry 4)*

As also detailed in Section 7.5.3 for the tidewater glacier model, the marginal glacier model is based on a simplified geometry with some model inputs such as surface runoff and baseline lake volume approximated from the F-Lake case-study. The channel growth over 10 hours and 30 days following lake drainage for the range of sensitivity tests can therefore be directly compared with the outputs for modelled geometries 1–3.

Short-term hydrological development (stage 3)

After 10 hours of drainage, channel growth is greater for the marginal glacier than in the other modelled geometries (see Fig. 7.13 and Table 7.1). The system with an initial channel size of 10 m^2 grows by 22.18 m^2 over 10 hours at the downstream model boundary (Fig. 7.13 h). However, if the initial channel size tests are discounted, a low channel roughness of n'=0.01 s m^{-3} allows growth of 0.18 m^2 over 10 hours, which is also greater than seen with the other model geometry outputs (Fig. 7.13 d).

Seasonal hydrological development (stage 4)

Maximum stage 4 conduit growth is for the system with a flowband width of 500 m, which allows channel growth of 3.44 m^2 over 30 days (Fig. 7.14 f). The system with a thin critical sheet of h_c^{sh} =0.05 m also allows greater channel growth than other tested parameters, with growth of 2.05 m^2 over 30 days (Fig. 7.14 c). The initial channel size of 10 m^2 shrinks throughout stage 4, and therefore, although showing large 'growth' in Figure 7.14 h, this is an artefact of the conduit growth in stage 3 relative to the initial channel size.

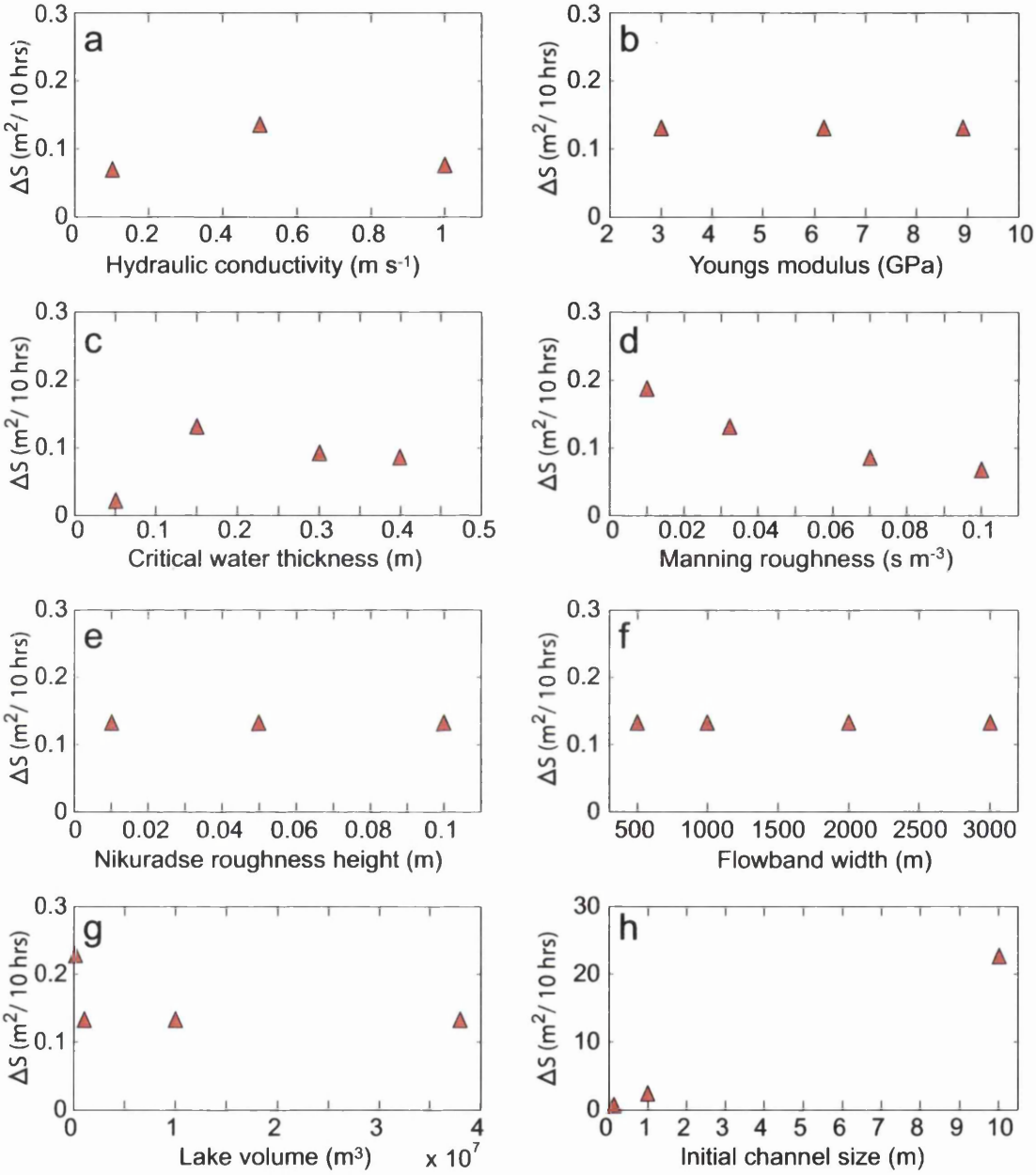

Figure 7.13: *Growth in channel cross-sectional area over the 10 hours following lake drainage initiation for the marginal glacier model. Each plot represents channel growth when varying one parameter from baseline values.*

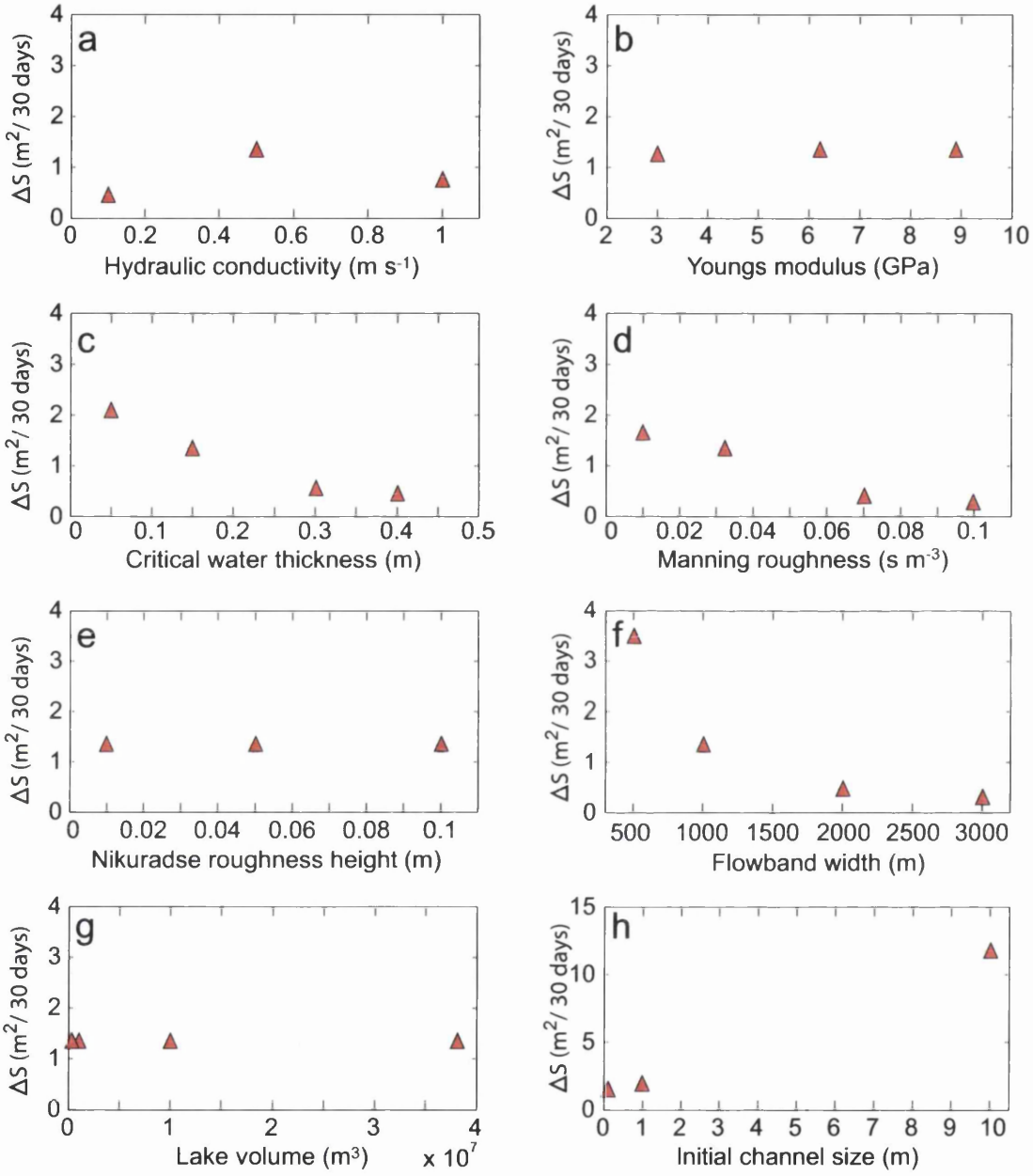

Figure 7.14: *Growth in channel cross-sectional area over the 30 days following lake drainage initiation for the marginal glacier model, driven by surface water inputs. Each plot represents channel growth when varying one parameter from baseline values.*

Interpretation

The conditions during lake drainage in the marginal glacier model allow continued pressurisation of the large initial channel of $10\,m^2$, despite the strong pressure gradient imposed in the model by the atmospheric outlet. There is therefore significant growth of this channel over the 10 hours following lake drainage. Once the lake water is removed from the region however, the large initial channel size of $10\,m^2$ shrinks implying insufficient water is available for continued pressurisation of the channel. Over the longer seasonal time-scale, greater channel growth is primarily as a result of parameters that cause higher pressurisation of the distributed system such as sheet critical thickness and the flowband width; this drives more water into the channels and allows continued pressurisation in the conduits preventing shrinkage. The strong pressure gradient in the marginal glacier model drives sufficient water through conduits that systems with higher sheet-to-conduit exchange allow the greatest conduit wall melting.

7.6 Additional tests

The tests reported in this section are dealt with separately from the parameter sensitivity tests reported in Sections 7.4 and 7.5 because, rather than examining a particular condition at the ice-bed interface or topographical setting for the model (i.e. inland, tidewater or marginal), they are more general tests of the impact of a) the ice surface slope, b) the ice thickness and c) the volume of surface runoff input during the melt-season on subglacial hydrological development.

7.6.1 *Surface slope*

The surface slope tests have only been run on the baseline F-Lake planar topography with tested gradients ranging between 0.5–1.5° (see Fig. 6.1a). Model outputs can be seen in Table C.5 and show that blister dispersal occurs considerably more quickly for higher surface slopes. For example, with P_{out}=P_i, the blister drains ~20 hours more quickly with a surface slope of 1.5° compared to a slope of 0.5°. Similarly, with an outlet pressure of $0.5\,P_i$, drainage occurs 14 hours earlier for the steepest slope compared to the shallowest slope. Over the 10 hours following lake drainage, the channel cross-sectional area expands more quickly for steeper slopes although in

all model runs, channel cross-sectional area growth is $<0.03\,m^2$ over 10 hours (see Fig. 7.15 a).

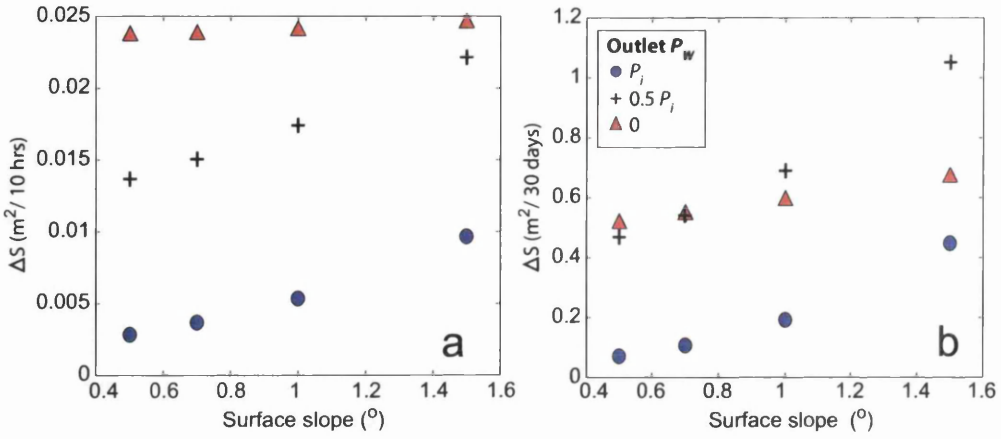

Figure 7.15: *Outputs for the baseline F-Lake planar model runs with different constant surface slopes: a) growth in channel cross-sectional area over the 10 hours following lake drainage initiation, and b) channel growth over the 30 days following lake drainage. Outputs for the systems with outlet water pressures of P_i, $0.5\,P_i$ and 0 are plotted as blue circles, black crosses and red triangles, respectively.*

As shown in Figure 7.15 b, channel growth over the 30 days following lake drainage is greatest for steeper surface slopes, particularly for the P_{out}=$0.5\,P_i$ system: the near-linear increase in channel growth with increasing surface slope is more gradual for outlet pressures of P_i and 0. The reason for this relationship between surface slope and outlet pressure is due to the competing influence between 1) hydraulic potential gradients from the change in surface slope and 2) the spatial gradient in water pressure; with an outlet pressure of $0.5\,P_i$, the surface slope has more influence than outlet pressure on channel growth, whereas the converse is true for an outlet boundary at atmospheric pressure.

7.6.2 *Ice thickness*

The impact of ice thickness on channel growth is tested for the F-Lake planar topography, the tidewater glacier and the marginal glacier models, all run with baseline parameters. As can be seen in Figure 7.16 and Table C.6, there is not a simple relationship between channel growth and the ice thickness. As with the surface slope tests there are competing factors affecting the channel growth rate. For example, in the F-Lake planar model, channel growth is greater for thicker ice in the early stages of lake drainage (apart from 400 m thick ice when the outlet is at atmospheric pres-

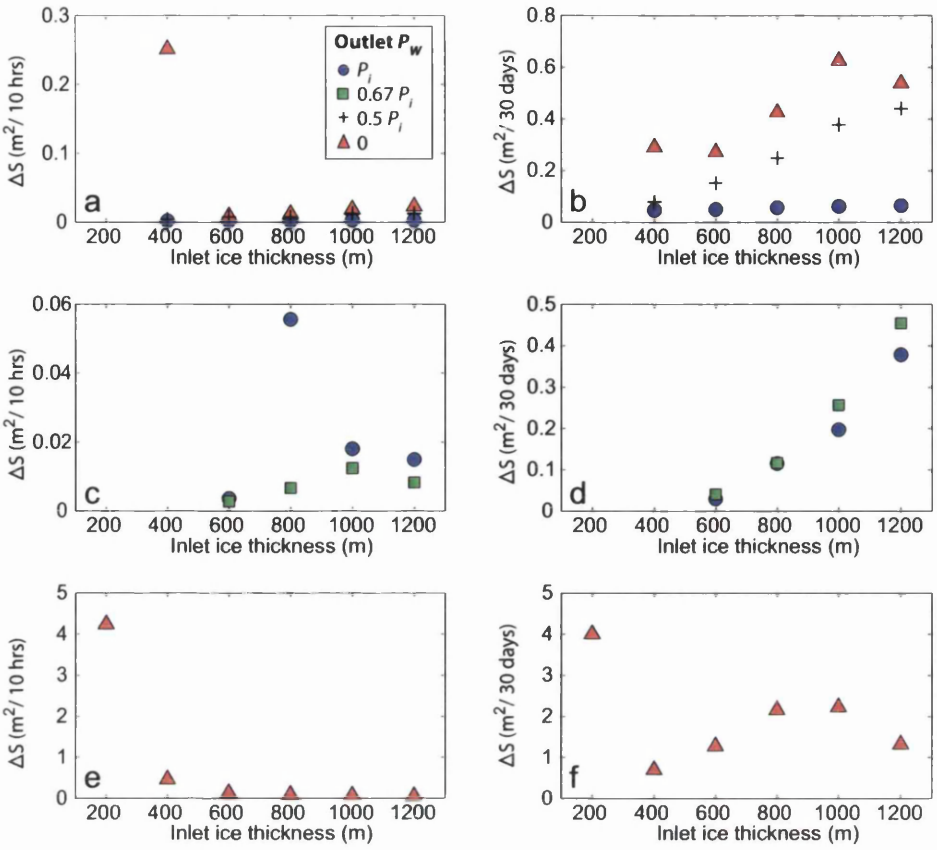

Figure 7.16: *Impact of ice thickness on growth in channel cross-sectional area for the F-Lake planar model over a) 10 hours and b) 30 days; the tidewater glacier model over c) 10 hours and d) 30 days; and the marginal glacier model over e) 10 hours and f) 30 days.*

sure; Fig. 7.16 a). However, it would be expected that the greater overburden from thicker ice would close channels more quickly. As the surface slope is static between thickness tests for the F-Lake planar model, this cannot explain why larger channels generally occur for greater ice thickness. Instead, the gradient in pressure between the inlet and outlet directly influences channel growth; with thicker ice, the relative change between the lake (or diurnal water) overpressure at the upstream inlet and the outlet pressure is greater than it would be for thinner ice. This relationship can be seen in the F-Lake planar model for channel growth both over the 10 hours and 30 days following drainage (Fig. 7.16 a and b). As with the other parameter experiments, a lower outlet pressure allows greater channel growth. However, with an atmospheric outlet, the influence of ice overburden pressure sometimes overrides the impact of the model pressure gradient. As a result, the channel growth for an ice thickness of 1200 m over 30 days is less than for 1000 m; similarly, an ice thickness of 400 m allows greater channel growth than 600 m over both 10 hours and 30 days.

The outputs for the tidewater and marginal glacier are complicated by the ice surface gradient, which becomes steeper with thicker upper boundary ice conditions because the model domain length is maintained throughout these tests. In the tidewater glacier (Fig. 7.16 c and d) the thicker ice (and resulting steeper slopes) allow greater channel growth over the longer term. However, within 10 hours of lake drainage, greatest channel growth is seen for an ice thickness of 800 m and an outlet pressure at overburden; this ice thickness imposes the most effective combination of lower overburden and sufficient surface slope to allow greater channel growth. In comparison, over 10 hours, an ice thickness of 1200 m has enough overburden to restrict short-term channel growth, whereas the surface slope with an ice thickness of 600 m is too shallow to promote channel growth; thus these two tests produce smaller channels than seen with the intermediate ice thicknesses.

With the marginal glacier, over 10 hours of drainage, the steeper surface slope with thicker ice does not appear to enhance channel growth (Fig. 7.16 e). As a result channel growth is greatest for the scenarios with the thinnest ice. However, over 30 days of drainage, the converse is true for ice thicknesses between 400-1000 m (Fig. 7.16 f). With 200 m thickness, the lack of overburden is more important for channel growth than the surface slope and larger channels can be maintained. With thickness >1000 m, the overburden is sufficient that the increase in surface slope does not allow greater channel growth than produced with thinner ice.

These ice thickness tests illustrate that determining the primary controls on channel growth is not simple and is highly dependent on the configuration of the model geometry.

7.6.3 *Runoff*

In order to determine the impact of a full season of surface water input following lake drainage, the baseline models have been run with 90 days of water input. Due to computational time, this experiment could not be run for all of the sensitivity tests. However, the same baseline seasonal experiments have been repeated but with half of the surface water input to determine the impact of the volume of water flowing through the system on the channel growth. Table C.7 shows the maximum conduit size for the full-seasonal water input; the reduced water input; and the 30-day drainage baseline tests. The maximum channel cross-sectional area values for the F-Lake planar, tidewater and marginal glacier runoff tests are also plotted in

Figure 7.17.

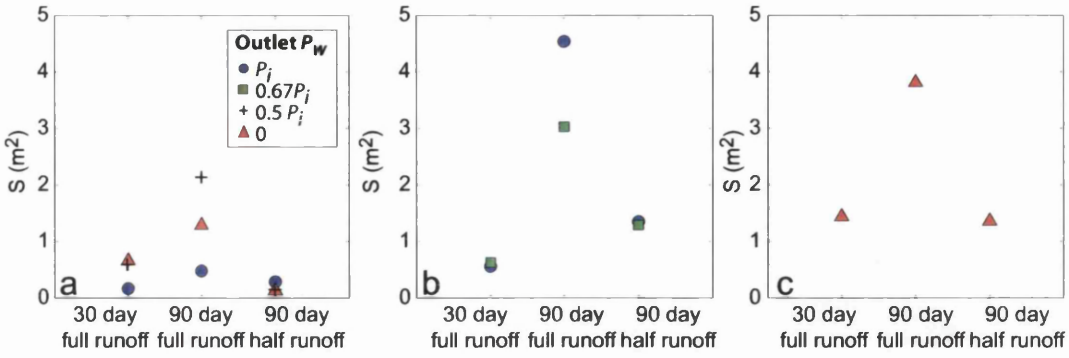

Figure 7.17: *Maximum channel cross-sectional area values as a result of 30 days of runoff following lake drainage, 90 days of (seasonal) runoff and half of the surface water input for 90 days plotted for the a) F-Lake planar model, b) tidewater glacier model and c) marginal glacier model.*

With 90 days of full surface water input, channels are larger than for the 30 days of water input for all model geometries and outlet water pressure conditions. The largest channels of $\sim$4.54 m^2 are seen for the tidewater glacier model with the full seasonal water input. The marginal glacier model has a slightly smaller maximum channel size of $\sim$3.81 m^2. Channels also grow to $>$1 m^2 for the F-Lake planar model when the outlet pressure is $\leq 0.5\,P_i$ over the full season.

With half the runoff for the 90 day season, the maximum channels are, in all cases, smaller than they are for the full seasonal runoff input. In the F-Lake planar model, with half runoff, maximum channel size is $<$0.3 m^2 for all outlet pressure conditions. For the tidewater glacier model, half runoff for the entire season produces larger channels at $\sim$1.35 m^2 than for 30 days of full runoff. However, the smallest channels of $\sim$1.36 m^2 in the marginal glacier model are produced with the seasonal half runoff input.

Figure 7.18 shows distance-time plots for the F-Lake planar model with an outlet pressure of $0.5\,P_i$, run with full runoff for the entire season. The conduit cross-sectional area and discharge can be seen to reach their maximum on day 60 following lake drainage (see Fig. 7.18 a and d). Diurnal variability can be seen in the temporal change in water sheet thickness (Fig. 7.18 c). A cessation of water input (around day 70), that can been seen at DOY 251 in Figure 6.2, causes rapid hydrological shut-down and closure of channels.

Figure 7.19 shows the same model system but run with half the surface water input. Diurnal variability in water thickness, water pressure and conduit cross-sectional

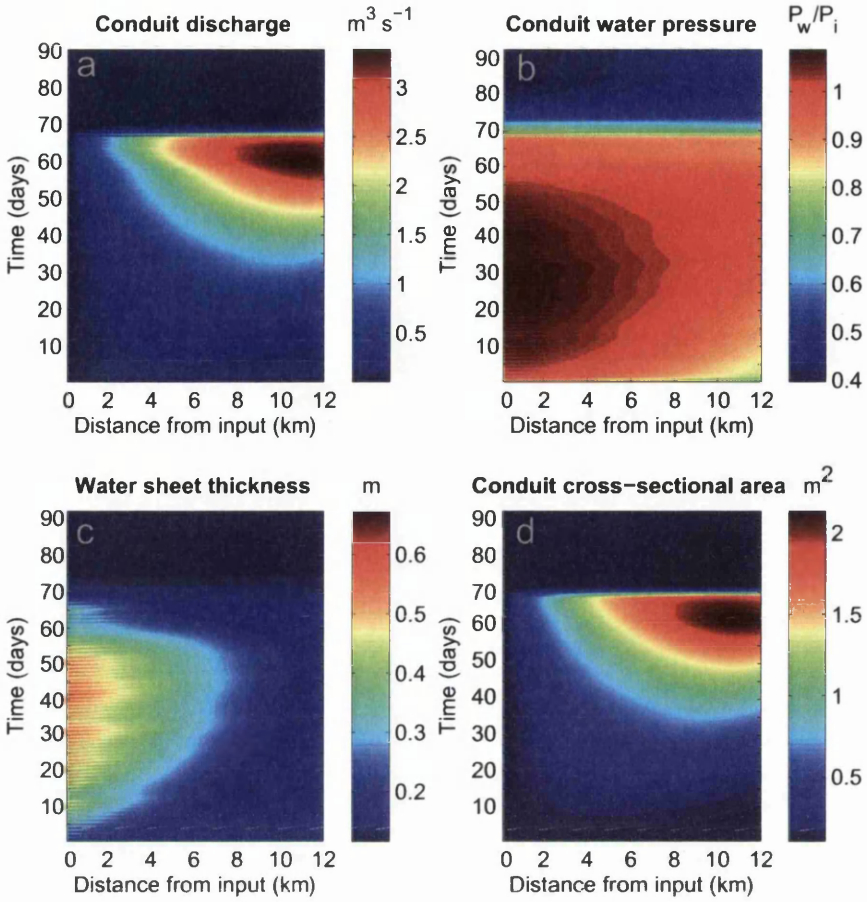

Figure 7.18: *Distance-time plots for the baseline F-Lake planar model and an outlet pressure of $0.5P_i$. This model was run with 90 days of surface water input. Around day 70, the surface water inputs cease due to freezing air temperatures (see Fig. 6.2).*

area can be clearly seen until hydrological shut-down around day 70. This suggests that with smaller water input, the basal system can equilibrate significantly more quickly than for the full runoff scenario.

7.7 Analysis

7.7.1 *Important parameters*

From the sensitivity experiments, several of the parameters stand out as having greater impact on conduit growth than others. Discounting initial channel size, a low Manning roughness of $0.01\,\mathrm{s\,m^{-3}}$ was the most influential parameter for growth within 10 hours of lake drainage for most runs (apart from the tidewater glacier

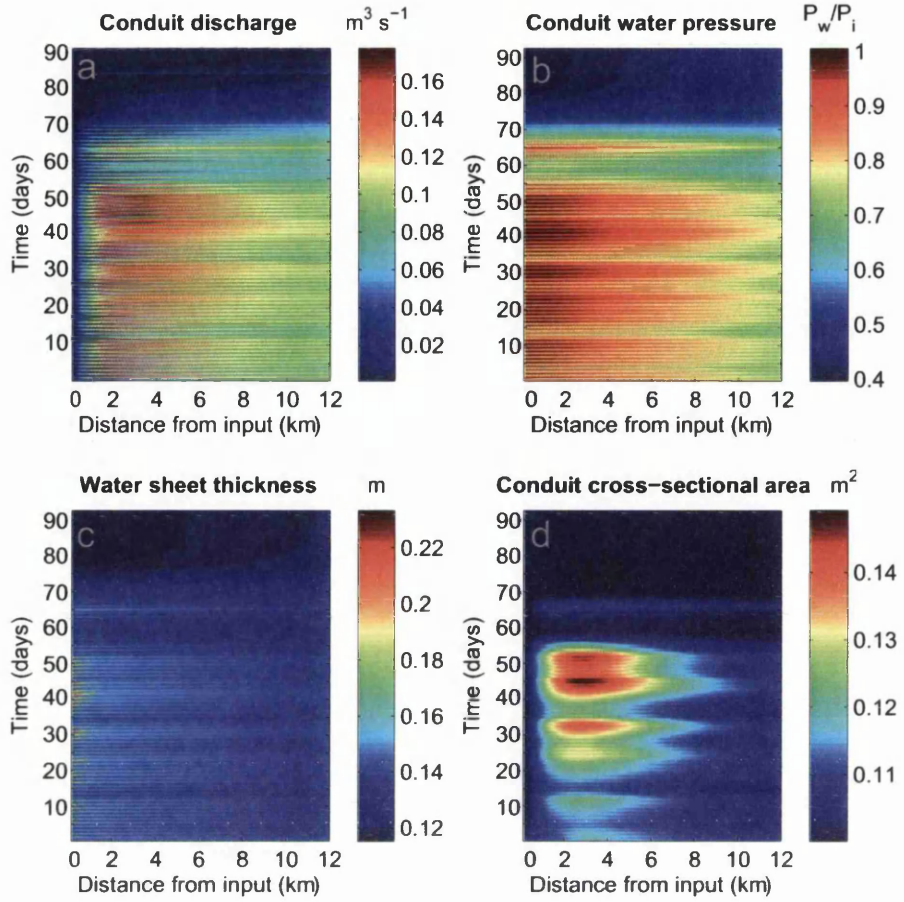

Figure 7.19: *Distance-time plots for the baseline F-Lake planar model and an outlet pressure of 0.5 P_i. This model was run with half of the surface water input volume for a total of 90 days.*

model, where a low hydraulic conductivity was more important). Over the 30 days following drainage, the low Manning roughness still caused the most channel growth for all systems with outlet pressures greater than atmospheric (again aside from the tidewater glacier model, P_{out}=0.67 P_i system, where a thin water sheet was the driver for greatest channel growth). The atmospheric outlet systems instead saw greatest channel growth for fixed flowband widths of 500 m.

An initial channel size of 1 m^2 allows growth over both 10 hours and 30 days for most systems (apart from the F-Lake real topography model, 0.5 P_i outlet for the former, and the F-Lake planar model, 0.5 P_i outlet for the latter). This means that, when S_c=1 m^2, the channel size is, at both 10 hours and 30 days, larger than for any of the other sensitivity tests. In contrast, an initial channel size of 10 m^2 shrinks in most model runs over both 10 hours and 30 days (apart from the F-Lake real topography model and the tidewater glacier model with outlet pressure at

overburden over 10 hours; and the marginal glacier model over 30 days). However, because of the significant size of the initial channel, shrinkage over 30 days still allows larger channels than produced in the other sensitivity tests. On the other hand, it is likely that these channels would shrink further with longer model runs.

The volume of runoff input once the lake has drained is also important for channel growth in all the tested model geometries (see Fig. 7.17) . It was beyond the scope of this study to determine a temporally accurate rate of seasonal runoff for the F-Lake region and so it is not possible to constrain channel size over the full season due to surface water input. However, this study does indicate that models of surface water input are an important aspect of subglacial hydrological development modelling.

7.7.2 *Modelled geometry result comparison*

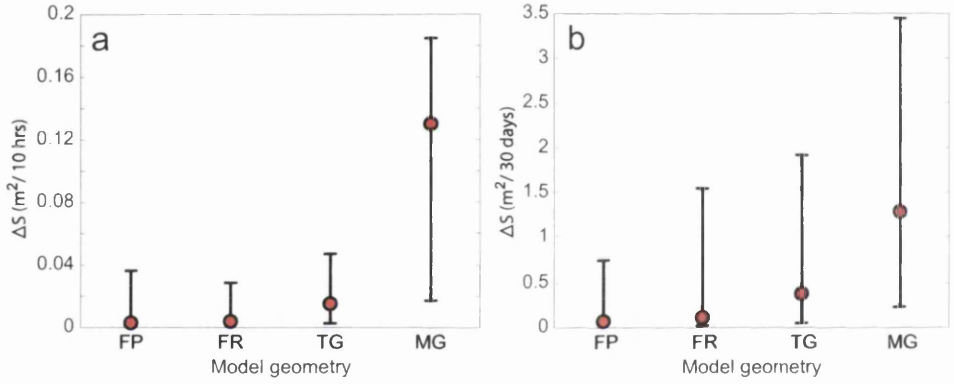

Figure 7.20: *Channel growth over a) 10 hours and b) 30 days following lake drainage for the 4 model geometries (F-Lake planar topography, FP; F-Lake real topography, FR; tidewater glacier, TG; and marginal glacier, MG). The red dots show the baseline channel growth and the error bars show the variation in growth determined from sensitivity testing and changes in the outlet water pressure condition.*

The range of channel growth over 10 hours and 30 days following lake drainage is shown for each model geometry in Figure 7.20. The red dots in this figure show the baseline channel growth results and the error bars encompass the results from the other sensitivity tests. Some tests are excluded from the plotted ranges including initial channel size (which is examined in Fig. 7.21), and the outputs from the F-Lake planar atmospheric tests because, although useful for comparing primary controls on channel growth between modelled geometries, it is highly unlikely that channels ~50 km from the ice margin under thick ice would be at atmospheric pressure.

Over the 10 hours following lake drainage, channel growth in the F-Lake models

(geometries 1 and 2), and the tidewater glacier model (geometry 3) is smaller than in the marginal glacier model (geometry 4). However, channels in any model geometry do not grow by more than 0.2 m^2 during this time. Conduit growth over 30 days is again greater in the marginal glacier model than the other modelled geometries, with the tidewater glacier model also producing generally greater growth than the F-Lake models. Baseline channel growth in geometries 1, 2 and 3 is <0.5 m^2 over 30 days, although with some sensitivity tests channel growth up to 2 m^2 over the same time is predicted (see Section 7.5 and Fig. 7.20). The marginal glacier model has the largest sensitivity test channel growth of up to 3.5 m^2 over 30 days.

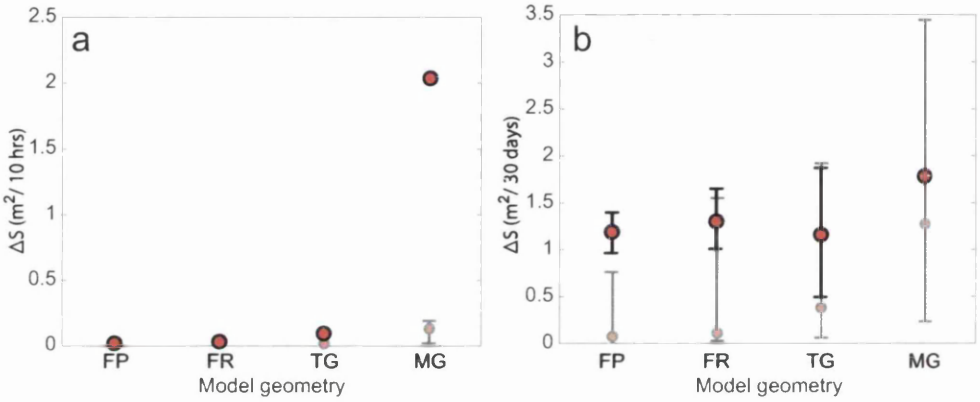

Figure 7.21: *Channel growth over a) 10 hours and b) 30 days following lake drainage for the 4 modelled geometries (F-Lake planar topography, FP; F-Lake real topography, FR; tidewater glacier, TG; and marginal glacier, MG). The red dots show the average growth for a system where the initial channel size is 1 m^2; the error bars show the range of growth as a result of the outlet pressure condition. The opaque red dots and error bars represent the range of channel growth due to other sensitivity tests as shown in Figure 7.20.*

Figure 7.21 shows the channel growth when the initial channel size is 1 m^2 (with the average plotted as red dots and the error bars encompassing variation from the outlet pressure conditions). The channel growth range from the remainder of the sensitivity tests (as shown in Fig. 7.20) are plotted as opaque error bars. As can be seen from Figure 7.21 a, channel growth over 10 hours in model geometries 1, 2 and 3 is not greatly increased relative to the other sensitivity tests. However, in the marginal glacier model, channel growth is an order of magnitude greater than when the initial channel size is 0.1 m^2. Over the 30 days following lake drainage, the channel growth as a result of a larger initial channel size is within the error bars of the remainder of the sensitivity runs for modelled geometries 2, 3 and 4 (Fig. 7.21 b). In the F-Lake planar model however, channel growth can be up to twice as much as seen with a smaller initial channel size.

Table 7.2: *Coupled hydrological model channel growth range for primary sensitivity parameters.*

Geometry		1 (FP)	2 (FR)	3 (TG)	4 (MG)
m^2/10 hrs	Min. ΔS	0.6×10^{-3}	1×10^{-3}	2×10^{-3}	0.02
	Max. ΔS excl. S_ϵ=1 m^2	0.02	0.02	0.05	0.13
	Max. ΔS incl. S_ϵ=1 m^2	0.02	0.05	0.13	2.04
m^2/30 days	Min. ΔS	0.01	0.02	0.05	0.23
	Max. ΔS excl. S_ϵ=1 m^2	0.57	0.46	1.67	3.44
	Max. ΔS incl. S_ϵ=1 m^2	0.96	1.30	1.87	3.44

The final ranges of minimum and maximum channel growth for the four modelled geometries are detailed in Table 7.2. Unlike Figures 7.20 and 7.21 and Table 7.1, which include the range of channel growth from most of the sensitivity tests, Table 7.2 only shows what are termed here as the primary sensitivity tests. Some parameters can be ruled out as unrealistic. For the F-Lake planar model, only records from the $P_{out} \geq 0.5\, P_i$ runs are included (with the atmospheric outlet results ignored), as these are the scenarios most indicative of likely conditions at the bed. In addition the lake volume tests from the F-Lake planar model are not included as the lake volume is known. As discussed in Sections 7.4.1, a Young's modulus value of 3 GPa does not match well with the in-situ surface records from the F-Lake drainage and is therefore not included in the primary sensitivity test results for geometries 1 and 2. For all geometries, a very smooth Manning's roughness value of 0.01 s m^{-3} is unlikely to occur in a channel at the ice-bed interface due to bedrock or clast roughness at the base. Finally, although a 1 m^2 channel is possible, the results suggest that channels with a cross-sectional area of 10 m^2 would be unlikely to form prior to lake drainage. After eliminating all of these values, the ranges of channel growth over 10 hours and 30 days for each modelled geometry are shown in Table 7.2.

7.8 Summary

In this chapter, the results of the coupled hydrological model sensitivity experiments have been presented. Initially, the blister model was tested against the surface data records from F-Lake. These experiments illustrated that the blister model matches

the F-Lake in-situ data well and is therefore highly appropriate for applying to this lake drainage event.

The impact of individual sensitivity parameters on hydrological development is explored to determine those most important for channel growth and system development. It was found that altering the values of Young's modulus, the creep parameter, geothermal heat flux, and Nikuradse roughness height does not significantly impact channel growth. The values of Manning roughness, sheet hydraulic conductivity, critical sheet thickness and the initial channel size, however, more significantly impact the rate of channel growth. Parameters including flowband width and initial lake volume only impact channel growth over longer (30 day) time-scales but have little influence on channel growth in the initial 10 hours of lake drainage.

However, these are general results for the impact of the parameters on channel growth. The sensitivity tests outputs differ for each modelled geometry and, as a result, the channel growth rates were examined for each modelled geometry separately to extract the most influential parameters in each. Initial channel size is important in all modelled geometries. Manning roughness value is also an influential parameter in the F-Lake models. For the tidewater and marginal glacier models however, the hydraulic conductivity, critical sheet thickness (for the former) and flowband width (for the latter) have more important roles for channel growth than Manning roughness. This is because, in models with a parabolic surface profile (geometries 3 and 4), the geometric hydraulic potential gradient drives enough water through the system that parameters allowing greater pressurisation of the distributed system (resulting in more exchange with the channel and therefore channel pressurisation) allow greater growth than parameters allowing more flux through the channels. In contrast, geometries 1 and 2 with a lower geometric hydraulic potential gradient have a sufficiently pressurised basal hydrological system that parameters causing more flux through channels allow greater growth.

Comparing the channel growth for all of the sensitivity tests, the marginal glacier model has by far the most conduit growth and the F-Lake planar model has the least. However, none of the model outputs, barring the initial channel size tests (in order to replicate an undeveloped hydrological system) have channel growth $>0.2\,m^2$ within 10 hours of lake drainage. Again excluding initial channel size, all channel growth for the marginal glacier model is $<3.5\,m^2$ over 30 days and, for the remaining modelled geometries is $<2\,m^2$ over 30 days. Looking at an initial channel size of $1\,m^2$, only the marginal glacier model has significantly more channel growth

within 10 hours of lake drainage. However, over 30 days of drainage, an initial channel size of $1\,m^2$ only allows greater growth in the F-Lake planar model when compared to outputs for initial channel sizes of $0.1\,m^2$.

The coupled hydrological model was also used for additional, more generalised, tests on model geometry and surface water input. A surface slope test for the F-Lake planar model indicates that steeper slopes allow greater channel growth due to the increase in geometric hydraulic potential gradient driving more water through the basal hydrological system. The impact of ice thickness on channel growth was tested with the F-Lake planar, the tidewater glacier and the marginal glacier models; the results are complicated by changes in pressure gradients and surface slope as a result of altering the ice thickness. As a result, most channel growth was usually seen for an intermediate ice thickness rather than the thinnest glaciers, as might be expected. The baseline runoff tests show that with half the estimated runoff over the full season, maximum channel size is much smaller than found with full seasonal runoff. Runoff therefore appears to be an important aspect of hydrological development, particularly if focussing on full seasonal drainage system evolution.

The results presented in this chapter identify a large range of drainage development characteristics and constrain a range of possibilities for channel growth during and following lake drainage events in different types of glaciological settings in Greenland.

Chapter 8

Seismic reflection studies

8.1 Introduction

Basal boundary conditions are an important feature of any hydrological or dynamic model applied to the GrIS. To date, modelling and dynamic assessment of the RGC has assumed that the bed is composed of rock rather than sediment (e.g. Bartholomew *et al.*, 2010; Schoof, 2010; Sundal *et al.*, 2011). A primary reason for this hard-bed assumption is the lack of evidence to the contrary, partially due to difficulty of access to the subglacial environment. Seismic reflection studies provide a method for remote imaging of the acoustic properties of the subsurface, including the ice-bed boundary. In this chapter, reflection seismic methods are utilised to examine the ice-bed interface of RGC. Amplitude-versus-angle (AVA) analysis provides information on the substrate mechanical attributes, such as the level of saturation and material porosity. The outputs from these seismic reflection investigations (along with results from studies by collaborators in the near vicinity of the F-Lake case-study site; see Section 3.6.3) are used to constrain the coupled hydrological model introduced in Chapter 5, and to assess the applicability of the model to the RGC.

This chapter begins with a summary of relevant reflection seismic theory and application, focussing on AVA analysis. Two case-study sites are then examined: one site ~13 km from the margin of Russell Glacier, and the other, ~5 km upstream of the F-Lake study site. Finally, the outputs of the reflection seismic analyses are considered in relation to the subglacial conditions of RGC and the applicability of

the coupled hydrological model discussed in Chapters 5–7.

8.2 Background

8.2.1 *Fundamental seismic theory*

Seismic waves can be divided into two categories: surface waves and body waves. Surface waves include Rayleigh waves (ground-roll), which are a prominent source of noise in unprocessed seismic data (Sheriff and Geldart, 1983). Body waves include 1) P-waves (primary waves) that cause elastic compression of particles in the direction of wave propagation, and are the main source of information in reflection seismic studies (Parasnis, 1975), and 2) S-waves (secondary waves) that cause particle motion transverse to the wave propagation direction; these latter waves are more difficult to detect in seismic reflection studies, unless a dedicated S-wave seismic source or specialist techniques are used (Sheriff and Geldart, 1983). P-waves reflect from boundaries with contrasting acoustic impedances (the product of density and velocity); it is these seismic reflection records that are examined in this thesis. Seismic waves are also refracted when they cross an acoustic impedance interface, by an angle that is determined by the respective velocities of the materials either side of the interface (Kearey and Brooks, 1984). P-wave velocity, V_p, is determined by

$$V_p = \sqrt{\frac{B + \frac{4}{3}\mu}{\rho}}, \tag{8.1}$$

where ρ is the material density, μ is the shear modulus and B is the compressibility (or bulk) modulus (Sheriff and Geldart, 1983; Kearey and Brooks, 1984). The latter is influenced by properties such as material porosity, grain size, grain shape and level of saturation (Nolan and Echelmeyer, 1999b). S-wave velocity, V_s, is calculated with

$$V_s = \sqrt{\frac{\mu}{\rho}}. \tag{8.2}$$

As materials such as rock or ice are rarely perfectly elastic, seismic waves attenuate and reduce in amplitude as they propagate. Attenuation, α, can be estimated following Aki and Richards (1980)

$$\alpha = -\frac{\pi f_s}{Q_s V_p}, \tag{8.3}$$

where f_s is the wavelet frequency and Q_s is the seismic quality factor. The reduction in amplitude of the seismic wavelets with propagation is known as geometrical spreading, the rate of which is proportional to the propagation distance of the wave from the source (Kearey and Brooks, 1984). Both attenuation and geometrical spreading must be compensated for prior to analysis of seismic amplitudes.

Seismic reflections at interfaces are governed by V_p, V_s, and the density of the material either side of an interface (Kearey and Brooks, 1984). When energy propagates normal to an interface, P-wave reflectivity is governed by contrasts in acoustic impedance, Z:

$$R(0) = \frac{Z_2 - Z_1}{Z_2 + Z_1}, \tag{8.4}$$

where Z is the acoustic impedance of the upper (1) and lower (2) layers (see Fig. 8.1) and $R(0)$ is termed the 'reflection coefficient' (Sheriff and Geldart, 1983; Kearey and Brooks, 1984). If the acoustic impedance of the upper layer is greater than the lower layer, $R(0)$ is negative and the polarity of the reflection phase at the boundary is reversed with respect to the direct wave polarity (Anandakrishnan, 2003).

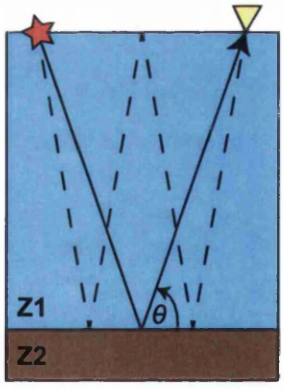

Figure 8.1: *Schematic of primary (solid) and multiple (dashed) reflections from the ice-bed interface. The star represents the shot and the triangle represents the geophone. Z1 is the acoustic impedance of the upper layer and Z2 the acoustic impedance of the lower; θ is the reflection angle. Adapted from Holland and Anandakrishnan (2009).*

With non-normal incidence, the reflection coefficient is also influenced by contrasts in Poisson's ratio, σ (Yilmaz and Doherty, 2001):

$$\sigma = \frac{\left(\frac{V_p}{V_s}\right)^2 - 2}{2\left\{\left(\frac{V_p}{V_s}\right)^2 - 1\right\}}. \tag{8.5}$$

Poisson's ratio ranges between 0 and 0.5, with higher values as a result of lower S-wave velocity. The S-wave velocity approaches zero with greater saturation in a material because the shear modulus, μ, is zero in fluid. Therefore a higher Poisson's ratio indicates greater levels of fluid saturation.

8.2.2 *Seismic reflection surveys*

Reflection seismic studies conducted surficially involve an impulsive energy source (such as explosives or hammer strikes) to create a wave that passes elastically through the earth, and is recorded at surface geophone locations. The geophones measure surface displacement and produce a 'trace', which is a time-series of seismic amplitude. Figure 8.2 shows a schematic of a shot gather where the energy transmitted from a shot location is recorded by several geophones. By combining the records from several shot gathers, boundaries in the subsurface where changes in acoustic properties occur, such as at the ice-bed interface, can be identified.

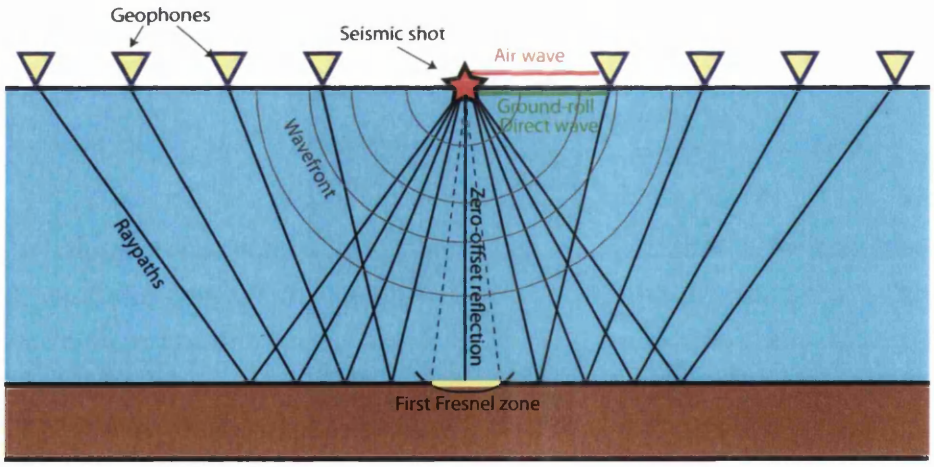

Figure 8.2: *Schematic of a seismic shot with eight geophones on the surface. The solid black lines show the seismic reflection raypaths, perpendicular to the wavefront in grey. The dashed black lines show the extent of the zero-offset reflection horizontal resolution, defined as the first Fresnel zone.*

The horizontal resolution of seismic reflection data is known as the first Fresnel zone and is calculated with (Sheriff and Geldart, 1983)

$$Fr = \left(\frac{\lambda_s h_p}{2}\right)^{1/2}, \tag{8.6}$$

where λ_s is the seismic wavelet wavelength and h_p is the depth of the primary reflection. Under thick ice, the Fresnel zone can be several hundred metres wide. Seismic vertical resolution is such that a reflection will only be clearly observable on a seismic return if the layers between interfaces have a thickness of at least $^1/_4$ of the seismic wavelength (Widess, 1973). For seismic studies of kilometre-thick ice, vertical seismic resolution at the ice-bed interface can be in the range of several metres.

8.2.3 *Amplitude-versus-angle (AVA) theory*

In AVA analyses, the change in the seismic reflectivity at the material interface is calculated with respect to changing angle of incidence, producing an AVA response curve. As it is often possible to estimate the P-wave and S-wave characteristics for the overlying material, the observed AVA response curve can be diagnostic of the nature of the underlying material. AVA response curves can be modelled using the Knott-Zoeppritz (K-Z) equations (utilising source code from CREWES; Margrave, 2013) by varying the P- and S-wave velocities and the bulk densities of the materials either side of an interface (e.g. Aki and Richards, 1980). Combinations of these three parameters can uniquely identify the underlying material as, for example, hard bedrock, water, lithified sediment or deforming sediment.

Figure 8.3 shows typical outputs from K-Z models with the upper layer defined as ice; properties for the upper and lower interfaces that produced these AVA response curves are shown in Table 8.1, following Peters *et al.* (2008).

8.2.4 *Measuring AVA in glaciology*

Much glaciological application of AVA theory lacks ground truth data (such as from ice-drilled boreholes) and therefore techniques that utilise only the observed change in seismic amplitude must be applied. As such, the zero-offset (i.e. θ=0, see Fig. 8.2) reflection coefficient can be determined by examining the amplitudes of both primaries and multiples recorded in the same trace (see Fig. 8.1), thus establishing the

Table 8.1: *AVA response curve properties in relation to those plotted in Fig. 8.3, calculated from the Knott-Zoeppritz equations.*

Material	P-wave velocity ($m\,s^{-1}$)	S-wave velocity ($m\,s^{-1}$)	Density ($kg\,m^{-3}$)	Curve colour
Ice	3800	1900	920	n/a
Bedrock	5200	2800	2700	red
Lithified sediment	3750	2450	2450	blue
Dilatant sediment	1700	200	1800	green
Water	1498	0	1000	black

reduction in energy, which is a representation of the material impedance (Smith, 2007):

$$R(0) = 2\left\{\frac{A_m(0)}{A_p(0)}\right\}e^{\alpha d_p(0)}, \tag{8.7}$$

where A_m is the amplitude of the multiple arrival, A_p is the amplitude of the primary arrival, α is the attenuation coefficient for ice, and d_p is the total travel distance of the primary arrival. When examining normal incidence reflections of primary and multiple amplitudes, reflections from up to 10 degrees can legitimately be included, as the difference in reflection coefficient between a primary and its corresponding multiple is very small at these angles (Smith, 2007). For the more usual case of non-normal incidence reflections, the reflection coefficient, $R(\theta)$, can be calculated following Peters *et al.* (2008):

$$R(\theta) = \frac{A_p(\theta)}{A_0}d_p(\theta)e^{\alpha d_p(\theta)}, \tag{8.8}$$

where A_0 is the source amplitude at normal incidence. It is possible to measure the primary reflection amplitudes, A_p, calculate the travel distance of the associated ray paths, d_p, and estimate α using Eq. 8.3. However, direct measurement of the source amplitude, A_0, in Eq. 8.8 is difficult due to noise in the seismogram from the direct wave and the ground-roll. However, an estimate of A_0 can be obtained from the ratio of the squared primary amplitudes of the ice-bed reflection to their corresponding first multiple (A_m) at normal incidence using

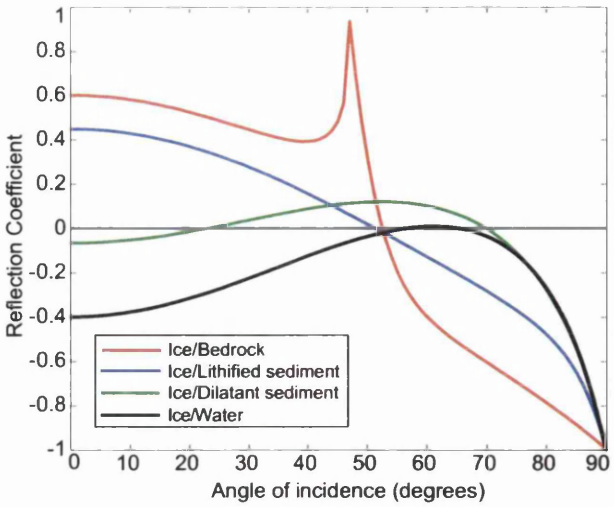

Figure 8.3: *Examples of reflection coefficient outputs for typical ice-interface boundaries using the Knott-Zoeppritz equations. Here, AVA curves for ice and bedrock, sediment and water are plotted using material properties as stated by Peters* et al. *(2008) and shown in Table 8.1.*

$$A_0 = \frac{A_p(0)^2}{A_m(0)} \frac{d_p(0)}{2}. \tag{8.9}$$

The resulting AVA response curve can then be compared with those produced using the K-Z equations having applied estimates of the ice velocity and density properties in order to categorise the basal material. For example, as shown in Fig. 8.3, the ice/rock (red) curve in has a strongly-positive intercept at normal incidence, a shallow gradient and a critical refraction at an incidence angle of ~47°. An ice/water boundary (shown by the black curve in Fig. 8.3) on the other hand is dominated by a negative reflection coefficient for all measurable angles of incidence because the acoustic impedance of water is substantially lower than that of ice, resulting in a phase reversal of seismic reflections relative to the direct wave when imaging subglacial water bodies (Peters *et al.*, 2008). Between ice/water and ice/rock AVA responses, all plausible scenarios are governed by sediment characteristics. The acoustic impedance of ice is similar to that of till saturated by water and therefore might not produce strong ice-bed reflections (Atre and Bentley, 1993). However, in circumstances when basal shear stresses and pore water pressures are high, water-saturated till can undergo deformation; the resulting shearing causes dilation of the sediment (which increases the till pore-space; Iverson *et al.*, 1994). Sediment that has been sheared is therefore referred to as dilatant till and, because of the larger pore spaces, water-saturated dilatant till will have a lower P-wave velocity

than water-saturated non-dilatant till (Anandakrishnan, 2003). With ice overlying dilatant sediments (shown by the green curve in Fig. 8.3), the reflection coefficient is initially negative and becomes increasingly positive at higher angles; the negative zero-offset reflection coefficient demonstrates that the underlying layer has a lower acoustic impedance than ice (Anandakrishnan, 2003), and the positive gradient over increasing angles indicates that the Poisson's ratio of the underlying layer is higher (i.e. more saturated) than the overlying layer (Booth *et al.*, 2012). Water-saturated non-dilatant till would produce a curve with a higher zero-offset reflection coefficient than that for dilatant till. A curve representing lithified till with low porosity (the blue curve in Fig. 8.3) begins with a positive reflection coefficient and becomes increasingly negative at higher incidence angles. This result indicates that lithified till has a higher acoustic impedance and lower Poisson's ratio than ice (Peters *et al.*, 2007).

Some assumptions are made when analysing AVA responses including that the substrate material is both continuous and homogeneous (Holland and Anandakrishnan, 2009), even though this will often not be the case (Nolan and Echelmeyer, 1999a). Instead, the AVA responses represent the amalgamation of the basal conditions sampled within the Fresnel zone. As a result, AVA responses represent an average response from the material at the ice-bed interface rather than implying that all the material sampled is the same. A second assumption when comparing reflection coefficients with K-Z models is that the AVA curve represents a boundary between two infinite and isotropic half-spaces (Booth *et al.*, 2012). However interference from layers thinner than the vertical seismic resolution (nominally $^1/_4$ of the dominant wavelength) can alter the reflection coefficient outputs (Nolan and Echelmeyer, 1999b) and the material characteristics are merged with the underlying or overlying material (Anandakrishnan, 2003; Booth *et al.*, 2012). For example, if there is constructive interference (i.e. wavelet peaks amalgamating) from both the top and bottom of a unit that is too thin to be resolved, it could output a higher reflection strength than would be found from the 2-layer model (King *et al.*, 2008; Booth *et al.*, 2012). In many seismic studies a layer of ~2–3 m would be below seismic resolution and, particularly when examining subglacial sediment that may be thinly layered, there could be significant misinterpretation of basal conditions (Booth *et al.*, 2012). In order to circumvent the problem of interfering seismic wavelets, Booth *et al.* (2012) used a rigorous forward modelling approach with simulated AVA responses for various thin-layer scenarios to best estimate the material properties at the bed. This thin-layer analysis is revisited in Section 8.4.5 for investigation of one of the

RGC seismic reflection sites presented in this thesis.

8.2.5 *Reflection seismic studies in glaciology*

In this thesis, seismic reflection studies are applied to analysis of glacial conditions at the ice-bed interface. In this section, a summary is given of seismic studies that have previously been applied to glaciological research.

Analysis of reflection amplitudes and AVA curves are often used in seismic campaigns to differentiate between types of basal conditions. Atre and Bentley (1993) examined the polarity of basal reflections, relative to the direct wave phase, to determine properties of the ice-bed interface underlying Ice Streams B and C, Antarctica. Basal phase changes were attributed to the presence of wet dilatant sediment, whereas a lack of polarity reversal suggested the basal sediment was lodged in some areas (Atre and Bentley, 1993). Similarly, Anandakrishnan (2003) used the changes in phase of primary reflections at given angles to determine that an area of wet dilatant till was underlying an area near the onset of the Ice Stream C fast flow region.

In some studies, a single reflection coefficient value and related substrate acoustic impedance were calculated at normal incidence. The seismic lines were then moved over several kilometres and reflection coefficients again measured to establish spatial changes in basal material characteristics. Vaughan *et al.* (2003) used such an approach to analyse basal conditions of four Antarctic ice streams and differentiated between lodged and deforming sediment. The differences in sediment characteristics were found to be highly correlated with the degree of basal slipperiness. Clarke and Echelmeyer (1996) identified a layer of lodged till underlying Jacobshavn Isbrae, Greenland, through point measurements of the reflection coefficient. They suggested this result implied most motion of Jacobshavn Isbrae occurred through internal deformation rather than basal sediment shearing. Nolan and Echelmeyer (1999b) examined temporal variations in point reflection coefficients at Black Rapids Glacier, Alaska, to establish changes in basal drainage conditions prior to and following several jökullhlaups. They identified a decrease in saturation of basal material after the glacial floods that was attributed to hydraulic jacking in the region of the seismic studies. Smith (2007) demonstrated that differences in acoustic impedance of basal sediment underlying the Rutford Ice Stream could be used to identify areas of deforming sediment, although layers less than 1 m thick could not be distinguished. These studies demonstrate that determining only the normal incidence substrate

acoustic impedance can still be highly valuable for distinguishing changes in basal characteristics.

In other studies, AVA curves (rather than reflection coefficient point measurements) have been fitted to determine basal conditions in one region. For example, Peters *et al.* (2008) identified a subglacial lake of ~20 m depth underlain by sediment near the south pole region by examining AVA response curves. Peters *et al.* (2007) also used AVA analysis to calculate porosity and water content of sediment underlying Ice Stream D, and compared the outputs with calculated hydraulic potential gradients to determine areas of storage and release of water under the ice stream. Most of the glaciological literature involving AVA analysis is dedicated to differentiating sediment characteristics at the ice-bed interface; AVA analysis is not generally used to identify subglacial hydrological features such as channels. For drainage pathways to be observable on seismic returns, Smith (2007) argued there would have to be a channel with a diameter greater than 0.5 m to be detected. However, King *et al.* (2004) modelled the effects of thin water layers on reflection coefficients to determine the thickness necessary to distinguish layers in a seismic record. From these models King *et al.* (2004) estimated a water body underlying Rutford Ice Stream of 0.4-0.6 m depth and argued that it represented a sediment canal (see Sections 2.2.3 and 2.4.3).

From this review of the glaciological reflection seismic literature it is clear that AVA analysis is an established technique for determining differences in basal conditions and the properties of subglacial sediment. This method is therefore highly applicable for determining ice-bed interface characteristics in the RGC.

8.3 Russell Glacier catchment

The coupled hydrological modelling case-study discussed in Chapters 5–7 involves a 12 km-long flowband initiating from a rapidly draining lake in the RGC. In order to apply the hydrology model it is necessary to make some assumptions about the basal material characteristics along that flowline.

During the 2010 summer field expedition, five reflection seismic lines were gathered at four sites, illuminating ~6 km of the bed; Figure 8.4 shows the location of these seismic lines. Three of the lines surrounding F-Lake were analysed by A. Booth, Swansea University (now at Imperial College, London) and are summarised in Sec-

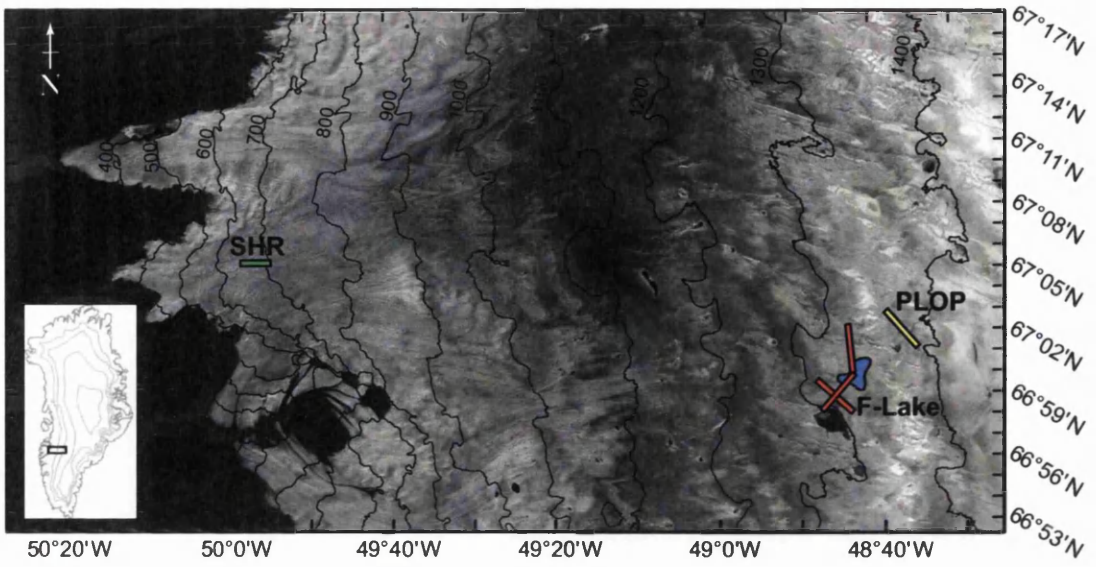

Figure 8.4: *Landsat image of Russell Glacier acquired on 18th August 2010 (at a resolution of 30 m) with the inset indicating the location in Greenland. Surface elevation contours are marked by the black curves at 100 m intervals. Seismic reflection lines at: a) SHR (green line) b) PLOP (yellow line) and c) F-Lake (red lines). F-Lake is indicated in blue.*

tion 3.6.3. This current chapter focusses on two of the remaining lines, the first (PLOP) directly upstream of the rapidly draining supraglacial lake, and the second (SHR) located ~13 km from the Russell Glacier terminus. Although the latter site is ~44 km from the end of the modelled flowline domain, determining the basal characteristics at SHR can add to the discussion of the applicability of the model to other regions of RGC. The characteristics of these two seismic sites are described in Table 8.2.

The following section will discuss the two seismic sites in turn, including the processing approach and results from seismic stacked sections and AVA analyses. For both sites, data acquisition was carried out A. Booth (Imperial College, London) and A. Gusmeroli (University of Alaska), both affiliated with Swansea University at the time. All subsequent data processing was carried out by the author.

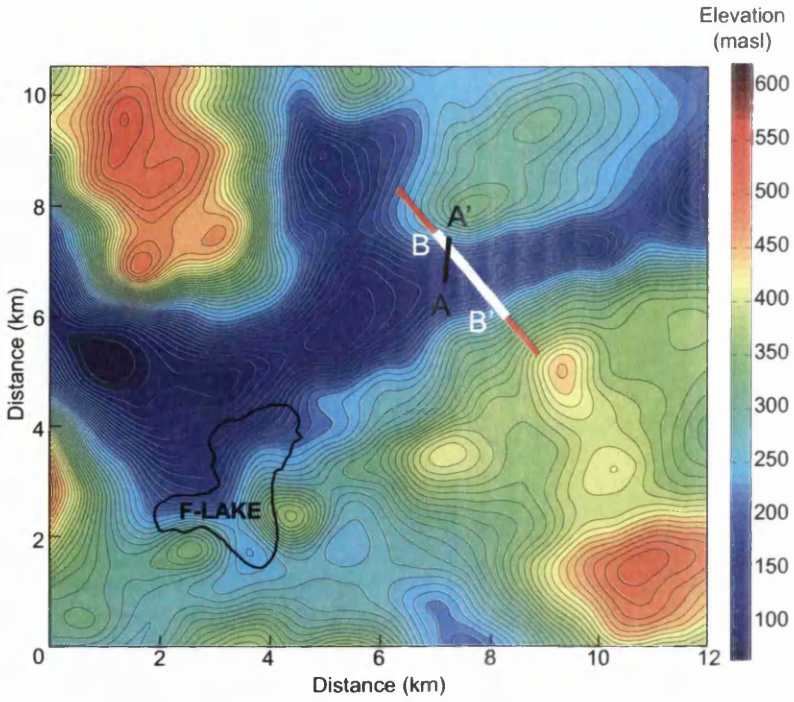

Figure 8.5: *Basal DEM of the PLOP site and F-Lake. The location of the seismic reflection line is indicated by the red line; the white line indicates the area of the bed sampled by the seismic profile (B to B'). The black line shows the area of the bed sampled by a ground penetrating radar survey (A to A').*

8.4 PLOP

8.4.1 *Aims*

A ground penetrating radar (GPR) campaign run by Rickard Petterson and Katrin Lindbäck (Uppsala University) in May 2010, upstream of the F-Lake study site (see Fig. 8.5), identified an area with a bright flat reflector underlying the ice (shown in Fig. 8.6). When compared to surrounding reflective indices it was determined that the substrate causing the flat reflector was likely water. Due to the high absorption of radar energy by water, the GPR returns can give little information on the depth of the potential water feature or the characteristics of the underlying material. By running a seismic line over this area, the aim was to determine the P-wave and S-wave velocities through the substrate and also the density of the basal material, allowing the depth and contents of any underlying basin to be estimated (assuming the bottom of the basin could be detected). In addition, by examining the topographic and material variability in the vicinity of the lake drainage site, the outputs

of the PLOP seismic analysis could contribute to basal boundary conditions in the coupled hydrological model. For example, if water was being stored and released from a subglacial basin at the PLOP site, it could have impacted basal drainage development prior to the rapid supraglacial lake drainage event.

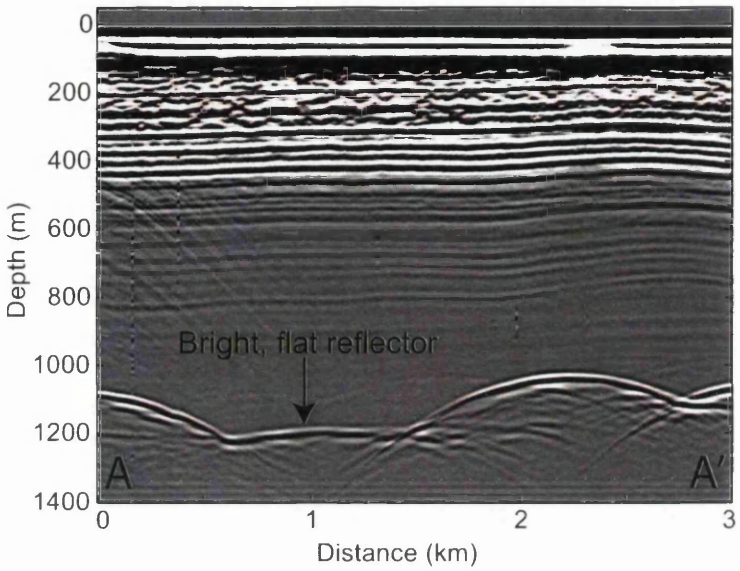

Figure 8.6: *Radar profile of the PLOP site indicated in Fig. 8.5 (A to A'). Depths are based on a radar velocity of 0.168 m ns^{-1}. These radar data are non-migrated and therefore there may be some misplacement in the basal topography.*

8.4.2 *Field site*

The seismic line at PLOP is located ~5 km to the NE of the F-Lake site (Fig. 8.4). PLOP was oriented in a WNW to ESE direction (in order to intersect the subglacial basin). The surface topography in this area was undulating with a total elevation change of 20.5 m (see Fig. 8.7 a). The spread of the reflection seismic deployment illuminated ~2 km of the ice-bed interface. The basal topography in the region is shown in Figure 8.5 with the seismic line indicated in red. From this figure it is clear that the subglacial basin being examined in the PLOP seismic line is, in fact, part of a trench that continues to the SW until it reaches the F-Lake site and then follows a route to the NW.

8.4.3 *Data acquisition*

Data were recorded using a Geometrics GEODE system, with 48 vertical-component 100 Hz geophones installed at 10 m intervals in a fixed array configuration. The geophones were set into concrete slabs (of dimensions 15×15×7 cm and weight 10 kg) to improve coupling with the ice, and buried with ice chips to reduce surface noise. A total of 50 shots were installed at a horizontal spacing of 80 m to a depth of ~3 m, covering 3920 m on the surface. The holes were loaded with a 25 ms delay detonator and a combined 250 g Pentalite and 400 g dynamite charge. Nine holes were loaded with additional charges of dynamite in order to provide better signal-to-noise ratio for AVA analysis. The seismic line was drilled and loaded on 18th July and fired on 19th July 2010. Charges were allowed to freeze overnight to improve coupling so that energy from the explosions would travel primarily down into the ice. Accurate differential GPS locations of the shot holes (using a Leica SR520 receiver differentially corrected against a bedrock-mounted reference station, to 10 cm precision) were collected in order to both establish the exact location of the shots and the elevation change along the line; these GPS locations were collected by A. Hubbard, Aberystwyth University and processed by S. Doyle, Aberystwyth University. In total, 2400 seismic traces were collected with a 6-fold common mid-point (CMP) coverage. The maximum source-receiver offset for the PLOP line was 2160 m.

8.4.4 *PLOP seismic stacked section*

This section focusses on the processing of the seismic gathers to create a seismic stack of the ice-bed interface. A CMP seismic stack sums traces from the same return point on the bed in order to increase signal-to-noise ratio. A normal move-out (NMO) correction is applied to the traces prior to stacking to correct for the variable distance travelled by the raypaths to the common mid-points. The resulting stacked section shows variations in amplitude with increasing travel-time that illustrates changing conditions of the subsurface; for this thesis it is the ice-bed interface that is of particular interest. In order to create a seismic stacked section that allows analysis of the subsurface, various processing steps are carried out; the processing flow for the PLOP site is detailed below prior ro analysis of the resulting stacked section.

Table 8.2: *Seismic line properties for the PLOP and SHR survey sites.*

	Line length (m)	Line direction	Shot start location	Shot end location	Start offset (m from phone 1)	End offset (m from phone 1)	No. of shots	Mis-fired shots
PLOP	3920	WNW–ESE	67.04922 N	67.02154 N	1760	2160	50	30 re-fired
			-48.648 W	-48.5926 W				
SHR	1920	W–E	67.09998 N	67.10005 N	1140	780	33	n/a
			-49.96061 W	-49.93841 W				

	Date fired (2010)	Mean ice thickness (m)	Mean bed elevation (masl)	Surface elevation change (m)	Section length (m)	Section start location	Section end location
PLOP	19 July	1160	1395	20.5	2000	67.04186 N	67.02777 N
						-48.6333 W	-48.6051 W
SHR	31 July	630	710	41.5	1075	67.08347 N	67.08336 N
						-49.92319 W	-49.95505 W

Methods

The PLOP seismic stacked section was processed using *ReflexW* (Sandmeier Software), a package used primarily for 2-D analysis of seismic and GPR datasets. A stacked seismic section will only display the relative depth of subsurface features once it has been corrected for changes in the surface elevation. Elevation corrections for the PLOP seismic line utilise GPS data collected at the site by A. Hubbard, Aberystwyth University; the surface elevation at PLOP is shown in Fig. 8.7 a. The seismic traces were corrected for changes in surface elevation using the following technique:

- The travel-time of the direct wave was picked for near-offset shots (in this case, five shots 160 m either side of the zero-offset geophone). It was assumed the direct waves in these shots were representative of surface conditions for the entire seismic line. Shot gathers were further separated into (a) and (b) categories for direct wave returns to geophones west and east of the shot, respectively.
- The velocity of the direct wave was established using least squares fitting between the shot-geophone separation distance and the direct wave travel-time for each (a) and (b) shot gather.
- An average direct wave velocity was calculated from the near-offset results. The shot velocity measurements and standard deviation values from the individual shot returns are shown in Table 8.3. The sample number record refers to the number of first breaks measured for each part of the gather. The mean direct wave velocity was $3736\,\mathrm{m\,s^{-1}}$ with a minimum mean velocity (using the standard deviation values) of $3700\,\mathrm{m\,s^{-1}}$ and a maximum mean velocity of $3831\,\mathrm{m\,s^{-1}}$.
- The differences in surface elevation along the line were divided by the mean velocity in order to find the corresponding time corrections necessary for the seismic traces.

Once this elevation correction was calculated, the seismic stacked section could be processed. The processing steps for producing a seismic profile are listed below with processing procedure values chosen after testing for the values that produced the clearest outputs:

Table 8.3: *PLOP surface elevation correction velocities.*

Shot no.	27a	27b	28a	28b	29a
Direct wave velocity ($m\,s^{-1}$)	3829.76	3718.69	3729.82	3701.6	3743.88
Std. Dev.	0.94	1.56	0.65	1.62	0.64
Sample no.	9	40	17	32	25
Shot no.	29b	30a	30b	31a	31b
Direct wave velocity ($m\,s^{-1}$)	3735.28	3707.58	3725.85	3732.16	3733.33
Std. Dev.	1.76	1.58	0.91	1.48	1.12
Sample no.	24	33	16	41	8

- A start-time static correction was used to remove the 25 ms delay from the charge detonator.

- An Ormsby bandpass filter was run through the data. The filter used a lower cutoff and plateau of 50 and 100 Hz respectively, and an upper plateau and cutoff of 300 and 600 Hz respectively; this bandpass filter was used to remove noise and reduce the ground-roll.

- A F-K filter was run to further suppress ground-roll noise, with an f and k cosine taper of 10 to prevent ringing. The FK filter involves fourier transform analysis of the frequency and wave-number for all shot gathers. The frequency spread can be more easily seen in FK-space and so, for example, ground-roll can be separated out and muted as it will be visible as a dipping event across all wave-numbers.

- Noisy traces were removed. These were primarily within the region of the near-offset double dynamite shots. In total, 21 traces were removed.

- The data were corrected for changes in surface elevation using the static correction described above.

- A NMO constant velocity stack was run for the CMP gathers. The constant velocity stack was tested with velocities of $3750\,m\,s^{-1}$, $3800\,m\,s^{-1}$, $3850\,m\,s^{-1}$ and $3900\,m\,s^{-1}$. It was found that the velocity choice of $3850\,m\,s^{-1}$ produced the clearest stacked section.

- After testing a range of migration combinations, a F-K (Stolt) migration was performed on the brute stack with a velocity of $3850\,m\,s^{-1}$ and a scaling factor

of 4 in order to compensate for variable basal topography by adjusting dipping reflectors and removing diffractions.

Results

The stacked section processing flow produces the stacked and migrated image shown in Figure 8.7 b. As indicated by the dashed line in Figure 8.7 c, there is a basin of around 900 m length beneath a bright reflection that represents the ice-bed interface. The topography in the ESE side of the section beyond the basin is significantly sloped with a maximum gradient of ~20 degrees. The mean ice thickness is ~1160 m and the mean elevation above sea level is ~1395 m. The total basal elevation change along the section is ~190 m. Prior to AVA analysis it is not possible to determine the true thickness of the material in the basin as the brute stack was created using a constant velocity (and the velocity of the material in the basin is likely to be different to that of ice). Three englacial reflections can be seen at a distance of between 900 and 1250 m along the section (see Fig. 8.7 c). Further processing would be necessary to analyse the characteristics of these englacial features but is not applicable to this study of subglacial hydrology and is therefore not pursued in this thesis.

8.4.5 *PLOP AVA*

Methods

In order to determine the AVA response from the seismic data, no processing can take place that might alter the amplitude of the waveform. The main processing step is to balance the traces prior to AVA analysis in order to counteract the effect of differences in surface elevation, geophone coupling, surface material characteristics and shot power on the seismic amplitude (King *et al.*, 2008). In order to remove the effects of such factors on the wavelets, the traces were balanced as follows:

- The 0.25 ms detonator delay was removed from the raw traces file.
- Noisy traces were set to zero. Noise was primarily in the region of the double dynamite shots (see Section 8.4.3) and these traces were removed to prevent biasing the trace balancing with non-representative high amplitude traces. Some noise was also due to ground-roll in particular shots.

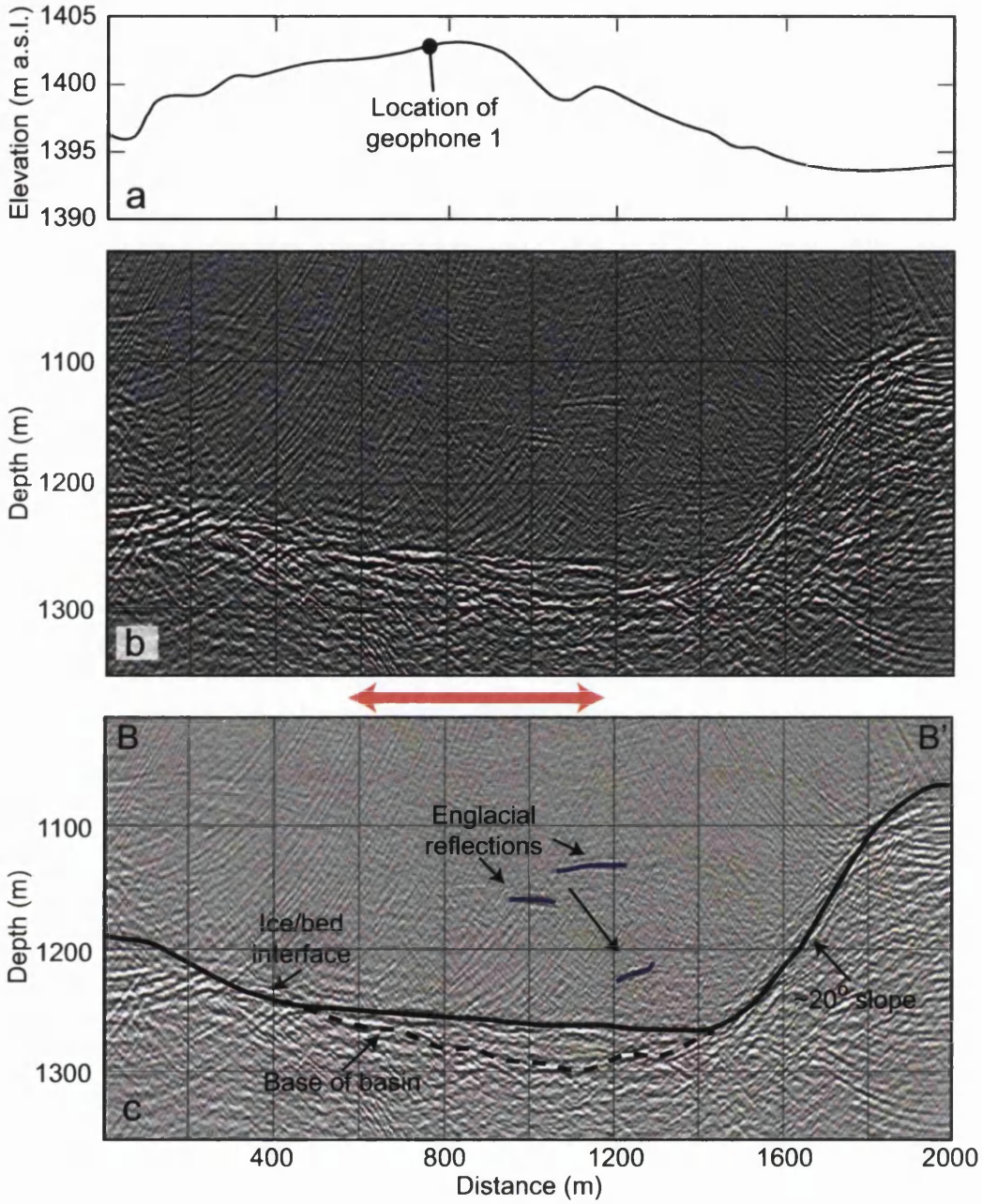

Figure 8.7: *a) Ice surface elevation at PLOP. Note the vertical exaggeration and scale on the elevation axis. b) Stacked and migrated seismic profile of the field site indicated in Fig. 8.5 (B to B′). The depth is based on a seismic velocity of 3850 m s^{-1} and is relative to the surface elevation in a). c) Interpretation of the main features in the stacked seismic profile in b). AVA analysis is applied to the area shown by the red double arrow.*

- Two surgical mutes were applied to the data. The first isolated the ground-roll over the full record by applying an inside mute of 1750 ms with a taper of 100 ms to the traces. The second was applied to the upper and lower portions of the record with a 100 ms filter in order to isolate the direct wave, using a velocity of 3800 m s^{-1} (which incorporates all the measured near-offset direct wave velocities shown in Table 8.3). The direct wave is examined for balancing as the amplitude should be relatively constant across the line, aside from the factors that require compensating, as listed above.

- The ground-roll and direct wave SEG-Y files were exported from *ReflexW* into Matlab using scripts developed by CREWES (Margrave, 2013) and all traces with ground-roll were muted in the direct wave file so that amplitude balancing could be performed due to differences only in the direct wave.

- Prior to amplitude balancing, the root mean squared (RMS) amplitude was calculated for the traces and then corrected for geometrical spreading (using the known shot and geophone offsets) and for attenuation using an α factor of 0.266 (the choice of attenuation value is explained below).

- The shot and geophone direct wave amplitudes were reshaped into a matrix and plotted as shown in Figure 8.8. Any vertical colour striping indicates the relative coupling of the geophone to the ice surface, whereas horizontal colour striping indicates the relative power of the shots. Large amplitude traces (i.e. $>2.5\times10^5$) identified in this plot could impact the balancing and so were removed from the original trace file. In addition, the number of samples used to calculate the RMS amplitude of the direct wave were examined and any traces with fewer than 200 samples (that could occur due to muting of the ground-roll) were removed in order to limit bias within the balancing.

- A geophone scalar was created by taking the mean over the geophone coupling outputs and dividing the matrix by the scalar to balance differences in the coupling.

- A shot scalar was created by taking the mean over the shot power outputs. Again, the matrix was divided to balance the amplitudes for differences in shot power.

- The full trace record was then normalised with respect to both the geophone and shot scalars.

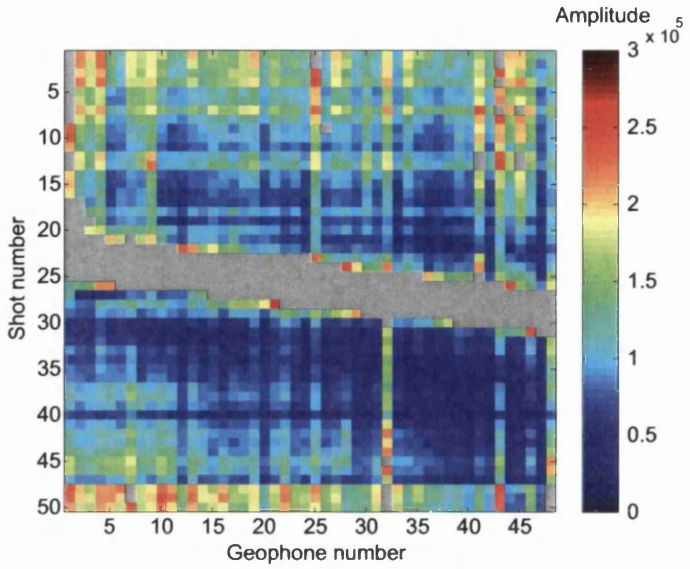

Figure 8.8: *Trace balancing matrix for the PLOP site indicating variations in shot power and geophone coupling. Traces were balanced based on these variations in amplitude along the seismic line. Grey squares indicate traces that have been removed due to noise that might bias the balancing.*

AVA analysis was applied to the balanced record in *ReflexW*. CMPs were chosen for the subglacial basin (between 580 and 1180 m along the stacked section; indicated by the red double arrow in Fig. 8.7) on the assumption that the material at the ice-bed interface would be similar within this region. The first Fresnel zone for this site is 154 m (see Eq. 8.6, with a wavelength of 38 m and a primary reflection depth of ~1250 m). The shot gathers indicate three strong reflections associated with the subglacial basin (Fig. 8.7 b and c); it is the upper reflection that is assumed to be the ice-bed interface and is analysed with the AVA technique. This upper primary reflection is clear in all shot gathers and therefore can be easily picked (see Fig. 8.9 a). Primary reflection amplitudes were picked at the peak of the first positive amplitude half-cycle from shot gathers. Care was taken to only pick clean reflections without influence from ground-roll (see Fig. 8.9 b for an example of the picks).

Although the primary reflection was easily identifiable, the multiples were not; as a result, the multiples could not be picked for all of the primary reflections. Any multiple reflections polluted with ringing or other reflections were not picked. In total, 91 multiple waveforms and corresponding primaries were picked; these matches were located closer to ~10°, where returns were less noisy than those near ~0° (although all within a near-offset range of ~10°, where the change in raypath travel-distance does not significantly impact the multiple amplitude).

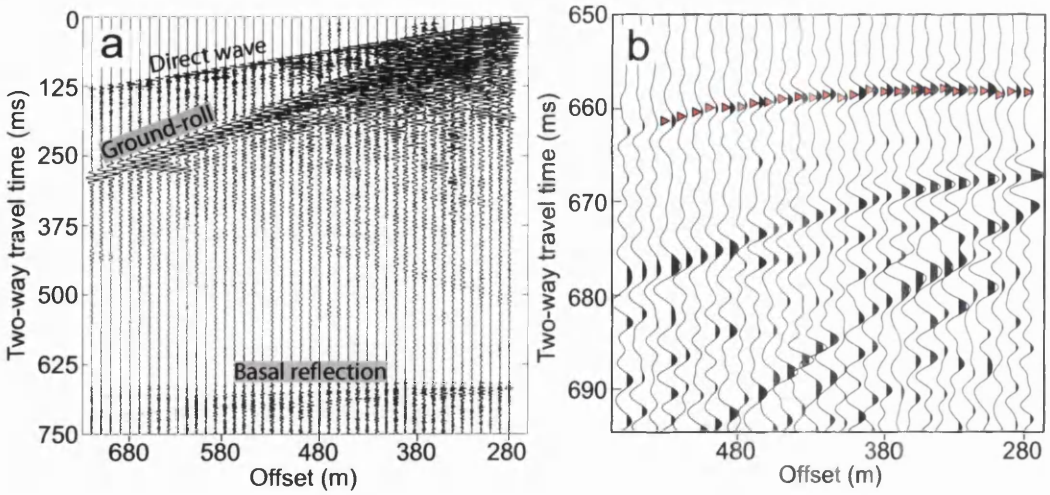

Figure 8.9: *Example shot gather from PLOP. a) Gather including the direct wave, ground-roll and bed reflection. b) Close-up of the bed reflection. AVA picks are shown by the red triangles.*

To conduct AVA analysis, Eqs. 8.8 and 8.9 described in Section 8.2.3 were applied to the PLOP dataset. The near-offset reflection coefficient was calculated using Eq. 8.7 and the remainder of the primary picks scaled relative to this value. In total, 541 primary picks were used for AVA analysis. Eq. 8.8 was used to calculate the AVA reflection coefficients for the basin. These equations include corrections for geometrical spreading and attenuation. The former requires calculating the raypath total travel distance (d_p). For the latter, the attenuation factor, α, must be estimated. During the 2010 summer field season, three other seismic lines were acquired and processed by A. Booth (see Section 3.6.3 and Booth *et al.*, 2012). During processing, an attenuation range of $0.266 \pm 0.088\,\mathrm{km}^{-1}$ between frequencies of 90-300 Hz was determined through spectral analysis of the primaries and multiples of the ice-bed reflector (pers. comm. A. Booth). As the PLOP field site is within 5 km of the acquisitions where attenuation was determined, it was deemed appropriate to apply the same attenuation factor to the PLOP site.

The AVA outputs were calculated for ice velocities between 3760 and $3850\,\mathrm{m\,s}^{-1}$ and for attenuation values between $0.178\,\mathrm{km}^{-1}$ and $0.354\,\mathrm{km}^{-1}$. Figure 8.10 shows an example output for PLOP assuming an ice velocity of $3800\,\mathrm{m\,s}^{-1}$ and $0.266\,\mathrm{km}^{-1}$ attenuation. For analysis of the AVA curve, the points are binned in 1 degree categories in order to increase the signal-to-noise ratio (see Fig. 8.11 a). Vertical error bars are calculated for the combined interquartile range of the values output from: a) the variations from the binning process and b) the variations from the

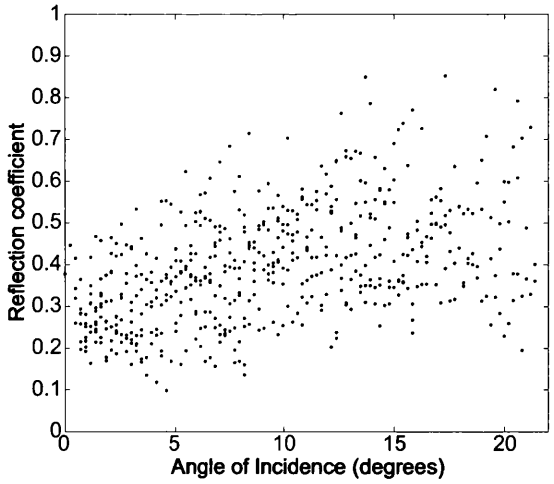

Figure 8.10: *AVA reflection coefficient outputs for all primary reflector picks over the basin at the PLOP site calculated with an example ice velocity of 3800 m s^{-1} and an attenuation value of 0.266 km^{-1}.*

ranges of applied attenuation coefficient and ice velocity values. The horizontal error ranges show the interquartile ranges of the incidence angle within each bin.

Once the AVA output has been obtained, the results can be analysed to assess the material characteristics of the substrate. This is achieved by applying the K-Z equations described in Section 8.2.3, which calculate reflection coefficients at angles between 0 and 90 degrees incidence for materials with different P-wave and S-wave velocities and different densities. The closest applicable K-Z models for the PLOP AVA output are shown in Figure 8.11 b. These model matches were determined by limiting the K-Z zero-offset reflection coefficient to a range of 0.34–0.41 (i.e. the zero-offset range indicated in the PLOP AVA outputs) and only allowing K-Z models with a positive gradient. It is apparent from Figure 8.11 b that the K-Z models do not match well with the PLOP AVA range as the gradient for the latter is too steep. The acoustic impedance values of these K-Z models range between 7.02–8.20 $\times$ 10^6 kg m^{-2} s^{-1} and the Poisson's ratios range between 0.42–0.50. This is not a plausible result for glaciological subsurface material as the high acoustic impedance implies lithified till or rock but the Poisson's ratio suggests water saturated soft material (see e.g. Peters *et al.*, 2008).

Booth *et al.* (2012) showed that, if AVA outputs are not easily comparable with the K-Z models it is likely that thin layers are present (see Section 8.2.5). They provide an equation for estimating what the acoustic impedance of the layer underlying the thin layer (Z_{under}) would be if some assumptions are made about the characteristics

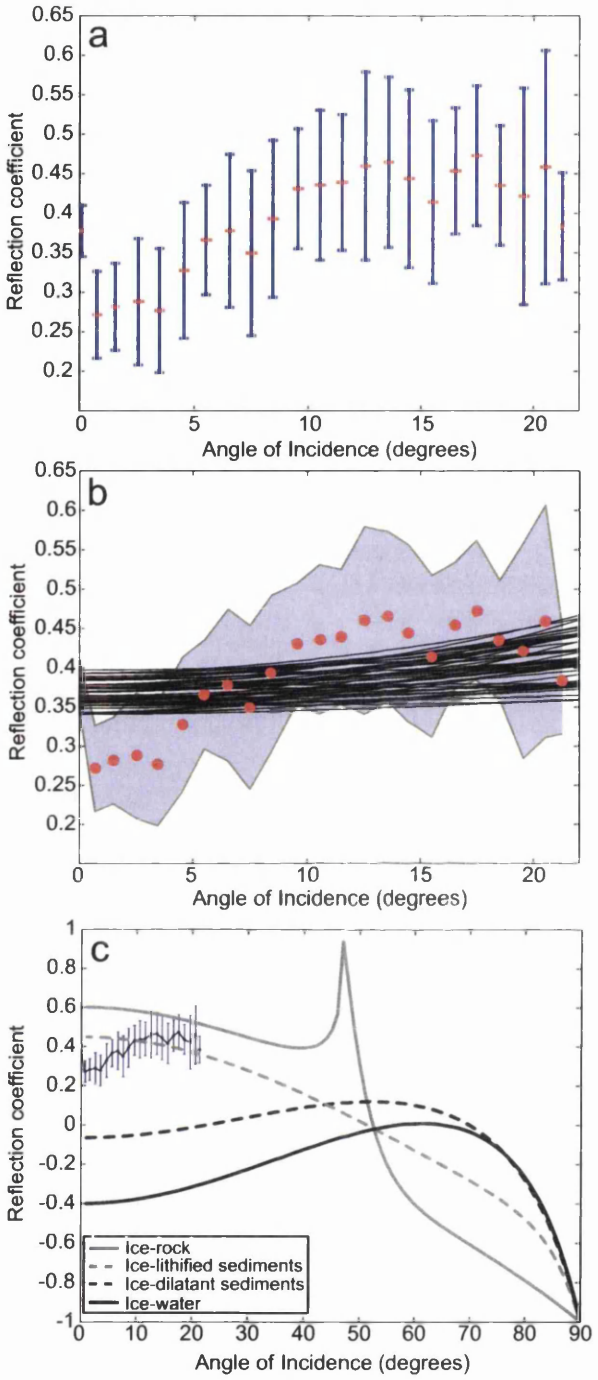

Figure 8.11: *Amplitude vs. angle reflection coefficient outputs for primary reflection picks over the basin at the PLOP site. a) AVA outputs averaged in 1 degree bins including error from variations in ice velocity and ice attenuation value and angle binning. b) K-Z models (black curves) within an applicable zero-offset range plotted with the calculated AVA range (blue shaded area). c) Calculated AVA output range with examples of reflection coefficient outputs for typical ice-interface boundaries using the K-Z equations. Here, AVA curves for ice with bedrock, sediment and water interfaces are plotted using material properties as stated by Peters* et al. *(2008, see Table 8.1).*

of the thin layer:

$$Z_{under} = Z_{thin} \frac{[(R0_{obs} - R0_1 + (1 - R0_1)^2]}{[(1 - R0_1)^2 - (R0_{obs} - R0_1)]}. \tag{8.10}$$

Here, $R0_{obs}$ is the zero-offset reflection coefficient calculated during AVA analysis, $R0_1$ is calculated from the known acoustic impedance of the overlying material (in this case, ice with an acoustic impedance of $3.5 \times 10^6\,\mathrm{kg\,m^{-2}\,s^{-1}}$) and an estimated thin layer acoustic impedance value (Z_{thin}). To assess the PLOP dataset, Eq. 8.10 is applied with $R0_{obs}$=0.35 (as suggested by the AVA outputs, see Fig. 8.11 a) and a Z_{thin} range of $1\text{–}9 \times 10^6\,\mathrm{kg\,m^{-2}\,s^{-1}}$, which incorporates all reasonable acoustic impedance values that would be found at the ice-bed interface. The outputs are shown as the green curve in Figure 8.12 with the possible range of acoustic impedance of the underlying substrate indicated on the y-axis.

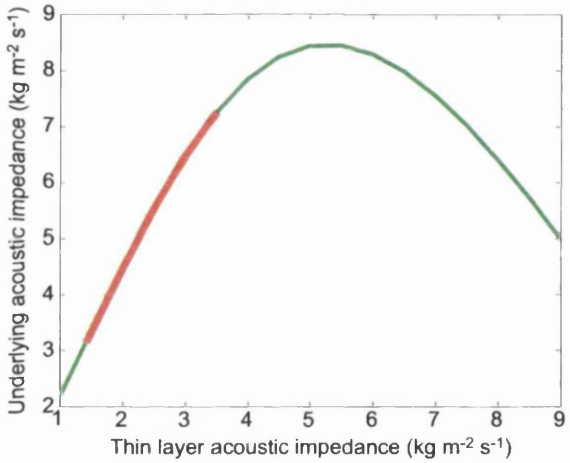

Figure 8.12: *Curve showing the acoustic impedance of the underlying substrate given a range of thin layer acoustic impedance values (green curve, see Eq. 8.10). The red curve indicates the likely acoustic impedance values of the thin layer and underlying substrate as discussed in Section 8.4.5.*

Results

Applying an AVA analysis approach assuming two infinite half-spaces does not produce plausible results for the PLOP site. Matching the closest K-Z models to the calculated AVA range implies an acoustic impedance value associated with rock-like sub-ice material, however the Poisson's ratio suggests a saturated soft sub-ice material. As a result it is likely that thin layers below the seismic resolution are merged

within the AVA signal and preventing accurate interpretation of the seismic returns. The approach suggested by Booth *et al.* (2012) produces a range of possible acoustic impedance values for both the thin layer and the underlying substrate. This range (shown for the PLOP site in Fig. 8.12) can be constrained further by assessing likely conditions at this site.

As there is a high Poisson's ratio output in the K-Z models that match with the calculated AVA range, one of the sub-ice layers is likely to be soft and saturated. It is not likely that a consolidated, dry material would overlie a soft, wet material and therefore it can be assumed that the overlying thin layer is soft. Such an assumption puts an upper constraint on the thin layer acoustic impedance of $\sim 3.5 \times 10^6\,\mathrm{kg\,m^{-2}\,s^{-1}}$ (Atre and Bentley, 1993). The thin layer will not have an acoustic impedance lower than that of water (i.e. $1.5 \times 10^6\,\mathrm{kg\,m^{-2}\,s^{-1}}$). These thin layer acoustic impedance limits constrain values for the underlying layer to 3.36–$7.27 \times 10^6\,\mathrm{kg\,m^{-2}\,s^{-1}}$ (see red curve in Fig. 8.12). The lower value would suggest a thin layer of water overlying dilatant till, whereas the upper value would suggest dilatant till overlying very stiff (approaching lithified) sediment.

Booth *et al.* (2012) demonstrated with ray-trace modelling that, although the seismic resolution for a clean wavelet (with no thin layer interference) is $\lambda_s/4$, the properties of the underlying layer will be sufficiently strong to allow accurate AVA interpretation. However, once the seismic resolution is $< \lambda_s/6$, the properties of the thin layer will produce a composite AVA response. The strongest frequency of the seismic waves for PLOP are at 100 Hz. First, assuming the thin layer is composed of dilatant till with a P-wave velocity of $1800\,\mathrm{m\,s^{-1}}$ (following Booth *et al.*, 2012), this would suggest $\lambda_s = 18$ and a maximum upper layer thickness of 3 m. However, if the thin layer is composed of water, the P-wave velocity would be $1498\,\mathrm{m\,s^{-1}}$ (following Peters *et al.*, 2008), this would give a wavelength of $\lambda_s = 15$ and a maximum water thickness of 2.5 m.

8.4.6 *PLOP Discussion*

The primary purpose of the PLOP reflection seismic line was to test the hypothesis that there was water underlying the ice in a basin, as indicated by a deep-look radar campaign in spring 2010. Although, due to the lack of comparability between the AVA output and the K-Z models, it is not possible to identify the basal material directly, some assertions can be made:

- As there is a thin layer response it can be assumed that any water present at the bed during the seismic survey is not deeper than 2.5 m. As a result, there was not an extensive subglacial lake present at this site.
- In areas of dilatant till, water will flow through pores and therefore a layer of water is unlikely to stably exist between till and overlying ice (Rempel, 2009a).
- It is not clear that till can remain dilatant to depths greater than ~6 m (Alley *et al.*, 1986); beneath this depth the till will become compressed and have reduced porosity. As a result it is unlikely that a thin layer of water would be underlain by a layer of dilatant till thicker than the seismic resolution. Therefore, a clear seismic response from water overlying dilatant till would be unlikely.
- Figure 8.7 shows the ice-bed interface as an uneven curve, which is more likely associated with a till sequence than a body of water that would likely return a flat reflector (due to equilibration melting of the overlying ice).

In light of these assertions, it appears more likely that the basin sampled by the PLOP seismic survey consists of a thin layer of dilatant till with a maximum thickness of 3 m underlain by lithified sediment. However, the analysis of the thin layers at the PLOP seismic site is based on the assumption that only two layers underlie the ice interface. It is possible (and perhaps likely) that multiple layers with different densities and seismic properties exist, particularly if unlithified sediments are present. It is not possible with current AVA analysis techniques in glaciology to distinguish between multiple layers. The Fresnel zone at PLOP is ~150 m with AVA responses calculated over a basal range of ~600 m; it is possible that there are multiple material types or levels of sediment saturation within this region.

Although the characteristics of the material within the basin at PLOP cannot be conclusively determined, it is highly likely that soft, water saturated sediments made up part of the basin at the PLOP seismic site.

8.5 SHR

8.5.1 *Aims*

The SHR site was chosen to contribute to data collected by an ice borehole drilling team from the Alfred Wegner Institute (see Smeets *et al.*, 2012). A seismic survey was necessary at this site to estimate basal characteristics that could not be determined from the two boreholes drilled at this site (primarily due to the fast closure times of the boreholes that required rapid instrumentation with pressure transducers and precluded the possibility of borehole surveys). This seismic survey provided an excellent opportunity to compare the basal conditions of a near-margin site of Russell Glacier with the F-Lake case-study site and allows analysis of the variability and impact of basal conditions on hydrological development in the wider RGC. When examining the location of SHR in relation to the main field site at F-Lake (Fig. 8.4), it is in a prime position to give information about basal conditions downstream of the modelled drainage network described in Chapters 5–7. Some of the analyses and results in this section have been published in the Annals of Glaciology (Dow *et al.*, 2013).

8.5.2 *Field site*

SHR is located ~13 km from Russell Glacier terminus (at 67° 06' N, 49° 55' W; Fig. 8.13) at an average surface elevation of 710 m a.s.l. SHR is of particular interest for examining the links between ice dynamics and basal properties in RGC as it was the site of both the fastest observed mean annual velocity (138 m yr^{-1}) and the largest summer-time acceleration (300%) along the K-transect flowline, between the period of 1990–2007 (van de Wal *et al.*, 2008). This region also experiences diurnal uplift and horizontal acceleration directly coupled to surface melt volumes (Shepherd *et al.*, 2009). In summer 2010, two boreholes were drilled to the bed at depths of 610 m and 632 m, and instrumented with an array of pressure sensors and thermistor strings (Smeets *et al.*, 2012).

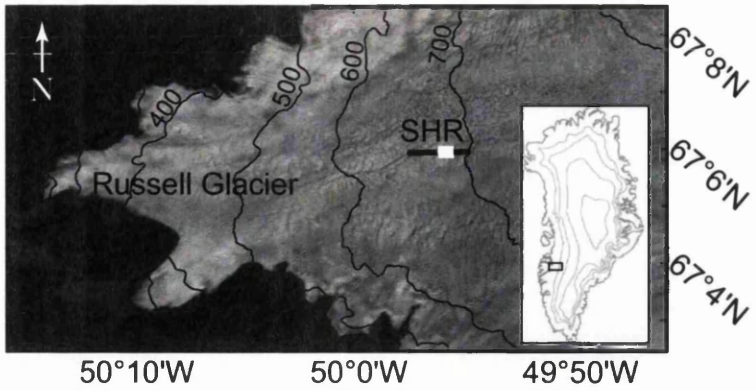

Figure 8.13: *Landsat image of Russell Glacier acquired on 18th August 2010 (at a resolution of 30 m) with the inset indicating the location in Greenland. Surface elevation contours are marked by the black curves at 100 m intervals. The location of the seismic reflection line is indicated by the black line; the thick white line indicates the area of the bed sampled by the seismic profile.*

8.5.3 *Data acquisition*

The seismic AVA experiment was carried out at SHR in late July 2010. The seismic line was oriented parallel to bulk ice flow (approximately NE-SW) and located ~50 m from the boreholes. Data were recorded using a Geometrics GEODE system, with 24 vertical-component 100 Hz geophones installed at 10 m intervals in a fixed array configuration. To increase coupling with the ice surface, geophones were mounted on 7 cm-thick, 10 kg concrete slabs that were allowed to freeze in overnight. A total of 33 shots were installed at a depth of 3 m with a horizontal separation of 60 m, covering 1920 m on the surface. Each hole was loaded with a combined 250 g Pentalite and 400 g dynamite charge, attached to electrical detonators with a 25 ms delay. The west side of the seismic line comprised 19 shots with a maximum surface offset of 1140 m from the first geophone. The east side of the seismic line was made up of 13 shots with a maximum surface offset of 780 m from the first geophone (see Fig. 8.14 a). Approximately 1100 m of the ice-bed interface was illuminated along the profile with a 3-fold CMP coverage and 792 traces. Elevations of the geophones and shot locations were surveyed using a Leica SR520 GPS receiver, differentially corrected against a bedrock-mounted reference station, to 10 cm precision by S. Doyle, Aberystwyth University. Unlike flat, snow-covered terrain where reflection seismic acquisition more typically takes place (e.g. Anandakrishnan, 2003; Smith, 2007; Peters *et al.*, 2008), the surface topography at SHR undulates substantially with ice ridges rising to several meters (see Fig. 8.14 a). The maximum elevation change over the seismic line totals 39 m. In the vicinity of the seismic line, crevasses,

moulins and surface streams were observed.

Table 8.4: *SHR surface elevation correction velocities.*

Shot no.	20	21a	21b	22a	22b	23a	23b	24a
Direct wave velocity ($m\,s^{-1}$)	3531.57	3267.26	3518.92	3156.08	3821.23	3427.70	4670.01	3604.57
Std. Dev.	4.97	2.04	3.29	1.23	5.74	1.63	10.07	1.35
Sample no.	24	6	18	12	13	18	7	24

8.5.4 *SHR seismic stacked section*

Methods

The SHR seismic stacked section was processed in *ReflexW* (Sandmeier Software). Elevation corrections were arrived at using the same method as described for PLOP in Section 8.4.4 with ice direct wave traveltime determined from four near-offset shots, 240 m to the east of the zero-offset geophone. The resulting velocities and standard deviations used to correct the trace start time are shown in Table 8.4; the velocity from shot 23b was discarded as an anomaly. The mean direct wave velocity from the surface velocity analysis is $3625\,m\,s^{-1}$. The processing steps used to produce a seismic profile for SHR are described below and, similar to the PLOP site, have been tested for the values that produce the clearest outputs; this processing flow is similar to that applied by A. Booth to the seismic reflection lines near F-Lake (see Section 3.6.3):

- A static correction was used to remove the 0.25 ms delay caused by the charge detonator delay.
- Due to an in-field error with the GPS on the shot boxes, traces 25–48, from shot 2 appeared to have 'slipped' relative to the other shots. It was calculated that the difference between the last geophone ms output of shot 3 and the first geophone ms output from shot 4 was 80 ms. This pattern was also consistent between shots 4 and 5. The distance however between the end of the 'slipped' shot 2 and the beginning of shot 3 was 637 ms. As a result the start-time for shot 2 was moved by -557 ms.
- An Ormsby bandpass filter was run through the data. The lower and upper cutoffs were 25 and 300 Hz respectively with the lower and upper plateaus, 50

and 150 Hz respectively. The bandpass was used to remove noise and reduce the ground-roll.

- A predictive deconvolution was run through the data to remove multiples. The filter length was 12 ms with a lag of 4 ms.
- A 0-lag spike deconvolution was applied with a filter length of 15 ms. This deconvolution was used to compress the wavelet over time, which produces more prominent reflection boundaries, removes wavelet delays and reduces noise.
- The data were corrected for changes in surface elevation using the static correction described above.
- A NMO constant velocity stack was run for the common mid-point gathers using a velocity of $3800\,\mathrm{m\,s^{-1}}$ (following the procedure of A. Booth).
- A range of migration operations were tested on the brute stack; a Kirchhoff migration with a summation width of 2 traces and a velocity of $3800\,\mathrm{m\,s^{-1}}$ produced the clearest output by collapsing diffractions and improving spatial resolution.

Results

Due to the irregular surface topography, the signal-to-noise ratio of the seismic returns was degraded by near-surface defocussing from rebound against the surface (see Fig. 8.15 for a representative shot gather). Crevasses and moulins were a potential source of additional diffractions within the data. The geophones were not evenly spaced, as projected onto the horizontal, due to the topography, and although elevation corrections were made for the profile, not all of these factors could be compensated for. As a result, the seismic returns are noisy in comparison with data collected from further inland on the GrIS, such as at the PLOP site, or the Antarctic (e.g. Smith, 2007; Peters *et al.*, 2008). Interpretation of the stacked section is more challenging as a result, due to loss of basal clarity by removing residual ground-roll. Notwithstanding, the ice-bed interface is distinct across most of the stacked section (Fig. 8.14 b and c). Up-glacier, in the eastern part of the seismic section, the bed appears to be flat with relatively minor undulations on the vertical scale of ~10 m. Ice thickness across the section is ~640 m. A weaker cross-cutting

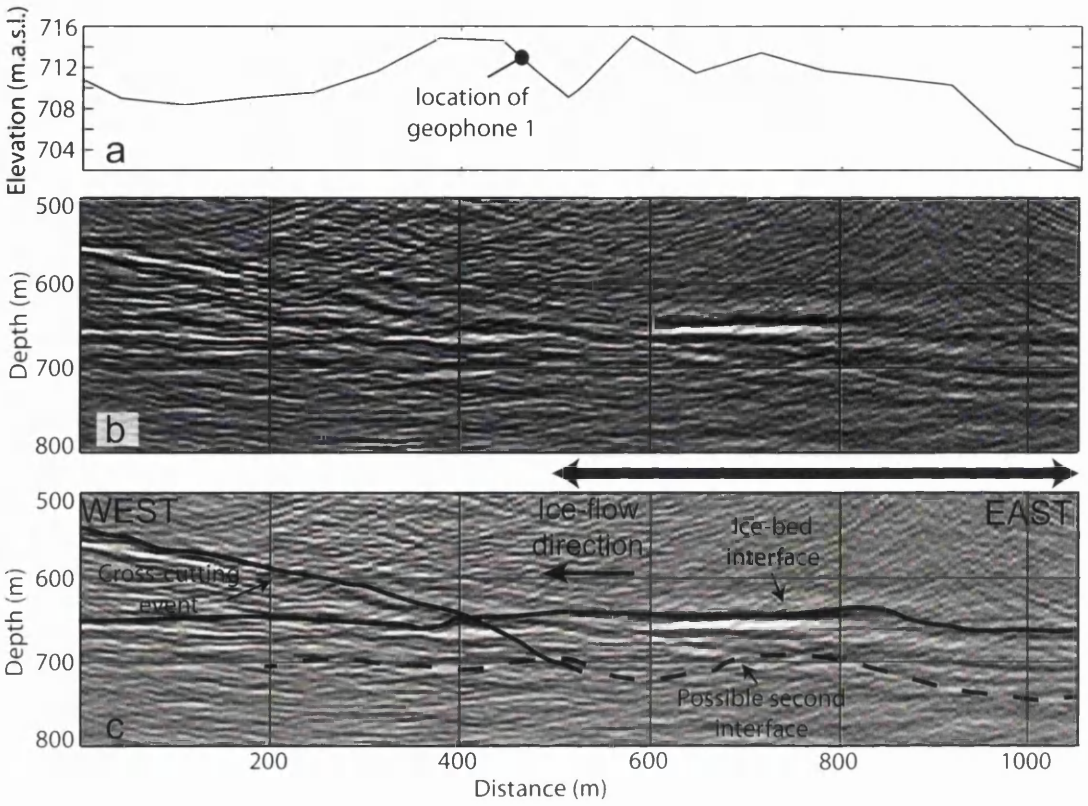

Figure 8.14: *a) Ice surface elevation at SHR. Note the vertical exaggeration and scale on the elevation axis. b) Seismic profile of the field site indicated in Fig. 8.13. The depth is based on a seismic velocity of 3800 m s^{-1} and is relative to the surface elevation in a). c) Interpretation of the main features in the seismic profile. AVA analysis is applied to the area shown by the black double arrow.*

event appears in the stacked section, likely due to an out-of-plane reflection, but will not impact the results as analysis is concentrated only on the non-contaminated areas of the flat reflection. A second weak reflection underlies the ice-bed interface, which is not a ghost reflection due to the shallow depth of the shot holes, but may be a reflection from an underlying horizon (Fig. 8.14 b and c).

8.5.5 *SHR AVA*

Methods

The primary purpose of the SHR site was to determine the characteristics of the basal materials using AVA analysis. For application of the AVA techniques described in Section 8.2.3, both primary and multiple reflection amplitudes are necessary. Un-

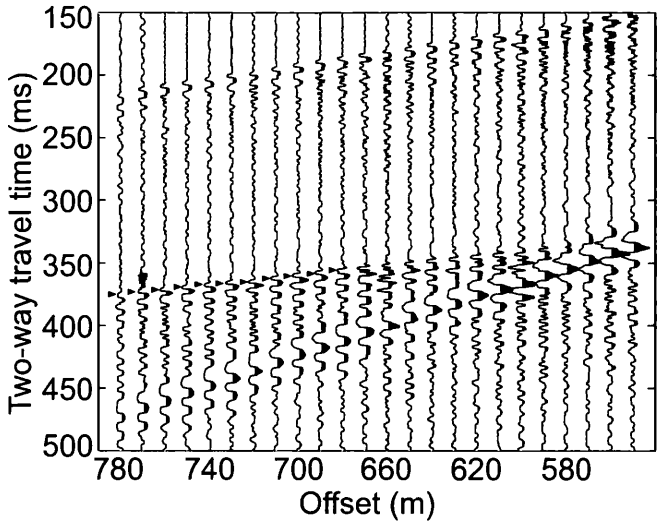

Figure 8.15: *Shot gather from SHR where it can be seen the basal reflection shows no polarity reversal. AVA picks are shown by the red triangles. Note that data affected by the ground-roll or other noise are not picked.*

fortunately, the seismic data acquired at SHR are sufficiently noisy that multiple amplitudes cannot be reliably measured, so that application of Eq. 8.9, and subsequently of Eq. 8.8, is not feasible since A_m is unknown. As a result, a new approach is developed to determine the AVA response, using the fact that A_m can only vary within a narrow range for any given reflection event in order to still be physically plausible. This alternative approach consists of four main steps:

1. Eq. 8.9 is used to calculate an associated range of source amplitudes (A_0) for any particular reflection event using the fixed, known, value of A_p and a narrow, physically plausible, range of A_m.

2. Known A_p, known d_p, a range of plausible α values, and the inferred range of A_0 are applied to Eq. 8.8, yielding a series of 'simulated AVA curves'.

3. A cumulative plot of all simulated AVA response curves is produced for all ice-substrate reflection events covered by the SHR seismic survey (Fig. 8.17).

4. A forward modelling approach is adopted by comparing the cumulative simulated AVA curves with a range of AVA curves modelled using the K-Z equations; this approach is demonstrated schematically in Figure 8.18.

By matching physically plausible simulated and modelled AVA curves, the nature of the substrate at SHR can be constrained, despite the uncertainty inherent to this

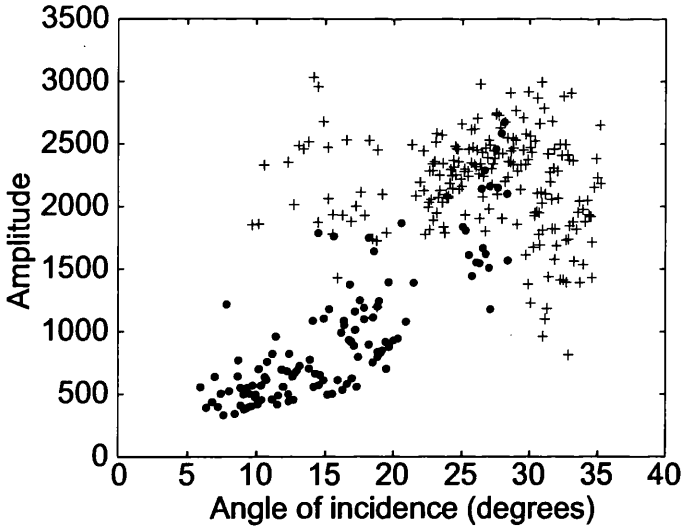

Figure 8.16: *Example of primary reflection amplitudes corrected for geometrical spreading and an illustrative attenuation of 0.4 km^{-1}. Amplitudes are divided into east data (dots) and west data (crosses; see Fig. 8.14).*

new approach.

For the SHR dataset, measured seismic amplitudes were balanced to correct for variations in geophone coupling and shot power by normalising each trace by the RMS direct-wave amplitude (Booth *et al.*, 2012), following the same processing steps for PLOP described in Section 8.4.5. The trace balances are shown in Figure 8.19. Primary reflection amplitudes were then picked at the peak of the first half-cycle from shot gathers, separated by the west (crosses) and the east (dots) gathers (divided by the location of the first geophone; an example of the primary reflection amplitudes corrected for geometrical spreading using an illustrative attenuation value of 0.4 km^{-1} is shown in Fig. 8.16, although the final analysis uses a range of attenuation values). A representative shot gather, with AVA picks indicated by triangles, is shown in Figure 8.15. Any primary reflections that had ground-roll interference were ignored as were any reflections that were not clean. The reflection amplitudes from the east side of the seismic line exhibit a positive near-linear relationship with respect to increasing angles of incidence whereas, likely due to the cross-cutting event, reflection amplitudes from the west side of the seismic survey lack a clear relationship with angle of incidence (Fig. 8.16). As a result, analysis is concentrated on the east side of the line. In the eastern gathers, data quality between angles of 0–6 and 22-24 degrees was sufficiently poor due to noise and ground-roll that they are not analysed.

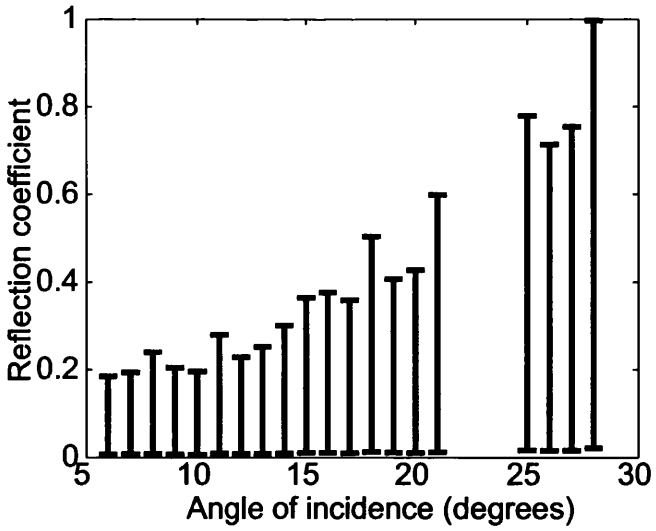

Figure 8.17: *A graph showing the range of simulated AVA outputs for SHR using a range of multiple and attenuation values, binned into angles of 1 degree.*

The plausible range of A_m values to apply to Eq. 8.9 is established by first examining the absolute value of the maximum primary reflection amplitude within the range of 6–10 degrees, which is 595; no data are available between 0–6 degrees. Multiple amplitudes (A_m) are therefore tested within the range of 0–600, but several constraints are imposed based on the AVA observations:

(a) No polarity reversal is observed, either with respect to the direct wave or across the offset range of the dataset (Fig. 8.15). This suggests that the minimum reflection coefficient at the base of the ice is 0 and therefore multiple amplitudes that deliver normal-incidence $R(0) < 0$ are rejected.

(b) A bedrock substrate has a normal-incidence reflectivity $R(0) = 0.6$ (Peters *et al.*, 2008). As subglacial materials will not have a higher normal-incidence reflectivity than bedrock, any multiple amplitude that delivers $R(0) > 0.6$ is rejected.

(c) The seismic wavelet cannot have a higher amplitude than that which was initially radiated (i.e., $A_p(\theta)d_p(\theta)\,e^{\alpha d_p(\theta)} > A0$), hence any multiple amplitude that delivers $R(\theta) > 1$, at any incidence angle, is rejected.

For each A_m test value, the attenuation coefficient (α) is varied between 0.2 and $0.6\,\mathrm{km}^{-1}$. The lower bound of $0.2\,\mathrm{km}^{-1}$, calculated by Bentley (1971) for cold Antarctic ice, represents a lower-end estimate of attenuation at the SHR site, where the ice is polythermal. The upper bound of $0.6\,\mathrm{km}^{-1}$ was derived by Kohnen (1969),

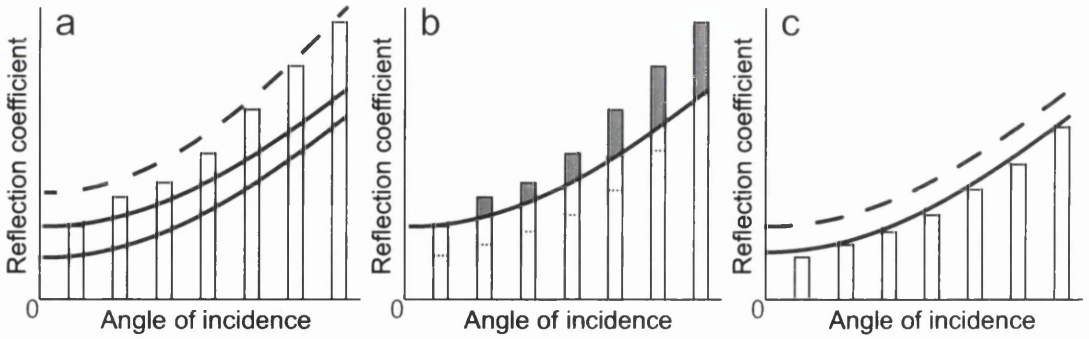

Figure 8.18: *Schematic of the procedure for comparing the simulated AVA range and the Knott-Zoeppritz AVA curves. a) The dashed Knott-Zoeppritz AVA curve R(0) lies above the simulated AVA R(0) and is therefore rejected. The solid Knott-Zoeppritz AVA curves lie below the simulated AVA R(0) and are therefore retained. b) The grey areas of the simulated AVA range bars are rejected as they lie above the R(θ) range of the Knott-Zoeppritz model. The dashed lines indicate where the simulated AVA range lies once all curves with any R(θ) above the Knott-Zoeppritz curve are rejected. c) The solid Knott-Zoeppritz AVA curve and the simulated AVA range are all within the same range and the Knott-Zoeppritz curve can then provide limits on the basal material properties at this site.*

for the GrIS. Because ice temperature data are not available at SHR, this wide attenuation range is applied, which is then reflected in the uncertainty of the final property estimation. The accepted range of simulated AVA observations, binned into angles of 1 degree, is shown in Fig. 8.17, and suggests that the normal-incidence reflectivity, $R(0)$, at SHR lies within a range of >0 to 0.19.

The simulated AVA range is now compared with known properties from K-Z AVA curves. K-Z curves are calculated for an upper ice layer and a lower layer with P-waves ranging between 1600–5200 m s^{-1}, S-waves between >0–2800 m s^{-1} and densities between 1000–2700 kg m^{-3}, at intervals of 100 that allow for the possibility of sediment or rock at the interface. The K-Z models that are comparable to the simulated AVA range are constrained by imposing the following criteria that are schematically illustrated in Fig. 8.18:

(a) The K-Z $R(0)$ value must lie within the $R(0)$ range output for the simulated AVA values with a tolerance of ± 0.005, reflecting the maximum inter-quartile variability in any simulated AVA bin (see Fig. 8.18 a).

(b) The binned AVA values must lie within the K-Z curve $R(\theta)$ range with a tolerance of ± 0.005 (see Fig. 8.18 b).

(c) The SHR raypath- and attenuation-corrected primary amplitudes (Fig. 8.16)

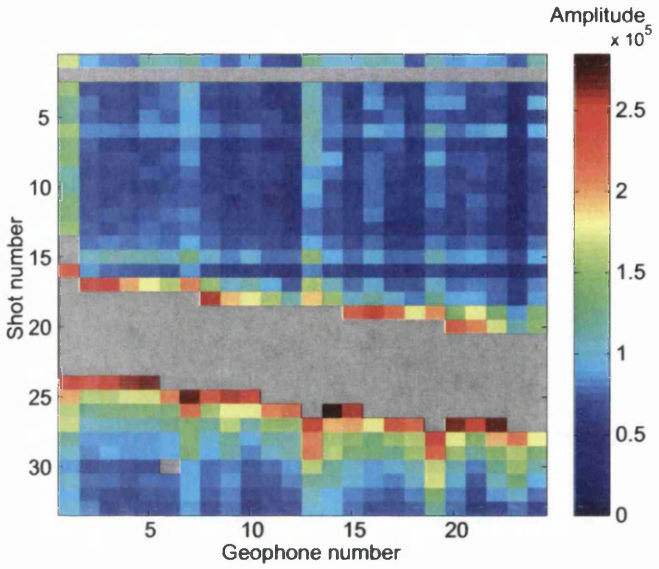

Figure 8.19: *Trace balancing matrix for the SHR site indicating variations in shot power and geophone coupling. Traces are balanced based on these variations in amplitude along the seismic line. Grey squares indicate traces that have been removed due to noise that might bias the balancing.*

increase with angle of incidence and therefore any K-Z $R(\theta)$ curve that decreases between 0 and 30 degrees is rejected.

(d) K-Z models with S-wave velocities of $0\,\mathrm{m\,s^{-1}}$ and densities lower than $1000\,\mathrm{kg\,m^{-3}}$ are rejected as both imply the presence of free water, which is not consistent with the lack of polarity reversal in the primary amplitudes.

Figure 8.18c illustrates the conditions under which a K-Z curve would be accepted in the analysis.

8.5.6 *Results*

Comparison of the range of K-Z models that correspond to the simulated AVA range (Fig. 8.20) yields the following characteristics for the substrate at SHR: an acoustic impedance between 3.50-3.68 $\times\ 10^6\,\mathrm{kg\,m^{-2}\,s^{-1}}$ and a Poisson's ratio (related to the level of saturation in a material) between 0.36–0.49. Illustrative examples of reflection curve properties from the simulated AVA range are given in Table 8.5, in relation to curves 1–4 highlighted in Fig. 8.20 b, to demonstrate the change in curve shape with variation in P-wave and S-wave velocities and density. In general, steeper

gradients are associated with a lower S-wave velocity. The illustrative curves are deemed plausible by the analysis described above, although curves 1 and 4 are close to the limit of the acceptable range of AVA outputs. As such the velocity and density values for the curves illustrate the uncertainty estimates within the approach. An acoustic impedance and Poisson's ratio value is calculated for each individual curve in Fig. 8.20 b. The final ranges of acoustic impedance of 3.50-3.68 $\times 10^6\,\mathrm{kg\,m^{-2}\,s^{-1}}$ and Poisson's ratio of 0.36–0.49 are therefore determined from the entire acceptable range of AVA curves and thus incorporate the uncertainty from the approach.

Table 8.5: *Reflectivity curve properties for the illustrative curves highlighted in Figure 8.20 b.*

Curve no.	1	2	3	4
P-wave ($\mathrm{m\,s^{-1}}$)	3300	1600	2100	3200
S-wave ($\mathrm{m\,s^{-1}}$)	100	100	600	1500
Density ($\mathrm{kg\,m^{-3}}$)	1100	2200	1700	1100

8.5.7 *SHR Discussion*

The SHR field site proved challenging for seismic analysis due to the highly variable surface topography and the presence of crevasses creating substantial noise within the data set. In this chapter, a modified technique for AVA analysis has been presented, using forward modelling with primary amplitude inputs that allows appraisal of the substrate from a seismic record with poorly defined or indistinguishable multiple reflections. Some properties of the basal material can be initially assessed from the primary reflection amplitude and the range of reflection coefficients. For instance, the absence of a polarity reversal throughout the dataset is inconsistent with the presence of a resolvable water body or dilatant till at the ice-bed interface. However, the positive gradient (as visible for the black dot datapoints in Fig. 8.16) implies a high Poisson's ratio that suggests the presence of water within a sediment matrix (Anandakrishnan, 2003). The limit of seismic resolution means that only layers thicker than approximately one quarter of the seismic wavelength can be distinguished. Sediment layers of < 1–$2\,\mathrm{m}$ thickness would not appear as individual layers at SHR, but could interfere with the seismic wavelets reflecting from underlying layers (see Section 8.4.6 and Booth *et al.*, 2012). Even considering these potential thin-layer effects at SHR, the primary amplitude polarity and gradient with respect to angle indicates that sediment is present at the ice-bed interface.

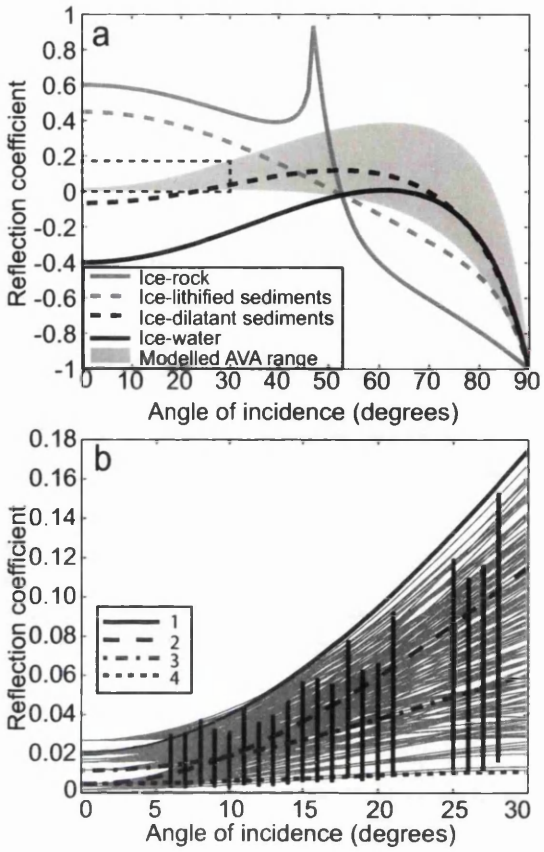

Figure 8.20: *a) The range of Knott-Zoeppritz models that correspond with the simulated AVA range at SHR (grey shaded zone) along with examples of reflection coefficient outputs for typical ice-interface boundaries using the Knott-Zoeppritz equations. Here, AVA curves for ice with bedrock, sediment and water interfaces are plotted using material properties as stated by Peters* et al. *(2008). The dashed box indicates the area highlighted in b). b) A close-up of the simulated AVA range (black bars) that correspond to K-Z models (grey curves) within the simulated AVA R(0) range. Properties of selected curves, labelled as 1–4, are shown in Table 8.5.*

If the primary reflection amplitude is assumed to be unaffected by thin-layer effects, the range of acoustic impedance and Poisson's ratio for SHR can be interpreted. Atre and Bentley (1993) suggest that lodged till has an acoustic impedance of 3.69–$3.90 \times 10^6\,\mathrm{kg\,m^{-2}\,s^{-1}}$ and a corresponding porosity of < 0.3. In contrast, saturated and possibly deforming sediment is argued to have an acoustic impedance of 3.00–$3.40 \times 10^6\,\mathrm{kg\,m^{-2}\,s^{-1}}$ (Atre and Bentley, 1993) and a porosity of 0.4 (Smith, 1997). Hence, the acoustic impedance range of 3.50–$3.68 \times 10^6\,\mathrm{kg\,m^{-2}\,s^{-1}}$ at SHR suggests that, at the time of the seismic experiment, the till was not stiff enough to be lodged but had a high porosity between 30% and 40%. As the shear strength of sediment reduces exponentially with increasing porosity (Tulaczyk *et al.*, 2000), the till was likely weak, although not dilated. The SHR Poisson's ratio between 0.36 and 0.49

indicates water was present in the sediment (Gercek, 2007), as do water pressures near overburden recorded in the SHR boreholes at the time of the seismic survey (Smeets *et al.*, 2012). The dashed box in Figure 8.20 a, which indicates the simulated AVA range, clearly shows that the subglacial material at SHR is sediment.

8.6 Applications

The aim of the seismic analysis was to determine variability in basal conditions at Russell Glacier and establish the applicability of the coupled hydrological model to the wider RGC. The results from SHR near the terminus suggest that soft sediment is present at the bed. The analysis by A. Booth of the F-Lake seismic sites (see Section 3.6.3) also suggest the presence of sediment, although in the drainage valley of F-Lake this till appears to be lithified. At PLOP, it is not possible to determine exactly what material is at the bed due to thin layer interference with the AVA signal, although it is likely a thin (< 3 m) layer of either water or dilatant sediment is present, with the latter being more plausible. The implications of possibly widespread sediment at the bed of RGC is discussed further in Section 9.2.5.

The coupled hydrological model is based on flow through channels with a hard base and a distributed network that could represent either linked cavities or Darcian flux through sediment. Currently there are no applicable models of fast-flow networks in sediment that evolve both spatially and temporally (see Section 2.4.3). As a result, it was beyond the scope of this study to model sediment canals or other sediment-based fast-flow pathways. The presence of soft sediment in a basin at the F-Lake perpendicular sites (B'–B and C'–C in Fig. 3.13) is not linked to the drainage of F-Lake as the hydraulic potential gradients preclude flow to the SW of the lake (see Fig. 3.4). However, soft sediment at the near-margin SHR is likely to interact with the flux of water. On the other hand, AVA analysis represents only a small portion of conditions at the ice-bed interface and analysis is often focussed on basins that would be more likely to include sediment (Booth *et al.*, 2012). Further analysis is therefore necessary to determine the extent of soft sediments in RGC.

The lithified till in the region of the F-Lake drainage suggests that annual downstream flux from the lake might remove soft sediment and leave lithified sediment at the base. If this is the case in the region of the lake drainage, the hard-bed configuration of the coupled hydrological model is applicable. The conditions further

downstream are not known, but if water from the lake drainage eventually flows through the SHR site, then the coupled hydrological model might not accurately replicate drainage conditions in this region. Upstream of F-Lake, the presence of a thin layer of water underlain by soft till or dilatant till underlain by sediment suggests that soft sediment occurs in basins in the inland region of RGC. Although the soft sediment sequences are not thick, they could still have an impact on drainage development. If a layer of water was present upstream of F-Lake prior to rapid drainage, the subglacial system may have been somewhat pre-developed. Such a condition is tested within the hydrology modelling sensitivity analysis (see Section 7.5.1).

8.7 Summary

In this chapter, two seismic reflection studies, both located in RGC have been discussed. The first site, PLOP is ~5 km NE of the case-study lake. This site was identified in a GPR campaign in spring 2010 as an area of possible subglacial water storage. The purpose of the seismic line was therefore to determine the characteristics of the material at the ice-bed interface. The seismic stacked section for PLOP shows the presence of a basin ~900 m wide with a steeply sloping wall to the ESE. The basin lies within a trough identified on the basal DEM that connects to the drainage route of F-Lake; PLOP could therefore be an important source of water prior to the lake drainage if the basin acts as a storage reservoir. AVA analysis was performed on the primary reflections from the PLOP basin, however, thin-layers complicated the interpretation of the AVA output and therefore the basal conditions cannot be fully determined. Despite this, thin layer analysis indicates that the basal material either consisted of a layer of water with underlying dilatant till or dilatant till with underlying lithified till. Of these two options a thin layer of dilatant till with underlying lithified till is the more likely because 1) it is not clear that a layer of water could exist for a long period over porous dilatant till and 2) a seismically-thick layer of dilatant till is not likely due to pore compression under weight of the overlying sediment. This analysis is based on the assumption of a two-layer substrate; a greater number of layers could be further influencing the AVA signal although it is likely that, if more than two layers were present, soft sediment would constitute at least one of those layers.

The second seismic reflection site, SHR is located ~13 km from Russell Glacier

terminus and is a region of substantial seasonal and annual velocity variation (van de Wal *et al.*, 2008; Shepherd *et al.*, 2009). This site was examined to provide basal conditions for a borehole drilling team but also to determine the applicability of the coupled hydrological model described in Chapters 5–7 to areas near the Russell Glacier terminus. The seismic stacked section at SHR illuminated 1100 m of the bed and revealed a largely smooth ice-bed interface at a depth of ~640 m. AVA analysis was complicated by the lack of multiples in the data due to highly undulating surface topography. In this chapter, a new technique for AVA processing using forward modelling with primary reflection amplitudes and simulated multiple amplitudes was presented, as published in Dow *et al.* (2013). The model-driven approach indicates that, even considering the effect of possible thin layers, sediment underlies the study site and should be considered in analyses of ice dynamics in this region. If thin-layers are not interfering with the seismic wavelets, the AVA results demonstrate the presence of weak sediment at the bed with porosity between 30% and 40%.

Analysis of three other seismic lines near the F-Lake site by collaborators (see Section 3.6.3) also indicate the presence of sediment at the bed. The coupled hydrological model is based on the premise of an ice-bedrock interface (and thus involves the growth of R-channels carved into the overlying ice). The seismic analysis for RGC implies that applying a model with an ice-rock boundary could be a limitation. However, the F-Lake seismic analysis indicates lithified sediment in the basal trench through which the rapidly draining lake water flowed. It is possible that it is due to the draining lake that little soft sediment lies within the flux region of F-Lake. Water would interact with lithified sediment (i.e. flow over the surface rather than through the pores) in a similar manner to bedrock and therefore, within the direct vicinity of F-Lake and along the 12 km flowband that runs along the trench to the NW (see Section 3.3) the coupled modelling approach assuming a hard bed is likely appropriate. The soft sediment identified at PLOP and SHR suggests that the model is perhaps not applicable in all regions of RGC. However, as the AVA analysis primarily targeted basins where sediment would be more likely to accumulate, further work is necessary to determine the extent of soft sediment in this glacier catchment. Despite this, future work modelling the development of basal hydrological networks in Russell Glacier and possibly elsewhere in Greenland should seek to develop equations for fast flow in soft sediment and incorporate variable basal characteristics.

Chapter 9

Discussion

9.1 Introduction

Both lake drainage in-situ data (Das *et al.*, 2008) and modelling studies (Sole *et al.*, 2011; Pimentel and Flowers, 2011) have suggested that large and efficient channels form rapidly during lake drainage; this argument has been restated in several studies (Howat *et al.*, 2010; Hoffman *et al.*, 2011; Bartholomew *et al.*, 2012; Cowton *et al.*, 2013). This argument for a rapid channelisation mechanism adds to the general consensus that Greenland hydrological systems act similarly to Alpine systems, with a spring event at the beginning of the melt-season allowing rapid ice acceleration followed by gradual deceleration as channels form, siphoning water from the lubricating distributed drainage network (Bartholomew *et al.*, 2010, 2011b, 2012; Chandler *et al.*, 2013; Cowton *et al.*, 2013; Joughin *et al.*, 2013). Because of the limiting effect of channels on ice dynamics, determining whether they do indeed grow to a significant size under the GrIS in response to lake drainage and moulin input is important for a better understanding of future response of the GrIS to climate change.

This thesis has aimed to address this issue by modelling hydrological development both during and after rapid lake drainage once a surface-to-bed connection has been made. In order to determine the impact of lake drainage on channel growth in different regions of the GrIS, a series of experiments have been run on four model geometries. These include: 1) a simple planar topography for an inland lake near the equilibrium line altitude (ELA) on the land-terminating RGC, based on collected

field data; 2)a more realistic topography for the same lake based on surface and basal DEMs; 3) a simple geometry representing a tidewater glacier with lake water input 30 km from the calving front; 4) a simple geometry for a lake located 23 km from the terminus of a land-terminating glacier (see Section 6.2). The modelling is imperfect and has several associated limitations, including limited knowledge of the basal conditions necessary for model parameter inputs. As a result, a series of sensitivity tests have been run, as detailed in Chapters 6 and 7, in order to show the range of possible model outputs. Using these tests it can be suggested under what conditions substantial channels can grow and persist under the GrIS.

This chapter will discuss the three case-studies (F-Lake, tidewater and marginal glaciers) in turn before turning to a general discussion about jökulhlaups, turbulent sheets and how the model outputs fit with the data collected by other researchers from RGC. In addition, the implications of the model outputs for understanding GrIS dynamics are discussed along with the limitations of the modelling approach that could impact interpretation of the outputs.

9.2 F-Lake (geometries 1 and 2)

In this section, the outputs from the F-Lake case-study models are discussed. This includes examining channel growth over the short- (diurnal) and long-term (seasonal) time-scales (as reported in Chapter 7) and comparing the results with those from the simple R-channel model (introduced in Chapter 4). The likelihood of a pre-existing channel occurring in the region of F-Lake is discussed, incorporating results from the AVA analysis presented in Chapter 8 and the coupled hydrological model results (Chapter 7). Following this, the impact of hydraulic potential gradients and rates of supercooling freeze-on on reverse slopes for hydrological development are examined. Using the results from AVA analysis in RGC (see Chapter 8), the impact of subglacial sediment on channel growth is also discussed. Finally in this section, the F-Lake rapid drainage event is analysed in terms of drainage initiation and hydrological development during and after the event, comparing the model outputs with surface GPS records.

9.2.1 *Channel growth*

The F-Lake case-study is the most detailed of the modelled geometries as several model inputs can be well-constrained due to data collected in-situ. The available data are described in Chapter 3 but, primarily, the important information for the hydrological modelling is the ice thickness, local surface and basal topography, lake volume and rate of water level lowering, and information about the substrate in the region. By taking account of uncertainties derived from the sensitivity tests described in Chapter 7 that were used to analyse the impact of unknown basal and ice characteristics on hydrological development, it is possible to give a likely estimate of drainage development. The following results are from the primary outputs for modelled geometries 1 and 2 (i.e. the F-Lake planar topography and the F-Lake real topography models); all parameter test outputs are included in these results aside from those that are deemed unsuitable, as discussed in Section 7.7.2 (the unsuitable parameters include outputs for an atmospheric outlet, n'=0.01 s m^{-3}, $h_c^{sh} \leq$=0.15 m, E=3 GPa, S_ϵ=10 m^2, or any lake volume or flowband width tests for the F-Lake domains).

The F-Lake results indicate that large channels do not form rapidly as a result of lake drainage. Maximum channel growth within 10 hours of drainage is 0.01 m^2 if the initial channel size is 0.1 m^2; with an initial channel size of 1 m^2, there is still only growth of 0.05 m^2 over 10 hours (see Table 7.2). These outputs suggest that the assertion that large channels form during lake drainage as a result of the large volumes of water reaching the ice-bed interface (Cowton *et al.*, 2013) is not applicable to all drainage events.

Once the lake drainage event has occurred, a surface-to-bed pathway is available to tap surface water runoff. This moulin can deliver diurnally-varying water inputs to the bed for the remainder of the melt-season and has been argued to be one of the most important impacts of rapid lake drainage for the GrIS (Gulley *et al.*, 2009). In order to test the effect of diurnal water inputs on hydrological development, the flowband model sensitivity tests were run for a further thirty days with estimated surface water influx as an upstream boundary input (see Section 5.4.5). Sustained water input to the basal hydrological system once a surface-to-bed connection has been made following lake drainage does appear to allow some channel growth in the F-Lake geometries. The maximum channel growth from the F-Lake primary sensitivity tests (with an initial channel size of 0.1 m^2) is 0.57 m^2 over 30 days. This growth increases to 1.30 m^2 if the initial channel size is 1 m^2 (see Table 7.2). However,

the relative importance of the distributed system and the channels for transporting basal water in the F-Lake system is shown in Figure 9.1 a and b, plotted for a full-season (90-day) model run. These plots are similar to those produced by Flowers (2008) and show total outlet discharge in black, distributed discharge in blue and channelised discharge in red. For the baseline F-Lake system with an outlet pressure at overburden (Fig. 9.1 a), the distributed system dominates throughout the season. With an outlet pressure at $0.5\,P_i$, channels become dominant within 55 days of lake drainage; however the distributed system once again becomes more influential for water transport within a further 12 days (Fig. 9.1 b).

The coupled hydrological model results are supported by outputs from the simple R-channel model (see Chapter 4), which demonstrate that it is difficult to grow channels under thick ice in any conditions unless a pre-existing channel is in place, and then only if consistent overpressure (i.e. an in-exhaustive water source) is involved (see Fig. 4.2). The reason for the lack of channel formation both during and after lake drainage is likely twofold. Firstly, the ice is too thick to allow channel growth without rapid closure and secondly, the surface slope is too shallow to present a strong hydraulic gradient to drive water flux. This is demonstrated by a smaller channel growth rate for lower surface slopes and thicker ice as illustrated in the coupled hydrological model general geometric tests shown in Figures 7.15 and 7.16.

9.2.2 *Pre-existing channel*

Results from the simple R-channel model suggest that pre-existing channels are unlikely to occur in the F-Lake region because, when pressures drop a few percent below overburden, the channels shrink within a period of days (see Fig. 4.6). In the coupled hydrological model it also appears that large channels are not sustainable in the F-Lake case-study, as indicated by the shrinkage of the $10\,m^2$ channels after 30 days of water input in all of the F-Lake tests (see Section 7.4.8). As a result, the $22\,m^2$ channel required for model stability by Pimentel and Flowers (2011) during lake drainage events is unrealistic for the F-Lake case-study.

It is possible however that some hydrological development could have occurred prior to the drainage of F-Lake. The reflection seismic survey at an upstream site $\sim$5 km NE of F-Lake (see Section 8.4.6) indicated the presence of wet sediment in a basin. It is not clear whether this basin contained water that might have flowed downstream prior to the F-Lake drainage event and allowed growth of channels. However, given

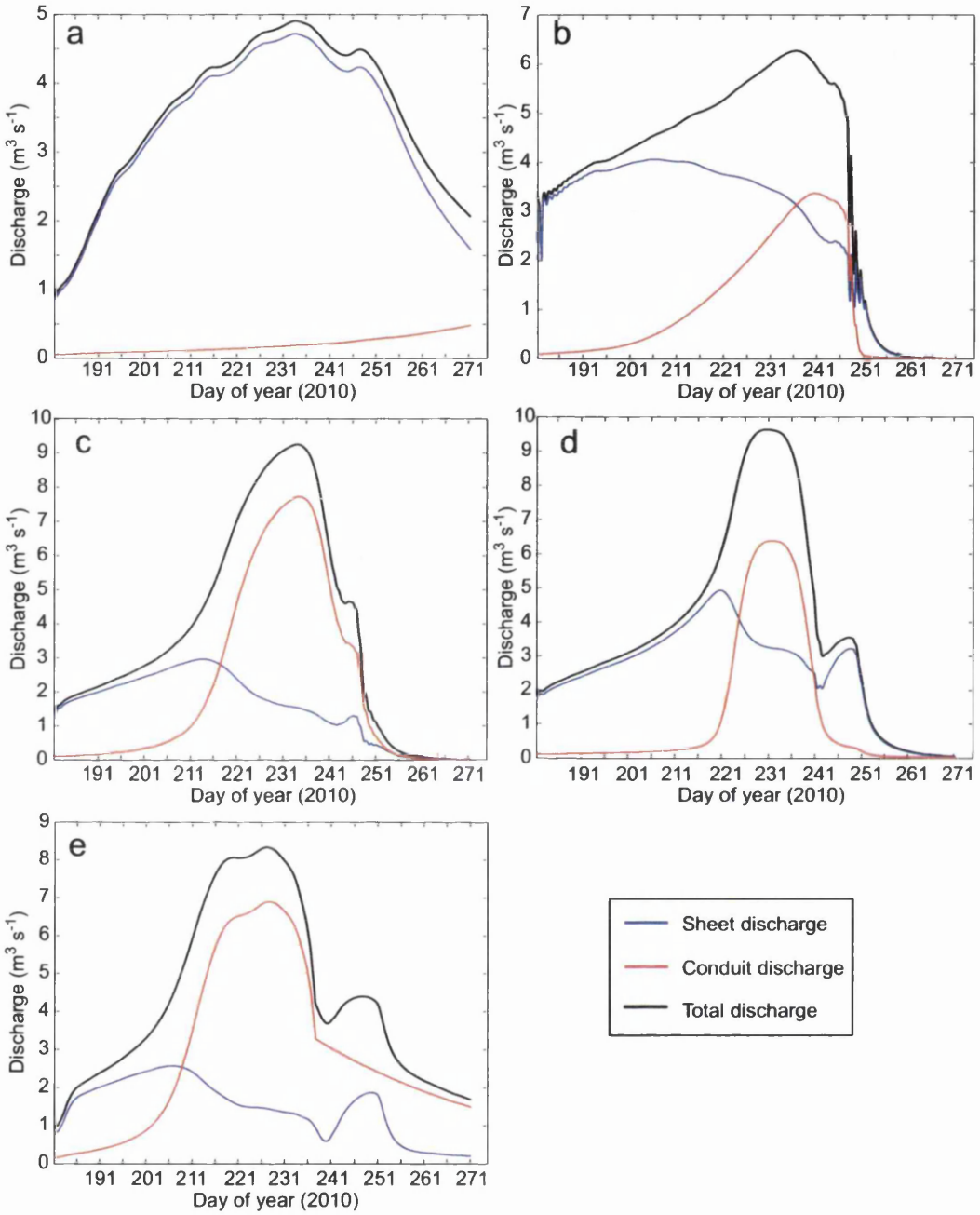

Figure 9.1: *Model outlet hydrographs with the total system discharge shown in black. The contribution to this discharge from the distributed system is plotted in blue and from the channel is plotted in red. All plots are for the baseline full-seasonal runs. a) F-Lake planar model with $P_{out} = P_i$, b) F-Lake planar model with $P_{out} = 0.5\,P_i$, c) Tidewater model with $P_{out} = P_i$, d) Tidewater model with $P_{out} = 0.67\,P_i$, e) Marginal model.*

that the lake drainage (which involved much greater volumes of water than could be contained in the sediment-filled basin) allowed only, at the most, $\sim 0.05\,m^2$ of channel growth (as predicted by the coupled hydrological model, see Section 9.2.1) it is unlikely that the subglacial basin would have had much impact on channel growth before the lake drained. For example, in order to produce a channel of $1\,m^2$, the coupled hydrological model results suggest that at least 30 days of continuous water input to the region would be necessary (see Table 7.2). Figure 3.1 shows that there were no upstream lake drainage events more than 3 days prior to F-Lake, although several drained at around the same time as F-Lake; for the same reasons as postulated for the subglacial basin, these drainage events are unlikely to have caused much channel growth. Some moulin drainage might have occurred prior to lake drainage; for example a small ($\sim$1 m diameter) moulin to the NW of F-Lake was observed to intake a small discharge prior to lake drainage (see M4 in Fig. 2: Doyle *et al.*, 2013). It is due to this possibility of water access to the bed prior to lake drainage that the results from the $1\,m^2$ initial channel size tests have also been discussed in Section 9.2.1.

9.2.3 *Hydraulic potential*

The F-Lake geometry 2 results presented in Section 7.5.2 are based on a smoothed topography extracted from surface and basal DEMs of the region (Fig. 3.3). The flowline chosen for the model is based on hydraulic potential gradients calculated for uniform overburden pressures (Fig. 3.4). As can be seen from Fig. 3.6, if the topography is not smoothed along the flowline, the water encounters reverse slopes that are sufficiently steep to prevent water flow at overburden pressure. The basal hydrological system would have to adjust in order to allow continuous flow either by developing channels along the margins of the overdeepened areas or by building up water pressure within the basins to allow flow up-slope. The flowband model is not sophisticated enough to determine which of these scenarios is more likely and, indeed, water flow through overdeepenings is an area of research that requires significantly more attention in order to better understand subglacial hydrological development (Dow *et al.*, 2011, Dow *et al.*, in prep.). As a result, to allow model stability, the geometry 2 topography was smoothed to remove reverse potential gradients. The impact of this smoothing on the model outputs is that the channel sizes predicted for geometry 2 are likely overestimates due to the limitations on water flux imposed by reverse slopes. Even with the smoothing, the impact of the reverse slopes can be seen

in the model outputs. Figure 7.3 e shows rapid spatial transitions between actively growing channels and minimum channel size dependent on the local topography; this is as a result of very low hydraulic potential gradients on the reverse slopes that result in very slow water flux. The F-Lake results therefore indicate that much more attention is required to examine flow over variable basal topography if subglacial drainage development is to be well understood.

The F-Lake regional hydraulic potential vectors are shown in Figure 3.4, and demonstrate that little gravitational drive is available to impact water flux under circumstances where water pressures are at overburden. During a lake drainage event however, the gravitational hydraulic potential gradient is overwhelmed by the overpressure introduced by the water in the surface-to-bed fracture and the resulting basal water blister. The difference between the overpressure at the lake input point and the overburden pressure in the remainder of the hydrological system presents a hydraulic potential gradient far greater than that attributed to the ice geometry. It is this steep gradient and the short-term separation of the ice and the bed, which allows rapid evacuation of the water from the lake drainage in the form of a turbulent water blister, rather than due to the formation of channels.

9.2.4 *Supercooling*

In addition to the restrictions to water flow along the F-Lake model flowline due to reverse overburden hydraulic potential gradients, supercooling freezing on reverse slopes can affect water flux by reducing the system hydraulic conductivity. As explained in Section 3.3.2, when water flows from an area of high pressure to low pressure it adjusts to the rise in pressure melting point by forming frazil ice. This ice accretion on riegels, for example, could rapidly shrink conduits. The rate of supercooling freeze-on is highly dependent on the water temperature, pressure and fluid velocity (Alley *et al.*, 1998). However, calculated regions of supercooling at overburden pressure appear to be prolific on the map shown in Figure 3.5. In addition, the modelled conduit flux rate over the F-Lake geometry 2 riegels is low (see Fig. 7.3 d). These features combine to suggest that channel growth is likely strongly inhibited by supercooling freeze-on on the reverse bed slopes. Most hydrological models to date do not take account of supercooling freeze-on and, given that basal topography is highly variable and overdeepenings prolific under both ice sheets and valley glaciers, it is an important area for future modelling projects. The impact

of supercooling on conduit growth in the F-Lake region is that efficient drainage is likely greatly hampered by reduced hydraulic conductivity on reverse slopes. This would act to enhance the spatially variable conduit growth pattern seen in Figure 7.3 e, where significant conduit growth can only occur between reverse slopes.

A substantially disjointed hydrological system is evident in the geometry 2 model runs so that the channelised system does not appear to be an efficient form of water transport and instead operates more like an inefficient distributed system (see Fig. 7.3 e). If supercooling freeze-on is sufficient to block flow pathways over riegels, water might have to pool within overdeepenings until the pressure is sufficient to overcome supercooling. This suggests that the small conduit growth produced in the geometry 2 model (see Table 7.2) might be an overestimate. However, blocked drainage pathways might also encourage water flux in other areas, such as around the margin of the overdeepenings, even though water flow in these regions is not predicted by the hydraulic potential gradients (Fig. 3.4). If the latter occurs, it is possible that efficient drainage can then occur although, with the thick ice and rapid closure times of conduits (within several hours), drops in the rate of surface water input could inhibit maintenance of efficient pathways even if the overdeepenings are avoided. The combination of reverse hydraulic potential slopes, supercooling freeze-on and rapid conduit closure likely act together to create a highly transient and often inefficient drainage system.

It is possible that the lake water reaches the bed at temperatures above the local pressure melting point. Clarke (2003) noted that when modelling jökulhlaups from Hazard Lake, Yukon, incorporating water temperature was an important factor in matching the model outputs with the outlet hydrographs. On the other hand, Fowler (2009) argued that any elevated temperature from rapid drainage is likely so small that it will not have much impact on melt rates of conduits. It would be a complex venture to calculate the temperature of lake drainage water once it had flowed through the englacial crack to the bed and therefore has not been included in the presented model. However, even if water temperatures are warmer at the input point, by 2–3 km along the flowband where the first overdeepening is located (see Fig. 3.3), it is likely water would have equilibrated to the local pressure melting point.

9.2.5 *Substrate*

The reflection seismic data presented in Chapter 8 suggest that sediment is widespread under RGC. In basins around F-Lake, soft sediment is identified (see Section 8.4); however in the flowpath of the F-Lake drainage water, lithified sediment is found (see Section 3.6.3). It is possible that soft sediment only accumulates in the basins where water might pool until sufficient pressure is maintained for flow out of the overdeepenings. Alternatively, it is possible that multiple years of flood water flowing through the trench to the NW of F-Lake (see Fig. 3.3) have removed any soft sediment, leaving only lithified till that is sufficiently stiff to act similarly to bedrock in regards to basal drainage development. Without further investigation it is not possible to determine which of these scenarios is correct. Towards the terminus of Russell Glacier, the AVA analysis identifies the presence of soft sediment in an area known to have large velocity variations (see Section 8.5). These results suggest that basal material characteristics are highly variable in RGC.

It is difficult to know what impact a sediment base would have on channel formation. If lithified sediment is present along most of the domain there is likely little difference between this substrate and bedrock for channel development. However, with soft sediment it is possible that canals could be eroded more easily into sediment than up into the ice. How long such features are stable before sediment begins to encroach or deform into the canals is not known. Also, the steady-state models of canals suggest that they would not form with diameters greater than 0.4 m (Ng, 2000a), and so they appear to be fairly small features. The presence of soft sediment beds would also likely encourage distributed flux by absorbing more water than perhaps would occur in a hard-based linked-cavity system. As a result of this, Flowers (2008) suggests that the presence of soft beds would hinder the development of conduits.

The model presented in this thesis is designed for calculations of semi-circular channel growth on a hard bedrock base. As explained in Section 2.4.3, there are very few models that calculate growth of canals within sediment; those that do exist are applicable only for steady-state systems. It was beyond the scope of this thesis to develop time-varying sediment canal equations, but is an important area for future research. As a result, without knowing the configuration of basal material along the F-Lake domain and lacking the necessary mathematical formulation for sediment canal growth, it is not possible to determine the impact of this material on channel formation rates.

9.2.6 *F-Lake drainage description*

By combining the outputs from the modelling sensitivity tests with the data collected both remotely and in-situ at the F-Lake drainage site it is possible to hypothesise about the primary characteristics of the rapid drainage event.

Drainage initiation

The air temperature data from an AWS located ~8.5 km from F-Lake show that average air temperatures were above freezing for five days preceding lake drainage on DOY 181, 2010 (see Fig. 3.14 a); this was the longest above-freezing period of the season up to that time. In addition, melt calculations by van As (GEUS) indicate that the day prior to lake drainage (DOY 180) had the second largest melt spike of the season, with the largest spike occurring on DOY 177 (Fig. 3.14 b). This evidence together might suggest that the largest volume of water flowing into the lake caused the rapid drainage event (due to the additional weight of the water allowing hydrofracture of basal crevasses; see e.g. Clason *et al.*, 2012). However, as can be seen from the pressure transducer data in Figure 3.8, the lake did not drain when it was at maximum volume indicating factors other than the water volume caused the lake to drain. It is possible that with warmer air temperatures and greater surface melt, that more water accessed the bed in the vicinity of F-Lake and altered the stress regime allowing hydrofracture from the lake to the bed. It is reported in Jones *et al.* (in prep.) that a build up of stress originating up-glacier from the lake site caused shearing and triggered the hydrofracturing that drained the lake; evidence to support this comes from GPS station and passive seismic records. The stress build up may have also been due to drainage of a lake to the east of F-Lake although, as shown in Figure 3.1, it is not clear whether this other lake drainage occurred prior to or following the F-Lake drainage event. If this lake to the east did drain, there would be up to three days of basal water flux through the F-Lake site that could impact local ice dynamics.

Drainage characteristics

Many of the details of the F-Lake drainage are described in Chapter 3. It is important to note that GPS 1, to the NW of the lake, was uplifted to a maximum of ~0.8 m, 1.7 hours after drainage initiation (see Figs. 3.11 and 9.2). GPS 1 uplift is

more than twice the uplift seen at the other GPS sites. This suggests that water primarily flowed to the NW along the subglacial flowpath implied by the geometric hydraulic potential gradients (Fig. 3.4). However, the uplift of the other three GPS units indicates that water did, to some extent, flow radially from the input point. Although the lack of topographical control on the blister expansion model could be argued to limit the applicability of the coupled hydrological model outputs, the shape of the uplift curve matches well with those recorded in the field; it is only the magnitude of uplift that cannot be fully replicated (see Fig. B.1). Also, the close match between the blister model predicted uplift for GPS 4 (NE) and the lake drainage rate (see Section 7.2.2) indicates that a radial subglacial water blister model satisfactorily replicates the initial stages of lake drainage.

It is therefore postulated that, at the initial stages of lake drainage, water intersected a distributed system at the ice-bed interface and, due to the overpressure and limited basal hydraulic conductivity, the ice was hydraulically jacked from the bed. This allowed the spread of a water blister radially from the input point. However, due to the basal topography, the blister could only extend radially from the lake up to a radius of ~2500 m (see Fig. 5.10); beyond this, steep basal slopes prevent further flow. As a result, water was then primarily directed downstream through the subglacial trough to the NW (Fig. 5.10). However, as the coupled hydrological model outputs suggest (see Section 9.2.1), during the period of lake overpressure and drainage there would likely be very little channel formation; the water would instead be drained by the turbulent sheet and through a subglacial distributed system. The uplift of the GPS units, particularly in the NW (see Figs. 3.11 and 9.2) indicates that the basal system was not sufficiently hydraulically conductive to remove the water and thus suggests that significant pre-existing channels were not present at the time of drainage. The characteristics of the F-Lake site that inhibit channel formation include: thick ice, a lack of strong geometric hydraulic potential gradients and variable basal topography, including the presence of substantial overdeepenings.

Post-drainage

Following the drainage of F-Lake it was noted during exploration of the lake basin on the July 2nd (DOY 183) that there was a small surface lake reforming in the deepest part of the basin in the region of F1 (see Fig. 3.7); this area had been free of water immediately after the lake drainage event. By July 3rd (DOY 184) this small lake had drained. Such a phenomenon suggests that water was backing up in

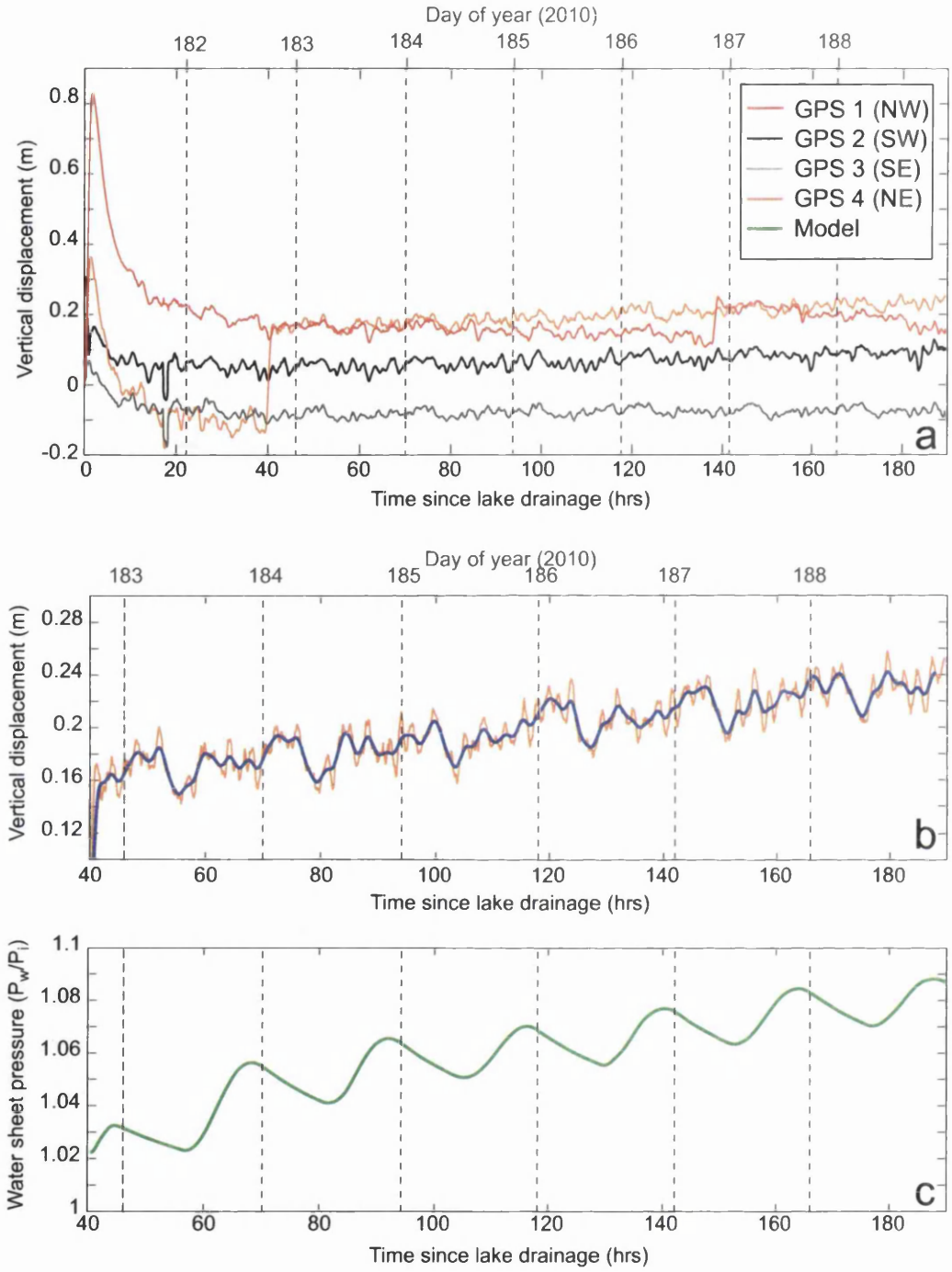

Figure 9.2: *a) Vertical displacement records from the F-Lake GPS stations. b) Enlarged plot of the GPS 4 (NE) record (orange curve); the blue curve shows the outputs from triangular filtering of the GPS 4 record, c) Water pressure records from the baseline F-Lake planar run with $P_{out} = P_i$ at a site 1 km from the water input; water pressure above overburden is used as a proxy to estimate the timing and amount of ice uplift.*

the hydrological system before the basal capacity could adjust to the rapid drainage influx. In order for water to pool on the surface, the basal pressure must have been above overburden for some time. The model outputs cannot replicate this feature because flux-inhibiting reverse slopes are smoothed out of the topography and supercooling is not included within the calculations. It is possible that water encountering the large overdeepening ~12 km downstream from the input point had to build up pressure, thus causing the system to back up to the moulin, before flowing over the riegel. Once a syphon effect had been established with flow over the riegel (allowing flux with somewhat lower water pressure), the water could be drained from the region and the pond would drain from the F-Lake basin. It would be interesting to examine how this type of water pooling would impact hydrological development but is beyond the scope of this thesis. An alternative explanation for pooling on the lake surface is that the connecting moulin froze shut, preventing further water flux. A similar englacial freezing phenomenon was reported by Boon and Sharp (2003) for lake drainage events on John Evans Glacier, Ellesmere Island. However, in their case the freezing occurred prior to full lake drainage. It is less likely that englacial freezing could close the large F-Lake fracture (see Fig. 3.12) following such rapid drainage and therefore pressurised basal conditions preventing flux from the lake seems a more plausible explanation for the temporary surface water ponding.

In the coupled hydrological model, the time taken for blister dispersion is tested by establishing when the water input grid-cell reaches overburden pressure (see Section 6.5). For the F-Lake primary parameter sensitivity tests, blister dispersion occurs between 15.1 and >40 hours (when stage 3 of the model process ceases; see Fig. 7.2 d for an example). On average, dispersion time for F-Lake geometries 1 and 2 is 36.7 hours. It is not straightforward to determine from the F-Lake GPS records at what point the blister water may have dispersed. The GPS 1 (NW) and 4 (NE) records plotted in Figure 9.2 a show settling of the GPS unit ~32 hours following initial lake drainage. If this downward vertical motion in the GPS records represents the removal of the overpressured lake water from the region, the coupled hydrological model prediction of blister dispersal appears to be in general agreement with the GPS records.

The GPS records show a diurnal pattern of uplift and subsidence over an eight-day period following lake drainage, after which the surface data are no longer available. Figure 9.2 b shows the GPS 4 (NE) vertical displacement in orange relative to the position of the unit at the initiation of lake drainage; the blue curve represents the

uplift data smoothed with a triangular running average. Between days 183 and 188 the maximum uplift occurs each day at ~04:50 UTC followed by subsidence to the minimum at ~09:30 UTC. Uplift each day is ~6 cm. It is likely that the large uplift around hour 40 (see Fig. 9.2 a) is an anomaly in the data. The coupled hydrological model outputs driven by surface water fluxes also vary diurnally. Because uplift is not directly calculated in the current application of the flowband model, sheet water pressure above overburden is used as a proxy. The average time for maximum and minimum diurnal pressures from the F-Lake planar topography primary outputs are ~21:20 UTC and ~12:44 UTC the following day, respectively. An example pressure record is plotted for a site 1 km from the water input for the baseline F-Lake planar topography run with an outlet pressure at overburden (Fig. 9.2 c). There is a ~7 hour delay between maximum modelled pressure and recorded surface uplift; the recorded surface displacement then subsides to a minimum within ~4.5 hours, preceding the modelled pressure minimum by 2.5 hours. The difference between the recorded GPS unit uplift and the modelled water pressure possibly reflects the limitations of using a simplified surface water input where runoff is estimated for the entire catchment without taking account of surface flux times or conditions (see 5.4.5). For example, delay in surface flux from the lake catchment likely causes the later maximum uplift seen in the GPS records, followed by a rapid drop to minimum pressures due to lack of surface melt as a result of freezing temperatures. With a more sophisticated approach to surface flux modelling, such as that developed by Banwell *et al.* (2012), it is possible the uplift and water pressure data would match more closely.

Downstream impacts

A GPS station is located ~17 km NW of F-Lake (and is therefore ~5 km beyond the end of the model flowline; Fig. 3.3). In 2010, this GPS station experienced acceleration on DOY 181 at 09:20 UTC (following lake drainage initiation at 01:40 UTC) and reached a maximum speed by 15:50 (Greenland Analogue Project Report, 2010). Although it is possible that other lake drainage events may have caused the acceleration of this GPS station, its proximity to the F-Lake drainage route makes it more likely that the dynamic response of the GPS unit was due to the F-Lake drainage. If this is the case, there is therefore a delay of ~7.5 hours for the lake water to reach the GPS site. With model geometries 1 and 2 limited to 12 km, the only comparison that can be made with the downstream GPS data is the time at which the F-Lake domain outlet becomes overpressurised as a result of the downstream propagation

Table 9.1: *F-Lake blister pressure wave arrival time, 12 km downstream of the input, calculated for geometry 2 with P_{out}=P_i.*

K ($m\,s^{-1}$)			E (GPa)		h_c^{sh} (m)				n' ($s\,m^{-3}$)			k			S_ϵ (m^2)	
0.1	**0.5**	**1**	**6.2**	**8.9**	**0.05**	**0.15**	**0.3**	**0.4**	**0.032**	**0.7**	**0.1**	**0.01**	**0.05**	**0.1**	**0.1**	**1**
>40	10.4	5.5	10.4	10.5	9.0	10.4	11.3	11.8	10.4	10.6	10.6	10.4	10.5	10.5	10.4	7.2

of the blister. In this discussion the F-Lake real topography (geometry 2) primary water pressure records are used because they are more likely to realistically represent the topographical controls on water flux at the case-study site (see Section 9.2.3). In addition, only the outputs for a domain outlet at overburden pressure are used due to the presence of the overdeepening at ~12 km distance which, at least within the time for blister propagation, would likely necessitate high basal water pressures. The results for the blister arrival time at 12 km distance from the input are given in Table 9.1. Depending on the sensitivity tests, arrival times range from 5.5 hours to more than 40 hours; the average arrival time is 10.0 hours. Compared to the measured arrival time of ~7.5 hours, the coupled hydrological model can therefore generally replicate what appears to be subglacial water flux times for the F-Lake drainage.

9.3 Tidewater glacier (geometry 3)

In this section, the results from the tidewater glacier model (see Section 7.5.3) are discussed. These include channel growth over both short- (diurnal) and long-term (seasonal) time-scales. The geometry 3 model outputs are then compared with measured rates of water flux in tidewater glaciers and assumed channel sizes reported in previous studies.

9.3.1 *Channel growth*

Model geometry 3 is a simplified version of a tidewater glacier, generally based on the model configuration applied by Pimentel and Flowers (2011) for the Das lake drainage (see Section 5.3.3). Because this modelled geometry is not based on as many known physical parameters as the F-Lake drainage, the lake volume and flowband width are also tested. The geometry 3 experiments are designed to give an idea of how drainage networks might develop in regions of the GrIS with tidewater glaciers,

although for an accurate examination of hydrological development, in-situ data for the tidewater glacier in question would be necessary. In addition, the inclusion of a tidally-varying outlet water pressure would be an interesting addition that could impact hydrological development. Instead, the approach in this thesis was to have a simpler pressure regime with either a) a floating glacier (so that the outlet pressure was always at overburden) or b) a grounded glacier (with the water pressure at the outlet set to $0.67\,P_i$, representing an ocean water depth of 300 m).

The tidewater glacier results (Section 7.5.3) suggest that in the period following lake drainage little channel growth occurs. Channel development is on a similar scale as seen in the F-Lake case-study with maximum channel growth of $0.08\,\mathrm{m}^2$ over 10 hours, if the initial channel size is $0.1\,\mathrm{m}^2$. A larger initial channel size of $1\,\mathrm{m}^2$ allows growth of $0.13\,\mathrm{m}^2$ and with a $10\,\mathrm{m}^2$ initial channel there is growth of $0.15\,\mathrm{m}^2$ over 10 hours if the outlet is at overburden (although this large initial channel size shrinks if the outlet pressure is $0.67\,P_i$). These growth rates within 10 hours of lake drainage concur with those produced for the F-Lake site and suggest that channels do not grow significantly during lake drainage events, even if a large pre-existing channel is in place.

After lake drainage, hydrological development is driven by the F-Lake surface catchment melt rate. This catchment might not be appropriate for a tidewater glacier 30 km from the terminus because the melt rates at lower elevations will likely be higher for the period of study. However, as the tidewater glacier model is not applied to a particular region of the GrIS the most appropriate option is to use the F-Lake surface water input. Applying the same runoff inputs also allows direct comparison between the different modelled geometry outputs. In the tidewater glacier scenario, channel growth is somewhat larger than that seen for the F-Lake case-study. Maximum channel growth for an initial channel of $0.1\,\mathrm{m}^2$ over 30 days of drainage is $1.67\,\mathrm{m}^2$. With an initial channel size of $1\,\mathrm{m}^2$ the growth is not much larger at $1.87\,\mathrm{m}^2$ over 30 days. With the larger initial channel of $10\,\mathrm{m}^2$, shrinkage occurs during the 30 days of surface water input.

In both the tidewater and the F-Lake model outputs, the channel growth with an initial channel size of $0.1\,\mathrm{m}^2$ was generally larger for the sensitivity tests with lower outlet water pressure. However, with a larger initial channel size, the greatest growth (or least shrinkage) in both case studies was for the systems with outlets at overburden (i.e. high outlet water pressure). The reason for this is likely that a steeper gradient between the water inlet and the lower pressure outlet acts to increase

the water flux; with larger channels, more water is necessary to keep them sufficiently pressurised to prevent ice creep and therefore the greater flux from steeper pressure gradients causes the pressure to drop enough that the channels shrink. Channel growth is therefore greater in conditions where the water in the domain is more pressurised.

The change from a sheet-dominated hydrological system to a channel-dominated hydrological system is analysed from the full-seasonal runoff model output from the baseline tidewater glacier model. With the outlet at overburden, channels become the dominant drainage mechanism 34 days following lake drainage (see Fig. 9.1 c). With $P_{out} = 0.67\,P_i$, channels begin to remove the most flux after 41 days of drainage (Fig. 9.1 d). However, within this system, the sheet once again becomes the most important drainage mechanism 55 days after the lake drainage event. As a result, channels are only the primary drainage mechanism for 14 days. This output suggests that even with seasonal input, the modelled tidewater distributed system can dominate drainage and has enough capacity for the surface water input without driving the formation of large channels.

The simple tidewater model was set up to resemble that used by Pimentel and Flowers (2011) for the Das lake drainage event. In these experiments, Pimentel and Flowers (2011) introduced a background flux of $100\,m^3\,s^{-1}$ into the simulation in order to create a pre-existing channel of $22\,m^2$. These parameters were introduced to allow the flood water to exit the region within 24 hours (as suggested by GPS records reported by Das *et al.*, 2008). For the Das lake drainage event, modelled maximum sheet discharge was $\sim 65\,m^3\,s^{-1}$, channel discharge $>500\,m^3\,s^{-1}$, and channel cross-sectional area $\sim 350\,m^2$. After 24 hours of drainage, the initial 8 km of the domain were still above overburden pressure (see Fig. 5.5). This can be compared with the baseline coupled hydrological outputs during lake drainage (for a system with an outlet at overburden): maximum sheet discharge is $\sim 21\,m^3\,s^{-1}$, channel discharge is $0.3\,m^3\,s^{-1}$, and channel cross-sectional area $\sim 0.12\,m^2$. Also, after 24 hours of drainage, the initial 3.4 km of the domain are at pressures greater than overburden. Even with an initial channel size of $10\,m^2$, the simple tidewater model produced a maximum sheet discharge of $\sim 19\,m^3\,s^{-1}$, channel discharge of $18\,m^3\,s^{-1}$, and channel cross-sectional area of $\sim 10.15\,m^2$. With this scenario, after 24 hours of drainage, a 1 km region at the upper end of the domain was above overburden pressure. The reason for the discrepancy between the Pimentel and Flowers (2011) results for the Das lake drainage and the coupled hydrological model is not due to the difference in model set-up but instead because of the continuous background flux of $100\,m^3\,s^{-1}$

in the Pimentel and Flowers (2011) model runs. This background flux allows rapid channel growth because of overpressurisation of the sheet to a much higher level than as a result of only the lake drainage water flux. It is possible that there is a background flux in the region of the Das lake drainage, but this would have to be determined by regional hydrological modelling and analysis of diurnal surface water inputs into the catchment. In order to see the impact of lake drainage on channel growth rates, the model presented in this thesis seems more appropriate and implies that, even with large pre-existing channels, the overpressure from the lake does not cause the channel growth rate and discharge suggested by the Pimentel and Flowers (2011) model.

Sole *et al.* (2011) modelled channel growth for the tidewater glacier Kangiata Nunata Sermia in south-west Greenland in response to supraglacial lake drainage events. The channels are argued to rapidly grow to $18\,m^2$ within two days and remain overpressurised for over 24 hours as a result of two lake drainage events at surface elevations of 1500 m and 1300 m. The model is applied with an ice thickness of 1200 m and with a range of initial channel size of $0.25\,m^2$–$20\,m^2$. All of the runs converge to a channel size of $18\,m^2$ within two days. These results are not consistent with the outputs from R-channel modelling in this thesis, from Pimentel and Flowers (2011) who required a steady-state with a background flux of $100\,m^3\,s^{-1}$ to produce a channel of $22\,m^2$, or from Greenlandic (e.g. Schoof, 2010; Hewitt *et al.*, 2012) or jökulhlaup (e.g. Nye, 1976; Clarke, 1982) modelling (see Section 9.5). Following the equations stated in the Sole *et al.* (2011) supplementary material, in order to melt a total of $16\,m^2$ of channel in two days, an average water velocity much greater than would be expected at the ice-bed interface (see e.g. Nienow *et al.*, 1998) would be necessary ($>20\,m\,s^{-1}$). Growth rates for more realistic water velocities, such as $1.5\,m\,s^{-1}$ (e.g. Chandler *et al.*, 2013; Cowton *et al.*, 2013), are much lower. As a result, the Sole *et al.* (2011) model outputs are unlikely to represent the hydrological development of Kangiata Nunata Sermia.

9.3.2 *Tidewater glacier water flux*

If the outputs from the baseline model are to be taken as the most likely scenario for channel growth, maximum channel size in the tidewater glacier model only reaches $0.63\,m^2$. This is not a particularly large channel after 30 days of drainage and suggests that, even with a parabolically increasing slope, the thick ice of the tidewater

glacier hinders much channel growth. Another important factor is likely the pressurised outlet that limits the pressure gradient that can occur within the domain and encourage water flux. This is an important aspect of tidewater glacier hydrology that has not been much examined. The difficulty of access to tidewater glaciers has meant that little research has been conducted on their subglacial hydrological configuration. However, the model outputs suggest that floating glaciers might hinder conduit growth and thus encourage the persistence of lubricating distributed systems. This perhaps has an impact on the dynamic response of tidewater glaciers to mass loss at the ice front.

The drivers for tidewater dynamics have been widely argued to be linked to ocean temperatures (see e.g. Chylek *et al.*, 2004; Holland *et al.*, 2008; Hanna *et al.*, 2009; Christoffersen *et al.*, 2011). However, if the basal hydrological system of these glaciers during the summer melt-season consists of large channels and very little distributed drainage, the increase in frontal melt and calving could cause minimal dynamic feedback due to the lack of a lubricating distributed system. On the other hand, large channels are assumed to occur because of the presence of plumes seen at the calving front of tidewater glaciers. For example, plume studies at the 5 km-wide Store Gletscher in West Greenland have suggested the presence of two channels of 50–100 m^2 cross-sectional area, each discharging an average of 100 $m^3 s^{-1}$ of water in the summer season (Xu *et al.*, 2012). The modelling by Xu *et al.* (2012) suggested that channel discharge would need to be at minimum 5 $m^3 s^{-1}$ for the upwelling water to reach the surface of the 500 m-deep fjord. However, a later study by Xu *et al.* (2013) on Store Gletscher estimated a channel flux of 10 $m^3 s^{-1}$ for three channel sizes of 20, 50 and 150 m^2. These estimates are to give a range of possibilities of plume formation with a modelled surface runoff of 1500 $m^3 s^{-1}$. The range of channel sizes and fluxes tested suggests that the size and efficiency of tidewater channels is not well known.

The outputs from the coupled hydrological model, although applied to a simplified model geometry, suggest that large channels do not easily form under tidewater glaciers. The outlet discharge plotted in Figure 9.1 c and d for tidewater channels is the largest seen for the full-seasonal baseline runs for all of the tested modelled geometries. This conduit discharge reaches a maximum of 7.72 $m^3 s^{-1}$ and, because of the full-seasonal run, the channel size at the outlet grows to a size of $\sim$4 m^2. It is here that the limitations of the current application of the coupled hydrological model become clear. The outputs presented here and in Chapter 7 are for a system developing as a result of a lake drainage event and runoff calculated for the F-Lake

$14\,km^2$ catchment ranging from an elevation of ~1350 m to ~1600 m. In reality, a tidewater glacier in Greenland will have a much larger catchment than the F-Lake case-study region. In addition, there will be many moulins and therefore many subglacial flowpaths contributing to the runoff for a typical tidewater glacier; this also means that pre-developed channels in regions of lake drainage on these tidewater glaciers are much more likely than for the inland F-Lake case-study. The fixed flowband width in the simple tidewater model of 1000 m is also likely an underestimate for a distributed flowpath in a Greenlandic tidewater glacier. Even a study on the smaller ocean-terminating LeConte glacier in Alaska found subglacial discharge ranging between 130–440 $m^3\,s^{-1}$ in the late melt-season of 2012 (Motyka *et al.*, 2013). This grounded glacier has an outlet width of 1000 m and a water depth of 250 m and therefore is more similar to the simple model geometry presented in this thesis that many Greenlandic tidewater glaciers. However, the recorded discharge at LeConte Glacier is still an order of magnitude greater than the ~9.5 $m^3\,s^{-1}$ combined maximum discharge output in the simple tidewater model from both the channelised and distributed system (see Fig. 9.1 d). One reason for this discrepancy between the modelled discharge and the measured discharge from a tidewater glacier is likely because the coupled hydrological model only calculates growth of one channel. In reality, there will be many arborescent channels contributing to the discharge at the front of the glacier (Banwell *et al.*, 2013) and the cumulative discharge will be greater than that measured from a single channel.

Although the simple tidewater glacier model is limited by a lack of realistic topographical and surface drainage rate inputs, the model outputs are still useful for comparing the rate of channel growth with the inland F-Lake case-study and the marginal glacier case-study to determine the important controls on hydrological development. For example, the similar upper domain boundary ice thickness in the F-Lake and tidewater glacier models combined with similar outlet pressures (see Section 6.2) suggests that the surface slope is a highly important feature for growth of larger channels in the tidewater glacier model compared ot the inland ice model. The limitations of the current application of the simple tidewater model opens up future areas of research by altering the coupled hydrological model geometry and calculating more realistic surface runoff inputs for a tidewater glacier to determine system hydrological development in a more appropriate setting. Because establishing the size of channels and their water flux is potentially important for determining frontal mixing and melt rates of ocean-terminating glaciers (Xu *et al.*, 2012), it should be an area of focus in future research.

9.4 Marginal glacier (geometry 4)

The results from the marginal glacier model are discussed in this section. Channel growth over both short- (diurnal) and long-term (seasonal) time-scales are examined first. The flux through the modelled channels is then compared with that measured from other studies at Leverett Glacier, directly adjacent to Russell Glacier, and the timing of hydrological efficiency and channel headward growth compared with dye tracing results from both studies at Leverett Glaicer and an Alpine glacier. Subglacial hydrology modelling results from other studies at the margin of the GrIS are also compared to the outputs from the coupled hydrological model.

9.4.1 *Channel growth*

Model geometry 4 was constructed to test channel growth rates in a region similar to the land-terminating Russell Glacier, closer to the margin than the F-Lake case-study. Similar to the tidewater glacier model, in addition to the general parameter tests, lake volume and flowband width are tested. For an accurate representation of the hydrological development near the margin of Russell Glacier, the model would have to be constructed, for example, with more accurate topography and surface runoff inputs; the latter is instead based on the F-Lake runoff calculations. Unlike the other modelled geometries, the marginal glacier was tested only with an atmospheric pressure outlet.

Channel growth during lake drainage is much greater for the marginal glacier than the other modelled geometries (see Section 7.5.4). However, over 10 hours, maximum channel growth is still only $\sim 0.2\,m^2$, with an initial channel size of $0.1\,m^2$. With an initial channel size of $1\,m^2$, growth over 10 hours is $2\,m^2$ and if a pre-existing channel of $10\,m^2$ is present, growth is $22\,m^2$ over 10 hours. Thus, the over-pressure from lake drainage in the marginal glacier scenario can cause rapid and significant channel growth. Because of the proximity of the modelled lake drainage to the glacier margin it is more likely that pre-existing channels would be present due to seasonal melt and the presence of moulins upstream of the modelled lake.

Channel growth as a result of surface runoff is also greater for the near-margin glacier when compared to the inland site and the tidewater glacier. Maximum channel growth over 30 days for an initial channel of $0.1\,m^2$ is $3.44\,m^2$ (see Table 7.2). However, with the baseline parameters and an initial channel of $1\,m^2$, growth by

30 days is only 1.78 m^2. The system with the pre-existing channel of 10 m^2 however, shrinks over the 30 days. As can be seen from Figure 9.1 e, the switch between a sheet-dominant to a channel-dominant system occurs 25 days after the lake drainage event and the channel is then the prevalent mechanism of water removal for the remainder of the melt-season.

9.4.2 *Marginal glacier water flux*

Following the lake drainage event, the outputs for the marginal glacier model are limited by the surface runoff input, calculated for F-Lake. To have a more realistic seasonal development, local runoff for the marginal area would have to be calculated. With runoff increasing at higher elevations during the melt-season, the volume of water reaching the marginal glacier site would cumulatively increase from both surface and basal sources during the season (with the latter due to input at higher elevation moulins or lake drainage events). The limits for using the F-Lake catchment runoff are evident in the maximum system drainage for the marginal glacier full-season scenario of 8.3 $m^3 s^{-1}$ (see Fig. 9.1e). This system runoff (i.e. including both channel and sheet drainage) is increased to 21.0 $m^3 s^{-1}$ when the initial channel size is 1 m^2 and 75.3 $m^3 s^{-1}$ when the initial channel size is 10 m^2, over the 30 day drainage model runs.

Measurements of Leverett Glacier (located directly to the south of Russell Glacier) pro-glacial river by Bartholomew *et al.* (2011a) showed that, in 2009, discharge was $<6\,m^3 s^{-1}$ up until June 1st, but then increased to 43 $m^3 s^{-1}$ by June 4th and, by the peak of the runoff in July 16th, was 317 $m^3 s^{-1}$. A similar trend was evident in 2010 but with the runoff reaching 340 $m^3 s^{-1}$ by July 1st and increasing to a peak of 400 $m^3 s^{-1}$ by July 30th (Cowton *et al.*, 2013). The catchment of this pro-glacial river is $>600\,km^2$. It therefore appears that the outputs from the marginal glacier model can only be compared with the Leverett Glacier near-margin hydrological system at the beginning of the season. However, the large discharge recorded from Leverett Glacier catchment does not necessarily suggest that large channels are transporting the water from far inland. As channels converge, the cumulative flux will allow additional growth so that by the terminus a large channel is expected, but this condition might not occur inland. For example, Banwell *et al.* (2013) modelled basal hydrological development for $\sim$20 km of the land-terminating Paakitsoq region of West Greenland and successfully produced discharge outputs up to $\sim 125\,m^3 s^{-1}$ that

closely matched the recorded pro-glacial discharge. In this model, approximately 22 channel tributaries were produced (from Fig. 3, in Banwell *et al.*, 2013)). If the discharge were divided evenly between these channels (which is not a realistic assumption but useful for determining average fluxes) each channel would transport a maximum water flux of $\sim 5.5\,m^3\,s^{-1}$. Although the spatial variability will, of course, be much more complex in the Banwell *et al.* (2013) model, this averaged water flux does illustrate that the outputs from the coupled hydrological model are not unrealistic for application to a marginal glacier region.

Even with the limitations of using the F-Lake runoff record, the hydrological development of the marginal glacier does appear to emulate an Alpine system much more than the F-Lake case-study site. At the marginal glacier with pre-existing channels (which is not an implausible scenario for this region), growth of conduits during lake drainage events can occur quickly. However, with a small pre-existing channel is takes between 14 to 30 days to grow reasonable-sized channels of $1\,m^2$. This can be compared with the results from repeat dye tracing experiments on Leverett Glacier in 2010 at a site 6.6 km from the glacier outlet (Cowton *et al.*, 2013). Using dye throughflow rates as a proxy for system drainage efficiency, it took ~22 days for channels to develop from inefficient to efficient. Similarly, dye tracing results from experiments at an Alpine glacier by Nienow *et al.* (1998) found efficient channel development within 17 days during the summer melt-season.

Further evidence of the applicability of the marginal glacier outputs come from examining outputs of other hydrological models in similar regions. Schoof (2010) modelled transitions between channels and linked cavities for Greenlandic subglacial hydrological systems and produced a maximum channel size of $\sim 2\,m^2$ in these simulations. A similar maximum conduit size was produced from the Hewitt *et al.* (2012) model that was constructed to represent either a large valley glacier or the margin of the GrIS. Bartholomew *et al.* (2012) modelled simple R-channel evolution for Leverett Glacier using the equations from Schoof (2010) and in-situ runoff calculations. Initial runs using this calculated runoff input produced limited diurnal variability, and as a result the surface water input was artificially increased by a factor of 2. With this amplified runoff, Bartholomew *et al.* (2012) found that for the 2010 melt year, the channel attained a maximum cross-sectional area of $3\,m^2$ at the beginning of the melt-season (around May 10th); this then reduced to an average conduit size of $<1\,m^2$ for the remainder of the season. All of these models produce channel fluxes and sizes that are consistent with those also seen in the coupled hydrological model and therefore the outputs from the latter are seen as applicable to the marginal

region of Greenlandic land-terminating glaciers. Examining Alpine systems, maximum channel sizes for an efficient system in Haut Glacier d'Arolla, Switzerland, were estimated through dye tracing studies to be $\sim 6\,m^2$ (Nienow *et al.*, 1998). Similar results were found when modelling channels at this same glacier (Arnold *et al.*, 1998). The evolution of subglacial channels at Storglaciären, Sweden were modelled by Cutler (1998) and achieved a maximum cross-sectional area of $\sim 0.6\,m^2$. Pimentel and Flowers (2011) applied their flowband model to an Alpine-like glacier and produced channels of $2\,m^2$ cross-sectional area. These results suggest that, with the current configuration of subglacial hydrological equations, it is difficult to grow and sustain large ($>3\,m^2$) channels.

Headward growth of channels is another feature attributed to Alpine-like glacier systems. Channels begin to form near the margin of the glacier where the greatest cumulative subglacial flux occurs and, as the melt-season progresses causing melt at higher elevations, basal channel growth occurs further upglacier (Nienow *et al.*, 1998). Dye tracing experiments by Nienow *et al.* (1998) at Haut Glacier d'Arolla demonstrated an average conduit headward growth of 65 m per day during July 1990, defined by when the system water velocity was greater than $0.5\,m\,s^{-1}$. The baseline full season run for the marginal glacier model cannot be tested with this criteria as the velocity in the conduits is above $0.5\,m\,s^{-1}$ over most of the domain (see Fig. 9.4 e). However, if a developed conduit is defined as having a cross-sectional area of $1\,m^2$, the average headward expansion in the coupled hydrological marginal model is 468 m per day. Headward expansion is fastest near the margin and becomes slower further inland. This rate of expansion is greater than in the Alpine system examined by Nienow *et al.* (1998) but perhaps reflects the difference in discharge, which is ~ 3 times greater input into the marginal glacier model than recorded at the Haut Glacier d'Arolla pro-glacial stream (Nienow *et al.*, 1998).

By comparing the marginal glacier coupled hydrological model outputs with the dye tracing and modelling studies applied to similar areas in Greenland and to Alpine glaciers, it can be seen that, even limited by the F-Lake runoff, the marginal system responds similarly to water input, becoming more efficient during the summer season and allowing rapid headward growth of channels.

9.5 Jökulhlaups

Jökulhlaups are similar to rapid supraglacial drainage events in many ways: they involve rapid fluxes of water into the basal system causing overpressurisation and are often associated with rapid channelisation (see Section 2.3.1). However, there are two categories of jökulhlaup, as shown in Figure 9.3. The first category involves relatively slow leakage of water along the bed and thus channel formation over a period of days to weeks (e.g. Nye, 1976; Clarke, 1982; Sturm and Benson, 1985; Walder and Costa, 1996; Ng and Björnsson, 2003). Icelandic jökulhlaups, for example, caused by geothermal heating or volcanic eruptions at the base of the ice often involve both higher water temperatures and greater volumes of water than seen for supraglacial lake drainage events in Greenland (Clarke, 2003; Roberts, 2005). Warmer water would allow channel formation to occur more quickly than for thermally equilibrated water and the larger volumes of water cause conditions of overpressure for much longer than seen with the Greenlandic rapid supraglacial lake drainage events. For example, Johannesson (2002) reports that the flood discharge from Grímsvötn, Vatnajökull, Iceland often exponentially increases over more than a week (as can be seen from Fig. 2.4). Such long-lasting floods involve sustained overpressure that can cause very large channel growth. Clarke (2003) modelled channel growth during the 1986 Grímsvötn flood and produced a maximum conduit cross-sectional area of $480\,m^2$ and a maximum outlet discharge of $1960\,m^3\,s^{-1}$ after $\sim$45 days following flood initiation. Another example is from a 1984 jökulhlaup at Triumvirate Glacier, Alaska reported by Sturm and Benson (1985). This flood lasted 20 days with an estimated maximum discharge of $6100\,m^3\,s^{-1}$ and an observed conduit radius of 10 m at the glacier terminus; if this conduit were semi-circular it would have a cross-sectional area of $\sim 157\,m^2$.

The second type of jökulhlaups is much more similar to the conditions seen in rapid Greenlandic supraglacial lake drainage events where a turbulent and pressurised sheet of water quickly spreads over the bed causing ice uplift and transient pressure waves (e.g. Tweed and Russell, 1999; Johannesson, 2002; Flowers *et al.*, 2004; Sugiyama *et al.*, 2007). These latter jökulhlaups are not associated with large channel growth (Johannesson, 2002; Flowers *et al.*, 2004; Sugiyama *et al.*, 2007). The Grímsvötn jökulhlaup of 1996 involved peak discharge of flood waters at the outlet within 14 hours of a subglacial eruption (Roberts *et al.*, 2000). Roberts (2005) argues that the linearly-increasing discharge during this type of event is as a result of mechanical ice uplift due to overpressured water that allows spread of a water

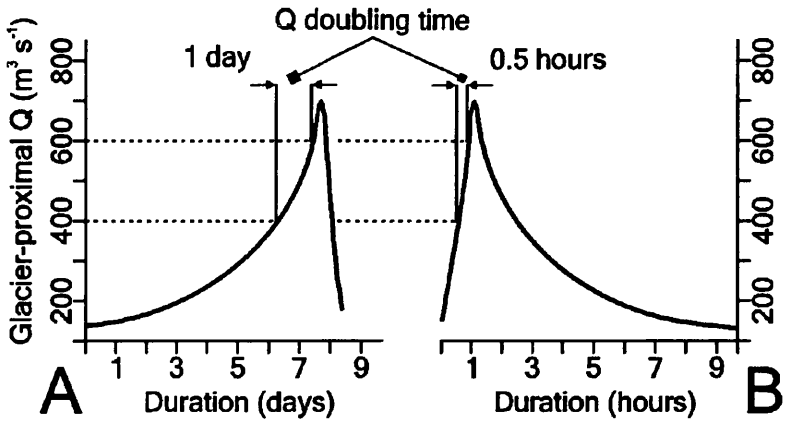

Figure 9.3: *Examples of two types of discharge hydrograph associated with jökulhlaups. A) Exponentially-rising discharge over several days, associated with flow through subglacial channels. B) Linearly-rising discharge within the period of a day associated with turbulent pressurised sheet flow at the ice-bed interface. From Roberts (2005).*

sheet. Another example is from Werder *et al.* (2009), who found that dye tracer velocities from a drainage event at Gornersee on Gornergletscher, Switzerland were slower than predicted from a channel-based jökulhlaup model. This, along with evidence of overpressure in the first 1.5 days of drainage, as indicated by overflow in the connecting moulin, was argued to show that water flowed laterally over the bed instead of entirely being concentrated in conduits.

The different discharge hydrograph characteristics for the two types of flood are illustrated in Figure 9.3 with A, a slower leaking jökulhlaup and B, a rapid drainage jökulhlaup (Roberts, 2005). The rapid flood events in Greenland are comparable with the jökulhlaups that have similar characteristics such as rapidly increasing discharge and short duration of overpressure. As the latter type of jökulhlaup does not involve significant channel growth it supports the results found from investigating lake drainage hydrological development with the coupled hydrological model.

9.6 Turbulent sheets

The formation of sheets of water between the base of the ice and the underlying substrate have been dismissed in the past as unlikely because of differential viscous heating as a result of bed roughness (Nye, 1973; Walder, 1982). However, Creyts and Schoof (2009) argued that sheets can stably exist due to bridging stress effects

from clasts on the bed. Once the sheet reaches a threshold thickness, an efficient drainage system will begin to develop. The water blisters modelled in this thesis differ somewhat as they are transient and temporary features. The idea of a water blister forming at the glacier bed as a result of pressurised water input was suggested long before the model of Tsai and Rice (2010) that is applied in this thesis. Iken and Bindschadler (1986) reported the propagation of a pressure wave at 100 m hr^{-1} in the form of a water sheet at Findelengletscher, Switzerland as a result of the inability of the existing basal hydrological system to adjust to a large and rapid influx of water. Lappegard and Kohler (2005) manually created a water blister by pumping water into a borehole and pressurising the basal system so that the ice was hydraulically lifted from the bed. They found that a lens-shaped water cavity was created but with fingers of water flowing from the blister into areas that had lower overburden stress.

Water blisters have been modelled in various forms by Weertman (1972); Iken *et al.* (1996) and Engelhardt and Kamb (1997). The outputs from their models and the Tsai and Rice (2010) model used in this thesis suggest that the presence of sheets can be stable on a time-scale of hours and can have important implications for short-term dynamics as shown by the acceleration of ice during lake drainage events (e.g. Das *et al.*, 2008; Doyle *et al.*, 2013). The coupled hydrological model suggests that the water blister is removed within 10–40 hours of drainage initiation depending on the model run (see Section 7.3). The primary argument for the prior presence and rapid growth of channels during lake drainage was due to the rapid lowering of GPS units following uplift at the initial stages of drainage, all within the space of several hours (Das *et al.*, 2008); the water was therefore assumed to have been efficiently removed from the system by channels within this period. However, the uplift of ice during lake drainage suggests that the capacity of the basal system is not sufficient to rapidly remove water from lake drainage events and instead the drainage system becomes highly pressurised. The timing of GPS station lowering seems to be similar to the time taken to dissipate the modelled turbulent sheet formed as a result of the pressurised lake water. Therefore, it is perhaps more likely that the downstream flux of this water sheet allows lowering of the GPS units following lake drainage instead of the formation of large channels. This argument is supported by the coupled hydrological model outputs that indicate that channel growth during rapid lake drainage is very limited for most subglacial hydrological systems. The evidence presented here therefore suggests that channels are not necessary to remove water during lake drainage and that the turbulent sheet is a highly efficient method

of removing water from the input region.

9.7 Russell Glacier catchment

In this section, the results from the F-Lake and marginal glacier models are compared with measurements made from studies on RGC and the adjacent Leverett Glacier catchment. First, the channel growth predicted by the coupled hydrological model is compared with other model outputs from the region. The results from dye tracing studies in the region are then compared with the coupled hydrological model outputs. Following this, the evidence from GPS surveys and satellite remote sensing measurements of ice velocity published for the RGC area is compared with ice dynamic characteristics in similar regions extrapolated from the coupled hydrological model outputs.

9.7.1 *Channel growth*

The evidence from the coupled hydrological model suggests that channel growth is a less dominant aspect of the subglacial hydrological system at the inland site, ~70 km from the margin. However, with the tests closer to the margin, an Alpine-like system does appear to form with efficient channels growing in a period of ~25 days (as defined by the switch between sheet-dominated and conduit-dominated flow shown in Fig. 9.1 e). With a larger initial channel size of $1\,m^2$, the time of efficient channel growth is shortened to ~14 days. In a model applied by Flowers (2008) to an Alpine glacier simulation it took nearly 40 days for channels to become the dominant drainage mechanism (see Fig. 3 in Flowers, 2008). Modelling of the distributed component of the Leverett Glacier drainage system using dye tracer velocities indicated that, at the beginning of the season within 14 km of the margin, channels had formed within four weeks from the time of surface melt onset (Cowton *et al.*, 2013). Chandler *et al.* (2013) used the Schoof (2010) equations to estimate conduit growth at tracer sites on Leverett Glacier catchment. They estimated that channels double from an initial cross-sectional area of $0.1\,m^2$ in 6, 23 and 28 days at sites 7, 41 and 57 km from the margin respectively (Chandler *et al.*, 2013). The equivalent distances of 7 km and 57 km from the margin in RGC can be examined with the marginal glacier model and the F-Lake planar topography model outputs, respectively. At 7 km in the baseline coupled hydrological model, channels take 14

days to double in size from 0.1 m^2, although the water input point in the marginal glacier model run is 16 km upstream from this point whereas the Chandler *et al.* (2013) tests are for a moulin at 7 km. At 57 km from the margin the channels double in 44 days when the outlet pressure is at overburden and in 17 days when the outlet pressure is half of overburden; again, the input for these coupled hydrological model tests is located 11 km upstream. However, even after these channels have doubled in size they are only 0.2 m^2 and as a result still greater time is required to form large (>1 m^2) channels at the bed. In both Alpine and Greenlandic systems, and even with high pressure jökulhlaups (see Section 9.5), it therefore seems that efficient channels take a matter of weeks to form, and not a matter of hours as suggested for Greenlandic lake drainage events (Das *et al.*, 2008; Sole *et al.*, 2011; Bartholomew *et al.*, 2012; Cowton *et al.*, 2013).

9.7.2 *Dye tracing evidence*

Dye tracing evidence from Leverett Glacier catchment broadly agrees with the RGC model outputs presented here. At a moulin 41 km from the margin, tracer velocity increased from 0.25 $m\,s^{-1}$ recorded on June 26 to 1.04 $m\,s^{-1}$ on August 1st, 2011 (Chandler *et al.*, 2013). As stated by Chandler *et al.* (2013), an efficient drainage system clearly develops up to 41 km from the margin and the system is therefore comparable to Alpine hydrological systems. However, the tracer tests from their site at 57 km had a slow return rate of 0.22 $m\,s^{-1}$ on August 12th, 2011, suggesting that the basal system at that elevation was inefficient (Chandler *et al.*, 2013). Cowton *et al.* (2013) also reported dye velocities for moulins on Leverett Glacier between 1–14 km from the drainage outlet. These varied from an early-season velocity of 0.04 $m\,s^{-1}$ to a peak water velocity of 1.49 $m\,s^{-1}$ around a month later. This can be compared with records of Alpine dye tracer velocities: for example, Nienow *et al.* (1998) recorded dye trace velocities of <0.8 $m\,s^{-1}$ for the efficient drainage system of Haut Glacier d'Arolla. These comparable dye trace velocities from an Alpine glacier and the near-margin Greenlandic system is therefore strong evidence for a similar type of system development (Cowton *et al.*, 2013). However, a large channel does not necessarily need to be present to allow fast water flow. The average conduit water flow velocity for the baseline model runs are shown in Figure 9.4 along with the average conduit cross-sectional area; these plots are for the full seasonal model runs.

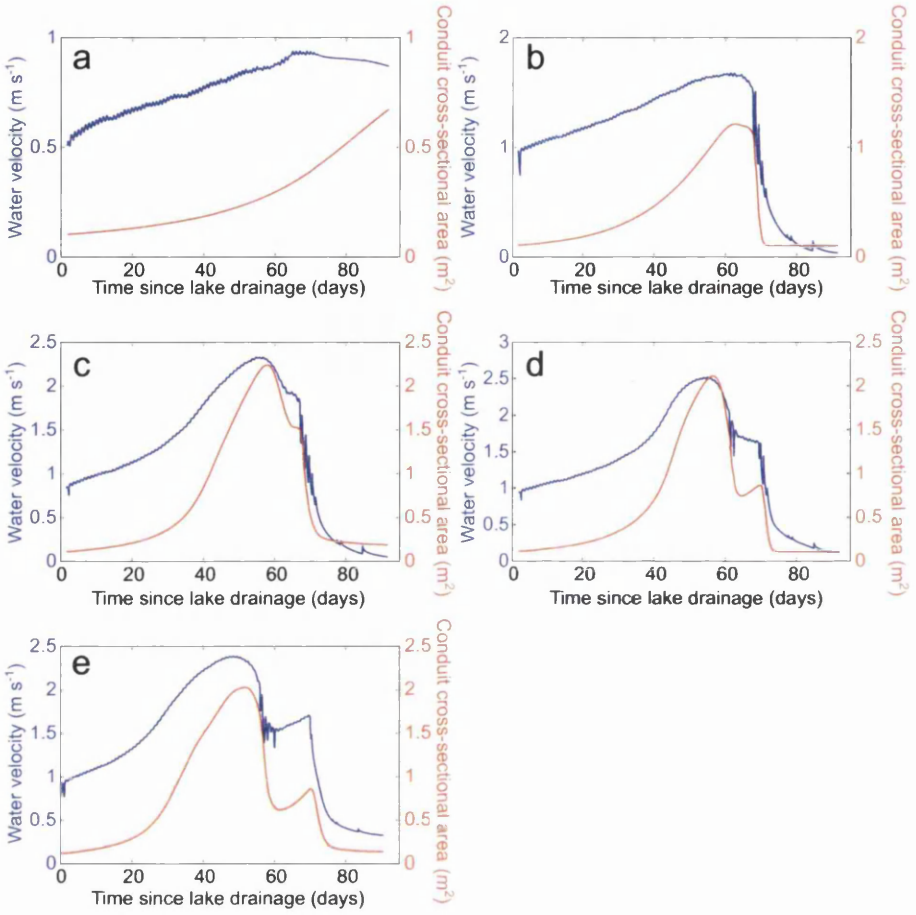

Figure 9.4: *Average water flow velocity (blue) and conduit cross-sectional area (red) across the spatial domain for the full seasonal baseline runs. a) F-Lake planar topography model with $P_{out} = P_i$, b) F-Lake planar topography model with $P_{out} = 0.5\,P_i$, c) Tidewater glacier model with $P_{out} = P_i$, d) Tidewater glacier model with $P_{out} = 0.67\,P_i$, e) Marginal glacier model.*

Figure 9.4 illustrates that, because the water velocity depends on the conduit cross-sectional area and the discharge, water fluxes can be relatively fast even with small channels. For the F-Lake case-study and an outlet pressure of 50% overburden, water velocity can be greater than $1\,\mathrm{m\,s^{-1}}$ even though the channel size is $\sim 0.15\,\mathrm{m^2}$ (Fig. 9.4 b). However, with an outlet pressure at overburden, the water velocity in the F-Lake region is $<1\,\mathrm{m\,s^{-1}}$ (Fig. 9.4 a). For the marginal glacier model, water velocity can reach $\sim 2.4\,\mathrm{m\,s^{-1}}$ in this simulation at a time when the channel cross-sectional area is $\sim 2\,\mathrm{m^2}$ (Fig. 9.4 e). These average velocity calculations from the marginal glacier model outputs overestimate the speed of water flux when compared to the Leverett Glacier catchment dye tracing results from Cowton *et al.* (2013) and

Chandler *et al.* (2013) (who see peak water flow velocities of $\sim$1.5 m s^{-1}). As a result, the modelled channel size and range of channel growth rates presented in this thesis seem to be appropriate for estimates in the different Greenlandic regions despite the lack of site-specific input data. In addition, the model results suggest that fast tracer velocities are not necessarily indicative of the presence of large channels.

Chandler *et al.* (2013) suggested that dye travel time could be as a result of flow through both distributed and channelised systems, thereby complicating interpretation of the basal hydrological system. However, Cowton *et al.* (2013) instead suggested that at Leverett Glacier, the system became channelised sufficiently quickly and effectively that all dye could be assumed to flow through channels instead of a distributed system. For example, Cowton *et al.* (2013) argue that higher levels of dye trace retardation at Leverett Glacier during the melt-season in May and June were not as a result of some flow through a distributed system but instead reflected 1) changes in the roughness and cross-sectional area of channels and 2) the amount of storage in the connected moulin. The reason for this argument is that the velocities of the tracers at the time of partial dye storage had increased to $\sim$1 m s^{-1} and this is suggested to indicate the presence of efficient channels. However, by comparing the discharge and velocity records from the coupled hydrological model outputs in Figure 9.1 and Figure 9.4 it can be seen that the distributed drainage system can be more important for water flux than channels even when channel flow velocity is greater than 1 m s^{-1}. The argument by Cowton *et al.* (2013) for increased moulin storage is because pressures were high and water was pooling in the moulin as a result of an inefficient basal system that could not effectively remove the large volumes of water. However, following Hubbard *et al.* (1995) it is also likely that such high pressure water was pushed into a distributed system, although this was not discussed by Cowton *et al.* (2013). As has been suggested in Section 9.6, a mechanically-induced turbulent sheet can be a highly efficient short-term mechanism for moving water at the ice-bed interface that does not require the presence of channels. On a diurnal scale, a water blister equivalent to that produced during a lake drainage event would not form due to moulin-based water input. However, Leverett Glacier GPS records indicate diurnal variability in horizontal velocity near the margin (see Fig. 9.5 from Bartholomew *et al.* (2012) for a site 7.3 km from the ice margin) that suggests the system is sensitive to the lubricating effect of greater volumes of water; this relationship indicates that channels are not effectively removing water because if they were, the dynamic impact of the lubricating water would be limited to the diameter of the channel and, given longitudinal coupling would be

unlikely to cause such distinct variation in diurnal acceleration (Bartholomew *et al.*, 2012).

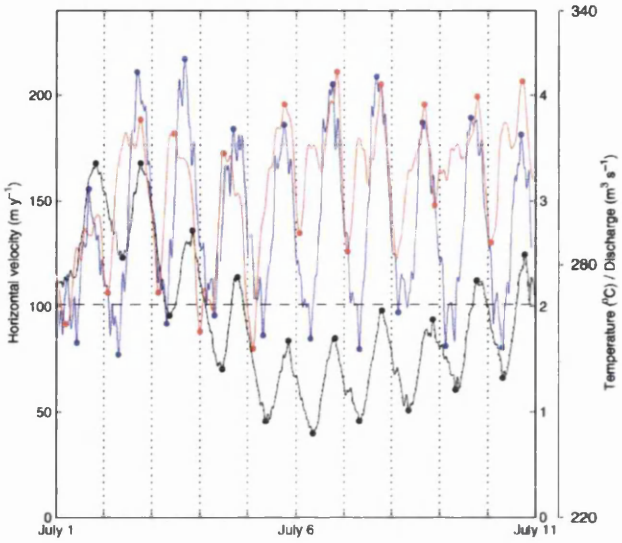

Figure 9.5: *Diurnal variability in horizontal velocity (blue curve), pro-glacial discharge (black curve) and air temperature (red) with daily maxima and minima marked by the dots. The average winter velocity is shown by the black dashed line. Data are from a 2010 GPS site on Leverett Glacier located 7.3 km from the ice margin. From Bartholomew* et al. *(2012).*

9.7.3 *GPS/velocity evidence*

The ice surface velocity of RGC and Leverett Glacier catchment has been measured from both GPS records and satellite measurements, and interpretations of the outputs have been used to define development of the basal hydrological system in this region. Fitzpatrick *et al.* (2013) used TerraSAR-X image pairs to examine near-margin velocity changes in the region of RGC during the 2010 melt-season. Changes in ice surface velocity relative to the winter mean can be seen in Figure 9.6 for a) 6th May, b) 19th June, c) 30th June and d) 22nd July; this figure illustrates that although acceleration is seen in the early season, the system slows down on average below the winter mean by July. This deceleration is attributed to development of a channelised drainage system that shrinks the distributed system, thereby reducing the lubricating impact of water influx (Fitzpatrick *et al.*, 2013). The results from the marginal coupled hydrological model support this as indicated by Figure 9.1 e, which shows channel-dominant drainage after 25 days of water input into the system. However, the distributed drainage system in the coupled hydrological model

continues to contribute to approximately one quarter of the total discharge of the system and therefore cannot be entirely discounted following channel development. Borehole water pressure measurements on RGC by Meierbachtol *et al.* (2013) indicated the presence of both distributed and channelised drainage networks within 15 km of the margin. Boreholes located 17 and 34 km from the margin showed no evidence of a channelised system, although given the spatially limited area of a bed that a borehole accesses this result does not mean channels do not exist this far inland. However, the borehole evidence does reiterate that a distributed system does continue to exist regardless of whether channels have formed.

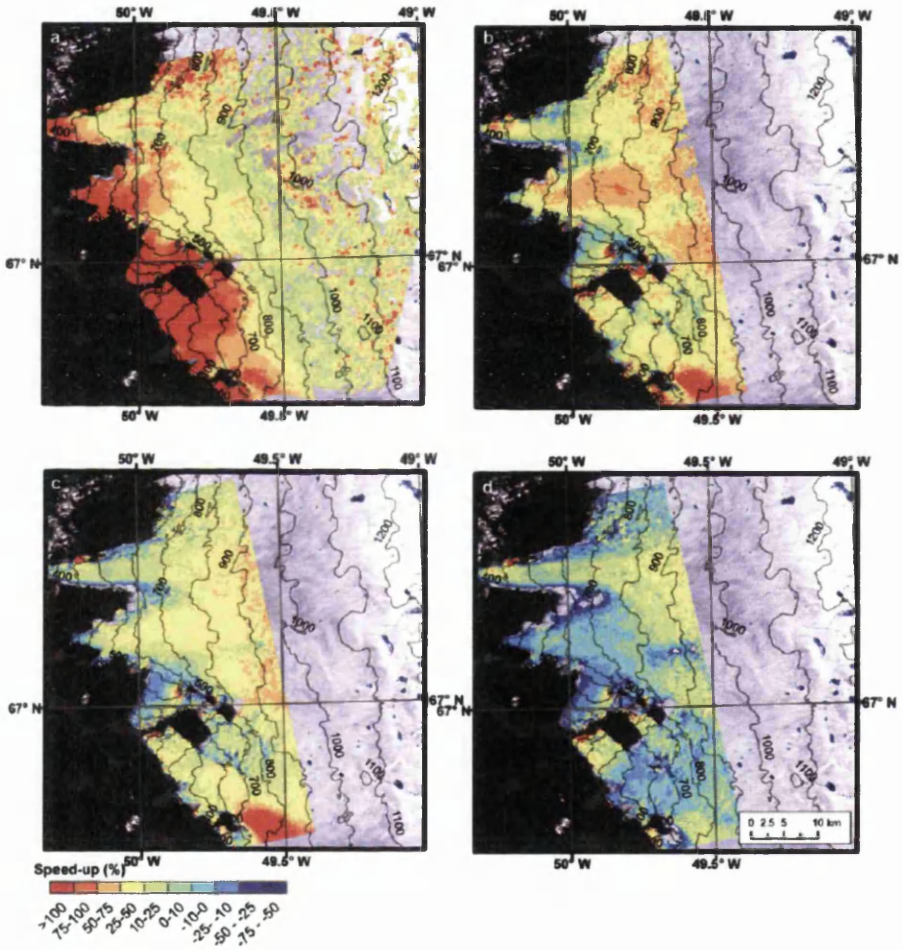

Figure 9.6: *Surface velocities in the RGC region derived from TerraSAR-X image pairs acquired in 2010 and plotted relative to the winter mean for a) May 6th, b) June 19th, c) June 30 and d) July 22nd. From Fitzpatrick* et al. *(2013).*

A more localised and short-term response of surface velocity to water input can be seen with GPS station records presented by Bartholomew *et al.* (2012). Figure 9.7 shows the surface velocity (blue curves), air temperature (red curves) and ice surface

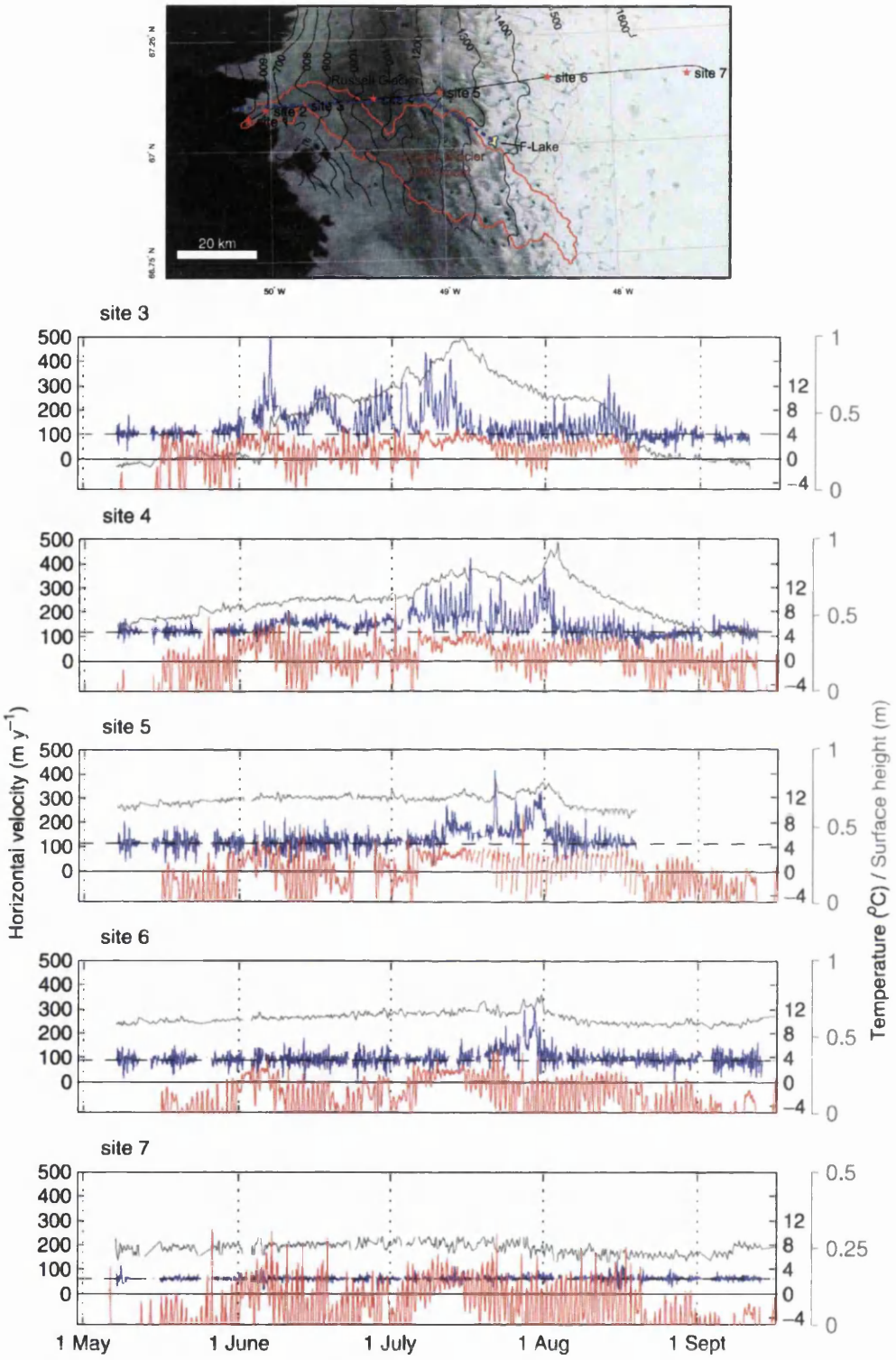

Figure 9.7: *Data from five GPS sites on Leverett Glacier and RGC in summer 2009. Site data include ice surface velocity (blue curves), de-trended ice surface height relative to an arbitrary datum (grey curves) and air temperature (red curves). Average winter velocity is shown by the black dashed line. The site location map also includes F-Lake and the flowline in Fig. 9.9, shown by blue curves; Leverett Glacier catchment is indicated by the red line. Adapted from Bartholomew* et al. *(2012).*

height (grey curves) for sites between 21 and 120 km from the margin (the location of these sites are also shown in Fig. 9.7). Bartholomew *et al.* (2012) argue that the lower sites (e.g. site 3) have faster surface velocity at the beginning of the melt-season and then decelerate as the season continues due to development of an efficient drainage system. However, because the system is not in steady state, increases in surface water runoff cause short-term acceleration as the basal system does not have time to adjust to the changes in water input (Schoof, 2010; Bartholomew *et al.*, 2012). Such a response can be seen in the marginal coupled hydrological model outputs where, despite channel growth throughout the season, the thickness and pressure in the distributed water sheet can be seen to vary diurnally (see Fig. 9.8).

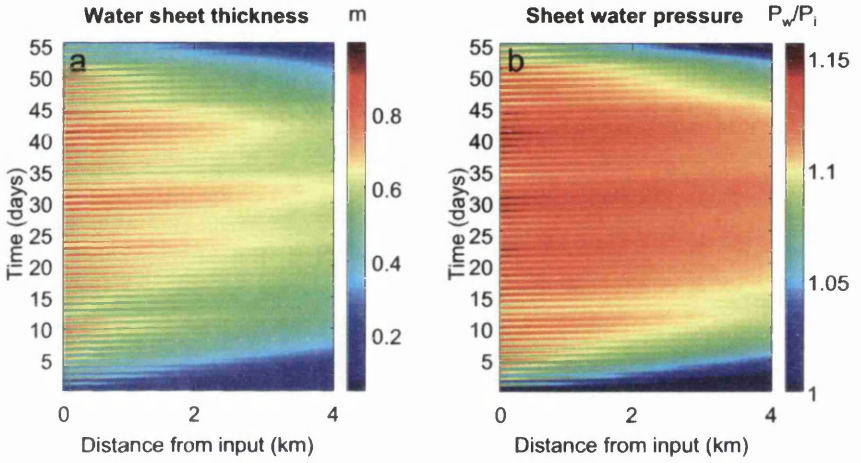

Figure 9.8: *Distance-time plots for the marginal glacier baseline model full seasonal run. Model outputs for 55 days following lake drainage over the initial 4 km of the domain are shown for a) areally-averaged water sheet thickness and b) water sheet pressure.*

At higher elevations in the Bartholomew *et al.* (2012) study (such as site 4), acceleration was delayed due to later surface melt and, at the elevations of sites 5 and 6, velocity increase likely only occurred once a surface-to-bed connection had been made (such as from a supraglacial lake drainage event). At the highest elevation (site 7), acceleration is argued to have only occurred due to longitudinal coupling (Bartholomew *et al.*, 2012). The F-Lake site lies between sites 5 and 6 shown in Figure 9.7. Although site 5 does record some deceleration during the season, likely due to channel development, site 6 does not. The paucity of days where surface meltwater forms at site 6 would contribute to limiting development of a basal hydrological system, but also the evidence from the coupled hydrological model suggests that large channels are unlikely to form in this region even with diurnal meltwater input.

The GPS records are useful for examining localised impacts of surface water input, however on the scale of the catchment there are likely regional trends in velocity change. For example, although Figure 9.6 shows general deceleration during the melt-season, it also shows strong topographical control on acceleration, likely following the basal topography and therefore the primary drainage routes of water. In all these plots by Fitzpatrick *et al.* (2013), the Russell Glacier terminus has higher than average flow velocities compared to the rest of the catchment suggesting this is a major route of water flow (likely in both a distributed and channelised system); the velocity of this tongue also does not seem to change much through the season implying that water flow in this region is important for ice dynamics throughout the observed period (Fitzpatrick *et al.*, 2013).

The satellite and GPS records therefore indicate that, although a general pattern of efficient development appears to occur near the margin of the GrIS, it is punctuated by short-term acceleration events that illustrate surface water input continues to interact with a subglacial distributed system. In addition, spatial variability in the ice sheet geometry appears to affect the ice dynamic response to surface water input.

9.7.4 *Controls on channel growth*

From the dye tracing and GPS station evidence it appears that, on RGC, efficient flow can occur up to ~40 km from the margin. However further inland the basal system appears to remain relatively inefficient throughout the melt-season. There are three likely controls on this pattern: 1) the ice thickness, 2) the surface slope and 3) the volume of water input.

The ice thickness tests presented in Section 7.6.2 are difficult to apply to RGC because they are tested on a fixed model domain length so that increasing the thickness in the marginal glacier test also increases the surface slope. However even with a steeper slope, an ice thickness >1000 m causes less channel growth than in thinner ice. From Figure 1 in Bartholomew *et al.* (2012) it is estimated that the ice becomes thicker than 1000 m at a distance of ~45 km from the margin.

An ice surface profile of RGC from the F-Lake drainage site to the margin is plotted in Figure 9.9 a with the change in slope along the transect in Figure 9.9 b (the location of this flowline is plotted in Fig. 9.7). The surface slope is ~0.5° for the initial 24 km downstream from F-Lake and begins to increase around 44 km from

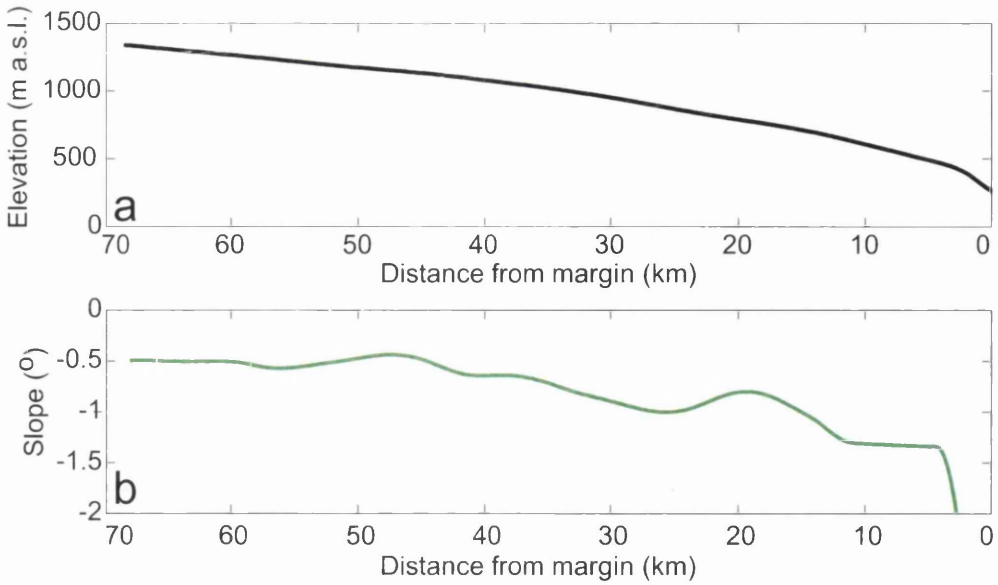

Figure 9.9: *a) Ice surface profile of RGC from a flowline originating at F-Lake and running to the margin, shown by the blue dashed line in Fig. 9.7. b) Averaged surface slope calculated from the ice surface profile in a). The flowline elevation was extracted from a surface DEM created from a SPOT 2008 image by A. Fitzpatrick, Aberystwyth University.*

the margin.

It is perhaps coincidence that the ice around 44 km from the margin becomes more Alpine-like in terms of thinner ice and steeper surface slopes whilst also seeing basal drainage development comparable to an Alpine glacier. For example, it might be the volume of water available for drainage development in this 44 km region that could allow greater drainage development. However, the F-Lake results suggest that a greater volume of water input into the system will not necessarily allow much channel growth. As a result, it seems more likely that the physical characteristics of the ice such as the thickness and slope-driven potential gradients impact drainage development in this area more than water input volume.

9.8 Ice dynamics

Determining whether Greenlandic basal hydrological systems rapidly channelise is important for establishing the dynamic impact of both greater volumes of water accessing to the bed and water forming at higher elevations on the ice sheet in a warming climate. The evidence from the coupled hydrological model suggests that

an efficient system does form towards the margin of the ice sheet where ice is thinner and surface slopes are steeper (see Section 9.4). As suggested by Bartholomew *et al.* (2010), this efficient system limits the dynamic impact of water flux if the channels are large enough to remove the water. However, the GPS station evidence from Bartholomew *et al.* (2012) and Sole *et al.* (2013) showing diurnal variability in horizontal ice surface velocities (Fig. 9.5) suggests that the marginal basal system is not sufficiently efficient to remove water and therefore water flux into a distributed system has a short-term dynamic impact. It is perhaps the thick ice in Greenland that allows rapid channel closure and therefore creates this transient subglacial drainage system. Such a transient system would imply that warmer years cause greater average ice velocity in the summer and indeed this is found by Sole *et al.* (2013). However, it should be noted that faster summer velocities are also associated with slower winter velocities and to some extent the total year-velocity averages out (Sole *et al.*, 2013). Even with a transient hydrological system, the GPS station evidence from Bartholomew *et al.* (2012) shows a seasonal deceleration in ice velocities in the late melt-season demonstrating that the system for several tens of kilometres from the margin of land-terminating glaciers in Greenland likely does become more efficient.

Both the coupled modelling outputs presented here and borehole measurements on RGC by Meierbachtol *et al.* (2013) show coincident occurrence of channelised and distributed drainage systems (see Fig. 9.1), and so the latter can certainly continue to influence ice dynamics to some extent. The region of pressure influence of channels that reduces the lubricating effect of a distributed system depends on the larger subglacial hydrological configuration and the geometric hydraulic potential gradients (Rempel, 2009a). In Greenland, the presence of sparsely located moulins as point sources of water to the bed will encourage the formation of limited water flux pathways. On the other hand, the presence of sediment at the bed, if as widespread as indicated by the results for RGC presented in this thesis (see Chapter 8), would encourage wider-spread distributed drainage and inhibit stable channel growth.

Inland from the marginal region, surface water accesses the bed more sparsely, ice is thicker and the surface slopes are more gentle; in this region the hypothesis of an Alpine-like hydrological system appears not to be applicable. Rapid lake drainage events that allow expansion of a turbulent sheet at the ice-bed interface can cause very high levels of acceleration up to 400% of background winter velocity (e.g. Hoffman *et al.*, 2011). However, this dynamic impact of lake drainage is a short-lived phenomenon lasting less than a day (Das *et al.*, 2008; Doyle *et al.*, 2013;

Tedesco *et al.*, 2013). Tedesco *et al.* (2013) suggest that given the limited number of rapid lake drainage events in Greenland (see e.g. Selmes *et al.*, 2011; Liang *et al.*, 2012), their short-lived dynamic response is not important for regional ice dynamics. Gulley *et al.* (2009) suggest that in areas of thick ice, the only plausible mechanism for initiating surface to bed drainage is through hydrofracture. This points towards perhaps the most dynamically important role of rapid supraglacial lake drainage, i.e. providing the conditions for moulin formation and seasonal access of surface meltwater to the bed. Howat *et al.* (2010); Sole *et al.* (2011); Bartholomew *et al.* (2012) and Cowton *et al.* (2013) suggest that the access of water to the bed in areas of thick ice, in particular due to the influx of high pressure water during lake drainage events, will produce efficient channels. In contrast, the evidence presented in this thesis indicates that growing channels under thick ice with low surface slopes is difficult (see Section 9.2.1). If large channels are formed they are quick to close once water pressures drop (Fig. 4.6). This suggests that in areas of inland ice, distributed systems dominate and that any channels that form are short-lived and unstable features (Fig. 9.1).

If a distributed system persists throughout the melt-season, areas of inland ice would be expected to accelerate in phase with the volume of water input into the system. However, given the limited areas where water can access the bed in inland regions (due to fewer moulins) local acceleration is perhaps dampened by longitudinal coupling to areas with less water flux. With warming at higher elevations on the GrIS likely causing more lake drainage events, it is possible that greater volumes of water will access the bed and allow wider spread inland acceleration. In contrast, marginal ice with a more efficient drainage systems will likely flow slower than the inland ice. This can be seen in the late season velocity map of Palmer *et al.* (2011) for the RGC area (Fig. 3.2) where inland acceleration occurs along subglacial valleys until ~40 km from the margin; this is the region where the evidence shown in Section 9.7 also suggests that efficient drainage networks can begin to form. It is not clear what impact faster inland speeds would have on overall ice dynamics given the counteracting influence of slower marginal ice. This is an interesting area for future work and could address questions such as whether inland ice acceleration and marginal deceleration would cause dynamic thickening at the transition zone.

A coupled hydrological and ice dynamic model by Hewitt (2013) shows that, although greater water volumes allow more rapid channelisation and ice deceleration at the margin, the velocity further inland increases in phase with water input. Upglacier from 25 km from the glacier margin, the ice does not appear to decelerate

during the summer melt-season while surface water continues to access the bed, suggesting that channels do not grow sufficiently large to impact ice dynamics in this region. This Hewitt (2013) model is a 2-D plan-form model that is applied to a 10 km-wide and 50 km-long region at the ice margin; surface water is input into 50 moulins with the density of water input greater near to the ice margin. As a result, the outputs are more sophisticated than those presented in this thesis. However, it is encouraging that similar results are produced in both the coupled hydrological model and the more complicated Hewitt (2013) model. This suggests that, although there are limitations for interpreting the marginal coupled hydrological model (such as the water input rate), it does successfully replicate the trend of seasonal development.

For GrIS mass loss, it is not the dynamics of land-terminating glaciers, but instead tidewater glaciers that are of most importance. In this thesis, studying RGC has been ideal for examining basal hydrological development. However, future work on tidewater glacier hydrology and dynamics is an important area of research. The tidewater model outputs presented in this thesis are limited in applicability to Greenland because they are based on a simplified geometry, as explained in Section 9.3. Howat *et al.* (2010) suggested that lake drainage events in the tidewater Store Gletscher, West Greenland, caused rapid channelisation and facilitated deceleration during the melt-season, similar to the process argued for the Greenlandic land-terminating glaciers (e.g. Bartholomew *et al.*, 2010, 2012). The evidence presented by Howat *et al.* (2010) shows deceleration over the period of a month following lake drainage events. Although applied to a simplified geometry, the coupled hydrological model outputs suggest that in tidewater glaciers, large channels do not form immediately following lake drainage events. However, within a month channels form that could impact the local ice dynamics by removing water from an adjacent distributed system, particularly if channels of $\sim$1 m^2 have grown within the region prior to the lake drainage and thus agree with the Howat *et al.* (2010) data. A significantly larger volume of water is argued to flow beneath tidewater glaciers in Greenland (Xu *et al.*, 2013), compared to inland areas of ice; pre-existing channels are therefore also more likely to occur in areas similar to that represented by modelled geometry 3. If pre-existing channels have not formed, the tidewater model outputs show that channels become dominant later in the season and for a shorter period of time than in the marginal system (Fig. 9.1 c and d). Maintenance of a distributed system would cause a faster response of tidewater glaciers to calving at the ice front. An efficient channelised system limiting the lubrication at the ice-bed interface however, could inhibit the glacier response to frontal retreat. Additional modelling is necessary to

determine whether a similar transition between inefficient and efficient drainage as argued here for the GrIS marginal glaciers occurs for the tidewater glaciers; however determining this could be quite important for establishing future impacts of warming ocean and air temperatures on the mass balance of the GrIS.

9.9 Limitations of approach

As with any modelling study there are limitations to the approach that should be taken into account when analysing the outputs. The specific methodological limitations of the coupled hydrological model are described in Section 5.4.7. Here, the processes that might under- or over-estimate the channel growth and therefore impact the interpretations presented earlier in this chapter are discussed. Some limitations such as the lack of local runoff calculations for the marginal and tidewater glacier tests are discussed throughout this chapter and will therefore not be reiterated here.

There are various features in the coupled hydrological model that do not allow the exact prediction of channel growth rate. Features that may underestimate channel growth include the lack of channel formation as the blister grows radially; a more sophisticated 3-D modelling approach would be necessary to remedy this. However, as the blister only grows to a maximum radius of 3 km primarily over a period of < 1 hour (see Tables C.1–C.4), it is unlikely that large channels could form within this time even with significant overpressure. Such an assertion is supported by the results from the simple R-channel model that suggest little channel growth could occur within this short time period (see Fig. 4.2).

The second feature that might allow underestimation of channel growth is the impact of disregarding changes in water temperature during the lake drainage event. However, melting is also not included in the englacial portion of the blister model and so it cannot be speculated how much of an impact water temperatures above the local pressure melting point could have on drainage development. For channel growth as a result of rapid fluxes of water, Fowler (2009) argued that the water temperature will not make much difference; if water temperatures at the bed are greater than the pressure melting point during lake drainage, however, it could mean that channel melt rates and growth is underestimated in the coupled hydrological model. It would be an interesting area of future research to test what changes occur

to the basal water temperatures as a result of rapid supraglacial lake drainage.

The features of the modelling that likely overestimate channel growth are the lack of supercooling equations in the code that would act to reduce channel growth on reverse slopes (see Section 9.2.4). In addition, the topography in the model has been smoothed so that water can flow up riegels without being blocked by hydraulic potential limits to flow. In reality, the highly variable basal topography likely creates a complex drainage network that cannot be replicated in detail by the coupled model approach (Section 9.2.3). However, the steep reverse slopes will, in general, inhibit channel growth and prevent formation of an efficient drainage pathway.

The presence of soft sediment at the ice-bed interface, as discussed in Section 9.2.5, could act to enhance growth of an efficient drainage system by allowing erosion of a sediment base in addition to melting of the overlying ice. However, canals eroded into sediment will likely be highly transient features, particularly if sediment deformation processes occur. Current hydrological models have not been developed to include sediment deformation and canal erosion, and it was beyond the scope of this thesis to address these issues. However it could be important for determining subglacial hydrological development characteristics and therefore should be the focus of future research.

The method of sensitivity testing where the parameters are each varied individually from a set of baseline parameters will not give the full range of responses from a hydrological system. For example, if two parameters that encourage channel growth occur simultaneously, greater growth could occur than reported here. However, the approach taken in this thesis was designed to examine the impact of individual parameters on channel development. The chosen baseline parameters appear to allow reasonable model outputs that fit well with the surface GPS station data, the recorded lake drainage rate and the regional response of the ice sheet to the lake drainage (see Section 9.2). The sensitivity tests in this thesis thus likely adequately capture the range of behaviours at the F-Lake case-study site. The tidewater glacier and marginal glacier models would benefit from better-constrained inputs such as topography, lake volume and surface water runoff determined for particular sites of interest. Although these modelling exercises cannot exactly predict the channel growth rates for particular areas of the GrIS they can help establish if there is a difference in hydrological development in these regions. It is believed that the coupled hydrological modelling exercise has achieved this and has made a step towards understanding the spatial variability in hydrological development in different areas

of the GrIS as a result of both lake drainage events and seasonal moulin drainage.

9.10 Summary

The results from this study of Greenland subglacial hydrological systems have been discussed in this chapter. The primary outcomes are that both the simple R-channel model and the coupled hydrological model suggest large channels do not form during lake drainage events. Instead, water in the short-term is evacuated from the lake drainage site primarily by a turbulent sheet of water and then by the local distributed drainage network. Channels do grow during this process but not at a sufficient rate to contribute significantly to the hydrological system. These modelling results are supported by in-situ GPS station uplift data that agree with model water pressure results, used as a proxy for levels of hydraulic jacking. In addition, measurements and models of other rapid drainage events such as those associated with jökulhlaups also suggest that channel growth occurs over a period of days rather than hours, even with highly pressurised subglacial water.

Over the longer term, once a surface-to-bed pathway has been established, the hydrological development suggested by the modelling outputs differs depending on where in Greenland the drainage is occurring. In the inland ice site, the model results suggest that distributed drainage systems dominate throughout most of the melt-season, due to the thick ice and low surface slopes preventing the growth and maintenance of larger channels. Dye tracing evidence from inland ice near RGC supports this model result. The marginal glacier model shows seasonal development of an efficient channelised system, as also suggested by the dye tracing and GPS records from research near RGC. The tidewater glacier model also shows greater channel development than found in inland ice and, over the course of a season, is similar to that seen at the marginal land-terminating glacier. The suggested hydrological configuration of a transition between distributed-dominated and channel-dominated drainage depending on the ice thickness and surface slope, if correct, has implications for ice dynamics. Possibly of most importance is that, with increased meltwater production at higher elevations, inland ice might flow faster in the summer season even if the near-margin ice is slower as a result of drainage development.

Although the coupled hydrological model has many associated limitations, as is found with any model of subglacial hydrology, the results from the experiments pre-

sented in this thesis improve understanding of the Greenland subglacial hydrological systems.

Chapter 10

Conclusions and further research

10.1 Motivation

The development of subglacial hydrological systems under the GrIS directly impacts ice dynamics (Zwally *et al.*, 2002; van de Wal *et al.*, 2008; Shepherd *et al.*, 2009; Bartholomew *et al.*, 2010; Sundal *et al.*, 2011). With a warming climate it is important to determine whether greater fluxes of water reaching the ice-bed interface will cause ice acceleration and mass loss. Recent research on land-terminating regions of West Greenland has suggested that the basal hydrological system develops in a similar fashion to Alpine hydrological systems (Shepherd *et al.*, 2009; Bartholomew *et al.*, 2010, 2012; Cowton *et al.*, 2013) i.e. water accessing a subglacial distributed hydrological system in the spring causes substantial ice acceleration, followed by deceleration over the season as the drainage system develops into a series of efficient conduits, lessening the spatial impact of the lubricating water (Price *et al.*, 2008). In particular, large ($>20\,m^2$ cross-sectional area) R-channels have been argued to exist in areas of rapid lake drainage (Pimentel and Flowers, 2011), where hydrofracture allows evacuation of millions of cubic meters of water from the ice surface to the bed in a matter of hours (Das *et al.*, 2008; Doyle *et al.*, 2013). Pre-existing channels are suggested to be necessary to efficiently evacuate these large volumes of water that reach the bed (Das *et al.*, 2008; Hoffman *et al.*, 2011; Pimentel and Flowers, 2011). However, significant differences between Alpine glaciers and ice sheets include the 1) ice thickness, which affects the creep closure rate of conduits and the relative pressure gradient, and 2) the surface slope, which impacts the geometric potential gradient.

The primary aim of this thesis has been to examine the role of rapid lake drainage in subglacial hydrological development, particularly in areas of thick inland ice, and also to investigate differences in drainage development as a result of the glaciological setting of lake drainage events.

10.2 Methods

In this thesis, a numerical modelling approach has been used to examine basal hydrological development, particularly in relation to rapid lake drainage events in different areas of the GrIS. Initially, a simple R-channel model (following Nye, 1976) was constructed to examine the general characteristics of channel growth in areas of thick ice with shallow surface slopes. Following this, a more complex modelling approach was taken using two previously developed models: 1) the Tsai and Rice (2010) radial blister model, and 2) the Pimentel and Flowers (2011) distributed and channelised hydrology flowband model. These two models have been adapted and linked by the author to produce a novel approach to lake drainage modelling. This coupled hydrological model allows radial expansion of a turbulent blister of water at the ice-bed interface; this blister growth is driven by overpressured water from the lake drainage that causes hydraulic jacking of the ice. Concurrently, the flowband model allows downstream development of the basal hydrological system. Following lake drainage, the flowband model is driven with estimated surface diurnal water inputs in order to examine further seasonal development of the subglacial drainage system.

The coupled hydrological model is applied to four model geometries representing different regions of the GrIS. Model geometries 1 and 2 are based on the case-study field site, F-Lake, located ~70 km inland from the margin of Russell Glacier, West Greenland. Data from a lake drainage event at F-Lake were collected in summer 2010 and are the basis for much of the model validation and input constraints presented in this thesis. In particular, local and regional GPS records, the lake water level record, and surface and basal DEMs (all of which have been analysed and provided by collaborators) have contributed to the modelling process. The first model geometry represents the F-Lake site with simple planar topography, whereas model geometry 2 is the F-Lake site with topography extracted from the surface and basal DEMs. The third model geometry is constructed to represent a tidewater glacier, within 30 km of the terminus, with outlet pressure conditions representing

both a floating tongue and grounded ice. The final, fourth, model geometry is based on the topography near the margin of RGC and is constructed with thinner ice and steeper surface slopes than the other modelled geometries. As many of the conditions at the ice-bed interface are unknown, a large number of sensitivity tests have been applied to the four modelled geometries in order to produce a likely range of possibilities for basal hydrological development.

An additional aim in this thesis was to examine the basal conditions that might impact hydrological development in RGC. This has been approached by analysing reflection seismic data collected at two sites, one $\sim$13, km from Russell Glacier terminus, and the second, $\sim$5, km to the NE of the F-Lake case-study site. From these data sets, seismic stack profiles have been created and amplitude-versus-angle (AVA) analysis conducted, with the latter allowing prediction of basal material characteristics.

10.3 Main findings

The simple R-channel model and the coupled hydrological model both predict that growing channels during lake drainage events is difficult, particularly for thick inland ice. The outputs from the sensitivity experiments indicate that maximum growth for any of the geometries is less than $0.2\,\mathrm{m}^2$ over the ten hours following lake drainage (aside from the test where a large, $10\,\mathrm{m}^2$, pre-existing channel was in place in the marginal glacier model, where much greater channel growth was possible). This result suggests that the overpressure from a lake drainage event does not allow rapid channel growth in most scenarios, and instead water accessing the bed during lake drainage is evacuated primary through a turbulent sheet that persists for several hours before the water is removed by the distributed drainage system. Similar drainage characteristics have been recorded for some jökulhlaups and ice-marginal lake drainage events (Tweed and Russell, 1999; Johannesson, 2002; Sugiyama *et al.*, 2007). Those jökulhlaups that are instead associated with large channel growth have overpressured conditions for much longer than the Greenlandic rapid lake drainage events (i.e. days instead of hours) and see substantial channel growth over tens of days (Nye, 1976; Clarke, 1982; Sturm and Benson, 1985; Walder and Costa, 1996; Ng and Björnsson, 2003).

For the inland ice case-study (F-Lake), the coupled hydrological model outputs sug-

gest that little seasonal channel growth occurs as a result of diurnal water inputs. Instead, the distributed drainage system dominates throughout the melt-season. This suggests that significant pre-existing channels are unlikely to form in areas of inland ice prior to lake drainage events, both as a result of lack of surface water input at these elevations but also due to the geometric characteristics of the ice that prevent channel growth and cause rapid shut-down of channels below overburden pressure. The coupled hydrological model results suggest that the shallow surface slope, which creates a small hydraulic potential drive for water flux, is the primary reason for limited channel growth; the secondary cause is the ice thickness, which causes rapid channel closure when water pressures are below overburden and also makes continuous pressurisation of channels more difficult. Variable basal topography that limits channel growth on reverse slopes also contributes to creating a highly transient and inefficient drainage system.

The tidewater glacier model results suggest that channels can grow more easily in this topographical setting than under inland ice. Although channel growth is small during the lake drainage event, with diurnal water inputs, larger channels begin to form at the margin of the tidewater glacier and progress up-glacier during the season. Over the course of the melt-season, channel growth in the tidewater glacier model is similar to that produced from the marginal glacier model, despite the thicker ice and the higher outlet water pressures in the tidewater model. This model would be significantly improved with a diurnal surface runoff rate calculated from a tidewater glacier catchment as opposed to running the model with the estimated runoff for the inland F-Lake catchment. It is possible that, with greater volumes of water input, seasonal channel growth in the tidewater glacier model could be much greater than reported in this thesis. However, the important outcome from this coupled hydrological modelling exercise is that the development of an efficient drainage system is much more of a feature in the tidewater glacier model compared to the inefficient drainage for the inland ice case-study.

The results from the marginal glacier model suggest that an efficient channelised system can form during the melt-season in areas near the ice margin where conditions (such as ice thickness and surface slope) are comparable with valley glaciers. The timing for development of an efficient system (over 14–30 days) in the marginal glacier model are comparable with measured channel development from dye tracing experiments near RGC (Cowton *et al.*, 2013) and at Alpine glaciers (Nienow *et al.*, 1998). The velocity of water flux through the channels is also comparable to that measured on RGC (Chandler *et al.*, 2013; Cowton *et al.*, 2013). However, the size

of channels produced in the marginal glacier model are not generally greater than $2\,m^2$ after 30 days of drainage. Similar sizes of channel have been produced in other models applied to the margin of the GrIS (Schoof, 2010; Hewitt *et al.*, 2012) and Alpine glaciers (Cutler, 1998; Pimentel and Flowers, 2011). This suggests that very large channels are perhaps not common even in the near-margin region of the GrIS. In addition, even though channels dominate the drainage system throughout much of the melt-season in the marginal glacier model, the distributed system continues to contribute to hydrological flux and thus remains an important feature at the ice-bed interface, particularly when examining ice dynamics.

The implications of the suggested subglacial hydrological conditions on ice dynamics are that, although the near-margin areas of the ice sheet appears to decelerate during the melt-season as a result of efficient channel formation, the inland region might not. It is possible that with greater water inputs at higher elevations in a warming climate, the resulting higher speeds of inland ice might drive overall ice sheet acceleration. Alternatively, inland ice acceleration might be prevented by the slower ice at the margin. All the model outputs suggest that, regardless of the topographic setting, subglacial channels in Greenland are fairly transient. This means that larger input of water from surface sources often causes pressurisation of the distributed system in addition to the channel and can cause local ice acceleration. Also, with water pressures below overburden, channels can close fairly quickly (within days) due to the thick ice and therefore variability in surface input can have a significant impact on local ice dynamics.

Results from the AVA analysis at sites on RGC suggest that subglacial sediment is a common feature. Near the margin, the subglacial sediment at the seismic reflection site was found to be soft and unlithified. Wet, soft sediment was also predicted for a basin upstream of the F-Lake drainage site. However, analysis of basal sediment (by a collaborator) along the F-Lake drainage flow path found lithified sediment. The latter would be similar to bedrock from a hydrological modelling perspective and therefore supports the applicability of the coupled hydrological model. However, the geophysical evidence suggests that variable basal sediment conditions should be taken into account in future modelling ventures of the basal hydrological system of the GrIS.

10.4 Future work

As with all models, the approach is limited by necessary approximations as discussed in Sections 5.4.7 and 9.9. There are various aspects of the hydrological modelling and related investigations that are highlighted throughout the thesis as areas needing attention in future research; these are summarised in this section.

10.4.1 *Topography and supercooling*

Many hydrological models use planar basal slopes (e.g. Flowers, 2008; Pimentel and Flowers, 2011; Hewitt *et al.*, 2012; Hewitt, 2013), such as geometries 1, 3 and 4 presented in this thesis. However, the outputs from the F-Lake real topography model illustrate that attention should be paid in the future to variable topography at the bed; the results indicate very spatially-transient hydrological development depending on the basal topography, and suggest that the idea of long, straight, continuous channels efficiently transporting water at the bed might not always be found in reality. The presence of overdeepenings can hinder water flow from reverse hydraulic potential gradients (Dow *et al.*, 2011) and also reduce hydraulic conductivity due to supercooling freeze-on narrowing flow paths on reverse slopes (Alley *et al.*, 1998). Most hydrological models used smoothed topography to avoid reverse slopes and do not include thermal calculations to adjust the water temperature to the local pressure melting point. In order to better understand hydrological development, these features should be included in models in the future.

10.4.2 *Sediment*

The AVA analysis presented in Chapter 8 indicates that sediment might be a widespread feature under RGC, and perhaps other areas of the GrIS. As explained in Section 2.4.3, there are currently no spatially and temporally variable models of water flux through sediment canals or any other fast-flow feature in sediment. The presence of sediment could allow channels (or canals) to erode more quickly than in a hard-bed scenario where channels are formed only from ice melting (Walder and Fowler, 1994). However, lower pressures in a sediment canal might also cause it to be refilled with sediment, thus creating a highly transient system dependent on factors such as water pressure, water flux and sediment grain size (Ng, 2000a).

Sediment-based drainage is therefore an area of research that would benefit from greater attention and the development of non-steady state sediment canal equations would contribute significantly to hydrological modelling in Greenland.

10.4.3 *Coupled hydrological model*

There are various aspects of the coupled hydrological model that could be improved but were beyond the scope of this thesis. Developing a blister model on variable basal topography rather than assuming radial expansion would likely better replicate the ice uplift measured in-situ at F-Lake (where uplift was greater in the direction of downstream subglacial water flow). The linkage between the blister model and the flowband model requires approximations, including assuming overburden pressure at the margin of the water blister, which is not the case in the equations, although is likely more representative of reality. In addition, stage 3 of the coupled modelling process approximates the volume of water in the blister into the flowband but does not entirely conserve mass; this is an improvement that could be incorporated into the coupled hydrological model in the future.

The flowband model could be improved to allow 2-D water flow so that the distributed system could be coupled to a developing arborescent channel network. This type of hydrological model has been recently developed by Schoof *et al.* (2012) and Hewitt *et al.* (2012). However, one improvement necessary in all of these hydrological models is the inclusion of hydraulic jacking during overpressured conditions. Although the Pimentel and Flowers (2011) flowband model includes equations for elastic beam uplift, it is not easily applied to an ice sheet with much wider regions of lateral coupling than found in a valley glacier and therefore has not been included in the coupled hydrological model application. An alternative would be to apply the hydraulic jacking from the elastic mechanics equations of the blister model to the entire flowband domain; this was beyond the scope of this thesis but would improve the coupled hydrological model for future applications.

10.4.4 *Modelled geometries*

Although the F-Lake modelled geometries 1 and 2 were based on in-situ data, the tidewater and marginal glacier geometries were fabricated. It would an interesting exercise to apply the coupled hydrological model to a real tidewater and marginal

glacier with known topography and calculated catchment runoff. The volume of water input diurnally into the F-Lake model is already simplified in that it does not take account of surface flux times and changes in melt rate with elevation in the F-Lake catchment; this would benefit from a more precise approach such as that taken by Banwell *et al.* (2012). Particularly for the tidewater and marginal glacier models, appropriate calculations of surface runoff for these regions would allow a stronger analysis of hydrological development. Tidewater glaciers appear to be more important for Greenland mass flux than land terminating glaciers (Rignot and Kanagaratnam, 2006; Bamber *et al.*, 2007; Howat *et al.*, 2007), and therefore understanding hydrological conditions under these glaciers is important for predicting future dynamics of the GrIS. If the tidewater basal drainage systems do channelise during the melt-season, it could hinder subglacial lubrication and the ice might not respond as rapidly to mass change as a result of calving at the ice front. The interaction between tidal variations in water pressure at the ice front and the flux through the subglacial hydrological system is also not clear. As basal hydrology directly impacts the dynamics of these ice arteries it requires attention in future research.

10.4.5 *Ice dynamics*

Finally, the results from the coupled hydrological model suggest that, although channelised conditions develop during the melt-season at the margin of the GrIS, similar to that seen in Alpine glacier systems, the inland region does not allow growth of efficient channels and therefore remains a primarily distributed system. For dynamics, this configuration would suggest that near-margin ice would decelerate during the melt-season whereas inland ice would continue flowing at higher velocities, similar to that seen at the beginning of the melt-season. It would be interesting to apply these hydrological conditions in an ice-dynamic model to assess the response of the ice mass to differential areas of acceleration; for example, would dynamic thickening occur at the transition zone between fast and slow flow, or would the slower marginal ice hinder fast inland ice flow? Seasonal satellite and GPS measurements could also be examined to determine whether there is a transition zone for ice speed and if it has an impact on regional ice velocity.

References

Ahlstrom, A. P., J. J. Mohr, N. Reeh, E. L. Christensen, and R. L. Hooke (2005). Controls on the basal water pressure in subglacial channels near the margin of the Greenland ice sheet. *Journal of Glaciology*, **51**(174):443–450.

Aki, K. and P. G. Richards (1980). *Quantitative seismology: Theory and methods*, volume 1. Freeman San Francisco.

Alley, R., D. Blankenship, C. Bentley, and S. Rooney (1986). Deformation of till beneath ice stream B, West Antarctica. *Nature*, **322**:57–59.

Alley, R. B. (1992). How can low-pressure channels and deforming tills coexist subglacially? *Journal of Glaciology*, **38**(128):200–207.

Alley, R. B. (1996). Towards a hydrological model for computerized ice-sheet simulations. *Hydrological processes*, **10**(4):649–660.

Alley, R. B., P. U. Clark, P. Huybrechts, and I. Joughin (2005a). Ice-sheet and sea-level changes. *Science*, **310**(5747):456–460.

Alley, R. B., T. K. Dupont, B. R. Parizek, and S. Anandakrishnan (2005b). Access of surface meltwater to beds of sub-freezing glaciers: preliminary insights. *Annals of Glaciology*, **40**(1):8–14.

Alley, R. B., D. E. Lawson, E. B. Evenson, and G. J. Larson (2003). Sediment, glaciohydraulic supercooling, and fast glacier flow. *Annals of Glaciology*, **36**(1):135–141.

Alley, R. B., D. E. Lawson, E. B. Evenson, J. C. Strasser, and G. J. Larson (1998). Glaciohydraulic supercooling: a freeze-on mechanism to create stratified, debris-rich basal ice: II. Theory. *Journal of Glaciology*, **44**(148):563–569.

Anandakrishnan, S. (2003). Dilatant till layer near the onset of streaming flow of Ice Stream C, West Antarctica, determined by AVO (amplitude vs offset) analysis. *Annals of Glaciology*, **36**(1):283–286.

Andersen, M. L., M. Nettles, P. Elosegui, T. Larsen, G. Hamilton, and L. Stearns (2011). Quantitative estimates of velocity sensitivity to surface melt variations at a large Greenland outlet glacier. *Journal of Glaciology*, **57**(204):609–620.

Arnold, N., K. Richards, I. Willis, and M. Sharp (1998). Initial results from a distributed, physically based model of glacier hydrology. *Hydrological Processes*, **12**(2):191–219.

van As, D., A. L. Hubbard, B. Hasholt, A. B. Mikkelsen, M. R. van den Broeke, and R. S. Fausto (2012). Large surface meltwater discharge from the Kangerlussuaq sector of the Greenland ice sheet during the record-warm year 2010 explained by detailed energy balance observations. *The Cryosphere*, **6**:199–209.

Atre, S. R. and C. R. Bentley (1993). Laterally varying basal conditions beneath Ice Streams B and C, West Antarctica. *Journal of Glaciology*, **39**(133):507–514.

Bamber, J., J. Griggs, R. Hurkmans, J. Dowdeswell, S. Gogineni, I. Howat, J. Mouginot, J. Paden, S. Palmer, E. Rignot, *et al.* (2013). A new bed elevation dataset for Greenland. *Cryosphere*, **7**(2):499–510.

Bamber, J. L., R. B. Alley, and I. Joughin (2007). Rapid response of modern day ice sheets to external forcing. *Earth and Planetary Science Letters*, **257**:1–13.

Banwell, A. F., N. S. Arnold, I. C. Willis, M. Tedesco, and A. P. Ahlstrøm (2012). Modeling supraglacial water routing and lake filling on the Greenland Ice Sheet. *Journal of Geophysical Research: Earth Surface*, **117**(F4):F04012.

Banwell, A. F., I. C. Willis, and N. S. Arnold (2013). Modeling subglacial water routing at Paakitsoq, W Greenland. *Journal of Geophysical Research: Earth Surface*, **118**:1–14, doi:10.1002/jgrf.20093.

Bartholomaus, T. C., R. S. Anderson, and S. P. Anderson (2007). Response of glacier basal motion to transient water storage. *Nature Geoscience*, **1**(1):33–37.

Bartholomew, I., P. Nienow, D. Mair, A. Hubbard, M. King, and A. Sole (2010). Seasonal evolution of subglacial drainage and acceleration in a Greenland outlet glacier. *Nature Geoscience*, **3**(6):408–411.

Bartholomew, I., P. Nienow, A. Sole, D. Mair, T. Cowton, and M. A. King (2012). Short-term variability in Greenland Ice Sheet motion forced by time-varying meltwater drainage: Implications for the relationship between subglacial drainage system behavior and ice velocity. *Journal of Geophysical Research*, **117**(F3):F03002.

Bartholomew, I., P. Nienow, A. Sole, D. Mair, T. Cowton, S. Palmer, and J. Wadham (2011a). Supraglacial forcing of subglacial drainage in the ablation zone of the Greenland ice sheet. *Geophysical Research Letters*, **38**:L08502, doi:10.1029/2011GL047063.

Bartholomew, I. D., P. Nienow, A. Sole, D. Mair, T. Cowton, M. A. King, and S. Palmer (2011b). Seasonal variations in Greenland Ice Sheet motion: Inland extent and behaviour at higher elevations. *Earth and Planetary Science Letters*, **307**(3):271–278.

Bentley, C. R. (1971). Seismic evidence for moraine within the basal Antarctic ice sheet. *Antarctic Research Series*, **16**:89–129.

Bindschadler, R. (1983). The importance of pressurized subglacial water in separation and sliding at the glacier bed. *Journal of Glaciology*, **29**(101):3–19.

Björnsson, H. (2003). Subglacial lakes and jökulhlaups in Iceland. *Global and Planetary Change*, **35**(3):255–271.

Boon, S. and M. Sharp (2003). The role of hydrologically-driven ice fracture in drainage system evolution on an Arctic glacier. *Geophysical Research Letters*, **30**(18):1916, doi:10.1029/2003GL018034.

Booth, A. D., R. A. Clark, B. Kulessa, T. Murray, and A. Hubbard (2012). Thin-layer effects in glaciological seismic amplitude-versus-angle (AVA) analysis: implications for characterising a subglacial till unit, Russell Glacier, West Greenland. *The Cryosphere*, **6**:909–922.

Boulton, G. S. and R. C. A. Hindmarsh (1987). Sediment deformation beneath glaciers: rheology and geological consequences. *Journal of Geophysical Research: Solid Earth (1978–2012)*, **92**(B9):9059–9082.

Box, J. E. and K. Ski (2007). Remote sounding of Greenland supraglacial melt lakes: implications for subglacial hydraulics. *Journal of Glaciology*, **53**(181):257–265.

van den Broeke, M., P. Smeets, J. Ettema, C. van der Veen, R. van de Wal, and J. Oerlemans (2008). Partitioning of melt energy and meltwater fluxes in the ablation zone of the west Greenland ice sheet. *The Cryosphere*, **2**:179–189.

Chandler, D. M., J. L. Wadham, G. P. Lis, T. Cowton, A. Sole, I. Bartholomew, J. Telling, P. Nienow, E. B. Bagshaw, D. Mair, *et al.* (2013). Evolution of the subglacial drainage system beneath the Greenland Ice Sheet revealed by tracers. *Nature Geoscience*, **6**(3):195–198.

Christoffersen, P., R. I. Mugford, K. J. Heywood, I. Joughin, J. A. Dowdeswell, J. P. M. Syvitski, A. Luckman, and T. J. Benham (2011). Warming of waters in an East Greenland fjord prior to glacier retreat: mechanisms and connection to large-scale atmospheric conditions. *The Cryosphere*, **5**(3):701–714.

Chu, V. W., L. C. Smith, A. K. Rennermalm, R. R. Forster, J. E. Box, and N. Reehy (2009). Sediment plume response to surface melting and supraglacial lake drainages on the Greenland ice sheet. *Journal of Glaciology*, **55**(194):1072–1082.

Chylek, P., J. E. Box, and G. Lesins (2004). Global warming and the Greenland ice sheet. *Climatic Change*, **63**:201–221.

Clarke, G. K. C. (1982). Glacier outburst floods from 'Hazard Lake' Yukon Territory, and the problem of flood magnitude prediction. *Journal of Glaciology*, **28**(98):3–21.

Clarke, G. K. C. (1987). Subglacial till: A physical framework for its properties and processes. *Journal of Geophysical Research*, **92**(B9):9023–9036.

Clarke, G. K. C. (1996). Lumped-element analysis of subglacial hydraulic circuits. *Journal of Geophysical Research*, **101**:17547–17559.

Clarke, G. K. C. (2003). Hydraulics of subglacial outburst floods: new insights from the Spring-Hutter formulation. *Journal of Glaciology*, **49**(165):299–314.

Clarke, T. S. and K. Echelmeyer (1996). Seismic-refection evidence for a deep subglacial trough beneath Jakobshavn Isbrae, West Greenland. *Journal of Glaciology*, **43**(141):219–232.

Clason, C., D. W. F. Mair, D. O. Burgess, and P. W. Nienow (2012). Modelling the delivery of supraglacial meltwater to the ice/bed interface: application to southwest Devon Ice Cap, Nunavut, Canada. *Journal of Glaciology*, **58**(208):361–374.

Colgan, W., H. Rajaram, R. Anderson, K. Steffen, T. Phillips, I. Joughin, H. J. Zwally, and W. Abdalati (2011). The annual glaciohydrology cycle in the ablation zone of the Greenland ice sheet: Part 1. Hydrology model. *Journal of Glaciology*. **57**(204):697–709.

Cook, S. J., R. I. Waller, and P. G. Knight (2006). Glaciohydraulic supercooling: the process and its significance. *Progress in Physical Geography*, **30**(5):577–588.

Cowton, T., P. Nienow, A. Sole, J. Wadham, G. Lis, I. Bartholomew, D. Mair, and D. Chandler (2013). Evolution of drainage system morphology at a land-terminating Greenlandic outlet glacier. *Journal of Geophysical Research: Earth Surface*, **118**:29–41.

Creyts, T. T. and C. G. Schoof (2009). Drainage through subglacial water sheets. *Journal of Geophysical Research: Earth Surface*, **114**(F4):F04008.

Cuffey, K. M. and W. S. B. Paterson (2010). *The Physics of Glaciers*. Academic Press.

Cutler, P. M. (1998). Modelling the evolution of subglacial tunnels due to varying water input. *Journal of Glaciology*, **44**(148):485–497.

Danielson, B. and M. Sharp (2013). Development and application of a time-lapse photograph analysis method to investigate the link between tidewater glacier flow variations and supraglacial lake drainage events. *Journal of Glaciology*, **59**(214):287–302.

Das, S. B., I. Joughin, M. D. Behn, I. M. Howat, M. A. King, D. Lizarralde, and M. P. Bhatia (2008). Fracture propagation to the base of the Greenland Ice Sheet during supraglacial lake drainage. *Science*, **320**(5877):778–781.

Dow, C. F., A. Hubbard, A. D. Booth, S. H. Doyle, A. Gusmeroli, and B. Kulessa (2013). Seismic evidence of mechanically-weak sediments underlying Russell Glacier, West Greenland. *Annals of Glaciology*, **54**(64):135–141.

Dow, C. F., J. Kavanaugh, J. W. Sanders, K. M. Cuffey, and K. R. MacGregor (2011). Subsurface hydrology of an overdeepened cirque glacier. *Journal of Glaciology*, **57**(206):1067–1078.

Doyle, S. H., A. L. Hubbard, C. F. Dow, G. A. Jones, A. Fitzpatrick, A. Gusmeroli, B. Kulessa, K. Lindback, R. Pettersson, and J. E. Box (2013). Ice tectonic deformation during the rapid in situ drainage of a supraglacial lake on the Greenland Ice Sheet. *The Cryosphere*, **7**(1):129–140. doi:10.5194/tc-7-129-2013.

Engelhardt, H. and B. Kamb (1997). Basal hydraulic system of a West Antarctic ice stream: constraints from borehole observations. *Journal of Glaciology*, **43**(144):207–230.

Evatt, G. W., A. C. Fowler, C. D. Clark, and N. R. J. Hulton (2006). Subglacial floods beneath ice sheets. *Philosophical Transactions of the Royal Society A: Mathematical, Physical and Engineering Sciences*, **364**(1844):1769–1794.

Fischer, U. H. and G. K. C. Clarke (2001). Review of subglacial hydro-mechanical coupling: Trapridge Glacier, Yukon Territory, Canada. *Quaternary International*, **86**(1):29–43.

Fischer, U. H., P. R. Porter, T. Schuler, A. J. Evans, and G. H. Gudmundsson (2001). Hydraulic and mechanical properties of glacial sediments beneath Unteraargletscher, Switzerland: implications for glacier basal motion. *Hydrological Processes*, **15**(18):3525–3540.

Fitzpatrick, A., A. Hubbard, J. Box, D. Quincey, D. van As, A. Mikkelsen, S. Doyle, C. Dow, B. Hasholt, and G. Jones (2014). A decade (2002–2012) of supraglacial lake volume estimates across russell glacier, west greenland. *The Cryosphere*, **8**(1):107–121.

Fitzpatrick, A. A., A. Hubbard, I. Joughin, D. J. Quincey, D. Van As, A. P. Mikkelsen, S. H. Doyle, B. Hasholt, and G. A. Jones (2013). Ice flow dynamics and surface meltwater flux at a land-terminating sector of the Greenland ice sheet. *Journal of Glaciology*, **59**(216):687–696.

Flowers, G. E. (2000). A multicomponent coupled model of glacier hydrology. *Ph.D.thesis (unpublished)*, **University of British Columbia, Canada**.

Flowers, G. E. (2008). Subglacial modulation of the hydrograph from glacierized basins. *Hydrological Processes*, **22**(19):3903–3918.

Flowers, G. E., H. Björnsson, and F. Pálsson (2003). New insights into the subglacial and periglacial hydrology of Vatnajökull, Iceland, from a distributed physical model. *Journal of Glaciology*, **49**(165):257–270.

Flowers, G. E., H. Björnsson, F. Pálsson, and G. K. C. Clarke (2004). A coupled sheet-conduit mechanism for jökulhlaup propagation. *Geophysical Research Letters*, **31**(LO5401):doi:10.1029/2003GL019088.

Flowers, G. E. and G. K. Clarke (2000). An integrated modelling approach to understanding subglacial hydraulic release events. *Annals of Glaciology*, **31**(1):222–228.

Flowers, G. E. and G. K. C. Clarke (2002). A multicomponent coupled model of glacier hydrology: 1. Theory and synthetic examples. *Journal of Geophysical Research*, **107**(B11):2287, doi:10.1029/2001JB001122.

Fountain, A. G. and J. S. Walder (1998). Water flow through temperate glaciers. *Reviews of Geophysics*, **36**(3):299–328.

Fowler, A. C. (2009). Dynamics of subglacial floods. *Proceedings of the Royal Society A: Mathematical, Physical and Engineering Science*, **465**(2106):1809–1828.

Gercek, H. (2007). Poisson's ratio values for rocks. *International Journal of Rock Mechanics and Mining Sciences*, **44**(1):1–13.

Glen, J. W. (1954). The stability of ice-dammed lakes and other water-filled holes in glaciers. *Journal of Glaciology*, **2**(15):316–18.

Greuell, W. and J. Oerlemans (2005). Assessment of the surface mass balance along the K-transect (Greenland ice sheet) from satellite-derived albedos. *Annals of Glaciology*, **42**(1):107–117.

Gulley, J. and D. I. Benn (2007). Structural control of englacial drainage systems in Himalayan debris-covered glaciers. *Journal of Glaciology*, **53**(182):399–412.

Gulley, J. D., D. I. Benn, E. Screaton, and J. Martin (2009). Mechanisms of englacial conduit formation and their implications for subglacial recharge. *Quaternary Science Reviews*, **28**(19-20):1984–1999.

Gulley, J. D., P. Walthard, J. Martin, A. F. Banwell, D. I. Benn, and G. Catania (2012). Conduit roughness and dye-trace breakthrough curves: why slow velocity and high dispersivity may not reflect flow in distributed systems. *Journal of Glaciology*, **58**(211):915–925.

Hanna, E., J. Cappelen, X. Fettweis, P. Huybrechts, A. Luckman, and M. H. Ribergaard (2009). Hydrologic response of the Greenland ice sheet: the role of oceanographic warming. *Hydrological Processes*, **23**(1):7–30.

Harper, J. T., N. F. Humphrey, W. T. Pfeffer, T. Fudge, and S. O'Neel (2005). Evolution of subglacial water pressure along a glacier's length. *Annals of Glaciology*, **40**(1):31–36.

Hewitt, I. J. (2011). Modelling distributed and channelized subglacial drainage: the spacing of channels. *Journal of Glaciology*, **57**(202):302–314.

Hewitt, I. J. (2013). Seasonal changes in ice sheet motion due to melt water lubrication. *Earth and Planetary Science Letters*, **371**:16–25.

Hewitt, I. J., C. Schoof, and M. A. Werder (2012). Flotation and free surface flow in a model for subglacial drainage. Part 2. Channel flow. *Journal of Fluid Mechanics*, **1**(1):1–31.

Hoffman, M. J., G. A. Catania, T. A. Neumann, L. C. Andrews, and J. A. Rumrill (2011). Links between acceleration, melting, and supraglacial lake drainage of the western Greenland Ice Sheet. *Journal of Geophysical Research*, **116**(F4):F04035.

Holland, C. W. and S. Anandakrishnan (2009). Subglacial seismic reflection strategies when source amplitude and medium attenuation are poorly known. *Journal of Glaciology*, **55**(193):931–937.

Holland, D. M., R. H. Thomas, B. de Young, M. H. Ribergaard, and B. Lyberth (2008). Acceleration of Jakobshavn Isbrae triggered by warm subsurface ocean waters. *Nature Geoscience*, **1**(10):659–664.

Hooke, R. L. (1989). Englacial and subglacial hydrology: A qualitative review. *Arctic and Alpine Research*, **21**(3):221–233.

Hooke, R. L., T. Laumann, and J. Kohler (1990). Subglacial water pressures and the shape of subglacial conduits. *Journal of Glaciology*, **36**(122):67–71.

Hooke, R. L. B., B. Wold, and J. O. Hagen (1985). Subglacial hydrology and sediment transport at Bondhusbreen, southwest Norway. *Geological Society of America Bulletin*, **96**(3):388–397.

Howat, I. M., J. E. Box, Y. Ahn, A. Herrington, and E. M. McFadden (2010). Seasonal variability in the dynamics of marine-terminating outlet glaciers in Greenland. *Journal of Glaciology*, **56**(198):601–613.

Howat, I. M., I. Joughin, and T. A. Scambos (2007). Rapid changes in ice discharge from Greenland outlet glaciers. *Science*, **315**(5818):1559–1561.

Howat, I. M., S. de la Peña, J. H. van Angelen, J. T. M. Lenaerts, and M. R. van den Broeke (2013). Brief communication "expansion of meltwater lakes on the greenland ice sheet". *The Cryosphere*, **7**(1):201–204. doi:10.5194/tc-7-201-2013.

Hubbard, B. P., M. J. Sharp, I. C. Willis, M. K. Nielsen, and C. C. Smart (1995). Borehole water-level variations and the structure of the subglacial hydrological system of Haut Glacier d'Arolla, Valais, Switzerland. *Journal of Glaciology*, **41**(139):572–583.

Iken, A. (1981). The effect of the subglacial water pressure on the sliding velocity of a glacier in an idealized numerical model. *Journal of Glaciology*, **27**(97):407–421.

Iken, A. and R. A. Bindschadler (1986). Combined measurements of subglacial water pressure and surface velocity of Findelengletscher, Switzerland: conclusions about drainage system and sliding mechanism. *Journal of Glaciology*, **32**(110):101–119.

Iken, A., K. Fabri, and M. Funk (1996). Water storage and subglacial drainage conditions inferred from borehole measurements on Gornergletscher, Valais, Switzerland. *Journal of Glaciology*, **42**(141):233–248.

Iken, A., H. Röthlisberger, A. Flotron, and W. Haeberli (1983). The uplift of Unteraargletscher at the beginning of the melt season - A consequence of water storage at the bed? *Journal of Glaciology*, **29**(101):28–47.

IPCC (2007). Climate change 2007: Synthesis report. *Based on Working Group contributions to the Fourth Assessment Report.*

Iverson, N. R. (2010). Shear resistance and continuity of subglacial till: hydrology rules. *Journal of Glaciology*, **56**(200):1104–1114.

Iverson, N. R., R. W. Baker, R. L. Hooke, B. Hanson, and P. Jansson (1999). Coupling between a glacier and a soft bed: I. A relation between effective pressure and local shear stress determined from till elasticity. *Journal of Glaciology*, **45**(149):31–40.

Iverson, N. R., B. Hanson, R. L. Hooke, and P. Jansson (1995). Flow mechanism of glaciers on soft beds. *Science*, **267**(5194):80–81.

Iverson, N. R., P. Jansson, and R. L. Hooke (1994). In-situ measurement of the strength of deforming subglacial till. *Journal of Glaciology*, **40**(136):497-503.

Johannesson, T. (2002). Propagation of a subglacial flood wave during the initiation of a jökulhlaup. *Hydrological sciences journal*, **47**(3):417–434.

Johansson, A. M., P. Jansson, and I. A. Brown (2012). Spatial and temporal variations in lakes on the Greenland Ice Sheet. *Journal of Hydrology*, **476**:314–320.

Jones, G. A., B. Kulessa, S. H. Doyle, C. F. Dow, and A. Hubbard (2013). An automated approach to the location of icequakes using seismic waveform amplitudes. *Annals of Glaciology*, **54**(64):1–9.

Joughin, I., S. B. Das, G. Flowers, M. D. Behn, R. B. Alley, M. A. King, B. Smith, J. Bamber, M. R. Van den Broeke, and J. Van Angelen (2013). Influence of ice-sheet geometry and supraglacial lakes on seasonal ice-flow variability. *Cryosphere*, **7**(4).

Joughin, I., S. B. Das, M. A. King, B. E. Smith, I. M. Howat, and T. Moon (2008a). Seasonal speedup along the western flank of the Greenland Ice Sheet. *Science*, **320**(5877):781–783.

Joughin, I., I. Howat, R. B. Alley, G. Ekstrom, M. Fahnestock, T. Moon, M. Nettles, M. Truffer, and V. Tsai (2008b). Ice-front variation and tidewater behavior on Helheim and Kangerdlugssuaq Glaciers, Greenland. *Journal of Geophysical Research*, **113**(F01004):doi:10.1029/2007JF000837.

Kamb, B. (1987). Glacier surge mechanism based on linked cavity configuration of the basal water conduit system. *Journal of Geophysical Research*, **92**(B9):9083–9100.

Kearey, P. and M. Brooks (1984). *An Introduction to Geophysical Exploration.* Blackwell Scientific Publications, Oxford, U.K.

King, E. C., A. M. Smith, T. Murray, and G. W. Stuart (2008). Glacier-bed characteristics of midtre Lovenbreen, Svalbard, from high-resolution seismic and radar surveying. *Journal of Glaciology*, **54**(184):145–156.

King, E. C., J. Woodward, and A. M. Smith (2004). Seismic evidence for a water-filled canal in deforming till beneath Rutford Ice Stream, West Antarctica. *Geophysical Research Letters*, **31**(20):L20401, doi:10.1029/2004GL020379.

Kohnen, H. (1969). Über die absorption elastischer longitudinaler wellen im eis. *Polarforschung*, **39**(1):269–275.

Krawczynski, M. J., M. D. Behn, S. B. Das, and I. Joughin (2009). Constraints on the lake volume required for hydro-fracture through ice sheets. *Geophysical Research Letters*, **36**(L10501):doi:10.1029/2008GL036765.

Kulessa, B., B. Hubbard, and G. H. Brown (2003). Cross-coupled flow modeling of coincident streaming and electrochemical potentials and application to subglacial self-potential data. *Journal of Geophysical Research-Solid Earth*, **108**(B8):2381.

Lampkin, D. J. and J. Vanderberg (2011). A preliminary investigation of the influence of basal and surface topography on supraglacial lake distribution near Jakobshavn Isbrae, western Greenland. *Hydrological Processes*, **25**(21):3347–3355.

Lappegard, G. and J. Kohler (2005). Determination of basal hydraulic systems based on subglacial high-pressure pump experiments. *Annals of Glaciology*, **40**(1):37–42.

Leeson, A. A., A. Shepherd, S. Palmer, A. Sundal, and X. Fettweis (2013). Simulating the growth of supraglacial lakes at the western margin of the Greenland ice sheet. *The Cryosphere*, **6**:1077–1086.

Liang, Y.-L., W. Colgan, Q. Lv, K. Steffen, W. Abdalati, J. Stroeve, D. Gallaher, and N. Bayou (2012). A decadal investigation of supraglacial lakes in West Greenland using a fully automatic detection and tracking algorithm. *Remote Sensing of Environment*, **123**:127–138.

Lliboutry, L. (1964). Sub-glacial 'supercavitation' as a cause of the rapid advances of glaciers. *Nature*, **202**(4927):77.

Lliboutry, L. (1968). General theory of subglacial cavitation and sliding of temperature glaciers. *Journal of Glaciology*, **7**(49):21–58.

Lliboutry, L. (1983). Modifications to the theory of intraglacial waterways for the case of subglacial ones. *Journal of Glaciology*, **29**(102):216–226.

Luthje, M., L. T. Pedersen, N. Reeh, and W. Greuell (2006). Modelling the evolution of supraglacial lakes on the West Greenland ice-sheet margin. *Journal of Glaciology*, **52**(179):608–618.

Magnússon, E., H. Björnsson, H. Rott, and F. Pálsson (2010). Reduced glacier sliding caused by persistent drainage from a subglacial lake. *Cryosphere*, **4**(1):13–20.

Mair, D., P. Nienow, M. Sharp, T. Wohlleben, and I. Willis (2002). Influence of subglacial drainage system evolution on glacier surface motion: Haut Glacier d'Arolla, Switzerland. *Journal of Geophysical Research*, **107**(B8):2175, 10.1029/2001JB000514.

Margrave, G. F. (2013). Consortium for research in elastic wave exploration seismology (CREWES) matlab library.

Maule, C. F., M. E. Purucker, and N. Olsen (2009). Inferring magnetic crustal thickness and geothermal heat flux from crustal magnetic field models. Danish climate centre report, Danish Meterorological Institute.

McGrath, D., K. Steffen, I. Overeem, S. H. Mernild, B. Hasholt, and M. van den Broeke (2010). Sediment plumes as a proxy for local ice-sheet runoff in Kangerlussuaq Fjord, West Greenland. *Journal of Glaciology*, **56**(199):813–821.

McMillan, M., P. Nienow, A. Shepherd, T. Benham, and A. Sole (2007). Seasonal evolution of supra-glacial lakes on the Greenland Ice Sheet. *Earth and Planetary Science Letters*, **262**:484–492.

Meierbachtol, T., J. Harper, and N. Humphrey (2013). Basal drainage system response to increasing surface melt on the Greenland Ice Sheet. *Science*, **341**(6147):777–779.

Moon, T. and I. Joughin (2008). Changes in ice front position on Greenland's outlet glaciers from 1992 to 2007. *Journal of Geophysical Research*, **113**(F02022):doi:10.1029/2007JF000927.

Motyka, R. J., W. P. Dryer, J. Amundson, M. Truffer, and M. Fahnestock (2013). Rapid submarine melting driven by subglacial discharge, LeConte Glacier, Alaska. *Geophysical Research Letters*, **40**:5153–5158.

Murray, T. and G. K. C. Clarke (1995). Black-box modeling of the subglacial water system. *Journal of Geophysical Research*, **100**(B7):10231–10245.

Ng, F. and H. Björnsson (2003). On the Clague-Mathews relation for jökulhlaups. *Journal of Glaciology*, **49**(165):161–172.

Ng, F. S. L. (2000a). Canals under sediment-based ice sheets. *Annals of Glaciology*, **30**(1):146–152.

Ng, F. S. L. (2000b). Coupled ice-till deformation near subglacial channels and cavities. *Journal of Glaciology*, **46**(155):580–598.

Nienow, P., M. Sharp, and I. Willis (1998). Seasonal changes in the morphology of the subglacial drainage system, Haut Glacier d'Arolla, Switzerland. *Earth Surface Processes and Landforms*, **23**(9):825–843.

Nolan, M. and K. Echelmeyer (1999a). Seismic detection of transient changes beneath Black Rapids Glacier, Alaska, USA: I. Techniques and observations. *Journal of Glaciology*, **45**(149):119–131.

Nolan, M. and K. Echelmeyer (1999b). Seismic detection of transient changes beneath Black Rapids Glacier, Alaska, USA: II. Basal morphology and processes. *Journal of Glaciology*, **45**(149):132–146.

Nye, J. F. (1953). The flow law of ice from measurements in glacier tunnels, laboratory experiments and the Jungfraufirn borehole experiment. *Proceedings of the Royal Society of London. Series A. Mathematical and Physical Sciences*, **219**(1139):477–489.

Nye, J. F. (1973). Water at the bed of a Glacier. In *Proceedings of Symposium on the Hydrology of Glaciers, Cambridge, 7-13 September 1969*, volume 95. International Association of Scientific Hydrology Publications, pages 189–194.

Nye, J. F. (1976). Water flow in glaciers: jökulhlaups, tunnels and veins. *Journal of Glaciology*, **17**(76):181–207.

Oerlemans, J. (2008). *Minimal glacier models.* Igitur, Utrecht Publishing & Archiving Services.

Palmer, S., A. Shepherd, P. Nienow, and I. Joughin (2011). Seasonal speedup of the Greenland Ice Sheet linked to routing of surface water. *Earth and Planetary Science Letters*, **302**(3):423–428.

Parasnis, D. S. (1975). *Principles of Applied Geophysics.* Chapman and Hall, London, U.K.

Paterson, W. S. B. (1994). *The Physics of Glaciers 3rd Edition.* Oxford, U.K.: Pergamon Press.

Pattyn, F., S. D. Brabander, and A. Huyghe (2005). Basal and thermal control mechanisms of the Ragnhild glaciers, East Antarctica. *Annals of Glaciology*, **40**(1):225–231.

Pattyn, F., C. Delcourt, D. Samyn, B. de Smedt, and M. Nolan (2009). Bed properties and hydrological conditions underneath McCall Glacier, Alaska, USA. *Annals of Glaciology*, **50**(51):80–84.

Peters, L. E., S. Anandakrishnan, R. B. Alley, and A. M. Smith (2007). Extensive storage of basal meltwater in the onset region of a major West Antarctic ice stream. *Geology*, **35**(3):251–254.

Peters, L. E., S. Anandakrishnan, C. W. Holland, H. J. Horgan, D. D. Blankenship, and D. E. Voigt (2008). Seismic detection of a subglacial lake near the South Pole, Antarctica. *Geophysical Research Letters*, **35**(23):L23501.

Pimentel, S. and G. E. Flowers (2011). A numerical study of hydrologically driven glacier dynamics and subglacial flooding. *Proceedings of the Royal Society A: Mathematical, Physical and Engineering Science*, **467**(2126):537–558.

Piotrowski, J. A., N. K. Larsen, and F. W. Junge (2004). Reflections on soft subglacial beds as a mosaic of deforming and stable spots. *Quaternary Science Reviews*, **23**(9):993–1000.

Price, S. F., A. J. Payne, G. A. Catania, and T. A. Neumann (2008). Seasonal acceleration of inland ice via longitudinal coupling to marginal ice. *Journal of Glaciology*, **54**(185):213–219.

Reeh, N., E. L. Christensen, C. Mayer, and O. B. Olesen (2003). Tidal bending of glaciers: a linear viscoelastic approach. *Annals of Glaciology*, **37**(1):83–89.

Rempel, A. W. (2009a). Effective stress profiles and seepage flows beneath glaciers and ice sheets. *Journal of Glaciology*, **55**(191):431–443.

Rempel, A. W. (2009b). Transient effective stress variations forced by changes in conduit pressure beneath glaciers and ice sheets. *Annals of Glaciology*, **50**(52):61–66.

Richards, K., M. Sharp, N. Arnold, A. Gurnell, M. Clark, M. Tranter, P. Nienow, G. Brown, I. Willis, and W. Lawson (1996). An integrated approach to modelling hydrology and water quality in glacierized catchments. *Hydrological Processes*, **10**(4):479–508.

Rignot, E. and P. Kanagaratnam (2006). Changes in the velocity structure of the Greenland Ice Sheet. *Science*, **311**(5763):986–990.

Roberts, M. J. (2005). Jökulhlaups: a reassessment of floodwater flow through glaciers. *Review of Geophysics*, **43**:1–21.

Roberts, M. J., A. J. Russell, F. S. Tweed, and O. Knudsen (2000). Ice fracturing during jökulhlaups: implications for englacial floodwater routing and outlet development. *Earth Surface Processes and Landforms*, **25**(13):1429–1446.

Röthlisberger, H. (1972). Water pressure in intra-and subglacial channels. *Journal of Glaciology*, **11**(62):177–203.

Röthlisberger, H. and H. Lang (1987). *Glacial Hydrology*, chapter Glacio-Fluvial Sediment Transfer: An Alpine Perspective. New York: John Wiley and Sons, pages 207–284.

Schoof, C. (2010). Ice-sheet acceleration driven by melt supply variability. *Nature*, **468**(7325):803–806.

Schoof, C., I. J. Hewitt, and M. A. Werder (2012). Flotation and free surface flow in a model for subglacial drainage. Part 1. Distributed drainage. *Journal of Fluid Mechanics*, **1**(1):1–31.

Schuler, T., U. H. Fischer, and G. H. Gudmundsson (2004). Diurnal variability of subglacial drainage conditions as revealed by tracer experiments. *Journal of Geophysical Research*, **109**(F02008):doi: 10.1029/2003JF000082.

Schuler, T. V. and U. H. Fischer (2009). Modeling the diurnal variation of tracer transit velocity through a subglacial channel. *Journal of Geophysical Research: Earth Surface*, **114**(F4).

Selmes, N., T. Murray, and T. D. James (2011). Fast draining lakes on the Greenland Ice Sheet. *Geophysical Research Letters*, **38**(15):L15501.

Sergienko, O. V. (2013). Glaciological twins: basally controlled subglacial and supraglacial lakes. *Journal of Glaciology*, **59**(213):3–8.

Shepherd, A., A. Hubbard, P. Nienow, M. King, M. McMillan, and I. Joughin (2009). Greenland ice sheet motion coupled with daily melting in late summer. *Geophysical Research Letters*, **36**(L01501):doi:10.1029/2008GL035758.

Shepherd, A. and D. Wingham (2007). Recent sea-level contributions of the Antarctic and Greenland ice sheets. *Science*, **315**(5818):1529–1532.

Sheriff, R. E. and L. P. Geldart (1983). *Exploration seismology. Volume 1: History, theory, and data acquisition.* Cambridge University Press, New York, NY.

Shoemaker, E. (1987). Pressure and temperature effects in Röthlisberger channels. *Cold Regions Science and Technology*, **14**(2):121–127.

Shoemaker, E. M. (1986). Subglacial hydrology for an ice sheet resting on a deformable aquifer. *Journal of Glaciology*, **32**(110):20–30.

Shreve, R. L. (1972). Movement of water in glaciers. *Journal Of Glaciology*, **11**(62):205–214.

Smeets, C., W. Boot, A. Hubbard, R. Pettersson, F. Willhelms, M. R. V. den Broeke, and R. S. W. V. de Wal (2012). Instruments and methods: A wireless subglacial probe for deep ice applications. *Journal of Glaciology*, **58**(211):841–848.

Smith, A. M. (1997). Variations in basal conditions on Rutford Ice Stream, West Antarctica. *Journal of Glaciology*, **43**(144):245–255.

Smith, A. M. (2007). Subglacial bed properties from normal-incidence seismic reflection data. *Journal of Environmental & Engineering Geophysics*, **12**(1):3–13.

Sole, A., P. Nienow, I. Bartholomew, D. Mair, T. Cowton, A. Tedstone, and M. A. King (2013). Winter motion mediates dynamic response of the Greenland Ice Sheet to warmer summers. *Geophysical Research Letters*, **40**(15):3940–3944.

Sole, A. J., D. W. F. Mair, P. W. Nienow, I. D. Bartholomew, M. A. King, M. J. Burke, and I. Joughin (2011). Seasonal speedup of a Greenland marine-terminating outlet glacier forced by surface melt–induced changes in subglacial hydrology. *Journal of Geophysical Research: Earth Surface*, **116**(F3):F03014.

Spring, U. and K. Hutter (1981). Numerical studies of jökulhlaups. *Cold Regions Science and Technology*, 4(3):227–244.

Spring, U. and K. Hutter (1982). Conduit flow of a fluid through its solid phase and its application to intraglacial channel flow. *International Journal of Engineering Science*, **20**(2):327–363.

Stenborg, T. (1973). Some viewpoints on the internal drainage of glaciers. In *Proceedings of Symposium on the Hydrology of Glaciers, Cambridge, 7-13 September 1969*, volume 95. International Association of Scientific Hydrology Publications, pages 117–129.

Stone, D. B., G. K. Clarke, and R. G. Ellis (1997). Inversion of borehole-response test data for estimation of subglacial hydraulic properties. *Journal of Glaciology*, **43**(143):103–113.

Sturm, M. and C. S. Benson (1985). A history of jökulhlaups from Strandline Lake, Alaska, USA. *Journal of Glaciology*, **31**(109):272–280.

Sugiyama, S., A. Bauder, M. Huss, P. Riesen, and M. Funk (2008). Triggering and drainage mechanisms of the 2004 glacier-dammed lake outburst in Gornergletscher, Switzerland. *Journal of Geophysical Research: Earth Surface*, **113**(F4):F04019.

Sugiyama, S., A. Bauder, P. Weiss, and M. Funk (2007). Reversal of ice motion during the outburst of a glacier-dammed lake on Gornergletscher, Switzerland. *Journal of Glaciology*, **53**(181):172–180.

Sundal, A. V., A. Shepherd, P. Nienow, E. Hanna, S. Palmer, and P. Huybrechts (2009). Evolution of supra-glacial lakes across the Greenland Ice Sheet. *Remote Sensing of Environment*, **113**(10):2164–2171.

Sundal, A. V., A. Shepherd, P. Nienow, E. Hanna, S. Palmer, and P. Huybrechts (2011). Melt-induced speed-up of Greenland ice sheet offset by efficient subglacial drainage. *Nature*, **469**(7331):521–524.

Tedesco, M., I. C. Willis, M. J. Hoffman, A. F. Banwell, P. Alexander, and N. S. Arnold (2013). Ice dynamic response to two modes of surface lake drainage on the Greenland ice sheet. *Environmental Research Letters*, **8**(3):034007.

Thomas, R. H., W. Abdalati, E. Frederick, W. B. Krabill, S. Manizade, and K. Steffen (2003). Investigation of surface melting and dynamic thinning on Jakobshavn Isbrae, Greenland. *Journal of Glaciology*, **49**(165):231–239.

Tsai, V. C. and J. R. Rice (2010). A model for turbulent hydraulic fracture and application to crack propagation at glacier beds. *Journal of Geophysical Research*, **115**(F3):F03007.

Tsai, V. C. and J. R. Rice (2012). Modeling turbulent hydraulic fracture near a free surface. *Journal of Applied Mechanics*, **79**(3):031003.

Tsai, V. C., J. R. Rice, and M. Fahnestock (2008). Possible mechanisms for glacial earthquakes. *Journal of Geophysical Research*, **113**(F03014):doi: 10.1029/2007JF000944.

Tsang, G. and T. O. Hanley (1985). Frazil formation in water of different salinities and supercoolings. *Journal of Glaciology*, **31**(108):74–85.

Tulaczyk, S., W. B. Kamb, and H. F. Engelhardt (2000). Basal mechanics of Ice Stream B, West Antarctica. I- Till mechanics. *Journal of Geophysical Research*, **105**:463–481.

Tweed, F. S. and A. J. Russell (1999). Controls on the formation and sudden drainage of glacier-impounded lakes: implications for jökulhlaup characteristics. *Progress in Physical Geography*, **23**(1):79–110.

Vaughan, D. G. (1995). Tidal flexure at ice shelf margins. *Journal of Geophysical Research: Solid Earth*, **100**(B4):6213–6224.

Vaughan, D. G., A. M. Smith, P. C. Nath, and E. L. Meur (2003). Acoustic impedance and basal shear stress beneath four Antarctic ice streams. *Annals of Glaciology*, **36**(1):225–232.

van der Veen, C. J. (1998). Fracture mechanics approach to penetration of surface crevasses on glaciers. *Cold Regions Science and Technology*, **27**(1):31–47.

van der Veen, C. J. (2007). Fracture propagation as means of rapidly transferring surface meltwater to the base of glaciers. *Geophysical Research Letters*, **34**:L01501.

Vivian, R. (1980). The nature of the ice rock interface: the results of investigation on 20000 m^2 of the rock bed of temperate glaciers. *Journal of Glaciology*, **25**(92):267–277.

Wadham, J. L., A. J. Hodson, M. Tranter, and J. A. Dowdeswell (1998). The hydrochemistry of meltwaters draining a polythermal-based, high Arctic glacier, south Svalbard: I. The ablation season. *Hydrological Processes*, **12**(12):1825–1849.

van de Wal, R. S. W., W. Boot, M. R. van den Broeke, C. Smeets, C. H. Reijmer, J. J. A. Donker, and J. Oerlemans (2008). Large and rapid melt-induced velocity changes in the ablation zone of the Greenland Ice Sheet. *Science*, **321**(5885):111–113.

van de Wal, R. S. W., W. Greuell, M. R. van den Broeke, C. H. Reijmer, and J. Oerlemans (2005). Surface mass-balance observations and automatic weather station data along a transect near Kangerlussuaq, West Greenland. *Annals of Glaciology*, **42**(1):311–316.

Walder, J. S. (1982). Stability of sheet flow of water beneath temperate glaciers and implications for glacier surging. *Journal of Glaciology*, **28**(99):273–293.

Walder, J. S. (1986). Hydraulics of subglacial cavities. *Journal of Glaciology*, **32**(112):439–445.

Walder, J. S. and J. E. Costa (1996). Outburst floods from glacier-dammed lakes: The effect of mode of lake drainage on flood magnitude. *Earth Surface Processes and Landforms*, **21**(8):701–723.

Walder, J. S. and A. Fowler (1994). Channelized subglacial drainage over a deformable bed. *Journal of Glaciology*, **40**(134):3–15.

Walder, J. S., D. C. Trabant, M. Cunico, S. P. Anderson, R. S. Anderson, A. G. Fountain, and A. Malm (2005). Fault-dominated deformation in an ice dam during annual filling and drainage of a marginal lake. *Annals of Glaciology*, **40**(1):174–178.

Weertman, J. (1972). General theory of water flow at the base of a glacier or ice sheet. *Reviews of Geophysics and Space Physics*, **10**(1):287–333.

Weertman, J. (1973). Can a water-filled crevasse reach the bottom surface of a glacier? In *Proceedings of Symposium on the Hydrology of Glaciers, Cambridge, 7-13 September 1969*, volume 95. International Association of Scientific Hydrology Publications, pages 139–145.

Werder, M. A. and M. Funk (2009). Dye tracing a jökulhlaup: II. Testing a jökulhlaup model against flow speeds inferred from measurements. *Journal of Glaciology*, **55**(193):899–908.

Werder, M. A., A. Loye, and M. Funk (2009). Dye tracing a jökulhlaup: I. Subglacial water transit speed and water-storage mechanism. *Journal of Glaciology*, **55**(193):889–898.

Widess, M. B. (1973). How thin is a thin bed? *Geophysics*, **38**(6):1176–1180.

Xu, Y., E. Rignot, I. Fenty, D. Menemenlis, and M. Flexas (2013). Subaqueous melting of Store Glacier, west Greenland from three-dimensional, high-resolution numerical modeling and ocean observations. *Geophysical Research Letters*, **40**(17):4648–4653.

Xu, Y., E. Rignot, D. Menemenlis, and M. Koppes (2012). Numerical experiments on subaqueous melting of Greenland tidewater glaciers in response to ocean warming and enhanced subglacial discharge. *Annals of Glaciology*, **53**(60):229–234.

Yilmaz, Ö. and S. M. Doherty (2001). *Seismic data analysis: processing, inversion, and interpretation of seismic data*, volume 1. Society of exploration geophysicists.

Zwally, H. J., W. Abdalati, T. Herring, K. Larson, J. Saba, and K. Steffen (2002). Surface melt-induced acceleration of Greenland ice-sheet flow. *Science*, **297**(5579):218–222.

Appendix A

Steady-state model inputs

This appendix contains a table of the flowband background flux (Q^c) inputs for the steady-state (stage 1) spin-up runs for the coupled hydrological model sensitivity tests. In addition, the number of model days run to achieve steady state are included in the table data in italicised brackets. The reason that different background flux values were necessary was because the system configuration differed with each run and, in some cases, the flowband could not stabilise without larger influxes of water. For example, systems with a stronger pressure gradient like the marginal glacier set-up required greater water flux to achieve steady state. Similarly, larger initial channel sizes often required greater water flux to maintain pressure and prevent shrinkage in the steady-state.

Table A.1: *Steady-state model inputs with background flux, Q^c ($m^3\,s^{-1}$), non-italicised and the number of days for the steady-state run in italicised brackets.*

Geometry	$\frac{P_{ic}}{P_i}$	K (m s^{-1})			E (GPa)			h_c^{sh} (m)				n' (s m^{-3})			
		0.1	**0.5**	**1**	**3.9**	**6.2**	**8.9**	**0.05**	**0.15**	**0.3**	**0.4**	**0.01**	**0.032**	**0.7**	**0.1**
1 (FP)	1	10^{-4} *(50)*	10^{-3} *(30)*	10^{-3} *(30)*	10^{-3} *(30)*	10^{-3} *(30)*	10^{-3} *(30)*	10^{-3} *(30)*	10^{-3} *(30)*	10^{-3} *(30)*	10^{-3} *(30)*	10^{-3} *(30)*	10^{-3} *(30)*	10^{-3} *(30)*	10^{-3} *(30)*
	0.5	10^{-4} *(90)*	10^{-3} *(30)*	10^{-3} *(30)*	10^{-3} *(30)*	10^{-3} *(30)*	10^{-3} *(30)*	10^{-3} *(30)*	10^{-3} *(30)*	10^{-3} *(30)*	10^{-3} *(30)*	10^{-3} *(30)*	10^{-3} *(30)*	10^{-3} *(30)*	10^{-3} *(30)*
	0	0.3 *(130)*	1 *(50)*	1 *(50)*	1 *(150)*	1 *(50)*	1 *(50)*	0.1 *(130)*	1 *(50)*	1 *(70)*	1 *(70)*	1 *(50)*	1 *(50)*	1 *(50)*	1 *(50)*
2 (FR)	1	10^{-4} *(100)*	10^{-3} *(30)*	10^{-3} *(30)*	10^{-3} *(30)*	10^{-3} *(30)*	10^{-3} *(30)*	10^{-3} *(30)*	10^{-3} *(30)*	10^{-3} *(30)*	10^{-3} *(30)*	10^{-3} *(30)*	10^{-3} *(30)*	10^{-3} *(30)*	10^{-3} *(30)*
	0.8	10^{-4} *(120)*	10^{-3} *(30)*	10^{-3} *(30)*	10^{-3} *(30)*	10^{-3} *(30)*	10^{-3} *(30)*	10^{-3} *(30)*	10^{-3} *(30)*	10^{-3} *(30)*	10^{-3} *(30)*	10^{-3} *(30)*	10^{-3} *(30)*	10^{-3} *(30)*	10^{-3} *(30)*
	0.5	10^{-4} *(120)*	10^{-3} *(30)*	10^{-3} *(30)*	10^{-3} *(30)*	10^{-3} *(30)*	10^{-3} *(30)*	10^{-3} *(30)*	10^{-3} *(30)*	10^{-3} *(30)*	10^{-3} *(30)*	10^{-3} *(30)*	10^{-3} *(30)*	10^{-3} *(30)*	10^{-3} *(30)*
3 (TG)	1	10^{-4} *(90)*	0.1 *(30)*	0.1 *(30)*	0.1 *(30)*	0.1 *(30)*	0.1 *(30)*	0.1 *(30)*	0.1 *(30)*	0.1 *(30)*	0.1 *(30)*	0.1 *(30)*	0.1 *(30)*	0.1 *(30)*	0.1 *(30)*
	0.67	10^{-4} *(90)*	1 *(50)*	1 *(50)*	1 *(50)*	1 *(50)*	1 *(50)*	0.1 *(50)*	1 *(50)*	1 *(50)*	1 *(50)*	1 *(50)*	1 *(50)*	1 *(50)*	1 *(50)*
4 (MG)	0	0.2 *(130)*	1 *(50)*	1 *(50)*	1 *(50)*	1 *(50)*	1 *(50)*	0.1 *(120)*	1 *(50)*	1 *(50)*	1 *(50)*	1 *(50)*	1 *(50)*	1 *(50)*	1 *(50)*

Continued on next page

Table A.1: *Steady-state model inputs (continued)*

Geometry	$\frac{P_w}{P_i}$	k			$W(km)$				V_0 ($m^3 \times 10^7$)				S_ϵ (m^2)		
		0.01	**0.05**	**0.1**	**0.5**	**1**	**1.5**	**2**	**0.01**	**0.1**	**1**	**3.8**	**0.1**	**1**	**10**
1 (FP)	1	10^{-3} (30)	10^{-3} (30)	10^{-3} (30)	10^{-3} (30)	10^{-3} (30)	10^{-3} (30)	10^{-3} (30)	10^{-3} (30)	10^{-3} (30)	10^{-3} (30)	10^{-3} (30)	10^{-3} (30)	10^{-3} (30)	10^{-3} (30)
	0.5	10^{-3} (30)	10^{-3} (30)	10^{-3} (30)	10^{-3} (30)	10^{-3} (30)	10^{-3} (30)	10^{-3} (30)	10^{-3} (30)	10^{-3} (30)	10^{-3} (30)	10^{-3} (30)	10^{-3} (30)	0.1 (30)	10 (30)
	0	10^{-3} (50)	10^{-3} (50)	10^{-3} (50)	1 (50)	1 (50)	1 (50)	1 (50)	10^{-3} (50)	10^{-3} (50)	10^{-3} (50)	10^{-3} (50)	10^{-3} (50)	5 (50)	50 (50)
2 (FR)	1	10^{-3} (30)	10^{-3} (30)	10^{-3} (30)	- (30)	- (30)	- (30)	- (30)	- (30)	- (30)	- (30)	- (30)	10^{-3} (30)	0.1 (30)	1 (30)
	0.8	10^{-3} (30)	10^{-3} (30)	10^{-3} (30)	- (30)	- (30)	- (30)	- (30)	- (30)	- (30)	- (30)	- (30)	10^{-3} (30)	1 (30)	1 (30)
	0.5	10^{-3} (30)	10^{-3} (30)	10^{-3} (30)	- (30)	- (30)	- (30)	- (30)	- (30)	- (30)	- (30)	- (30)	10^{-3} (30)	10^{-3} (30)	1 (30)
3 (TG)	1	0.1 (30)	0.1 (30)	0.1 (30)	0.1 (30)	0.1 (30)	0.1 (30)	0.1 (30)	0.1 (30)	0.1 (30)	0.1 (30)	0.1 (30)	0.1 (30)	0.1 (30)	0.1 (30)
	0.67	1 (50)	1 (50)	1 (50)	1 (50)	1 (50)	1 (50)	0.1 (50)	1 (50)	1 (50)	1 (50)	1 (50)	1 (50)	1 (50)	1 (50)
4 (MG)	0	1 (50)	1 (50)	1 (50)	1 (50)	1 (50)	1 (50)	0.1 (50)	1 (50)	1 (50)	1 (50)	1 (50)	1 (50)	5 (50)	75 (50)

Appendix B

Baseline results example: F-Lake planar geometry

In this appendix, examples of outputs from stages 2–4 of the coupled hydrological model are provided. The data produced during the 288 sensitivity tests is too extensive to separately plot and therefore here, the F-Lake planar model baseline results for an outlet pressure of $0.5\,P_i$ are presented to illustrate typical model outputs.

Figure B.1 shows the blister model outputs (stage 2) with the F-Lake planar results plotted alongside the in-situ surface GPS and lake drainage data. The blister model curves can be seen to match well with the recorded data curves but do not have the same magnitude. Figure B.2 shows the development of the flowband domain during model linkage in stage 2 of the modelling process. The grey shaded areas illustrate where the domain has been overlapped by the blister. Figure B.3 shows outputs from stage 3 of the modelling process, where the blister disperses within the flowband domain until the water input grid-cell reaches overburden, suggesting full blister dispersal. Finally, Figure B.4 shows the flowband outputs for stage 4 of the modelling process where hydrological development is driven by surface water inputs. Diurnal variability can be clearly seen in the sheet discharge and water sheet thickness plots (Fig. B.4 a and c, respectively).

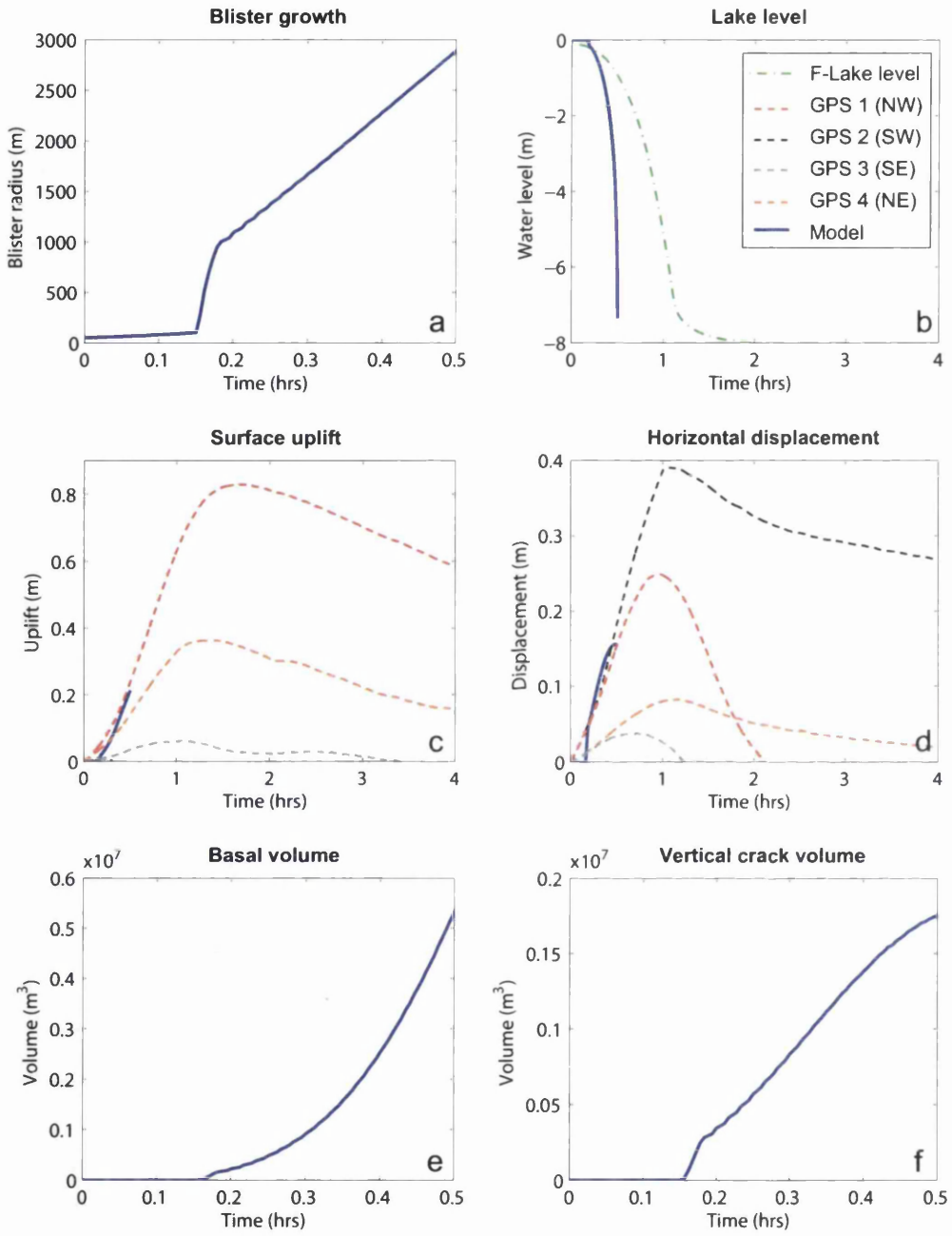

Figure B.1: *Blister model outputs for the baseline geometry 1 run with an outlet pressure at $0.5\,P_i$ (blue curves). Recorded F-Lake water level is shown by the green dashed line. Surface GPS records are shown by the dashed red (GPS 1), black (GPS 2), grey (GPS 3) and orange curves (GPS 4).*

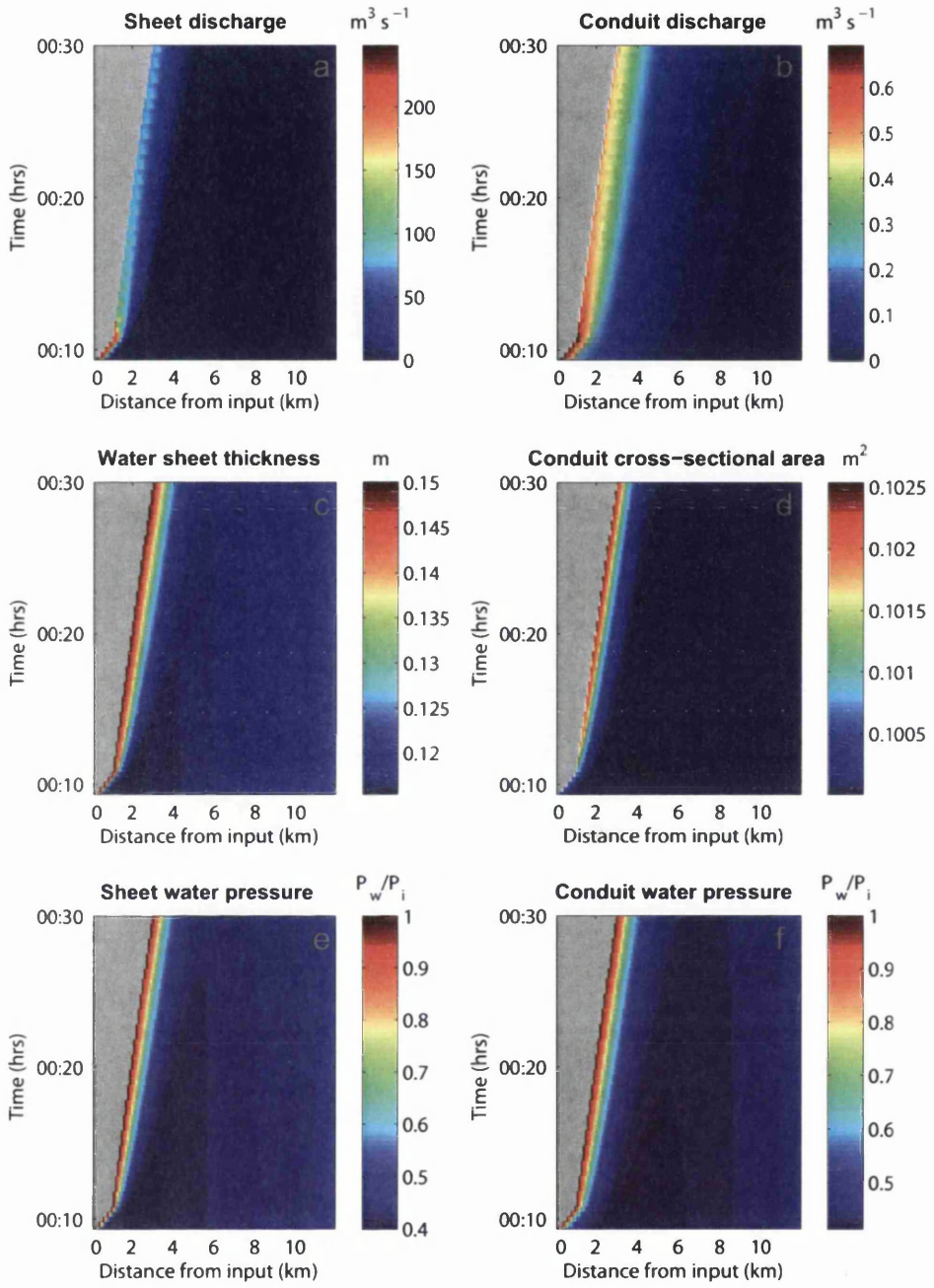

Figure B.2: *Distance-time plots of the primary variables from the flowband model during linkage. These examples are from a geometry 1 baseline run with an outlet pressure of $0.5P_i$. Blister overlap is shown in grey. Note that the start time of flowband hydrological development is from initiation of lake drainage and therefore includes blister growth prior to model linkage.*

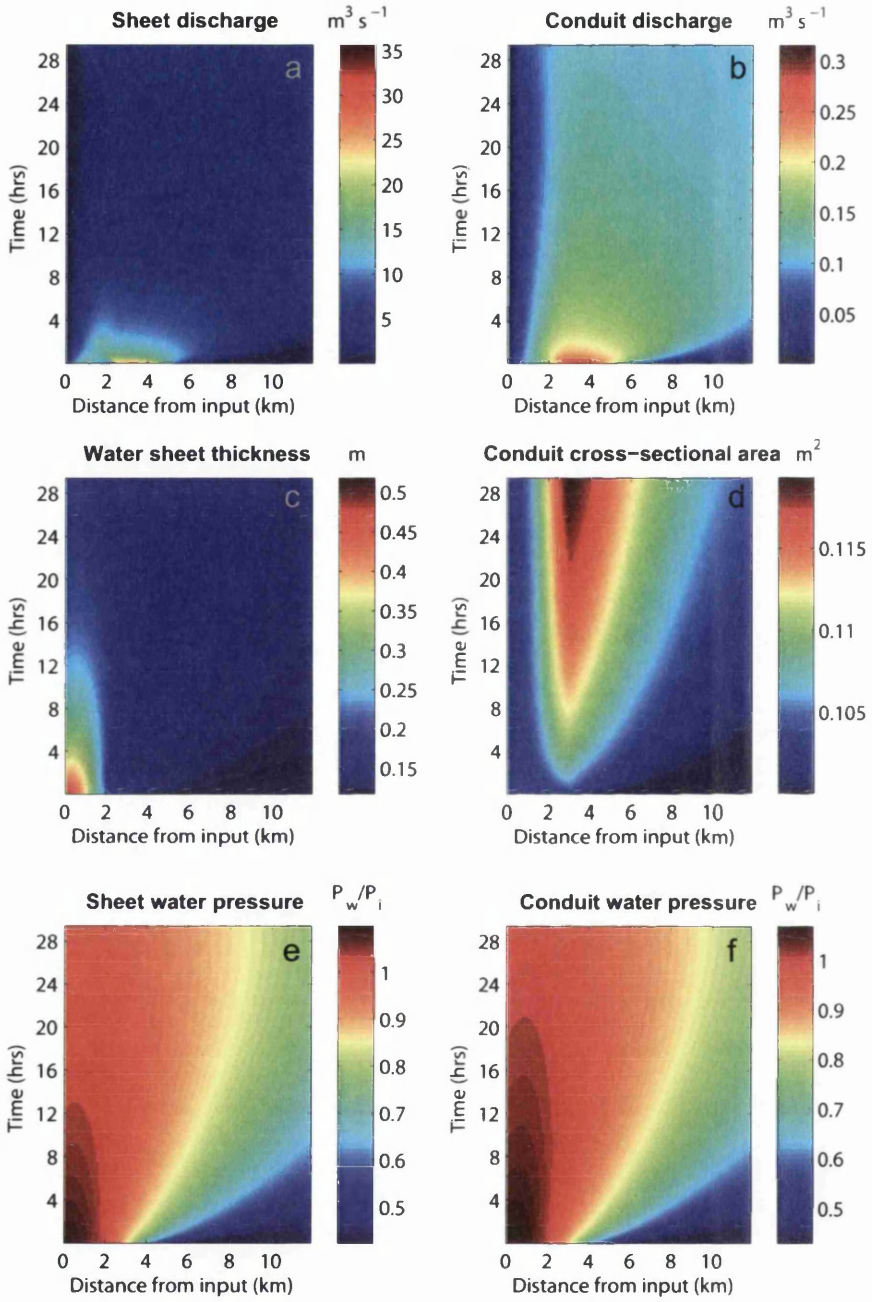

Figure B.3: *Distance-time flowband diagrams for stage 3 of the coupled model. These examples are from a geometry 1 baseline run with an outlet pressure of $0.5P_i$. The y-axes show time since lake drainage initiated. These stage 3 outputs cease at ~29 hours as the water input (at 0 km) has reached overburden pressure, implying the blister has dispersed.*

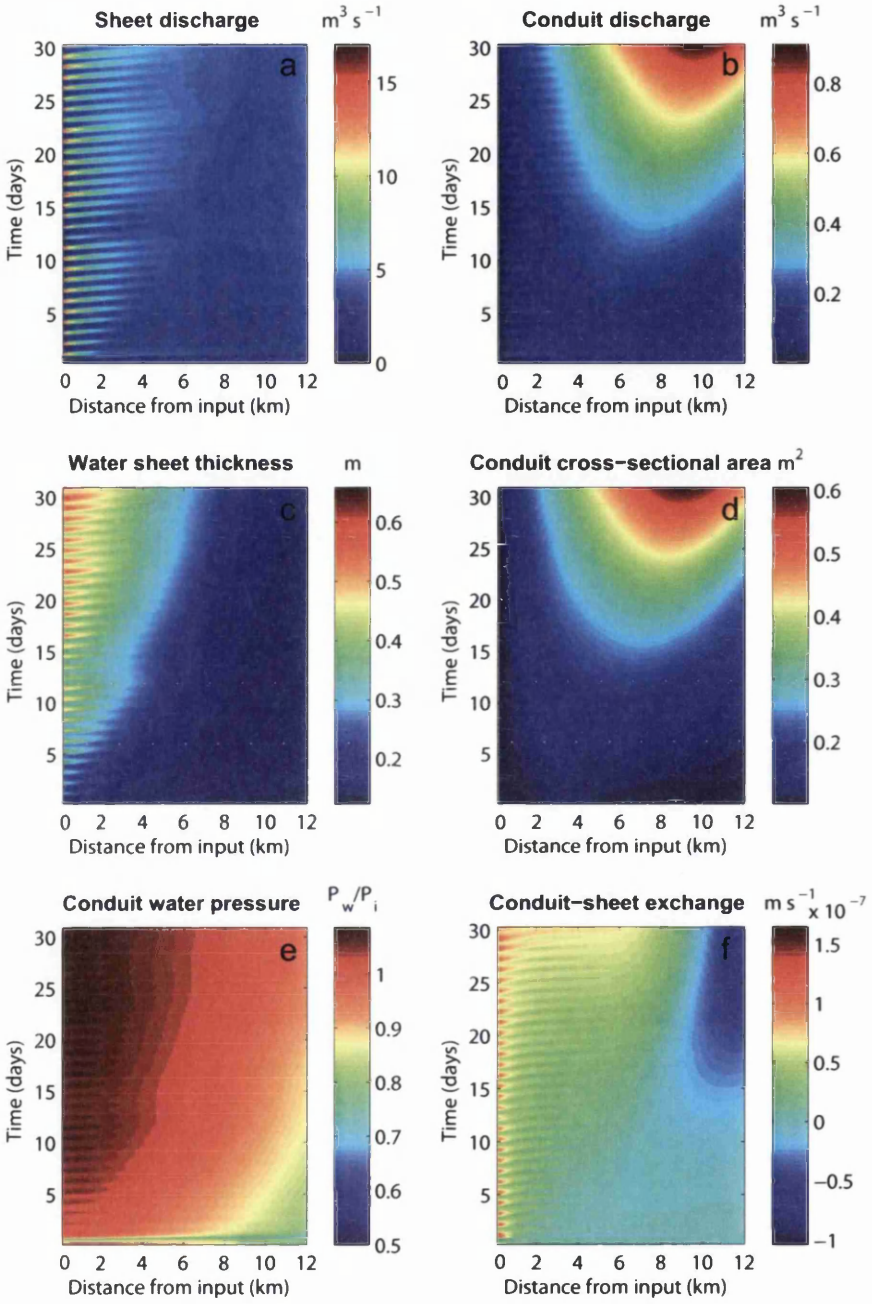

Figure B.4: *Stage 4 distance-time flowband plots for key variables. These outputs are for the baseline geometry 1 run with an outlet pressure of $0.5\,P_i$. Diurnal variability due to surface water inputs can be seen in the development of the hydrological system. The y-axes show time in days since the initiation of the lake drainage event. The exchange in water between the conduit and sheet (f) is also included to demonstrate the dynamic coupling within the flowband model.*

Appendix C

Coupled hydrological model results

The results from the coupled hydrological model sensitivity tests are provided in this appendix. For each modelled geometry, the results are given for: maximum blister radius, L; blister dispersion time (determined as the time when the water input grid-cell in model stage 3 reaches overburden); channel growth (ΔS) over both 10 hours following drainage and 30 days following drainage; maximum channel cross-sectional area at any point in the stage 4 (seasonal) model run; and the location of the largest channel in the domain. Outputs for the modelled base parameters are highlighted in bold italics. Results are given in Table C.1 for the F-Lake planar sensitivity tests; Table C.2 for the F-Lake real topography tests; Table C.3 for the tidewater glacier tests; and Table C.4 for the marginal glacier tests. Model outputs for additional sensitivity tests are also given in Table C.5 for the surface slope tests run on the F-Lake planar geometry; Table C.6 for the ice thickness tests conducted on the F-Lake planar, the tidewater glacier and the marginal glacier geometries. Finally, Table C.7 gives the model results for the surface water runoff tests run on the F-Lake planar, the tidewater glacier and the marginal glacier geometries.

Table C.1: *Geometry 1 (F-Lake planar) results from the coupled hydrological model sensitivity tests.*

		K (m s^{-1})			E (GPa)			h_c^{sh} (m)				n' (s m^{-3})			
	$\frac{P_w}{P_i}$	**0.1**	**0.5**	**1**	**3.9**	**6.2**	**8.9**	**0.05**	**0.15**	**0.3**	**0.4**	**0.01**	**0.032**	**0.7**	**0.1**
Max. L (m)	1	2872	2889	2888	2133	2889	3377	2873	2889	2888	2893	2890	2889	2890	2890
	0.5	2878	2891	2874	2174	2891	3368	2890	2891	2892	2881	2892	2891	2893	2893
	0	2878	2888	2889	2168	2888	3373	2898	2888	2890	2871	2875	2888	2892	2889
L dispersion	1	>40	>40	>40	>40	>40	>40	>40	>40	16.5	3.7	>40	>40	>40	>40
time	0.5	>40	29.9	15.6	12.4	29.9	38.9	>40	29.9	4.0	1.4	28.1	29.9	30.7	30.8
	0	>40	16.2	7.5	7.3	16.2	21.1	>40	16.2	2.7	1.2	14.0	16.2	16.7	16.8
ΔS	1	0.00	0.00	0.00	0.00	0.00	0.00	0.00	0.00	0.00	0.00	0.01	0.00	0.00	0.00
(m^2/10 hrs)	0.5	0.02	0.01	0.01	0.01	0.01	0.01	0.01	0.01	0.01	0.00	0.04	0.01	0.01	0.00
	0	0.03	0.02	0.02	0.02	0.02	0.02	0.04	0.02	0.00	0.00	0.07	0.02	0.01	0.01
ΔS	1	0.15	0.07	0.04	0.06	0.07	0.07	0.10	0.07	0.05	0.04	0.36	0.07	0.03	0.02
(m^2/30 days)	0.5	0.39	0.45	0.03	0.43	0.45	0.46	0.57	0.45	0.05	0.01	0.76	0.45	0.12	0.07
	0	0.57	0.51	0.00	0.53	0.51	0.52	1.01	0.51	0.00	0.00	0.30	0.51	0.19	0.11
Max. S (m^2)	1	0.26	0.17	0.15	0.17	0.17	0.17	0.20	0.17	0.15	0.14	0.51	0.17	0.13	0.12
	0.5	0.53	0.60	0.14	0.58	0.60	0.61	0.75	0.60	0.15	0.11	1.01	0.60	0.24	0.18
	0	0.71	0.66	0.12	0.64	0.66	0.67	1.22	0.66	0.11	0.11	0.48	0.66	0.31	0.22
Max. S	1	5.70	4.80	4.30	4.80	4.80	4.80	8.20	4.80	3.40	3.00	11.90	4.80	3.10	2.80
location (km)	0.5	9.30	9.00	2.40	9.00	9.00	9.00	11.90	9.00	2.20	1.60	8.80	9.00	9.00	9.00
	0	8.90	4.20	2.90	4.20	4.20	4.20	11.90	4.20	2.40	2.70	4.80	4.20	3.80	3.70

Continued on next page

Table C.1: *Geometry 1 results (continued)*

		k			$W(km)$				V_0 ($m^3 \times 10^7$)				S_ϵ (m^2)		
	$\frac{P_w}{P_i}$	**0.01**	**0.05**	**0.1**	**0.5**	**1**	**1.5**	**2**	**0.01**	**0.1**	**1**	**3.8**	**0.1**	**1**	**10**
Max. L (m)	1	2889	2898	2879	2896	2873	2889	2883	565	1338	3321	6179	***2889***	2867	2878
	0.5	2891	2876	2882	2892	2879	2891	2891	522	1334	3330	6175	***2891***	2893	2876
	0	2888	2893	2893	2871	3030	2888	2869	501	1398	3322	6183	***2888***	2868	2900
L dispersion	1	>40	>40	>40	>40	>40	>40	>40	0.3	0.3	>40	>40	***>40***	>40	28.6
time (hrs)	0.5	29.9	29.5	30.1	30.3	29.2	29.9	29.9	0.3	0.3	>40	>40	***29.9***	25.6	12.6
	0	16.2	16.8	17.0	15.6	23.9	16.2	15.4	0.3	0.4	39.0	>40	***16.2***	21.4	12.7
ΔS	1	0.00	0.00	0.00	0.00	0.00	0.00	0.00	0.00	0.00	0.00	0.00	***0.00***	0.01	-0.08
(m^2/10 hrs)	0.5	0.01	0.01	0.01	0.01	0.01	0.01	0.01	0.00	0.00	0.01	0.01	***0.01***	0.02	-6.55
	0	0.02	0.02	0.02	0.02	0.02	0.02	0.02	0.00	0.00	0.03	0.03	***0.02***	0.14	-6.86
ΔS	1	0.07	0.07	0.07	0.10	0.08	0.07	0.06	0.07	0.07	0.07	0.07	***0.07***	0.96	-4.68
(m^2/30 days)	0.5	0.45	0.45	0.45	0.63	0.58	0.45	0.36	0.44	0.45	0.52	0.76	***0.45***	0.54	-8.30
	0	0.51	0.51	0.51	1.50	0.98	0.51	0.02	0.51	0.52	0.55	0.95	***0.51***	-0.10	-9.17
Max. S (m^2)	1	0.17	0.17	0.17	0.21	0.18	0.17	0.16	0.17	0.17	0.17	0.17	***0.17***	2.05	9.77
	0.5	0.60	0.60	0.61	0.83	0.75	0.60	0.50	0.54	0.55	0.68	0.94	***0.60***	1.61	3.19
	0	0.66	0.66	0.66	1.81	1.20	0.66	0.13	0.61	0.62	0.71	1.11	***0.66***	1.13	2.91
Max. S	1	4.80	4.80	4.80	5.30	4.90	4.80	4.70	4.60	4.60	4.90	6.60	***4.80***	11.90	11.90
location (km)	0.5	9.00	9.00	9.00	11.90	11.90	9.00	5.90	9.00	9.00	9.30	11.60	***9.00***	7.40	5.50
	0	4.20	4.20	4.20	11.90	8.60	4.20	2.90	4.20	4.20	4.20	6.20	***4.20***	2.90	4.10

Table C.2: *Geometry 2 (F-Lake real topography) results from the coupled hydrological model sensitivity tests.*

	$\frac{P_w}{P_i}$	K (m s^{-1})			E (GPa)			h_c^{sh} (m)				n' (s m^{-3})				k			S_ϵ (m^2)		
		0.1	**0.5**	**1**	**3.9**	**6.2**	**8.9**	**0.05**	**0.15**	**0.3**	**0.4**	**0.01**	**0.032**	**0.7**	**0.1**	**0.01**	**0.05**	**0.1**	**0.1**	**1**	**10**
Max. L	1	2918	2906	2905	2181	2906	3402	2929	2906	2914	2916	2906	2906	2912	2910	2906	2912	2914	***2906***	2913	2908
	0.8	2917	2902	2921	2141	2902	3396	2914	2902	2910	2906	2902	2902	2898	2898	2902	2916	2927	***2902***	2916	2911
	0.5	2928	2921	2924	2164	2921	3414	2914	2921	2921	2913	2917	2921	2921	2922	2921	2907	2924	***2921***	2903	2921
L **disp.**	1	>40	>40	37.8	>40	>40	>40	>40	>40	15.7	4.3	>40	>40	>40	>40	>40	>40	>40	***>40***	>40	32.7
time (hrs)	0.8	>40	>40	31.2	27.3	>40	>40	>40	>40	10.0	2.5	>40	>40	>40	>40	>40	>40	>40	***>40***	>40	18.2
	0.5	>40	34.7	18.9	13.7	34.7	>40	>40	34.7	4.8	1.7	32.3	34.7	35.3	35.7	34.7	34.5	36.0	***34.7***	27.0	13.8
ΔS	1	0.01	0.00	0.00	0.00	0.00	0.00	0.00	0.00	0.00	0.00	0.01	0.00	0.00	0.00	0.00	0.00	0.00	***0.00***	0.05	0.33
(m^2/10 hrs)	0.8	0.01	0.00	0.00	0.00	0.00	0.00	0.01	0.00	0.00	0.00	0.01	0.00	0.00	0.00	0.00	0.00	0.00	***0.00***	0.02	-1.95
	0.5	0.02	0.01	0.01	0.01	0.01	0.01	0.01	0.01	0.01	0.00	0.03	0.01	0.00	0.00	0.01	0.01	0.01	***0.01***	-0.01	-6.00
ΔS	1	0.14	0.11	0.11	0.12	0.11	0.11	0.12	0.11	0.12	0.13	0.31	0.11	0.06	0.05	0.11	0.11	0.11	***0.11***	1.01	-0.24
(m^2/30 days)	0.8	0.22	0.14	0.14	0.14	0.14	0.14	0.15	0.14	0.16	0.17	1.07	0.14	0.07	0.05	0.14	0.14	0.14	***0.14***	1.30	-6.81
	0.5	0.40	0.45	0.10	0.42	0.45	0.46	0.38	0.45	0.15	0.02	1.55	0.45	0.14	0.09	0.45	0.45	0.45	***0.45***	0.95	-7.29
Max. S	1	0.26	0.22	0.22	0.22	0.22	0.22	0.22	0.22	0.23	0.23	0.43	0.22	0.17	0.15	0.22	0.22	0.22	***0.22***	2.07	10.29
(m^2)	0.8	0.34	0.25	0.25	0.25	0.25	0.25	0.26	0.25	0.26	0.27	1.35	0.25	0.17	0.15	0.25	0.25	0.25	***0.25***	2.39	6.90
	0.5	0.53	0.59	0.21	0.56	0.59	0.60	0.52	0.59	0.26	0.12	1.69	0.59	0.25	0.19	0.59	0.59	0.59	***0.59***	2.04	3.62
Max. S	1	7.90	1.30	1.00	1.30	1.30	1.30	8.00	1.30	1.00	1.00	8.00	1.30	1.00	1.00	1.30	1.30	1.30	***1.30***	8.00	8.00
location	0.8	8.00	8.00	8.10	8.00	8.00	8.00	8.00	8.00	1.00	1.00	9.40	8.00	1.20	1.00	8.00	8.00	8.00	***8.00***	8.00	12.40
(km)	0.5	8.00	8.10	1.40	8.10	8.10	8.10	12.40	8.10	1.30	1.00	8.00	8.10	9.30	9.30	8.10	8.10	8.10	***8.10***	8.00	6.10

Table C.3: *Geometry 3 (tidewater glacier) results from the coupled hydrological model sensitivity tests.*

		K (m s^{-1})			E (GPa)			h_c^{sh} (m)				n' (s m^{-3})			
	$\frac{P_w}{P_i}$	**0.1**	**0.5**	**1**	**3.9**	**6.2**	**8.9**	**0.05**	**0.15**	**0.3**	**0.4**	**0.01**	**0.032**	**0.7**	**0.1**
Max. L (m)	1	2921	2944	2934	2185	2944	3432	2943	2944	2945	2933	2944	2944	2919	2944
	0.67	2943	2921	2921	2179	2921	3432	2937	2921	2933	2931	2922	2921	2942	2942
L dispersion time (hrs)	1	>40	36.8	19.1	15.1	36.8	>40	>40	36.8	5.4	1.7	32.7	36.8	36.0	38.2
	0.67	>40	39.6	17.6	10.0	39.6	>40	>40	39.6	5.3	1.7	33.9	39.6	>40	>40
ΔS (m^2/10 hrs)	1	0.05	0.01	0.01	0.01	0.01	0.01	0.02	0.01	0.01	0.01	0.04	0.01	0.01	0.00
	0.67	0.03	0.01	0.01	0.02	0.01	0.01	0.01	0.01	0.01	0.01	0.03	0.01	0.00	0.00
ΔS (m^2/30 days)	1	0.42	0.38	0.28	0.36	0.38	0.39	1.67	0.38	0.23	0.18	1.92	0.38	0.10	0.06
	0.67	0.49	0.45	0.36	0.46	0.45	0.46	1.51	0.45	0.32	0.19	0.73	0.45	0.11	0.06
Max. S (m^2)	1	0.55	0.56	0.43	0.53	0.56	0.57	2.09	0.56	0.33	0.28	2.04	0.56	0.22	0.17
	0.67	0.63	0.63	0.51	0.58	0.63	0.64	1.83	0.63	0.43	0.29	1.27	0.63	0.22	0.17
Max. S location (km)	1	7.50	21.70	16.40	21.60	21.70	21.70	29.80	21.70	12.50	7.20	29.80	21.70	29.80	29.80
	0.67	7.80	17.30	10.80	17.30	17.30	17.40	23.60	17.30	8.50	3.30	12.10	17.30	17.20	17.30

		k			$W(km)$				V_0 (m$^3\times10^7$)				S_ϵ (m^2)		
	$\frac{P_w}{P_i}$	**0.01**	**0.05**	**0.1**	**0.5**	**1**	**2**	**3**	**0.01**	**0.1**	**1**	**3.8**	**0.1**	**1**	**10**
Max. L (m)	1	2944	2943	2933	2935	2944	2943	2932	532	1341	3393	6019	***2944***	2922	2943
	0.67	2921	2942	2934	2919	2921	2945	2933	555	1376	3417	6023	***2921***	2939	2946
L dispersion time (hrs)	1	36.8	37.3	36.8	36.3	36.8	36.6	35.4	0.3	0.4	>40	>40	***36.8***	23.9	9.1
	0.67	39.1	>40	>40	39.9	39.6	>40	40.3	0.3	0.4	>40	>40	***39.1***	22.0	8.0
ΔS (m^2/10 hrs)	1	0.01	0.01	0.01	0.01	0.01	0.01	0.01	0.01	0.01	0.01	0.01	***0.01***	0.13	0.15
	0.67	0.01	0.01	0.01	0.01	0.01	0.01	0.01	0.08	0.01	0.01	0.01	***0.01***	0.05	-0.95
ΔS (m^2/30 days)	1	0.38	0.38	0.38	1.26	0.38	0.23	0.16	0.40	0.40	0.43	0.75	***0.38***	1.87	-0.46
	0.67	0.45	0.46	0.46	0.92	0.45	0.32	0.05	0.48	0.48	0.52	0.78	***0.45***	0.49	-9.04
Max. S (m^2)	1	0.56	0.56	0.56	1.84	0.56	0.36	0.28	0.50	0.50	0.63	1.06	***0.56***	3.25	10.15
	0.67	0.63	0.63	0.63	1.39	0.63	0.46	0.16	0.58	0.58	0.70	1.01	***0.63***	1.55	9.13
Max. S location (km)	1	21.70	21.70	21.70	29.80	21.70	12.20	4.70	21.40	21.40	22.20	29.80	***21.70***	29.80	29.80
	0.67	17.30	17.30	17.30	24.60	17.30	8.30	2.80	17.30	17.30	17.80	19.70	***17.30***	6.30	29.90

Table C.4: *Geometry 4 (marginal glacier) results from the coupled hydrological model sensitivity tests.*

	K (m s^{-1})			E (GPa)			h_c^{sh} (m)				n' (s m^{-3})			
	0.1	**0.5**	**1**	**3.9**	**6.2**	**8.9**	**0.05**	**0.15**	**0.3**	**0.4**	**0.01**	**0.032**	**0.7**	**0.1**
Max. L (m)	3011	3014	3013	3012	3014	3013	3013	3014	3013	3017	3015	3014	3012	3014
L dispersion time (hrs)	27.1	8.6	3.9	40.1	8.6	2.1	>40	8.6	0.7	0.6	7.2	8.6	8.9	9.1
ΔS (m^2/10 hrs)	0.06	0.13	0.07	0.13	0.13	0.13	0.02	0.13	0.09	0.08	0.18	0.13	0.08	0.06
ΔS (m^2/30 days)	0.41	1.28	0.69	1.21	1.28	1.29	2.05	1.28	0.50	0.38	1.59	1.28	0.34	0.23
Max. S (m^2)	0.56	1.44	0.79	1.59	1.44	1.40	2.41	1.44	0.60	0.48	1.73	1.44	0.45	0.33
Max. S location (km)	11	22.8	22.8	22.8	22.8	22.8	22.8	22.8	22.8	22.8	22.8	22.8	22.8	22.8

	k			$W(km)$				V_0 (m$^3\times$10^7)				S_ϵ (m^2)		
	0.01	**0.05**	**0.1**	**0.5**	**1**	**2**	**3**	**0.01**	**0.1**	**1**	**3.8**	**0.1**	**1**	**10**
Max. L (m)	3014	3012	3015	3014	3014	3011	3022	623	2177	3014	3014	***3014***	3010	3010
L dispersion time (hrs)	7.8	7.8	7.9	8.9	8.6	8.2	8.3	0.3	5.1	8.6	8.6	***8.6***	6.0	3.4
ΔS (m^2/10 hrs)	0.13	0.13	0.13	0.13	0.13	0.13	0.13	0.22	0.13	0.13	0.13	***0.13***	2.04	22.18
ΔS (m^2/30 days)	1.28	1.28	1.28	3.44	1.28	0.42	0.24	1.28	1.29	1.28	1.28	***1.28***	1.78	11.54
Max. S (m^2)	1.44	1.44	1.44	3.64	1.44	0.52	0.34	1.38	1.42	1.44	1.44	***1.44***	3.04	32.29
Max. S location (km)	22.8	22.8	22.8	22.8	22.8	22.8	22.8	22800	22.8	22.8	22.8	***22.8***	22.9	22.9

Table C.5: *Surface slope results from the coupled hydrological model additional sensitivity tests, applied to the F-Lake planar model.*

Surface slope (°)	$\frac{P_w}{P_i}$	0.5	0.7	1	1.5
Max. L (m)	1	2887	2898	2876	2896
	0.5	2888	2878	2880	2886
	0	2888	2875	2874	2877
L dispersion	1	>40	>40	32.69	20.70
time (hrs)	0.5	29.10	24.90	20.61	15.42
	0	16.12	15.32	14.92	14.02
ΔS	1	0.00	0.00	0.01	0.01
(m^2/10 hrs)	0.5	0.01	0.02	0.02	0.02
	0	0.02	0.02	0.02	0.02
ΔS	1	0.07	0.10	0.16	0.36
(m^2/30 days,)	0.5	0.47	0.54	0.69	1.05
	0	0.52	0.55	0.59	0.67
Max. S (m^2)	1	0.18	0.20	0.27	0.51
	0.5	0.62	0.71	0.88	1.32
	0	0.67	0.71	0.77	0.87
Max. S	1	4.9	5.4	6.3	8.5
location (km)	0.5	9.1	9.3	9.7	10.2
	0	4.2	4.4	4.8	5.7

Table C.6: *Ice thickness results from the coupled hydrological model additional sensitivity tests applied to the F-Lake planar (1), the tidewater glacier (3) and the marginal glacier (4) models.*

Ice thickness (m)	Geometry	$\frac{P_w}{P_i}$	1200	1000	800	600	400	200
Max. L (m)	1	1	2944	3456	4021	3010	2028	
		0.5	2930	3469	4017	3013	2044	
		0	2942	3467	4016	3014	2028	
	3	1	2944	3443	4017	3011		
		0.67	2921	3465	4019	3010		
	4	0	2931	3448	4016	3014	2015	1129
L dispersion	1	1	>40	>40	>40	16.32	0.42	
time (hrs)		0.5	35.92	>40	>40	7.31	0.44	
		0	19.54	>40	36.23	7.73	0.42	
	3	1	36.75	>40	>40	>40		
		0.67	39.64	>40	>40	15.07		
	4	0	17.36	35.74	30.00	8.58	0.39	
ΔS	1	1	0.00	0.00	0.00	0.00	0.00	
(m^2/10 hrs)		0.5	0.01	0.01	0.01	0.01	0.00	
		0	0.02	0.02	0.01	0.01	0.25	
	3	1	0.01	0.02	0.06	0.00		
		0.67	0.01	0.01	0.01	0.00		
	4	0	0.05	0.07	0.09	0.13	0.47	4.24
ΔS	1	1	0.07	0.06	0.06	0.05	0.05	
(m^2/30 days)		0.5	0.44	0.38	0.25	0.15	0.08	
		0	0.54	0.63	0.42	0.27	0.29	
	3	1	0.38	0.20	0.12	0.03		
		0.67	0.45	0.26	0.12	0.04		
	4	0	1.33	2.23	2.16	1.28	0.70	4.01
Max. S (m^2)	1	1	0.17	0.17	0.16	0.15	0.15	
		0.5	0.59	0.52	0.38	0.25	0.18	
		0	0.69	0.79	0.57	0.38	0.39	
	3	1	0.56	0.33	0.22	0.13		
		0.67	0.63	0.39	0.23	0.15		
	4	0	1.78	2.35	2.55	1.44	0.80	4.34
Max. S	1	1	4.8	4.9	4.8	4.5	4.3	
location (km)		0.5	9.2	10.8	11.9	11.9	11.9	
		0	4.50	6.3	8.1	10.1	2.1	
	3	1	21.7	29.8	29.8	3.1		
		0.67	17.3	17.9	17.5	16.4		
	4	0	10.1	22.8	22.8	22.8	22.8	22.9

Table C.7: *Surface water input results from the coupled hydrological model additional sensitivity tests applied to the F-Lake planar (1), the tidewater glacier (3) and the marginal glacier (4) models.*

	Geometry	$\frac{P_w}{P_i}$	90 days full runoff	90 days half runoff	30 days full runoff
Max. S (m^2)	1	1	0.48	0.29	0.17
		0.5	2.14	0.15	0.60
		0	1.29	0.13	0.66
	3	1	4.54	1.35	0.56
		0.67	3.03	1.29	0.63
	4	0	3.81	1.36	1.44
Max. S location (km)	1	1	11.9	11.9	4.8
		0.5	10.8	2.7	9.0
		0	5.0	2.9	4.2
	3	1	29.80	15.00	21.7
		0.67	15.90	10.60	17.3
	4	0	22.80	22.80	22.8
Max. S time (days)	1	1	90.00	90.00	30.00
		0.5	60.58	44.14	30.00
		0	51.47	0.10	30.00
	3	1	62.38	56.53	30.00
		0.67	53.41	56.00	30.00
	4	0	52.92	51.94	30.00